



HAL
open science

Rydberg excitation dynamics and correlations in arbitrary 2D arrays of single atoms

Henning Labuhn

► **To cite this version:**

Henning Labuhn. Rydberg excitation dynamics and correlations in arbitrary 2D arrays of single atoms. Optics [physics.optics]. Université Paris Saclay (COMUE), 2016. English. NNT : 2016SACLO002 . tel-01346557

HAL Id: tel-01346557

<https://pastel.hal.science/tel-01346557>

Submitted on 19 Jul 2016

HAL is a multi-disciplinary open access archive for the deposit and dissemination of scientific research documents, whether they are published or not. The documents may come from teaching and research institutions in France or abroad, or from public or private research centers.

L'archive ouverte pluridisciplinaire **HAL**, est destinée au dépôt et à la diffusion de documents scientifiques de niveau recherche, publiés ou non, émanant des établissements d'enseignement et de recherche français ou étrangers, des laboratoires publics ou privés.

NNT : 2016SACLO002

THÈSE DE DOCTORAT
DE
L'UNIVERSITÉ PARIS-SACLAY
PRÉPARÉE À
L'INSTITUT D'OPTIQUE GRADUATE SCHOOL

ÉCOLE DOCTORALE N°572
Ondes et Matière

Spécialité de doctorat : Physique

Par

M Henning Labuhn

Rydberg excitation dynamics and correlations
in arbitrary 2D arrays of single atoms

Thèse présentée et soutenue à Palaiseau, le 26 février 2016 :

Composition du Jury :

M. Gerhard Birkel	Professeur	Universität Darmstadt	Rapporteur
M. Matt Jones	Professeur	Durham University	Rapporteur
M. Pierre Pillet	Directeur de Recherche	Laboratoire Aimé Cotton	Président du jury
M. Matthias Weidemüller	Professeur	Universität Heidelberg	Examineur
M. Antoine Browaeys	Directeur de Recherche	Laboratoire Charles Fabry	Directeur de thèse
M. Thierry Lahaye	Chargé de Recherche	Laboratoire Charles Fabry	Invité

Meinen Eltern

Contents

1	Introduction	9
2	Exciting a single atom to a Rydberg state	17
2.1	The interesting properties of Rydberg atoms	17
2.2	A short overview of the experimental setup	19
2.2.1	The experimental apparatus	21
2.2.2	Trapping a single atom in an optical microtrap	22
2.3	Atom-light interaction	23
2.4	Driving coherent optical ground-Rydberg transitions	24
2.4.1	Ground state preparation	24
2.4.2	Coherent two-photon excitation	24
2.4.3	Excitation lasers	27
2.5	Driving coherent microwave Rydberg-Rydberg transitions	29
2.6	Rydberg-Rydberg interactions	31
2.7	Conclusion	35
3	Generation of arbitrary 2D arrays of optical dipole traps	37
3.1	Spatial phase manipulation of a Gaussian beam	37
3.1.1	Optical phase modulation using a spatial light modulator	38
3.1.2	The Gerchberg-Saxton phase retrieval algorithm	40
3.1.3	Phase retrieval on a discrete grid	42
3.2	Implementation of the SLM in the experiment	44
3.2.1	Optics setup	47
3.2.2	Numerical implementation	48
3.3	Aberration correction	51
3.3.1	Correcting the aberrations of the optical components	52
3.3.2	Quantifying the effect of the aberration correction	56
3.4	Feedback for intensity homogeneity	59
3.5	Gallery of trap arrays	63
3.6	Conclusion	65

4	Spatially resolved state detection and manipulation in arrays of single atoms	67
4.1	Determination of the state of the atoms in the microtraps	67
4.1.1	Detection of the atomic fluorescence	67
4.1.2	Loading statistics	71
4.1.3	Detection of Rydberg excitations	74
4.1.4	Impact of detection errors	76
4.2	Single site resolved addressing	77
4.2.1	Locally blocking Rydberg excitations	81
4.2.2	In-trap Rydberg excitation	83
4.2.3	Local manipulation of a two-body wave function	84
4.3	Conclusion	86
5	The collective enhancement of the Rydberg excitation in fully blockaded ensembles	89
5.1	The role of the anisotropy of the interaction	91
5.2	Experimental observation of the Rydberg blockade in a fully blockade ensemble	93
5.3	Analysis of the experimentally observed imperfect blockade	98
5.3.1	Analysis of the possible sources of noise	98
5.3.2	Double-excitation analysis	102
5.4	Conclusion	104
6	Realisation of the Quantum Ising model in 1D and 2D arrays of Rydberg atoms	105
6.1	A ring of 8 atoms	107
6.2	Partially filled quasi-1D array	115
6.3	Partially filled 7x7 square lattice	120
6.4	Conclusion	125
7	The Rydberg blockade in the resonant dipole-dipole regime	127
7.1	Theoretical description	127
7.2	Microwave spectroscopy of a resonantly interacting two-atom system	129
7.3	A possible extension to many atoms	131
7.4	Conclusion	133
8	Conclusion and outlook	135
	Publications	139
	Bibliography	189

Introduction

The ability to experimentally isolate, manipulate, and observe quantum systems at the single particle level has developed to an important tool in the study of quantum mechanics. Even though Erwin Schrödinger himself said as late as 1952 that it “is fair to state that we are not experimenting with single particles, any more than we can raise Ichthyosauria in the zoo”, only that “in thought experiments, we sometimes assume that we do” [Schrödinger, 1952], scientist have long begun to study quantum mechanics on a single particle level. In 2012, the Nobel Prize in physics was awarded to Serge Haroche and David Wineland for their “ground-breaking experimental methods” in this field [Haroche, 2013; Wineland, 2013]. Since their pioneering results, one line of evolution from those fundamental experiments was to extend the investigation of single quantum systems to ensembles of larger numbers of interacting quantum particles. This allowed the study of fundamental quantum mechanical effects such as entanglement, probing e.g. the Bell inequalities [Brunner *et al.*, 2014] or the propagation of entanglement [Cheneau *et al.*, 2012; Jurcevic *et al.*, 2014].

The outstanding level of experimental control over such multi-particle quantum systems has furthermore led to a new field of research in quantum physics, the simulation of physical systems under well controlled conditions. Richard Feynman [1982] first proposed this idea of a quantum simulator more than 30 years ago, motivated by the fact that the information one needs to store on a classical computer for the numerical treatment of a quantum mechanical problem scales exponentially with the number of particles [Hauke *et al.*, 2012; Georgescu, Ashhab, and Nori, 2014].

For instance, due to the small length scales in condensed matter systems, it is often impossible to probe microscopic physical properties *in situ*. Likewise, the theoretical study of strongly correlated quantum systems on a microscopic level, such as electrons in a high T_c superconductor, often reaches the limit of what is possible to calculate numerically on a classical computer, as soon as the system size exceeds a few tens of particles.

Quantum simulation is an alternative approach to study such effects, which consists in ‘building’ a well-controllable quantum system, rules by the same many-body

Hamiltonian as the simulated system, with access to microscopic observables and phase diagrams in the laboratory. A prime example of this approach is the study of spin Hamiltonians. Despite their seemingly simple character, they can often be used to describe the complex dynamics in strongly correlated materials [Auerbach, 2012], yet for many cases especially the dynamics of the system cannot be computed on classical computers as soon as the system size exceeds a few tens of spins.

A useful quantum simulator, independent of the chosen system, needs to fulfil three main technical requirements, assuming already a successful implementation of a given model, i.e. that there is a direct mapping between the simulated system and the simulator [Somaroo *et al.*, 1999]. First, the quantum simulator needs to be scalable to large number of particles, in order to play out its advantage for example over a numerical simulation on a classical computer. Second, its coherence time needs to be sufficiently larger than the important timescales of the involved physics, in order to retain the quantum nature of the simulation. Third, the quantum simulator needs to be benchmarked, for instance against an analytically known solution or a numerical calculation in a regime where this is still possible, or a different quantum simulator, in order to affirm the validity of a result when simulating a given problem.

The realisation of a fully reconfigurable quantum simulator fulfilling all three requirements has yet to be demonstrated. However, implementing aforementioned spin Hamiltonians in the lab has already proven to be successful with various quantum systems [Georgescu, Ashhab, and Nori, 2014].

Ions, trapped in a combination of static and oscillating electric and / or magnetic fields, arrange themselves due to their strong Coulomb repulsion, forming a so-called Coulomb crystal [Britton *et al.*, 2012; Monroe and Kim, 2013]. Both their internal and external degrees of freedom of the ions can be manipulated with high precision using lasers or microwave fields. The dynamics of the Coulomb crystal depends on the applied fields, and can be tuned such that it can be mapped to a spin Hamiltonian, with tunable, long-range interactions [Blatt and Roos, 2012; Schneider, Porras, and Schaetz, 2012; Monroe *et al.*, 2015]. Increasing the number of ions also increases the number of vibrational modes in the crystal, making the experimental control of the Coulomb crystal increasingly challenging when increasing the number of spins. However, a recent report claimed the generation of entanglement in a system of more than 200 ions [Bohnet *et al.*, 2015].

The quantum simulation of spin Hamiltonians with ultra-cold polar molecules is likewise under investigation [Ortner *et al.*, 2009; Peter *et al.*, 2015], and despite being technically challenging, large progress has been made in this field recently [Moses

et al., 2015].

Another promising platform are single neutral atoms trapped in optical lattices. The combination of tunnelling and on-site interaction of the atoms for example can be mapped on an Ising-type Hamiltonian [Simon *et al.*, 2011; Struck *et al.*, 2011]. The number of spins, i.e. single atoms, can be scaled relatively easily by increasing the size of the optical lattice, with the arrangement of the atoms being given by the underlying shape of the optical lattice. Even though complex geometries such as kagome lattices can be realised [Windpassinger and Sengstock, 2013], the flexibility of the geometry of optical lattices is somewhat limited. The generally weak interactions of neutral atoms provide a good isolation from the environment, thus limiting the effects of decoherence in the quantum system. However, the atom-atom interactions are therefore usually limited to nearest neighbours.

One possibility to generate interactions among neutral atoms that extend beyond nearest neighbours is to excite them to so-called Rydberg states, which are states where one of the electrons of the atom possesses a high principal quantum number n . In a classical picture of the atom, this corresponds to one electron orbiting far away from the ionic core on atomic length scales, thus forming an oscillating electric dipole. Two of such Rydberg atoms can show very strong dipolar interactions over distances of several tens of microns [Gallagher, 2005; Saffman, Walker, and Mølmer, 2010].

One consequence of those strong long-range interactions, and a major motivation for the study of Rydberg atoms itself, is the Rydberg blockade. It plays an important role in numerous proposals for both quantum simulation and its generalisation to any sort of computational problem [Nielsen and Chuang, 2011] in quantum information processing. The Rydberg blockade was first proposed for applications in quantum information by Jaksch *et al.* [2000] and Lukin *et al.* [2001]. The Rydberg blockade lies at the heart of many applications of Rydberg atoms, as for example for the realisation of quantum gates (see e.g. [Wilk *et al.*, 2010; Maller *et al.*, 2015; Jau *et al.*, 2015], or [Saffman, Walker, and Mølmer, 2010] for a review) highly non-classical states of light [Gorniaczyk *et al.*, 2014; Baur *et al.*, 2014], or the study of self-ordered phases of matter [Schauss *et al.*, 2015].

To picture the concept of Rydberg blockade, we consider an ideal two-level atom, made up of the ground state $|g\rangle$ and the Rydberg state $|r\rangle$, which are laser coupled with a coupling strength set by the Rabi frequency Ω . For two of those atoms, if their interatomic distance R is large, such that the van der Waals interaction V_{vdW} can be neglected compared to the laser coupling strength, i.e. $V_{\text{vdW}} \ll \hbar\Omega$, the atoms can be seen as independent particles, and thus both can be excited to the Rydberg state at

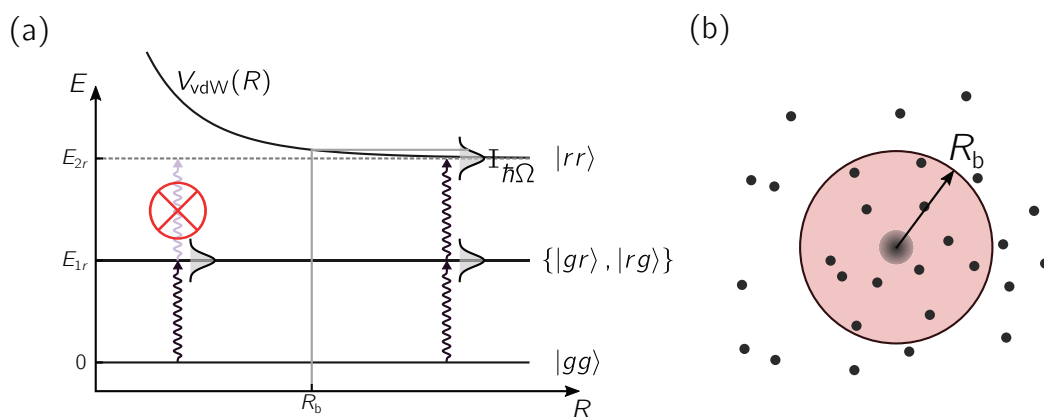


Figure 1.1: Illustration of the Rydberg blockade in the van der Waals regime. For large interatomic distances R , the energy shift $V_{vdW}(R)$ can be neglected compared to the coupling strength $\hbar\Omega$ between the ground and the Rydberg state, and the atoms behave independently from each other. For distances smaller than the blockade radius R_b , the excitation of $|rr\rangle$ is no longer resonant, leading to the blockade of a second Rydberg excitation. (b) Blockade sphere in an ensemble of atoms, for isotropic interactions.

the same time. On the other hand, for small interatomic distances, the van der Waals interaction between the Rydberg states can become very strong, and lead to an energy shift of the state $|rr\rangle$ where both atoms are in the same Rydberg state, of magnitude $V_{vdW}(R) = C_6/R^6$. If this energy shift is larger than the laser coupling strength, i.e. $V_{vdW}(R) \gg \hbar\Omega$, then the excitation of the doubly excited state is no longer possible, as depicted in Figure 1.1(a). This suppression of having more than a single excitation inside a certain volume is called Rydberg blockade. For the van der Waals interaction, the extension of the blockade volume is given by the blockade radius, the distance at which the interaction and the coupling strength are equal,

$$R_b = \sqrt[6]{\frac{C_6}{\hbar\Omega}}. \quad (1.1)$$

As the van der Waals interaction scales as $C_6 \sim n^{11}$, the blockade radius thus increases as $n^{11/6}$ with the principal quantum number n . For typical parameters of our experiment, the blockade radius is usually in a 2 – 20 μm range. The Rydberg blockade has been observed experimentally in cold atomic gases [Tong *et al.*, 2004; Singer *et al.*, 2004; Comparat and Pillet, 2010], optical lattices [Viteau *et al.*, 2011], Bose-Einstein condensates [Heidemann *et al.*, 2008; Balewski *et al.*, 2013], and for two single atoms [Urban *et al.*, 2009; Gaëtan *et al.*, 2009; Hankin *et al.*, 2014].

In this thesis, we present an original and complementary experimental approach for the quantum simulation of spin-1/2 particles, using single neutral atoms trapped in arbitrary two-dimensional arrays of microtraps, excited to Rydberg states. We holographically create 2D arrays of optical single-atom traps in arbitrary geometries, with trap separations ranging from $\sim 3 \mu\text{m}$ to a few tens of μm . In order to create strong correlations among the atoms, we coherently couple the ground-state atoms to Rydberg states. This allows us to observe the Rydberg blockade in systems of up to 15 atoms, having exact knowledge of the initially prepared number of ground state atoms. In a second set of experiments we reduce the Rydberg blockade radius to a few lattice sites. We can thereby simulate a system of spin-1/2 particles governed by the quantum Ising model, in different one- and two-dimensional arrays of up to 30 atoms. We benchmarked the measured Rydberg dynamics and correlations against a numerical simulation of an equivalent spin-1/2 system.

The results of this thesis have been realised together with Sylvain Ravets and Daniel Barredo, on an experiment built by Lucas Béguin and Aline Vernier [Béguin, 2013]. During the course of this thesis, we probed the interaction between two and three atoms, both for the regime of the van der Waals interaction and the regime of resonant dipole-dipole interaction [Ravets, 2014]. The main goal of my work was to extend the existing experimental setup to create arrays of single neutral atoms in arbitrary 2D geometries. The results presented here show that our experiment is an ideal candidate to study strongly-correlated many-body quantum systems.

This thesis is organised in the following way. In Chapter 2 we give an overview of the general experimental setup, the cooling and trapping of single atoms, and our Rydberg excitation scheme. In Chapter 3 we show how we can holographically create arbitrary arrays of optical microtraps by manipulating the spatial phase of a laser beam with a spatial light modulator. We thereafter in Chapter 4 present the spatially resolved state detection and manipulation of trapped single atoms. We present the main results obtained during this thesis, the collective Rydberg excitation of ensembles of up to 15 atoms in Chapter 5, and the observed spatial correlations of Rydberg excitation dynamics in various dimensions and geometries in Chapter 6. In Chapter 7 we probe the Rydberg blockade and the resulting collective enhancement for the case of resonant dipole-dipole interaction between two single atoms.

Parts of the results obtained during this thesis have been published in the following publications:

- **Single-atom trapping in holographic 2D arrays of microtraps with arbitrary geometries**

Florence Nogrette, Henning Labuhn, Sylvain Ravets, Daniel Barredo, Lucas Béguin, Aline Vernier, Thierry Lahaye and Antoine Browaeys,
Physical Review X **4**, 021034 (2014)

- **Single-atom addressing in microtraps for quantum-state engineering using Rydberg atoms**

Henning Labuhn, Sylvain Ravets, Daniel Barredo, Lucas Béguin, Florence Nogrette, Thierry Lahaye and Antoine Browaeys,
Physical Review A **90**, 023415 (2014)

- **Demonstration of a strong Rydberg blockade in three-atom systems with anisotropic interactions**

Daniel Barredo, Sylvain Ravets, Henning Labuhn, Lucas Béguin, Aline Vernier, Florence Nogrette, Thierry Lahaye and Antoine Browaeys,
Physical Review Letters **112**, 183002 (2014)

- **Coherent excitation transfer in a “spin chain” of three Rydberg atoms**

Daniel Barredo, Henning Labuhn, Sylvain Ravets, Thierry Lahaye, Antoine Browaeys and Charles S. Adams,
Physical Review Letters **114**, 113002 (2015)

- **Coherent dipole-dipole coupling between two single Rydberg atoms at an electrically-tuned Förster resonance**

Sylvain Ravets, Henning Labuhn, Daniel Barredo, Lucas Béguin, Thierry Lahaye and Antoine Browaeys,
Nature Physics **10**, 914917 (2014)

- **Measurement of the angular dependence of the dipole-dipole interaction between two individual Rydberg atoms at a Förster resonance**

Sylvain Ravets, Henning Labuhn, Daniel Barredo, Thierry Lahaye and Antoine Browaeys,
Physical Review A **92**, 020701(R) (2015)

-
- **A highly-tunable quantum simulator of spin systems using two-dimensional arrays of single Rydberg atoms**

Henning Labuhn, Daniel Barredo, Sylvain Ravets, Sylvain de Léséleuc, Tommaso Macrì, Thierry Lahaye and Antoine Browaeys,

accepted for publication in Nature (2016), arXiv preprint 1509.04543v2 (2015)

Exciting a single atom to a Rydberg state

In recent years, research about Rydberg physics has seen an enormous revival. After the properties of Rydberg atoms had been studied extensively throughout the 20th century, its possible applications in quantum information, quantum simulation, and the study of fundamental physics re-sparked a large interest in the beginning of the 21st century [Saffman, Walker, and Mølmer, 2010].

Nowadays, the fields in which the properties of Rydberg states are used and studied, extend from cold [Mourachko *et al.*, 1998; Singer *et al.*, 2004] and ultra-cold atoms [Heidemann *et al.*, 2008; Viteau *et al.*, 2011; Schauß *et al.*, 2012] to hot vapours [Kübler *et al.*, 2010], ions [Feldker *et al.*, 2015], and even excitons in natural copper oxide crystals [Kazimierczuk *et al.*, 2014]. During the course this thesis, we have studied Rydberg excitations of arrays of single neutral atoms trapped in individual optical microtraps.

In this chapter, we will describe the characteristics of Rydberg states which are of importance for the rest of this thesis. We will then give a brief overview of the general setup of the experiment, and the mechanism which allows us to isolate a single neutral atom. We will show how we coherently couple the ground state of the single atom to a given Rydberg state using a coherent optical two-photon transition, and finally present the two regimes of the Rydberg-Rydberg interaction which are important in this thesis.

2.1 The interesting properties of Rydberg atoms

Rydberg atoms are atoms in an electronically highly excited state, meaning that one of its electrons has a large principal quantum number n , typically in the range $30 < n < 200$. They are named after Swedish physicist Johannes Rydberg, who generalised the empirical formula for the wavelengths of the spectral lines in hydrogen found by Balmer [Balmer, 1885] to other elements [Rydberg, 1890]. Building upon

the work of Rydberg, Niels Bohr later found a theoretical model [Bohr, 1913] for the binding energies in hydrogen,

$$E_n = -hc \frac{R_\infty}{n^2}, \quad (2.1)$$

which depends solely on the principal quantum number n of the atom, the Planck constant h , the speed of light c and the Rydberg constant R_∞ . The Rydberg constant itself is defined only in terms of fundamental physical constants:

$$R_\infty = \frac{m_e e^4}{8 \varepsilon_0^2 h^3 c}, \quad (2.2)$$

where m_e is the rest mass of the electron, e the elementary charge and ε_0 the vacuum permittivity. One finds that, just like the binding energy, most properties of the hydrogen atom follow a characteristic scaling with n .

Alkali atoms, the elements in the first main-group of the periodic table, show a very similar behaviour, as they, just like hydrogen, possess only one valence electron. The electrons on the inner shells of the alkali atoms ‘shield’ all but one electric core charge. In good approximation, the single valence electron effectively only sees a single core charge, and thus behaves very similar to a hydrogen atom. However, if the valence electron is in low orbital angular momentum states $l \leq 3$, it can penetrate the inner shells of the atom, and thus see a slightly increased core charge compared to the valence electron of a hydrogen atom. One can use quantum defect theory [Jungen, 1988; Gallagher, 2005] to correct for this slight modification of the core charge. The

Table 2.1: Selection of scaling laws for properties of Rydberg atoms. The properties of Rydberg atoms follow universal scaling laws as a function of the effective principal quantum number n^* (from [Gallagher, 2005]).

property	expression	scaling	value for 82D
binding energy	E_n	$(n^*)^{-2}$	500 GHz
electron orbital radius	$\langle r \rangle$	$(n^*)^2$	$0.5 \mu\text{m}$
lifetime (at $T = 300$ K)	τ	$(n^*)^3$	$200 \mu\text{s}$
polarisability	α	$(n^*)^7$	$2500 \text{ MHz}/(\text{V}/\text{cm})^2$
transition dip. matrix element	$\langle 5P \hat{d} nD \rangle$	$(n^*)^{-3/2}$	$0.01 e a_0$
energy level spacing	$E_{n+1} - E_n$	$(n^*)^{-3}$	12 GHz
resonant dipole-dipole coupling	C_3	$(n^*)^4$	$25 \times 10^4 \text{ MHz } \mu\text{m}^3$
van der Waals coefficient	C_6	$(n^*)^{11}$	$-9 \times 10^6 \text{ MHz } \mu\text{m}^6$

Rydberg formula then changes to

$$E = -hc \frac{R^*}{(n^*)^2}, \quad (2.3)$$

with $n^* = n - \delta_\ell$ being the effective quantum number of the valence electron, δ_ℓ the so-called quantum defect, and the effective Rydberg constant $R^* = \frac{R_\infty}{1+m_e/m_c}$, where m_e and m_c are the electron and the atomic core mass respectively. The quantum defect is different for different electronic states, and depends mostly on the orbital angular quantum number ℓ and becomes small for $\ell \geq 3$. It also depends to a lesser extent to the total angular momentum quantum number j . Quantum defects for Rubidium have been measured accurately by millimetre-wave spectroscopy [Li *et al.*, 2003; Han *et al.*, 2006]. Together, one can easily compute the values of various atomic properties of different atomic species by using simple scaling laws, with a selection of them shown in Table 2.1.

We see that the strong scaling with n of both the resonant dipole-dipole interaction (scaling as $1/R^3$ with the distance) and the van der Waals interaction (scaling as $1/R^6$ with the distance) can result in interaction strengths of many MHz for atomic separations of several μm for high principal quantum numbers, making Rydberg states an ideal ‘tool’ for our experiment. The Rydberg-state lifetimes in the order of $100 \mu\text{s}$ are much longer than a typical duration of our experiment of $\sim 3 \mu\text{s}$. On the other hand, the strong polarisability of Rydberg states makes them very sensitive to electric fields, so one needs to take care in the design of the experiment to keep the electric field as small as possible.

2.2 A short overview of the experimental setup

An experimental apparatus to perform Rydberg experiments with single atoms has to fulfil several requirements. We need:

- A reservoir of cold atoms, from which we eventually load atoms into the microtrap. A good loading rate of atoms into the trap is needed to ensure a fast duty cycle of the experiment.
- An optical dipole trap capable of reliably trapping a single atom.
- Both electric and magnetic field control to compensate for stray fields in the vicinity of the atoms, in order to achieve long coherence times.

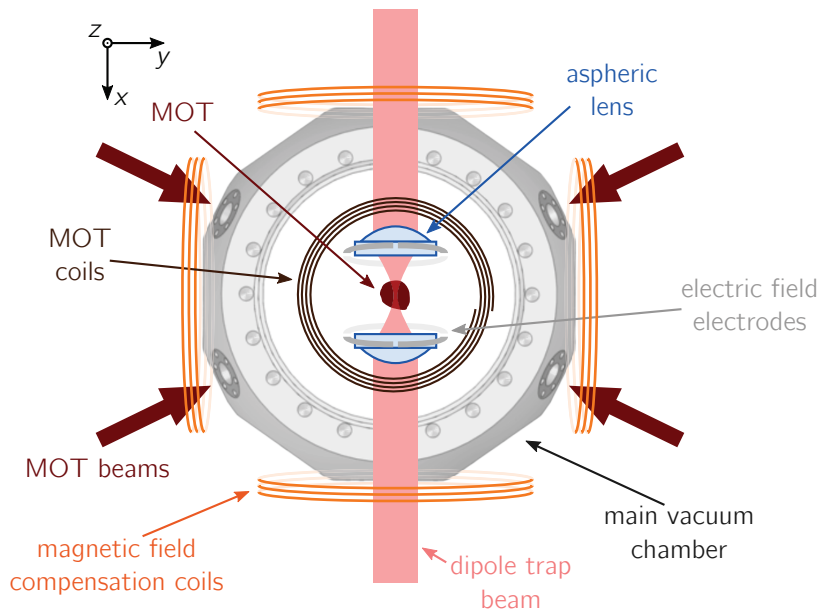


Figure 2.1: Schematics of the experimental vacuum chamber. The dipole trap beam is focused and recollimated by the pair of aspheric lenses. Its focus with a $\simeq 1 \mu\text{m}$ size is in the centre of a MOT of cold ^{87}Rb atoms. Four electrodes are placed around each aspheric lens, in order to apply arbitrary electric fields at the position of the atoms. Three pairs of magnetic field coils are used to define a quantisation axis in z -direction, and to compensate any transversal magnetic field in x - and y -direction. (The MOT beams, MOT and magnetic compensation coils in z -direction are not shown.)

- A laser system to coherently couple the ground state of the atom to Rydberg states.
- An imaging system capable of a spatially resolved state detection of the atoms.

In the following we will see how these points are realised in our experiment. An overview of the general experimental setup is given in the rest of this chapter. A more detailed description can be found in the PhD thesis of Lucas Béguin [2013]. The extension of the experiment to perform Rydberg experiments with arrays of single atoms, carried out during this thesis, will be described in the following chapters. The detailed implementation of creating arbitrary multi-trap arrays will be discussed in Chapter 3, and of the state detection of the atoms in Chapter 4.

2.2.1 The experimental apparatus

A schematic overview of the main vacuum chamber is shown in Figure 2.1. A magneto-optical trap (MOT) is loaded from a Zeeman slower to create our reservoir of cold ^{87}Rb atoms. As the interaction between Rydberg atoms is fairly independent of the atomic species, we chose to work with ^{87}Rb , since it is an element which is comparably straightforward to cool and trap. Additionally, since it is an alkali atom, its single valence electron is only weakly bound and can be excited to Rydberg states with commercially available lasers systems.

The MOT is placed between a pair of custom aspheric lenses¹ with a high numerical aperture of $\text{NA} = 0.5$ and an effective focal length of $f = 10$ mm, which focuses the dipole trap beam of wavelength 850 nm down to a waist $w_0 \simeq 1 \mu\text{m}$ [Sortais *et al.*, 2007]. The dipole trap beam is recollimated by the second aspheric lens, to image the trap intensity at the focal plane of the lenses onto a CCD camera.

As the polarisability of Rydberg states scales as n^7 with the principal quantum number, they become more and more sensitive to electric fields as one increases n . In order to avoid the mixing of Rydberg states due to electric fields, it is important to reduce the electric field at the position of the atoms as good as possible. In order to have very low stray fields in the first place, the flat side of the aspheric lenses facing the atoms is coated with a $\simeq 200$ nm thick conductive layer of indium tin oxide (ITO) which is connected to ground.

In order to null any remaining electric fields, or to apply a specific electric field in any direction if needed, a set of eight electrodes is placed around the two aspheric lenses. This configuration allows to easily control the amplitude and the direction of the electric field at the position of the atoms. By performing Stark spectroscopy on Rydberg states we can compensate for stray electric fields, and achieve residual fields well below $\simeq 5$ mV/cm. A more detailed description of the electric field control can be found in the PhD theses of Lucas Béguin [2013] and Sylvain Ravets [2014].

Three independent pairs of Helmholtz coils, centred on the main axis of the vacuum chamber as shown in Figure 2.1, are used to apply a +6 G quantisation field along the z -direction, while at the same time minimising stray transversal magnetic fields at the position of the single atoms. The calibration of the magnetic fields was done using Raman spectroscopy with Rydberg states, as was explained in [Béguin, 2013].

¹The aspheric lenses were fabricated by LightPath Technologies.

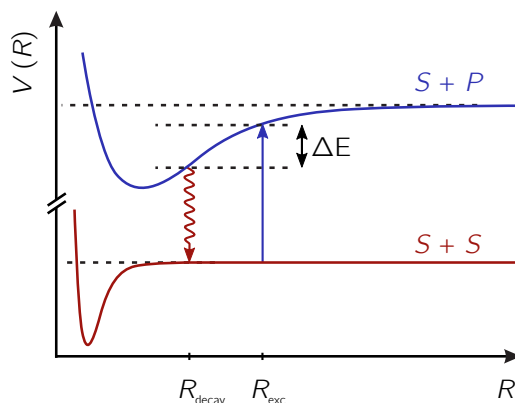


Figure 2.2: Schematics of the light-assisted collisions. The light from the collision beam (in our case the MOT beams) creates a loosely bound pair of an S - and P -state Rb atom. After a some time the pair decays back to ground state, with a kinetic energy ΔE acquired by the atoms.

2.2.2 Trapping a single atom in an optical microtrap

The core of our experimental apparatus is the possibility to trap an individual neutral ^{87}Rb atom in an optical microtrap. This technique was pioneered by [Schlosser *et al.* \[2001\]](#) at the Institut d’Optique more than a decade ago.

The optical microtraps are produced by focusing a far red-detuned dipole trap beam down to a $1/e^2$ -radius of $w_0 \simeq 1 \mu\text{m}$, approximately at the centre of our MOT. The light exerts a dipole force on the atoms, creating a conservative potential

$$U(\mathbf{R}) \propto \frac{I(\mathbf{R})}{\Delta} \quad (2.4)$$

for the atoms, with the dipole trap intensity $I(\mathbf{r})$ and the detuning Δ from the atomic transition [[Grimm, Weidemüller, and Ovchinnikov, 2000](#)]. With a typical total power of $P_0 \simeq 3.5 \text{ mW}$ in the trap beam we measure a trap depth of $U_0 \simeq h \times 20 \text{ MHz} \simeq k_B \times 1 \text{ mK}$.

Atoms will continuously enter the trap at random times from the reservoir of atoms in the MOT around the microtrap. The small volume of our trap, on the order of $\sim 1 \mu\text{m}^3$, allows us to work in a regime where, in timescales relevant to our experiment, at most one atom is present in the trap at the same time. This is due to inelastic light-assisted collisions between pairs of atoms in the microtrap. The principle of these collisions is depicted in [Figure 2.2](#). When a pair of atoms in the $5S$ ground state is present in the trap, the MOT cooling light, which is slightly red-detuned from the

$5S \leftrightarrow 5P$ transition, will photo-associate the atoms to a loosely bound pair, with one atom in the $5S$ and the other atom in the $5P$ state. The pair will pick up kinetic energy ΔE by approaching the minimum of the potential curve, before radiatively decaying back to the ground state, after a time given by the lifetime of the bound state. As $\Delta E > U_0$, the two atoms are expelled from the trap², on a timescale of ~ 1 ms [Fuhrmanek *et al.*, 2012].

In order to have at most one atom in the trap, the two-body loss rate must be larger than the rate with which the atoms are loaded into the microtrap from the MOT. This can easily be achieved by adjusting the density of atoms in the MOT [Schlosser, Reymond, and Grangier, 2002].

2.3 Atom-light interaction

All of the manipulations of our atoms are purely done by optical means. Moreover, the excitation of the atom to a Rydberg state is done in a coherent way using optical pulses. We can see the atoms as a two-level system consisting of the ground state $|g\rangle$ and a Rydberg state $|r\rangle$, which is coherently driven by the excitation light field. Such systems have been studied extensively (see e.g. [Cohen-Tannoudji, Dupont-Roc, and Grynberg, 1998]). Its dynamics can be described by the optical Bloch equations

$$\dot{\hat{\rho}} = -\frac{i}{\hbar} [\hat{H}, \hat{\rho}] + \hat{\mathcal{L}}[\hat{\rho}], \quad (2.5)$$

with the Hamiltonian

$$\hat{H} = \begin{pmatrix} 0 & \Omega/2 \\ \Omega/2 & \delta \end{pmatrix}. \quad (2.6)$$

Here Ω and δ are the two-level Rabi frequency and the detuning from the atomic resonance. Dissipation, in our case mainly due to off-resonant spontaneous emission through the intermediate state, is taken into account by the Lindblad superoperator

$$\hat{\mathcal{L}}[\hat{\rho}] = \frac{\gamma}{2}(2\hat{\sigma}_{gr}\hat{\rho}\hat{\sigma}_{rg} - \hat{\sigma}_{rr}\hat{\rho} - \hat{\rho}\hat{\sigma}_{rr}), \quad (2.7)$$

with σ_{rg} , σ_{gr} being the transition operators between the ground and Rydberg state, σ_{rr} the projection operator on the Rydberg state, and γ a phenomenological damping rate.

²If the kinetic energy ΔE is shared unevenly among the atoms, it can happen that only one of the two atoms leaves the trap. We typically observe a probability of one atom remaining in the trap of $\sim 5\%$

One finds that, assuming that at $t = 0$ the entire population of the atom is in $|g\rangle$, the probability of a resonantly driven atom ($\delta = 0$) to be in the Rydberg state as a function of time is given by [Loudon, 2000]

$$P_r(t) = 1 - \frac{\Omega^2}{2\Omega^2 + \gamma^2} \left[1 + e^{-3\gamma t/4} \left(\cos(\tilde{\Omega}t) + \frac{3\gamma}{4\tilde{\Omega}} \sin(\tilde{\Omega}t) \right) \right], \quad (2.8)$$

with $\tilde{\Omega} = \sqrt{\Omega^2 + \gamma^2/4}$. For $\Omega \gg \gamma$, the population will thus undergo Rabi oscillations between the two states $|g\rangle$ and $|r\rangle$, with Rabi frequency Ω .

2.4 Driving coherent optical ground-Rydberg transitions

As soon as a single atom has been detected in the microtrap (for a description of the state detection of the atoms, see Chapter 4), we dispose of the atomic reservoir by turning off the MOT light for a few milliseconds, ending up with a single atom in the microtrap surrounded by vacuum. In this section we will describe how we coherently excite this isolated single ground state atom to a Rydberg state.

2.4.1 Ground state preparation

In order to coherently excite the trapped atom to a given Rydberg state with high efficiency, we need to prepare the atom in a well-defined initial ground state. After the MOT cooling light has been switched off, the MOT repumping light, driving the $|5S_{1/2}, F = 1\rangle \leftrightarrow |5P_{3/2}, F' = 2\rangle$ transition, is left on to trap the atomic state in the $F = 2$ hyperfine manifold of the $5S_{1/2}$ state. We then apply a $|\mathbf{B}| = +6.6$ G magnetic field along the z -axis to have a well-defined quantisation axis, and optically pump the atom in the $|g\rangle = |5S_{1/2}, F = 2, m_F = 2\rangle$ stretched state, by a σ^+ -polarised laser beam near-resonant with the $|5S_{1/2}, F = 2\rangle \leftrightarrow |5P_{3/2}, F' = 2\rangle$ transition.

2.4.2 Coherent two-photon excitation

The transition frequencies between the ground state and Rydberg states are typically in the ultraviolet. For Rubidium the transition frequency corresponds to a wavelength of ~ 297 nm. Coherent Rydberg excitations using single photon transition have been demonstrated recently [Hankin *et al.*, 2014], but the operation of laser systems with the appropriate wavelength is not an easy task, which is why we chose to use an

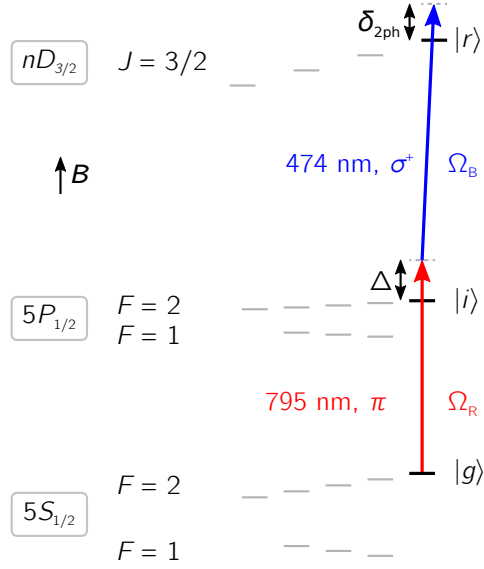


Figure 2.3: Relevant atomic states involved in the Rydberg excitation. The atoms are initially prepared in the ground state $|g\rangle = |5S_{1/2}, F = 2, m_F = 2\rangle$. A two-photon transition, off-resonant from the intermediate state $|i\rangle = |5P_{1/2}, F = 2, m_F = 2\rangle$ by $\Delta = 2\pi \times 740$ MHz, couples to the Rydberg state $|r\rangle = |nD_{3/2}, m_j = 3/2\rangle$. As the hyperfine structure of Rydberg states is smaller than the linewidth of the laser excitation, we express the Rydberg state in the fine structure basis (level spacings are not to scale).

off-resonant two-photon excitation scheme instead (see Figure 2.3).

We couple the ground state $|g\rangle$ to the Rydberg state $|r\rangle = |nD_{3/2}, m_j = 3/2\rangle$, with a detuning from the intermediate state $|i\rangle = |5P_{1/2}, F = 2, m_F = 2\rangle$ of $\Delta = 2\pi \times 740$ MHz, and single photon Rabi-frequencies Ω_R and Ω_B for the lower (red) and upper (blue) transition respectively.

We choose to work with Rydberg D - instead of S -states, since they show stronger optical coupling strengths, and larger Rydberg-Rydberg interactions, and the anisotropy in the van der Waals interaction of D states can lead to interesting physics in itself [Glaetzle *et al.*, 2014]. In addition, we experimentally observe a strongly increased dephasing of the Rydberg excitation when using S Rydberg state, that we so far cannot explain.

Since for our laser parameters $\Omega_R, \Omega_B \ll \Delta$, we can describe our two-photon excitation scheme as an effective one photon excitation of a two-level system, comprising the ground state $|g\rangle$ and the Rydberg state $|r\rangle$, with an effective two-level Rabi

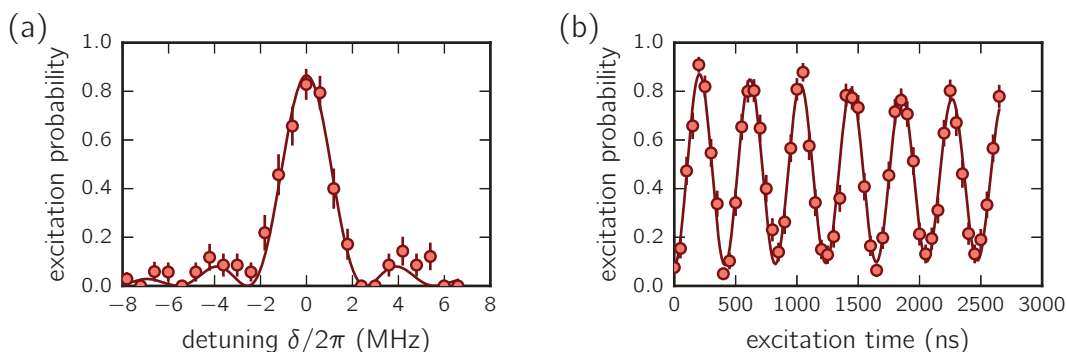


Figure 2.4: Rydberg excitation spectrum and Rabi oscillation. The plots show typical measurements for a Rydberg excitation, in this case of the $|55D_{3/2}\rangle$ state. (a) Rydberg excitation probability when scanning the laser detuning from the two-photon ground-Rydberg resonance. (b) The Rydberg excitation probability as a function of the excitation time for $\delta = 0$, showing the typical Rabi oscillation between the ground and Rydberg state. For each data point, the experiment was repeated ~ 100 times.

frequency and detuning given by

$$\begin{aligned}\Omega &= \frac{\Omega_R \Omega_B}{2\Delta} \\ \delta &= \delta_{2\text{ph}} - \left(\frac{\Omega_R^2}{4\Delta} - \frac{\Omega_B^2}{4\Delta} \right).\end{aligned}\tag{2.9}$$

Two typical experiments to measure the parameters of the light-atom interaction with Rydberg states on a single atom are shown in Figure 2.4. We usually perform an experiment ~ 100 times for each data point to reconstruct the populations in the ground and Rydberg state. We can discriminate between ground and Rydberg atoms, since an atom is lost from the experiment if it was in the Rydberg state at the end of the excitation pulse, while it remains in its trap if it was in the ground state. A detailed description of our Rydberg detection scheme is given in Chapter 4. For both experiments, we start out with the atom in the ground state. Panel (a) shows the probability of the atom to be excited to the $|55D_{3/2}\rangle$ Rydberg state, as a function of the laser detuning δ from the effective two-photon resonance defined in Equation 2.9. The solid line shows a fit to the data of the function

$$P_r(\delta) = A + B \frac{\Omega^2}{\Omega^2 + \delta^2} \sin\left(\frac{\tau}{2} \sqrt{\Omega^2 + \delta^2}\right)^2,\tag{2.10}$$

with A and B being empirical fit parameters to incorporate the small detection error and the finite excitation efficiency (see Section 4.1.3 for details). Panel (b) again shows

the Rydberg excitation probability, this time for a resonant excitation ($\delta = 0$), as a function of the excitation time. As one expects, the atom undergoes Rabi oscillations between the ground and the Rydberg state. We typically work with optical Rabi frequencies between 0.5 MHz and 10 MHz. Smaller frequencies are limited by the maximum duration of our experiments of a few μs before we lose too many ground state atoms (see Section 4.1.3), for larger frequencies the decay from the intermediate state $|i\rangle$ in the two-photon excitation gets too large.

We observe single atom Rydberg excitation efficiencies of more than 95%, which is the highest contrast of the Rabi oscillations that we measure on our experiment. The missing few percent in the contrast are due to an imperfect optical pumping to the ground state $|g\rangle$, and the spontaneous decay from the intermediate state in the two-photon excitation, which depends on the detuning Δ (which is fixed throughout this thesis), and the single photon Rabi frequency Ω_R of the first excitation step.

2.4.3 Excitation lasers

The light for the two-photon excitation is provided by two commercial lasers systems. For the 795 nm light we use a TOPTICA DL100, giving a total power of $\simeq 12$ mW at the position of the atoms, for the 474 nm light we use a frequency doubling TOPTICA TA-SHG-110 laser system, with $\simeq 90$ mW seen by the atoms. Both laser systems are frequency locked to a commercial ultra-stable ULE reference cavity from Stable Laser Systems, with a specified finesse of $\geq 20\,000$ and a free spectral range of 1.5 GHz.

By analysing the light reflected from the reference cavity we estimate laser linewidths of < 10 kHz for both the red and the blue excitation laser on the timescale of a few milliseconds. A linear drift of the cavity resonance was measured elsewhere to be ~ 10 kHz/day [Schauß, 2014], which is compatible with what we observe on our experiment. A more detailed description of the laser lock can be found in the thesis of Sylvain Ravets [2014], and a description of the laser optics and pulse shaping in the thesis of Lucas Béguin [2013].

Since according to Equation 2.9 both the effective Rabi frequency and detuning are dependent on the red and blue single photon Rabi frequencies, it is desirable to have the excitation light intensities as homogeneous as possible over a 2D array of atoms. We therefore use concave-convex cylindrical telescopes to magnify both beams by a factor ~ 4 in the axis which is parallel to the atomic plane, before focusing the red beam with an $f = 750$ mm plano-convex lens, and the blue beam with an $f = 300$ mm lens doublet (see Figure 2.5).

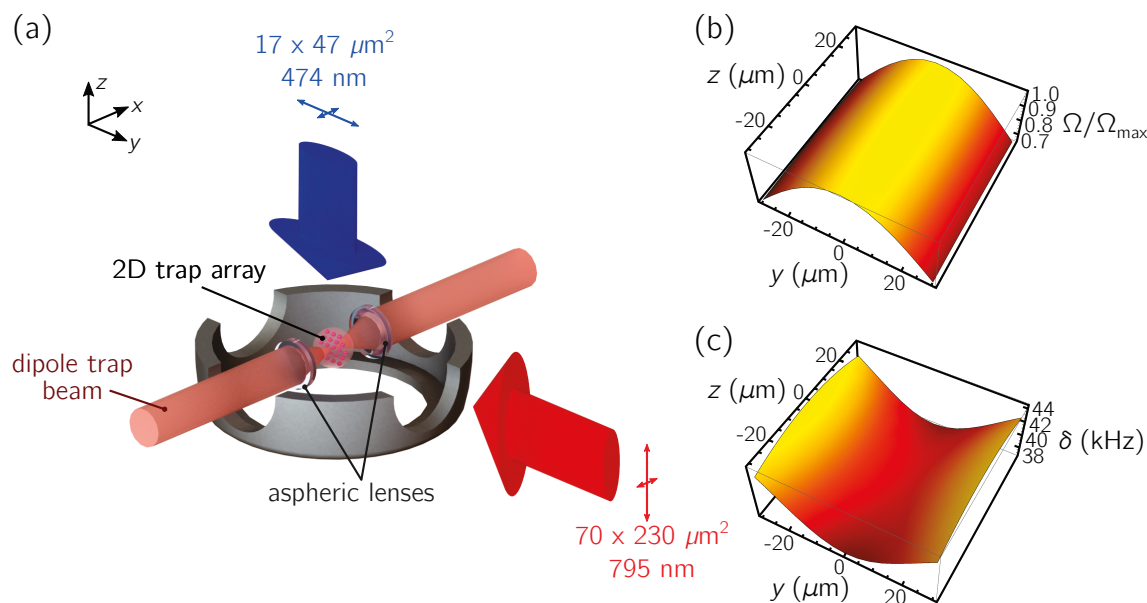


Figure 2.5: Shape of the excitation beams. (a) Sketch of the elliptical Rydberg excitation beams to ensure a homogeneous light intensity of both the 795 nm and the 474 nm beam even over large 2D arrays of single atoms in the yz -plane. For a typical Rydberg excitation experiment, with $n = 80$ and single photon Rabi frequencies $\Omega_{\text{R}} = 146$ MHz and $\Omega_{\text{B}} = 32$ MHz, the expected variations of Rabi frequency (b) and light shift (c) are shown for a $50 \times 50 \mu\text{m}^2$ area in the atom plane.

By measuring the two-photon Rabi frequency between the ground and a Rydberg state for different positions of a single atom in the focal plane of the aspheric lens, we determined $1/e^2$ -radii of $w_{\text{R}}^{(x,z)} = (70, 230) \mu\text{m}$ for the red and $w_{\text{B}}^{(x,y)} = (17, 47) \mu\text{m}$ for the blue beam. With these measured beam parameters we expect variations of the effective Rabi frequency below 30%, and variations of the light shift below 10 kHz, in a $25 \times 25 \mu\text{m}^2$ square in the atomic plane (see Figure 2.5(b,c)). These remaining inhomogeneities, especially in the Rabi frequency, are due to the still relatively small waist w_{B}^y of the blue beam. Having chosen a larger waist would have meant a lower overall intensity of the blue light, thus smaller achievable Rabi frequencies. Choosing a higher aspect ratio while keeping the same peak intensity would have led to a very small w_{B}^x , which would be difficult to achieve due to possible aberrations when focusing the beam through the viewport. In addition, the beam would be difficult to align on the atoms and its position would have to be kept stable on a μm scale over several days.

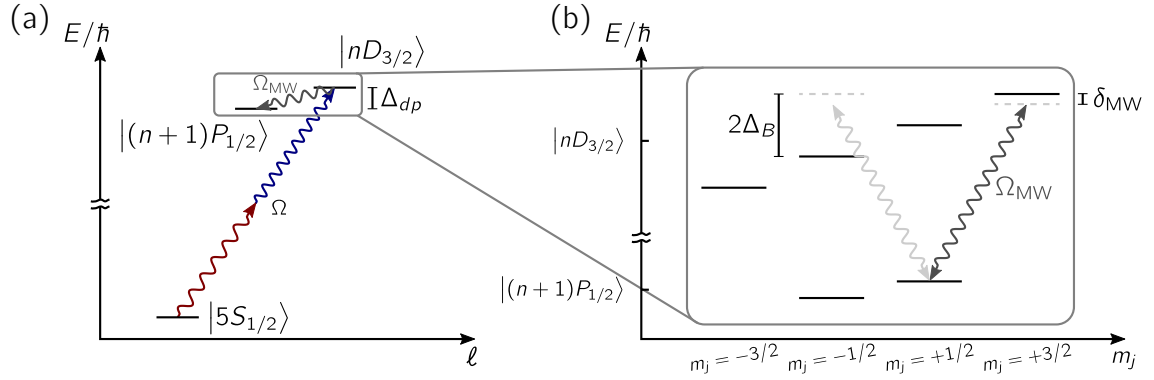


Figure 2.6: Realisation of Rydberg-Rydberg microwave transitions. (a) We first optically excite a ground state atom to a $|d\rangle = |nD_{3/2}\rangle$ Rydberg state. We turn off the optical light field, and use microwave radiation to drive transitions e.g. to a $|p\rangle = |(n+1)P_{1/2}\rangle$ state. (b) As our microwave field is unpolarised, we need the microwave coupling Ω_{MW} to be smaller than the Zeeman splitting Δ in order to be in the two-level regime.

2.5 Driving coherent microwave Rydberg-Rydberg transitions

In addition to driving coherent ground-Rydberg transition, it is also possible to drive coherent population transfers in the Rydberg manifold itself. The frequencies of these Rydberg-Rydberg transitions are typically a few to a few tens of GHz, making them convenient to drive with microwave fields from a standard microwave synthesiser. In our setup, we use a Rohde & Schwartz SMA100A microwave generator, connected to a simple antenna consisting of a 5 mm long end of a wire, positioned outside the vacuum chamber, just above a large viewport and about 20 cm away from the atoms. Due to the metallic parts of the aspheric lens mounts close to the atoms, which have spacings comparable to the microwave wavelength, the polarisation of the microwave field at the position of the atoms is unknown and is likely to have both circular and linear components.

To drive a single atom Rydberg-Rydberg transition, we first coherently excite the atom to a $|d\rangle = |nD_{3/2}\rangle$ Rydberg state by sending an optical π -pulse as described in Section 2.4.2. We then send in a coherent microwave pulse to transfer the population to another Rydberg state. Since we want to restrict the microwave transfer to a two-level process, it is convenient to drive microwave transitions to P states (see Figure 2.6(a)), which have a fine-structure splitting of a few hundred MHz, compared to a fine-structure splitting of around one MHz for F states. As we assume the microwave field to be unpolarised, we need the Zeeman splitting of the $|nD_{3/2}\rangle$ state Δ_B to

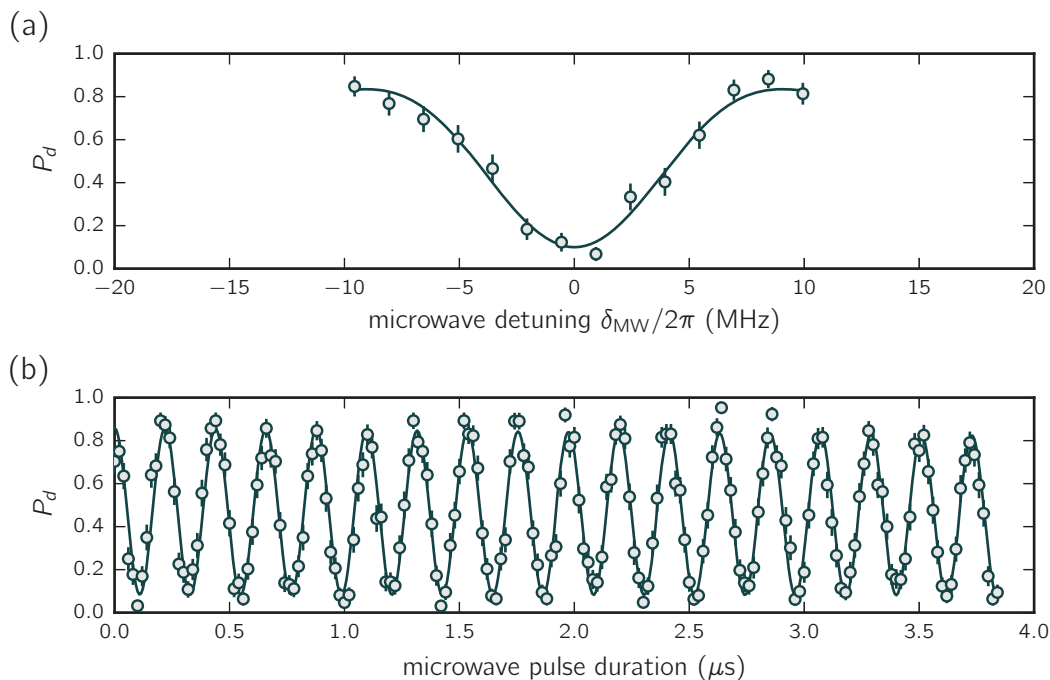


Figure 2.7: Microwave excitation spectrum and Rabi oscillation. We probe the microwave transition between the $|d\rangle = |62D_{3/2}\rangle$ and the $|p\rangle = |63P_{1/2}\rangle$ states. The atom is initially prepared in the $|d\rangle$ state. Probability P_d to find the atom in $|d\rangle$ as a function of (a) the detuning from resonance δ_{MW} after sending a $0.1 \mu\text{s}$ microwave pulse (the absolute transition frequency is $9\,131.6$ MHz), and (b) the microwave pulse length at $\delta_{\text{MW}} = 0$. We measure a Rabi frequency of $\Omega_{\text{MW}} \simeq 2\pi \times 4.5$ MHz without seeing any noticeable damping of the oscillation.

be larger than the microwave coupling strength Ω_{MW} , in order not to transfer any population into other Zeeman-sublevels of the D -state, as depicted in Figure 2.6(b).

To detect whether the atom was in the $|d\rangle$ or in another Rydberg state at the end of the experiment, we again shine in another optical π -pulse which transfers all population in $|d\rangle$ back to the ground state $|g\rangle$. If the optical down-transfer were perfect, measuring the population in $|g\rangle$ would give the population in $|d\rangle$ at the end of the experiment.

Figure 2.7 shows an experiment probing the microwave transition between the $|d\rangle = |62D_{3/2}\rangle$ and the $|p\rangle = |63P_{1/2}\rangle$ state. In this case we have a Zeeman splitting of $\Delta_B \approx 7.5$ MHz for the D -state for our magnetic field of $|\mathbf{B}| = 6.6$ G. We use an output power of the microwave synthesiser of about -15 dBm, with which we expect a Rabi frequency of about $2\pi \times 5$ MHz for the chosen states. Panel (a) shows the final population in $|g\rangle$ after having shone in a microwave pulse with a $0.1 \mu\text{s}$ duration, as a function of the detuning δ_{MW} from the $|62D_{3/2}\rangle \leftrightarrow |63P_{1/2}\rangle$ resonance. We

find an absolute value of $\Delta_{dp} \simeq 2\pi \times 9\,131.6$ MHz, close to the calculated value of $2\pi \times 9\,131.5$ MHz using quantum defect theory.

For the same experimental parameters, we tune the microwave frequency to resonance, i.e. $\delta_{\text{MW}} = 0$, and measure the final population in $|d\rangle$ as a function of the microwave pulse length. We fit the data by a damped sine, and find a Rabi frequency $\Omega_{\text{MW}} \simeq 4.558$ MHz. In contrast to the optical Rabi oscillation, we do not see any measurable damping in the microwave driven Rabi oscillation. This is because we do not suffer from the same sources of decoherence, namely that there is no short-lived intermediate state involved in the transition, and the microwave synthesiser is extremely stable both in frequency and in power. In addition, we can conclude that the microwave field is mainly a combination of σ_+ and σ_- polarisation, as we do not seem to couple to the $|62D_{3/2}, m_j = +1/2\rangle$ state. If we increase the Rabi frequency such that $\Omega_{\text{MW}} \approx 2\Delta_B \approx 2\pi \times 15$ MHz, we indeed do see a strong damping of the Rabi oscillation as we now start to transfer a significant amount of the population into different Zeeman-sublevels of the $|d\rangle$ state as described above. The finite contrast of the oscillation is fully attributed to the finite optical excitation and de-excitation probability.

2.6 Rydberg-Rydberg interactions

The principal motivation to use Rydberg states are their large interaction strengths. For two Rydberg atoms separated by a few μm , which is the typical interatomic separation in the experiments in this thesis, the Rydberg-Rydberg interaction is usually in the order of MHz and thus more than 10 orders of magnitude larger than the interaction between two ground state atoms at the same distance [Saffman, Walker, and Mølmer, 2010]. Moreover, one can easily tune the strength of the interaction by choosing Rydberg states with different principal quantum numbers, or by changing the distance between the atoms.

Due to the large transition dipole matrix element between Rydberg states, the dominant interaction between two Rydberg atoms is by far the dipole-dipole interaction, as long as the atomic separation is larger than the extend of the electronic wave function, i.e. $|\mathbf{R}| \gg n^2 a_0$. In a quantum mechanical picture, the interaction between two Rydberg atoms is described by the dipole-dipole interaction operator

$$\hat{V}_{\text{dd}}(\mathbf{R}) = \frac{1}{4\pi\epsilon_0} \left(\frac{\hat{\mathbf{d}}_1 \cdot \hat{\mathbf{d}}_2}{R^3} - \frac{3(\hat{\mathbf{d}}_1 \cdot \mathbf{R})(\hat{\mathbf{d}}_2 \cdot \mathbf{R})}{R^5} \right), \quad (2.11)$$

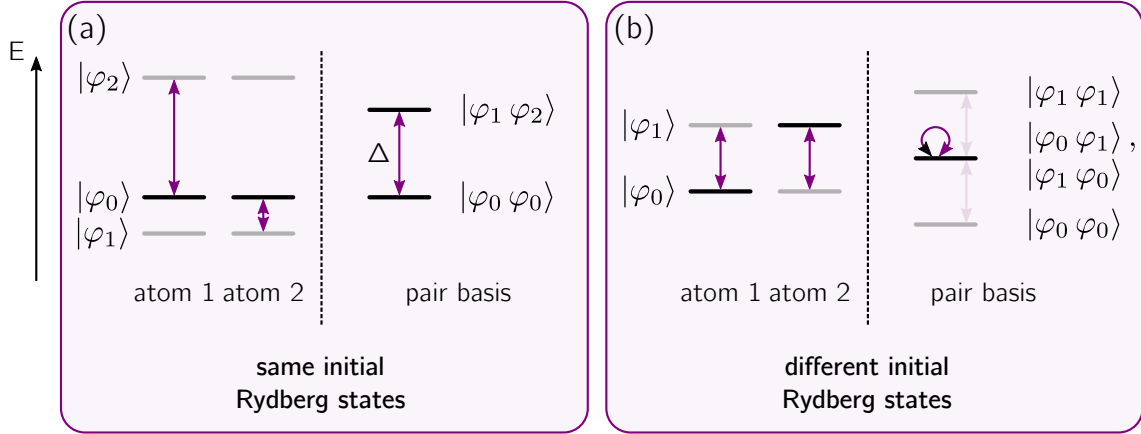


Figure 2.8: Schematic energy levels of atomic pair states. (a) Both atoms prepared in the state same state $|\Phi_0\rangle = |\varphi_0\varphi_0\rangle$, which is coupled by the dipole-dipole interaction to a state $|\Phi_1\rangle = |\varphi_1\varphi_2\rangle$ with an energy difference Δ . (b) The atoms are prepared in two different Rydberg states, $|\Phi_0\rangle = |\varphi_0\varphi_1\rangle$, which is degenerate and thus resonantly coupled to $|\Phi_1\rangle = |\varphi_1\varphi_0\rangle$, where the atoms have exchanged their Rydberg states.

where $\hat{\mathbf{d}}_1$ and $\hat{\mathbf{d}}_2$ are the electric dipole moment operators of atom one and two respectively, \mathbf{R} the vector connecting the two atoms and $R = |\mathbf{R}|$.

Since the internal electronic dynamics of Rydberg atoms typically happens much faster than their external dynamics, i.e their motion, we can treat the atomic cores as fixed in space when calculating the eigenenergies of the interacting system. When the atomic separation is larger than the spatial extend of the electron wave function, which is always the case in the experiments presented in this thesis, the two-atom Hamiltonian can be written as

$$\hat{H} = \hat{H}_1 \otimes \mathbb{1} + \mathbb{1} \otimes \hat{H}_2 + \hat{V}_{\text{dd}}(\mathbf{R}), \quad (2.12)$$

where \hat{H}_1 and \hat{H}_2 are the free atom Hamiltonians of the two atoms.

In order to find the eigenenergies of the interacting two-atom system, one can diagonalise the Hamiltonian numerically. In theory one needs to take into account all possible atomic pair states for the interaction. However, only pair states that are energetically close to the original state contribute significantly to the interaction.

Here, in order to gain qualitative insight into the different regimes of the dipole-dipole interaction, we will consider a simple model system of two atoms with only two possible pair states $|\Phi_0\rangle$ and $|\Phi_1\rangle$, as shown in Figure 2.8. In the pair basis $\{|\Phi_0\rangle, |\Phi_1\rangle\}$, the

Hamiltonian of the system is given by

$$\hat{H} = \begin{pmatrix} 0 & V_0/R^3 \\ V_0/R^3 & \Delta \end{pmatrix}, \quad (2.13)$$

with $V_0/R^3 = \langle \Phi_1 | \hat{V}_{\text{dd}}(\mathbf{R}) | \Phi_0 \rangle$ being the dipole-dipole coupling strength between the two pair states, and Δ their energy difference. The eigenenergies of the system are given by

$$E_{\pm} = \frac{1}{2} \left(\Delta \pm \sqrt{\Delta^2 + 4V_0^2/R^6} \right). \quad (2.14)$$

We see that the eigenenergies depend strongly on the distance R between the atoms, and one can identify two very distinct regimes of the interaction.

- **van der Waals interaction** ($V_0/R^3 \ll \Delta$):

Let us first consider the case where both Rydberg atoms are initially in the same state, e.g. $|\Phi_0\rangle = |\varphi_0\varphi_0\rangle$, where φ_i are the atomic states in the single atom basis, as shown in Figure 2.8(a). In most cases, the dipole-dipole coupling strength V_0/R^3 for interatomic distances presented in this thesis is much smaller than the energy difference Δ between the different atomic pair states, so the interaction can be treated as a small perturbation on the eigenenergies of the non-interacting pair states. The eigenenergies of Equation 2.14 can therefore be approximated by

$$E_+ \simeq \Delta + \frac{C_6}{R^6} \quad \text{and} \quad E_- \simeq -\frac{C_6}{R^6},$$

with $C_6 = V_0^2/\Delta$, leading to the well-known van der Waals interaction with its R^{-6} scaling, and increasing with the principal quantum number as $C_6 \sim n^{11}$.

For typical experimental parameters in our experiment, with the principal quantum number n ranging between 50 and 100, and interatomic distances between 3 and 10 μm , the interaction strengths in the van der Waals regime can range from a few kHz to hundreds of MHz. This demonstrates the versatility of Rydberg atoms, as it is easily possible for us to tune the interaction strength between the atoms by a few orders of magnitude only by changing the position of the atoms or their principal quantum number³. The van der Waals interaction

³For lower principal quantum numbers the finite lifetime of the Rydberg atoms becomes non-negligible for the timescales of our experiments, whereas for higher ones it gets more and more difficult to compensate stray electric fields to a satisfactory level, as the polarisability of the Rydberg states grows with $(n^*)^7$ and gets very large for high lying Rydberg states.

is the only relevant interaction in the experiments presented in this thesis except for Chapter 7, as we always couple all the atoms to the same Rydberg state.

- **Resonant dipole-dipole interaction** ($V_0/R^3 \gg \Delta$):

The second interaction regime occurs when the dipole-dipole interaction couples two pair states resonantly, i.e. the energy difference Δ is zero or negligible compared to the dipole-dipole coupling strength V_0/R^3 . The eigenenergies of the pair state from Equation 2.14 then simplify to

$$E_{\pm} \simeq \pm \frac{V_0}{R^3} = \pm \frac{C_3}{R^3}, \quad (2.15)$$

with $V_0 = C_3$, showing the typical R^{-3} scaling of the resonant dipole-dipole interaction. The condition $\Delta \simeq 0$ can be achieved in two different ways.

Förster resonance: If both atoms are initially in the same Rydberg states, as shown in Figure 2.8(a), it is still possible to find cases where the interaction is dominated by the resonant dipole-dipole interaction. This is the case if the initial pair state is near-degenerate with a second pair state where both atoms have a different Rydberg state, and both states are coupled via the dipole-dipole interaction. In general, there exist very few pair states in nature that fulfil this condition. One can, however, tune two quasi-degenerate pair states into resonance, for example by applying an electric field [Walker and Saffman, 2005; Anderson, Veale, and Gallagher, 1998; Mudrich *et al.*, 2005], as we have demonstrated in [Ravets *et al.*, 2014, 2015]. Using electric fields, it is even possible to find degenerate triple-states, as was demonstrate recently by Faoro *et al.* [2015].

Excitation transfer: If the two atoms are in two different Rydberg states, i.e. $|\Phi_0\rangle = |\varphi_0\varphi_1\rangle$, there exists another degenerate⁴ pair state $|\Phi_1\rangle = |\varphi_1\varphi_0\rangle$ where the atoms have exchanged their states, depicted in Figure 2.8(b).

The two states are thus coupled resonantly by the dipole-dipole interaction, as now $\Delta = 0$, and the system will oscillate between $|\Phi_0\rangle$ and $|\Phi_1\rangle$ with a frequency $C_3/(hR^3)$, as we have shown in [Barredo *et al.*, 2015]. The pair state $|\Phi_0\rangle$ is naturally still coupled to other off-resonant states by the van der Waals interaction, but if $\Delta n = |n_1 - n_0| \approx 0$ then the resonantly coupled state completely dominates the interaction and the van der Waals interaction can usually be neglected.

⁴Assuming the absence of spatially varying electric or magnetic fields.

The effect of the resonant dipole-dipole interaction will be discussed briefly in Chapter 7.

2.7 Conclusion

In this chapter we presented the setup to trap a single atom in a microtrap created by the focus of an optical dipole trap beam, and coherent excitation scheme to couple the atom to a Rydberg state. The strong interaction between Rydberg atoms make them an ideal tool to engineer strongly interacting many-body quantum systems in the laboratory. In order to achieve this goal, we need to create not only one, but large arrays of single-atoms traps. In the following chapter we will see how we can create arrays of microtraps in arbitrary 2D configurations by manipulating the phase of our dipole trap beam.

Generation of arbitrary 2D arrays of optical dipole traps

In order to study the many-body physics of interacting Rydberg atoms, it is necessary to multiply the number of microtraps. In the Rydberg physics community, multiple approaches have been taken to create arrays of atomic traps containing either one or an ensemble of atoms. The techniques used range from simply using multiple dipole trap beams [Béguin *et al.*, 2013; Hankin *et al.*, 2014; Ebert *et al.*, 2015] to optical lattices [Schauß *et al.*, 2012] and arrays of microtraps created by fixed optics [Maller *et al.*, 2015].

A drawback of those approaches is the lack of flexibility in the arrangement of the atoms. One possibility to overcome this limitation is the use of a spatial light modulator (SLM) to either imprint an intensity pattern on the Rydberg excitation light [van Bijnen *et al.*, 2015], or to create reconfigurable arrays of microtraps [Bergamini *et al.*, 2004; Kruse *et al.*, 2010; Schlosser *et al.*, 2011; Nogrette *et al.*, 2014].

For the work of this thesis we chose the latter approach, ‘cloning’ the single microtrap by imprinting an appropriate spatial phase on the dipole trap beam, allowing us to create up to ~ 100 traps in easily reconfigurable 2D geometries.

This chapter is based on our publication [Nogrette *et al.*, 2014]. We will first discuss the principle of manipulating the spatial phase of a Gaussian beam to change its intensity distribution in the focal plane of a lens in Section 3.1. In Section 3.2 we present the actual implementation in the experiment. Finally, we will see how we use the SLM to correct for aberrations of the trapping beam in Section 3.3, and the use of a closed feedback loop to achieve uniform trap intensities in Section 3.4.

3.1 Spatial phase manipulation of a Gaussian beam

Holography was originally intended to record both the intensity and the spatial phase information of a light field [Gabor, 1948]. Only later the technique was used to actively

manipulate the light-intensity distribution, typically by using a transparent optical element with a spatially varying index of refraction, and uniform absorption. Such elements have to be specifically fabricated for a certain desired intensity pattern.

A major evolution of the field was thus the emergence of digital holography and the use of liquid crystal devices called spatial light modulators (SLMs) [Osten, 2006], allowing the dynamic manipulation of the spatial phase of the light field. SLMs are arrays of pixels consisting of bi-refracting liquid crystals, similar to those found in liquid crystal displays. Each pixel can introduce a polarisation-dependent phase shift to either a reflected or transmitted light field, depending on the type of SLM, with a magnitude that can be controlled for each pixel independently. It is therefore possible to control the local phase of the light field with a resolution equal to that of the pixel array of the SLM.

There are two different types of SLMs, *optically*-addressed spatial light modulators (OASLMs) and *electrically*-addressed spatial light modulators (EASLMs), the difference being that the former one uses a control light field to imprint the phase information on the pixel array, the latter one by applying a computer controlled electric field to each pixel. For our experiment we use an EASLM, which we will from now on only refer to simply as SLM. Nowadays SLMs are commercially available with resolutions up to several megapixels, with a resolution of the phase shift better than $2\pi/100$ on each pixel and refresh rates of up to more than 100 Hz.

SLMs have seen various applications in physics research, ranging from the manipulation of angular momentum states of light [Curtis and Grier, 2003; Gibson *et al.*, 2004; Bozinovic *et al.*, 2013], trapping of polarisable particles [Grier, 2003], aberration correction in astronomy [Hardy, 1998], laser pulse shaping [Weiner, 2000], to the manipulation of degenerate quantum gases [Boyer *et al.*, 2006; Becker *et al.*, 2008] and creating exotic trap potentials for them [Gaunt and Hadzibabic, 2012].

For all above mentioned applications it is crucial to find an appropriate phase to imprint on the light field in order to create the desired intensity distribution. One way this can be achieved will be detailed in the following two subsections.

3.1.1 Optical phase modulation using a spatial light modulator

We will now discuss the working principle to create a desired intensity distribution of a light field in the focal plane of a lens by altering the spatial phase of a Gaussian beam. The most simple use of an SLM is shown schematically in Figure 3.1. Note that the coordinate system (x, y, z) used to describe the light field for the SLM is different

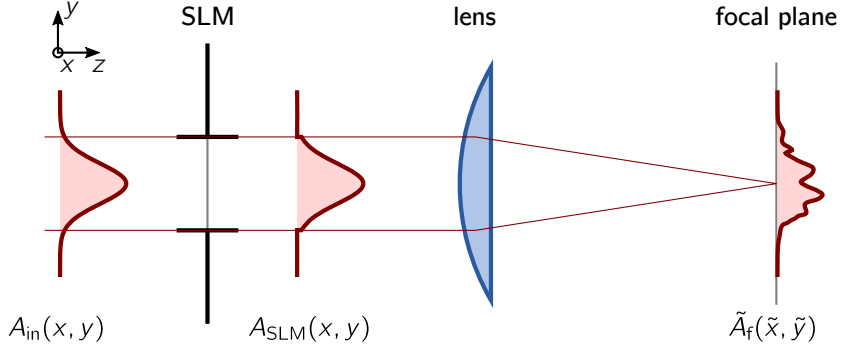


Figure 3.1: Principle of the phase manipulation with an SLM. The SLM imprints a chosen phase $\varphi(x, y)$ onto the light field. Due to its finite size, the SLM effectively acts as an aperture, but besides that does not alter the intensity of the light field. The intensity distribution in the focal plane of a lens depends strongly on the spatial phase of the collimated beam.

from the coordinate system of the actual experiment. A collimated Gaussian beam with a uniform spatial phase and a real-valued amplitude $A_{in}(x, y) = |A_{in}(x, y)|$ is incident on the SLM. We assume the SLM to act as a rectangular aperture, with the size $L_x \times L_y$ of the SLM, which modifies the phase of the beam at position (x, y) by an amount $\varphi(x, y)$. Immediately after the SLM the complex amplitude of the beam is then given by

$$A_{SLM}(x, y) = A_{in}(x, y) e^{i\varphi(x, y)} \text{rect}\left(\frac{x}{2L_x}, \frac{y}{2L_y}\right), \quad (3.1)$$

with $\text{rect}(\cdot)$ being the rectangular function making up for the finite aperture of the SLM. When the beam is now focused by a lens of focal length f , its amplitude in the focal plane is given by

$$\tilde{A}_f(\tilde{x}, \tilde{y}) = \mathcal{F}[A_{SLM}(x, y)]_{\frac{\tilde{x}}{\lambda f}, \frac{\tilde{y}}{\lambda f}}. \quad (3.2)$$

Here λ is the wavelength of the light field and $\mathcal{F}[\cdot]_{\mu, \nu}$ the Fourier transform at frequencies μ, ν .

Since the result of the Fourier transform in Equation 3.2 can depend strongly on the phase $\varphi(x, y)$, we can drastically change the intensity distribution $I_f = |\tilde{A}_f|^2$ in the focal plane of the lens by changing $\varphi(x, y)$. The easiest way to achieve any arbitrary intensity distribution in the focal plane would be to take the inverse Fourier transform of $\sqrt{I_f}$, and modify the phase and the amplitude of the light field accordingly. This is not applicable here since the SLM which we use in the experiment only allows the manipulation of the phase φ , not the amplitude $|A_0|$. It is therefore not possible,

except for some trivial cases, to find a phase φ which will exactly give a desired target intensity distribution I_t such that $|\tilde{A}_f|^2 = I_t$. However, it is possible to find phases φ which will give a good approximation for any given desired intensity distribution in the focal plane. A trivial case to manipulate the light field will be given in the following, namely displacing the trap transversally with respect to the optical axis, before detailing the Gerchberg-Saxton algorithm to find appropriate phases for arbitrary target intensity distributions.

The most simple manipulation of the phase of the light field is to move a single trap transversally in the focal plane. This is achieved in general by adding a tilt to the wavefront of the laser beam, which can be achieved by adding with the SLM a phase shaped as a blazed grating of the form

$$\varphi(x, y) = \left(\frac{2\pi}{\Lambda_x}x + \frac{2\pi}{\Lambda_y}y \right) \pmod{2\pi}, \quad (3.3)$$

where Λ_x and Λ_y are the fringe periods of the grating in x - and y -direction. Such a grating can be superimposed on any phase on the SLM in order to shift the intensity distribution as a whole transversally in the focal plane of the lens by a quantity $(\Delta x, \Delta y) = (f\lambda/\Lambda_x, 1/f\lambda/\Lambda_y)$, f being the focal length of the lens and λ the wavelength of the light.

Furthermore, we can display any analytically calculable phase on the SLM. A simple example is to display two areas of constant phase with a π phase jump between them, changing the Gaussian beam from a TEM₀₀ to a TEM₀₁ mode. In the focal plane, this will lead to two sharply separated traps with a peak-to-peak distance of $\sim 1.6 \mu\text{m}$. This is the fundamental limit of how close we can bring two traps together. Preliminary experiments showed that the atom-loss probability is significantly increase for such a small distance, but nevertheless allowed us to perform a two-atom Rydberg experiment.

3.1.2 The Gerchberg-Saxton phase retrieval algorithm

In order to create arbitrary intensity distributions in the focal plane of a lens with a phase-only SLM, the algorithm of choice is usually the Gerchberg-Saxton algorithm [Gerchberg and Saxton, 1972], which is explained schematically in Figure 3.2. It was originally developed to retrieve the phase information of an electron beam from its intensity distribution. It can however also be used to find an approximate phase for a laser beam to generate a desired light intensity in the focal plane of a lens, which is

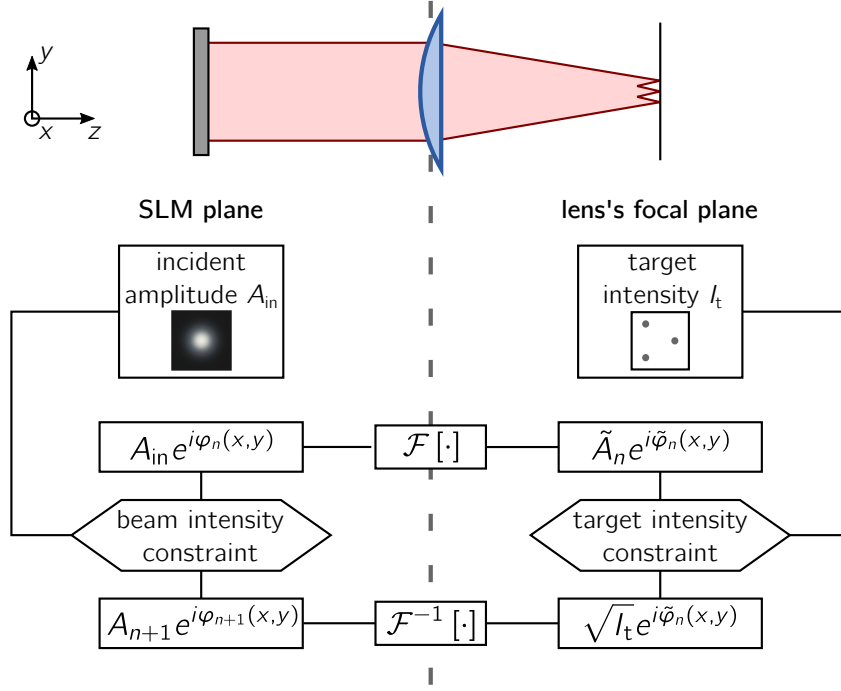


Figure 3.2: Principle of the Gerchberg-Saxton algorithm. In the algorithm, the light field is repeatedly propagated back and forth between the SLM plane and the focal plane by Fourier and inverse Fourier transform. In each iteration n of the algorithm, the amplitude in the SLM plane is replaced by the real incident amplitude A_0 , and the amplitude in the focal by the target amplitude $\sqrt{I_t}$, keeping only the complex phase.

exactly what we are looking for to create arbitrary trap geometries with our SLM.

The principle of the GS algorithm is to virtually propagate the light field back and forth between the plane of the SLM and the focal plane of the lens, iteratively converging towards an appropriate phase to create a given intensity distribution. Since we work in the far field regime, the light field propagation can be done by Fourier and inverse Fourier transform [Goodman, 1996]. One iteration of the algorithm looks as follows:

- We start out with the actual real amplitude of the light field A_{in} , which in our case is a Gaussian beam having passed through an aperture the size of the SLM.
- The light field is propagated to the focal plane of the lens by Fourier transform, giving us the amplitude \tilde{A} and the phase $\tilde{\varphi}$ of the focused beam.
- In the focal plane, we replace the calculated amplitude \tilde{A} by the amplitude of the target intensity distribution $\sqrt{I_t}$, while keeping the calculated phase $\tilde{\varphi}$.

- We propagate the light field back to the SLM plane by inverse Fourier transform.
- The calculated amplitude in the SLM plane is now replaced by the actual real amplitude A_{in} of the incident light field, while keeping again the calculated phase φ .
- We repeat the algorithm until the calculated amplitude in the SLM plane $|\tilde{A}e^{i\tilde{\varphi}}|^2$ does not evolve anymore, usually after a few tens of iterations.

Note that this algorithm only converges to an *approximation* of the targeted intensity distribution I_t , as we are not able to manipulate the amplitude of the light field. In fact, there exist a large number of different phases that lead to equally good approximations of I_t . As the algorithm is completely deterministic, the phase which is finally found only depends on the initial implementation of the algorithm¹. The numerical implementation of the Gerchberg-Saxton algorithm will be detailed in the following Section.

3.1.3 Phase retrieval on a discrete grid

In order to calculate an appropriate phase pattern to create a specific microtrap array, we need to implement numerically the Gerchberg-Saxton algorithm presented in the last subsection. For this we first have to discretise the light field, as depicted in Figure 3.3, by describing its complex amplitude $A(x, y)e^{i\varphi(x, y)}$ in the SLM plane by a matrix, of dimension $N_x \times N_y$, with each entry of the matrix standing for the complex amplitude of the light field in a region of size $\Delta_x \times \Delta_y$, giving a total physical size of the discretised light field of $L_x \times L_y = N_x \Delta_x \times N_y \Delta_y$. Likewise, we describe the field in the focal plane by a matrix of the same dimension $N_x \times N_y$, but with different sizes $\tilde{\Delta}_x \times \tilde{\Delta}_y$ of the matrix entries and a total physical size $\tilde{L}_x \times \tilde{L}_y = N_x \tilde{\Delta}_x \times N_y \tilde{\Delta}_y$.

Following the thesis of van Bijnen [2013], we will call $\Delta_x \times \Delta_y$ an *SLM unit* and $\tilde{\Delta}_x \times \tilde{\Delta}_y$ a *focal unit*. They are important dimensions in the numerical treatment of the light field, and are related by

$$\tilde{\Delta}_x \times \tilde{\Delta}_y = \frac{\lambda f}{L_x} \times \frac{\lambda f}{L_y} \quad (3.4)$$

$$\tilde{L}_x \times \tilde{L}_y = \frac{\lambda f}{\Delta_x} \times \frac{\lambda f}{\Delta_y}, \quad (3.5)$$

¹We initialise the algorithm with an initial random phase φ_{in} of the light field in the SLM plane. The finally obtained phase is thus slightly different for each initial phase.

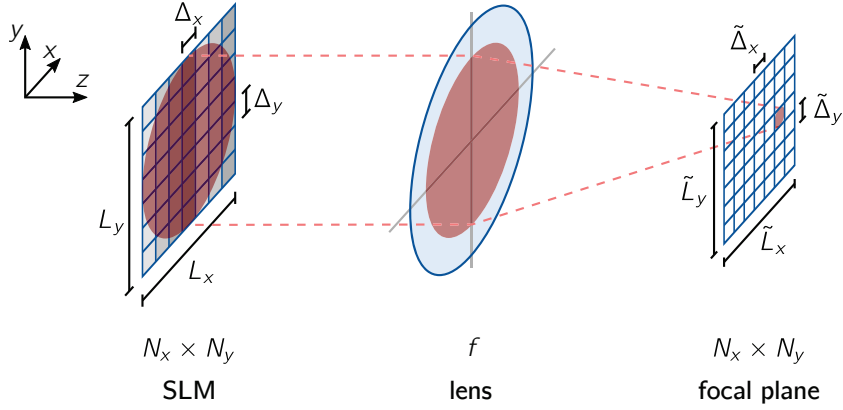


Figure 3.3: Illustration of the spatial dimensions in the SLM and focal plane.

When treated numerically, the amplitude $A_{\text{SLM}}(x, y)e^{i\varphi(x, y)}$ is described by a $N_x \times N_y$ matrix, with each entry giving the amplitude for a region of size $\Delta_x \times \Delta_y$, so that the entire array has the size $L_x \times L_y = N_x \Delta_x \times N_y \Delta_y$. In the focal plane of a lens with focal length f , the matrix has the same number of entries, but now each entry stands for a region of different physical size $\tilde{\Delta}_x \times \tilde{\Delta}_y$, with $\tilde{\Delta}_{x,y} = \lambda f / L_{x,y}$, λ being the wavelength of the light field.

with λ the wavelength of the light field and f the focal length of the lens.

To understand the effect of the pixelation, we first approximate the continuous light field in the SLM plane as a sum of delta-peaks,

$$A_{\text{SLM}}(x, y) \simeq \sum_k^{N_x-1} \sum_l^{N_y-1} \delta(x - k\Delta_x) \delta(y - l\Delta_y) A_{\text{in}}(k\Delta_x, l\Delta_y) e^{i\varphi_{kl}}. \quad (3.6)$$

Here A_{in} is the amplitude in the SLM plane, $(k\Delta_x, l\Delta_y)$ the physical coordinates of pixel (k, l) and φ_{kl} the phase delay of that pixel which is imprinted on the incoming light field $A_{\text{in}}(x, y)$. We now propagate the light field by Fourier transforming the above equation according to Equation 3.2. The amplitude of the light field in the focal plane of the lens, on a grid of focal units $\tilde{\Delta}_x, \tilde{\Delta}_y$, is then given by

$$\tilde{A}_f(m\tilde{\Delta}_x, n\tilde{\Delta}_y) = \sum_k^{N_x-1} \sum_l^{N_y-1} A_{\text{in}}(k\Delta_x, l\Delta_y) e^{i\varphi_{kl}} e^{-2\pi i(km/N_x + ln/N_y)}, \quad (3.7)$$

with $m \in [0, N_x - 1]$ and with $n \in [0, N_y - 1]$. This shows that the amplitudes of the

light fields are related by discrete Fourier transform (DFT):

$$\tilde{A}_{f,nm} = [\text{DFT}[A_{\text{SLM}}]]_{nm} = \sum_k^{N_x-1} \sum_l^{N_y-1} A_{\text{SLM},kl} e^{-2\pi i(km/N_x + ln/N_y)}, \quad (3.8)$$

with the amplitude just after the SLM being

$$A_{\text{SLM},kl} := A_{\text{in}}(k\Delta_x, l\Delta_y) e^{i\varphi_{kl}}, \quad (3.9)$$

and the amplitude in the focal plane

$$\tilde{A}_{f,nm} := \tilde{A}_f(m\tilde{\Delta}_x, n\tilde{\Delta}_y). \quad (3.10)$$

We see that the pixel size of the discretised amplitudes are the SLM unit and the focal unit respectively when taking the definition of Equation 3.4. This has two important implications: (i) To increase the accessible region size in the focal plane $\tilde{L}_x \times \tilde{L}_y$, one needs to increase the resolution in the SLM plane, i.e. decrease $\Delta_x \times \Delta_y$ while keeping $L_x \times L_y$ constant. (ii) To increase the spatial resolution in the focal plane, one needs to increase the SLM size $L_x \times L_y$, while keeping its resolution constant.

3.2 Implementation of the SLM in the experiment

In the previous section we saw how it is possible to achieve arbitrary intensity distributions of a Gaussian beam in the focal plane of the lens by only manipulating its phase before focusing the beam with a lens of focal length f . In this section, we will show how we implemented the SLM in our experiment, with the goal of creating arbitrary 2D arrays of microtraps for single-atom trapping.

We use a [Hamamatsu X10468-02](#) liquid crystal on silicon (LCOS) SLM. It has a 792×600 pixel resolution controlled by a computer via an 800×600 DVI signal (in the longer direction, the outer 4 pixels of the signal on each side are not used), with an 8 bit ‘dynamic phase range’ and a pixel size of $20 \times 20 \mu\text{m}^2$. The effective size of the SLM chip is $15.8 \times 12 \text{mm}^2$, with a fill factor of the pixels of 98%.

The pixel value to achieve a 2π phase shift compared to a pixel value of 0 depends on the wavelength of the light field. For our 850 nm trapping light, a 2π phase shift is achieved with a pixel integer value of 223 (see Figure 3.4(a)). We can thus manipulate the phase with a $2\pi/223$ resolution.

As the SLM diffraction efficiency depends strongly on the polarisation of the incident

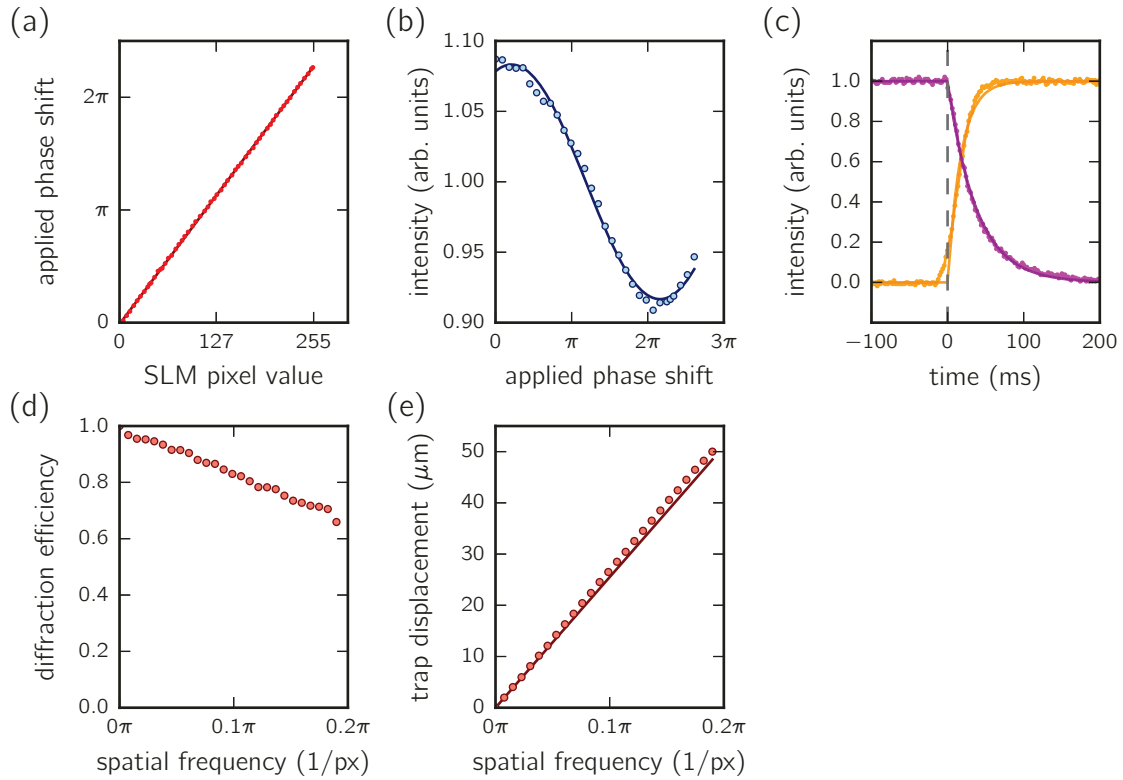


Figure 3.4: Characteristics of our Hamamatsu X10468-02 SLM. (a) The phase shift on the light field as a function of the grey level value displayed on the SLM (data from Hamamatsu). (b) Intensity modulation of a light field with a misaligned polarisation when applying a uniform phase shift on the SLM (the fit gives a $(3.9 \pm 0.1)\pi$ applied phase shift period). (c) Response of the light field when using the SLM to hide ($\tau_{\text{off}} = 37.7$ ms) and unhide ($\tau_{\text{on}} = 17.7$ ms) the light, by displaying and hiding a blazed grating which moves the sp. (d) Diffraction efficiency of the SLM vs. the spatial frequency of an displayed blazed grating which moves the focus such that it is blocked by an aperture. (e) Displacement of the focal spot as a function of the spatial phase frequency of a displayed blazed grating (points) and the expected displacement (line).

light field, the SLM can act as a waveplate, with a polarisation rotation depending on the displayed phase, thus distorting the polarisation of the diffracted light field. For a misaligned polarisation, the intensity of the diffracted light field measured after a polarisation analyser will thus depend on the phase displayed on the SLM. For an incident light field with slightly misaligned linear polarisation we detect an amplitude modulation of $\pm 10\%$, with a period equalling a phase shift of about 4π displayed on the SLM (see Figure 3.4(b)). After proper alignment of the polarisation the amplitude modulation is $< 2\%$.

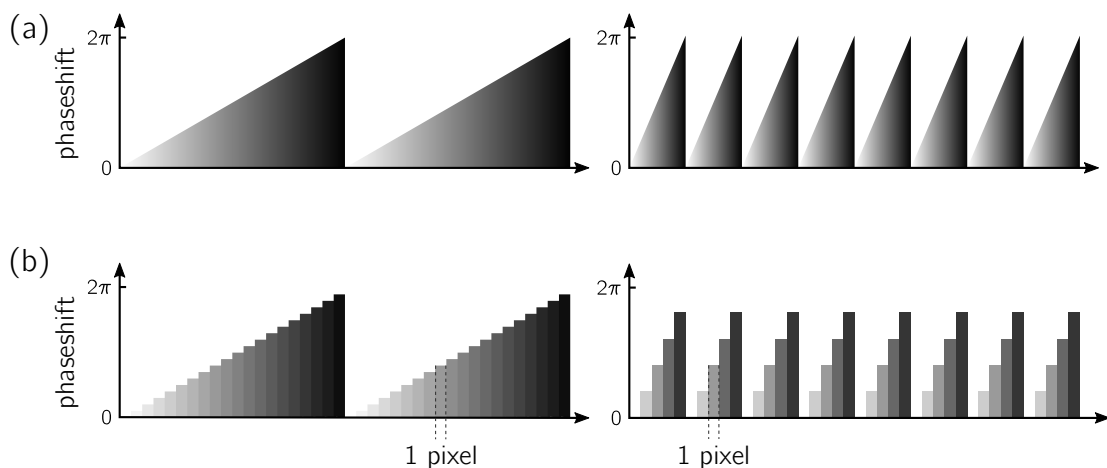


Figure 3.5: Visualisation of the pixelation. (a) A given continuous phase, as the blazed grating here, can only be approximated on the SLM due to the finite size of the SLM pixels. (b) Discretised phase patterns with a low spatial frequency (left) resemble the continuous phase more closely than one with a high spatial frequency (right). The SLM therefore shows a higher diffraction efficiency for low-frequency phase patterns.

The response time of the SLM is limited by the 60 Hz refresh rate of DVI protocol used to control the SLM. To quantify the switching times of the SLM we alternately display a blazed grating which displaces the diffracted beam such that it is blocked by an aperture (see Figure 3.6), and another blazed grating which lets it pass the aperture. The measured power of the light field right after the aperture is displayed in Figure 3.4(c), showing that the switching times are close to the expected $(60 \text{ Hz})^{-1} = 17 \text{ ms}$ (see Figure 3.4(c)). However, these switching times are far too slow to dynamically change the SLM generated trap pattern during our Rydberg experiments, which have a timescale of a few microseconds.

Finally, we also analyse the effect of the spatial frequency of the displayed phase pattern on the reflected light field, by displaying blazed gratings with different frequencies on the SLM and measuring the diffraction efficiency, shown in Figure 3.4(d-e). The diffraction efficiency decreases with the displayed spatial frequency, because a rapidly-varying continuous phase can no longer be well approximated by the pixelated SLM, as depicted in Figure 3.5. The measured diffraction efficiency decreases roughly linearly with the spatial frequency, being about 66% for a spatial frequency of $0.1 \times 2\pi/\text{pixel}$. For comparison, the typical spatial frequency of a phase pattern to create a 10×10 trap array with a $4 \mu\text{m}$ trap spacing is about $0.03 \times 2\pi/\text{pixel}$, which would correspond to a diffraction efficiency of still about 90%.

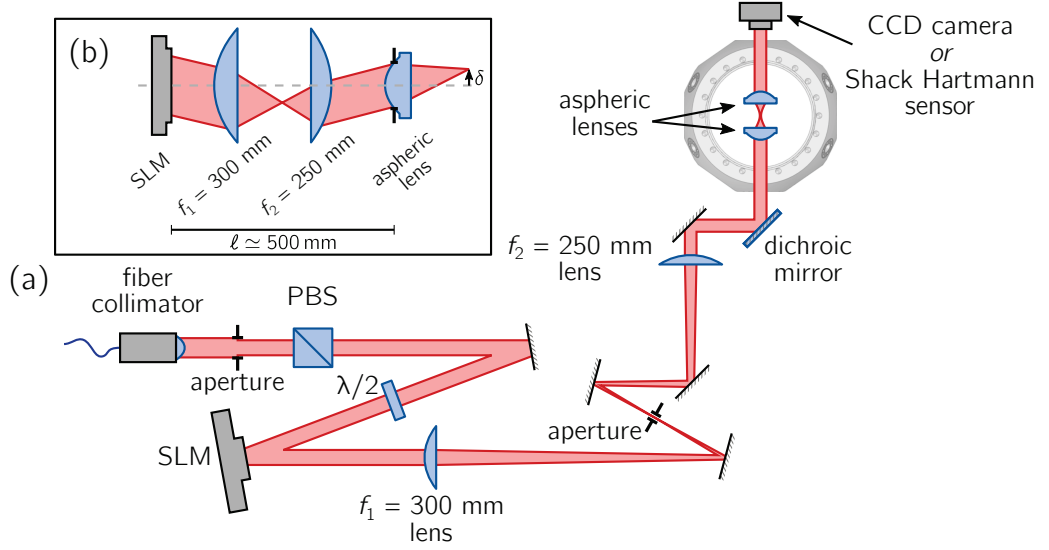


Figure 3.6: Optics setup for the SLM. (a) The Gaussian laser beam, coming from a single mode fiber, is reflected off the SLM, after which it passes through a telescope, reducing the beam from a 6 mm to a 5 mm $1/e^2$ -radius. The inset (b) illustrates the use of the telescope, imaging the SLM plane onto the aspheric lens aperture, reducing the effect of clipping on the lens for traps that are not lying on the optical axis (distances not to scale).

3.2.1 Optics setup

The setup of the optics used to manipulate the phase and focus the dipole trap beam in order to create 2D arrays of microtraps is shown in Figure 3.6. For the experiments presented in this thesis we used a **Toptica TA Pro** diode laser with a tapered amplifier at a wavelength of 850 nm as a light source. By now the laser has been replaced by a Ti:sapphire laser to achieve a higher output power, thus allowing larger number of microtraps in the arrays.

We start out with a beam coming from a single mode, polarisation maintaining optical fiber, with a 6.7 mm $1/e^2$ radius, clipped by a circular iris with a 12 mm diameter to adapt the beam size to the size of the SLM aperture. We then use a polarising beamsplitting cube (PBS) to have a clean polarisation of the beam, and a half-wave plate ($\lambda/2$) to adapt the polarisation of the light field to the SLM, as its diffraction efficiency depends strongly on the polarisation of the incident light field.

After the SLM we use an achromatic telescope with an $m = -10/12$ transverse magnification to adapt the beam size to the $D = 10$ mm aperture of the aspheric lens used to focus the beam in the vacuum chamber. The distances between the SLM and

the telescope and the aspheric lens were chosen such that the telescope conjugates the plane of the SLM with aperture of the aspheric lens, as shown in Figure 3.6(b). This avoids that light which creates off-axis traps is clipped by the aperture of the aspheric lens. For example, due to the relatively long distance between the SLM and the aspheric lens of $\ell \simeq 500$ mm, a beam that focuses $\delta = 20$ μm off the optical axis would hit the aspheric lens about 1 mm off-axis. In the implementation of the Gerchberg-Saxton algorithm the telescope can be omitted, if we replace the focal length f of the lens by a lens with an effective focal length $f_{\text{eff}} = f/|m| = 12$ mm.

An aperture placed in the focus of the telescope allows to block certain parts of a trap array, as well as all the non-diffracted light.

A Zemax calculation, with a flat mirror replacing the SLM, has been performed to check the quality of the optical setup, giving a Strehl ratio, i.e. the calculated peak intensity in the focus of the aspheric lens over the theoretical peak intensity for a diffraction-limited system, of $S \geq 0.88$ over a 20×20 μm^2 field in the focal plane.

3.2.2 Numerical implementation

We now describe how we implemented the Gerchberg-Saxton algorithm to calculate phase patterns for the experiment using Matlab, discretising the light field as a matrix, as described in Section 3.1.3. The physical size $\Delta_x \times \Delta_y$ of each entry in the matrix is given by the actual SLM pixel size $\Delta_x = \Delta_y = 20$ μm . The number of entries in the matrix can be chosen freely, as long as it is larger than the 600×792 pixel resolution of the SLM. Note that calculating fast Fourier transforms (FFTs) is much faster with array sizes of a powers of two [Cooley and Tukey, 1965; MathWorks, 2015].

As the target image, i.e. the desired intensity distribution in the focal plane I_t in Figure 3.2, we use an empty matrix, and add traps by setting the pixel which is closest to the trap maximum to a value corresponding to its relative intensity, and normalise the matrix such that the sum of all pixels equals 1. From the calculated $N_x \times N_y$ phase matrix, we take the central 600×792 pixels that correspond to the actual pixels on the SLM, and use this as the phase pattern φ_{array} to be displayed on the SLM.

According to Equation 3.4, taking a matrix with dimension $N_x \times N_y = 2^{10} \times 2^{10} = 1024 \times 1024$ to describe the light field would correspond to a focal unit size of $\tilde{\Delta}_x \times \tilde{\Delta}_y \simeq 0.4 \times 0.4$ μm^2 . We noticed that with such a large focal unit, the spread of distances between the traps in a given trap array, measured on the CCD camera, can be relatively high (see Figure 3.7, left panels). We thus increase the matrix size in the numerical implementation of the Gerchberg-Saxton algorithm to

3.2 Implementation of the SLM in the experiment

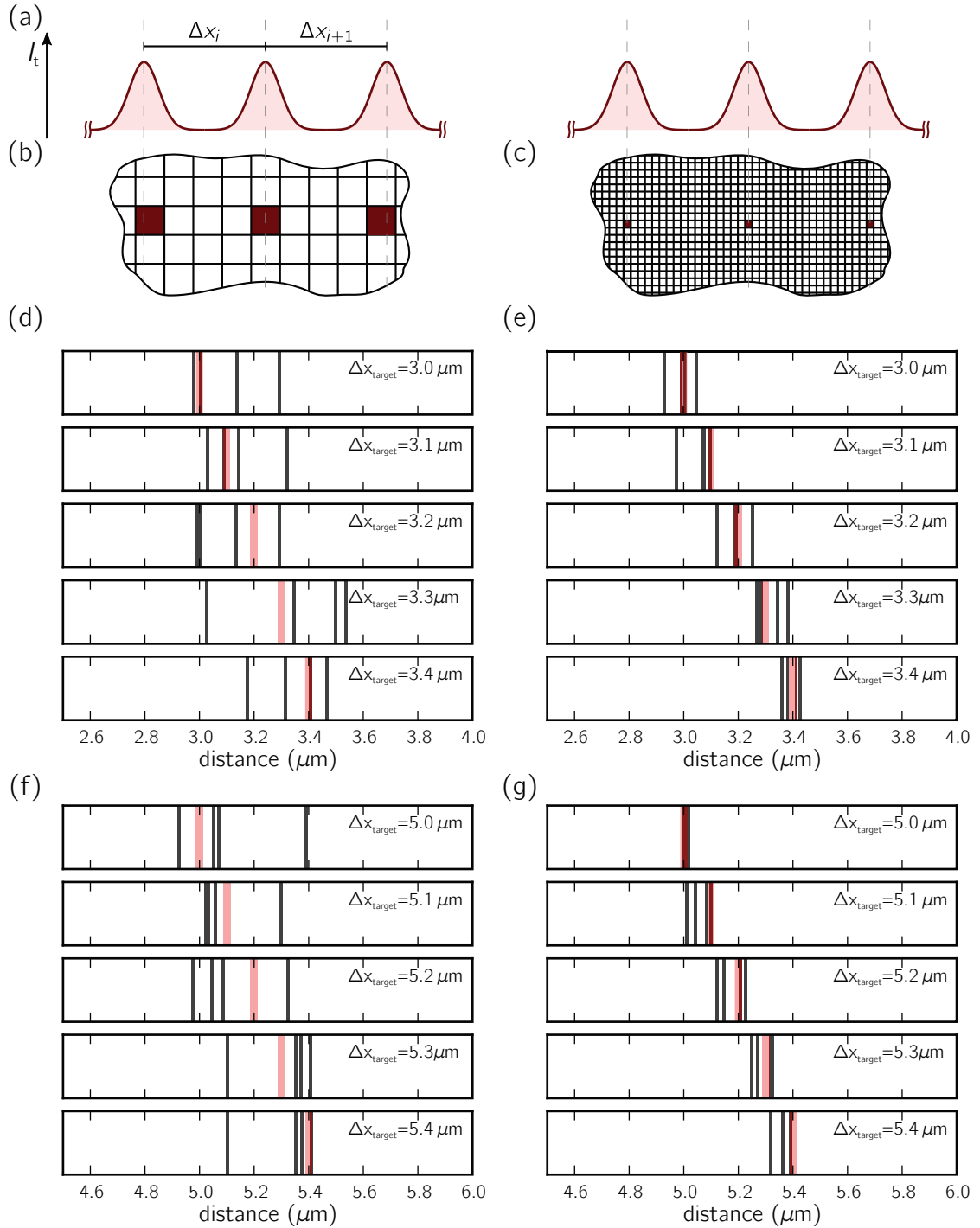


Figure 3.7: Effect of the SLM focal unit size on a 5×1 trap array. (a) We set a 5×1 trap array with equal inter-trap spacings $\Delta x = \Delta x_1 = \Delta x_2 = \Delta x_3 = \Delta x_4$ as the target image. For various target trap-spacings Δx_{target} (light red vertical lines in d-g) we measure the obtained trap spacings (black vertical lines in d-g), with the Gerchberg-Saxton loop run for 40 iterations. We once use a 1024×1024 matrix (b,d,f), and once a 4096×4096 matrix (c,e,g) in the calculation, while keeping the physical size of the matrix entries $\Delta_x \times \Delta_y$ in the SLM plane constant, thus increasing the resolution of the target image by a factor 4, as shown in the sketch in (b,c).

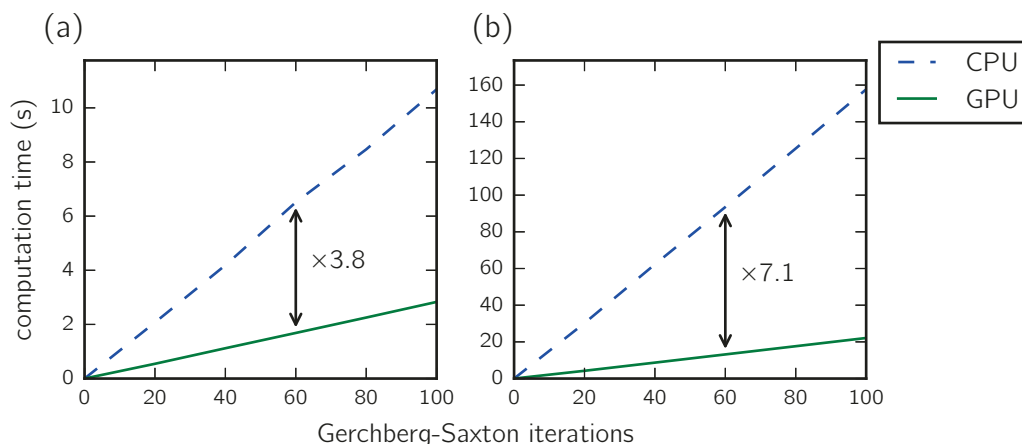


Figure 3.8: Computation times of the Gerchberg-Saxton algorithm. The timings to run the Gerchberg-Saxton algorithm for 100 iterations decrease significantly when running the code on a NVIDIA Quadro K2000 GPU (green lines) instead of an Intel i5 4570 3.20 GHz CPU (blue lines). The increase in calculation speed is even larger for a 4096×4096 matrix size (b) than for a 1024×1024 matrix size (a).

$N_x \times N_y = 2^{12} \times 2^{12} = 4096 \times 4096$ entries, corresponding to a focal unit size of $\tilde{\Delta}_x \times \tilde{\Delta}_y \simeq 0.1 \times 0.1 \mu\text{m}^2$. With this higher resolution for the target image, the created trap arrays are closer to the given target image, with a smaller distance spread between the individual traps (Figure 3.7, right panels).

The advantage of the increased focal plane resolution due to the larger matrices used in the numerical calculation comes at the cost of an increased computation time, which scales roughly with the number of entries in the matrices, from a few seconds for a $2^{10} \times 2^{10}$ grid to more than a minute for a $2^{12} \times 2^{12}$ grid. To keep the computation time at a feasible length for everyday use in the lab, in particular when using the trap intensity feedback loop (described in Section 3.4), it is possible to run the Gerchberg-Saxton algorithm on a graphics card (GPU), instead of the main processor (CPU). The difference between the two processing units is that CPUs are elaborate general purpose processors, optimised for running linear sets of instructions very fast. GPUs on the other hand contain up to a few thousand simple processing units, and are optimised to perform computations on these units in parallel [Texas Advanced Computing Center, 2010].

As the FFT of a large matrix can be computed very efficiently in parallel, and MATLAB offers a toolbox to conveniently run code on certain graphics cards, we could reduce the computation time for calculating phase arrays by up to a factor

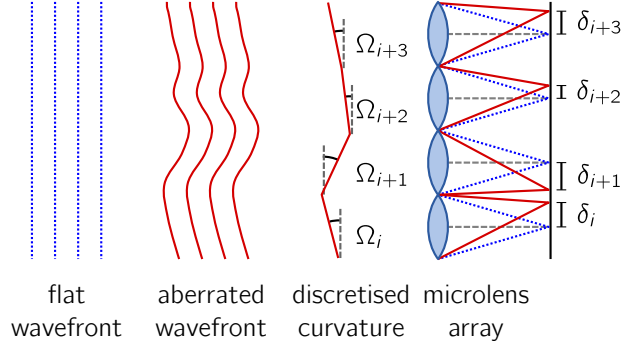


Figure 3.9: Principle of a Shack-Hartmann sensor A Shack-Hartmann sensor consists of a microlens array and a photon sensor (typically a CCD or CMOS chip). For a laser beam with a flat wavefront (blue dotted lines), the foci of the individual microlenses lie on their respective optical axis (grey dashed lines). The wavefront of an aberrated laser beam (red solid lines) can locally be approximated by a plane wave with a tilted wavefront with an angle Ω_j . Each of the foci of the lens array is then displaced by $\delta_j = f\Omega_j$ with respect to the optical axis, f being the focal length of the lenses. One can therefore reconstruct the wavefront by measuring the foci displacements δ_j .

seven when running the calculation on our GPU² (see Figure 3.8). The 2 GB memory of the GPU limits us to a maximum matrix size of $2^{12} \times 2^{12}$, which is sufficient for our purposes, as larger matrices do not seem to further improve the quality of the produced trap arrays.

3.3 Aberration correction

Even with a careful implementation of the SLM and the optical components to bring the trapping light to the trapping region inside the vacuum chamber, the trap quality in large trap arrays with a number of traps $N_{\text{traps}} \gtrsim 10$ is no longer satisfactory (see Figure 3.11(c)). This is due to aberrations of the trap beam introduced by the optical components in the setup. These aberrations not only decrease the Strehl ratio of the focused beam, thus decreasing the achievable trap depth for a given laser power. They also invalidate the assumption in the calculation of the phase pattern of having an ideal Gaussian beam with a flat wavefront, thereby reducing the quality of the generated hologram. Especially for large trap arrays, which require more complex phase patterns with higher spatial frequencies, the latter effect becomes critical.

²The computer to calculate the phase patterns has an Intel i5 4570 four-core 3.20 GHz CPU and a NVIDIA Quadro K2000 graphics card.

However, as aberrations are solely the deviations of the actual wavefront from the ideal wavefront of a laser beam, we can easily correct for the aberrations using the SLM, as soon as we know the deformation of the wavefront [López-Quesada, Andilla, and Martín-Badosa, 2009].

Correcting the non-flatness SLM chip surface

The most drastic aberration in the optical setup is introduced by the SLM itself. In the calculation of the phase patterns, we consider the SLM as a perfect mirror. Due to the manufacturing process though, its surface is slightly uneven. The SLM manufacturer provided us with a phase pattern (which we will call φ_{factory} , shown in Figure 3.12), which corrects for this non-flatness. The SLM chip surface appears to be slightly curved, with a peak-to-valley deviation of 2.4λ , with $\lambda = 850 \text{ nm}$ being the wavelength of our trap laser.

This factory correction phase pattern φ_{factory} is always added to the phase patterns that we display on the SLM.

3.3.1 Correcting the aberrations of the optical components

Additional aberrations can be introduced to the trap beam by the remaining optical components of our setup, whose arrangement is shown in Figure 3.6. In order to measure the aberrations of the beam (with the factory correction phase pattern φ_{factory} already applied), we used a Shack-Hartmann sensor [Platt and Shack, 2001]. Such a device can reconstruct the wavefront of an incident laser beam by using a microlens array and measuring the focus displacement of each microlens due to local tilts of the wavefront (see Figure 3.9 for further explanations). In our case, we used a commercial Imagine Optics HASO4 FIRST Shack-Hartmann sensor, with an aperture of $3.6 \times 4.6 \text{ mm}^2$ and an array of 32×40 lenses.

We analyse the wavefront aberrations by using a single trap, centred on the optical axis of the aspheric lenses. For this the only phase displayed on the SLM is the phase correction pattern φ_{factory} to make up for the non-flatness of the SLM chip, superimposed on a blazed grating φ_{grating} to centre the trap on the optical axis of the aspheric lens pair. We use an $f = 200 \text{ mm}$ achromatic doublet lens between the vacuum chamber and the Shack-Hartmann, to slightly focusing the beam to adapt its size to the aperture of the latter (see sketch in Figure 3.10). The quadratic phase introduced by the lens can be removed from the detected wavefront after the measurement.

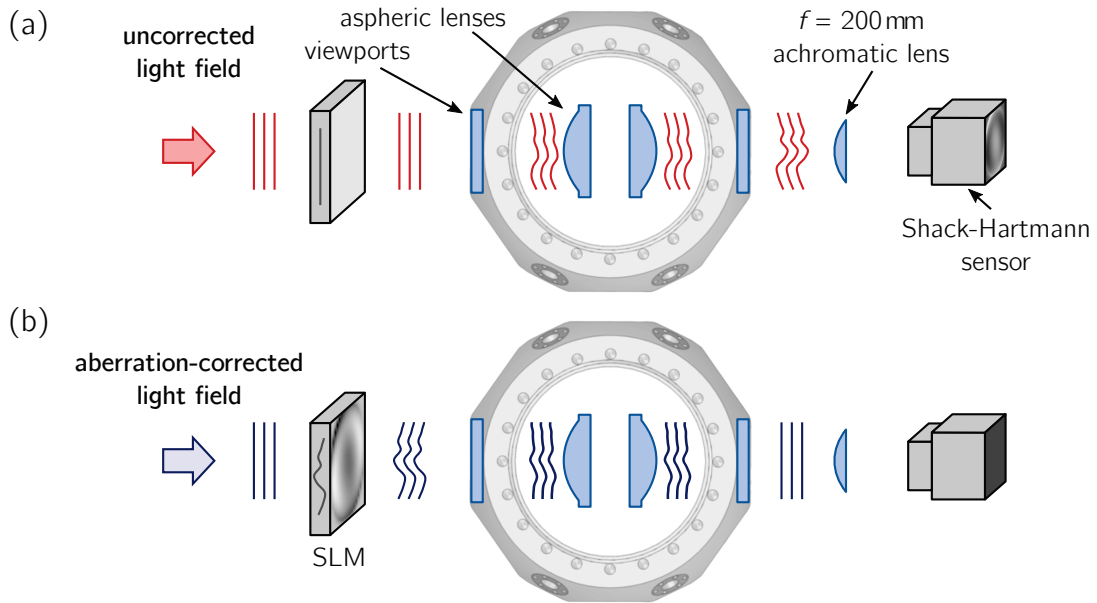


Figure 3.10: Measurement of the aberrations with the Shack-Hartmann sensor.

(Note: in this sketch we assume that only the two viewports introduce aberrations)

(a) The wavefront of the trap beam was measured with a Shack-Hartmann sensor behind the vacuum chamber, using an $f = 200$ mm doublet to adapt the beam size to the Shack-Hartmann aperture. This measurement may introduce the following error: (b) if significant aberrations are introduced by the second lens or viewport, they are also taken into account when correcting them with the SLM. We might thus *overcorrect* the aberrations at the position of the atoms.

It is convenient to express aberrations in the form of Zernike polynomials [Zernike, 1934; Born *et al.*, 1999], a set of orthogonal functions on the unit disk³. The first terms of the Zernike polynomials correspond to aberrations often observed in optical tests, such as astigmatism, coma, etc. By fitting the Zernike polynomials to the measured wavefront, one can therefore deduce the types of aberration present in the optical path by looking at the coefficients of the respective terms. The measured aberrations are shown in Figure 3.11(a) in terms of Zernike coefficients, giving a total rms deviation from a flat wavefront of $\delta_{\text{rms}} = 0.15 \lambda$. Here we ignore the tilt and focus terms, as they are only introduced by a tilt of the Shack-Hartmann itself and the achromatic lens doublet before the Shack-Hartmann respectively⁴. Figure 3.11(b)

³The measured aberrations are discontinuous at the edge of the disk. In order to avoid a phase discontinuity on the SLM, we run a Gaussian filter over the edge of the aberration correction phase pattern, without altering the correction pattern itself.

⁴When using with the Shack-Hartmann without the achromatic doublet lens focus term is indeed negligible.

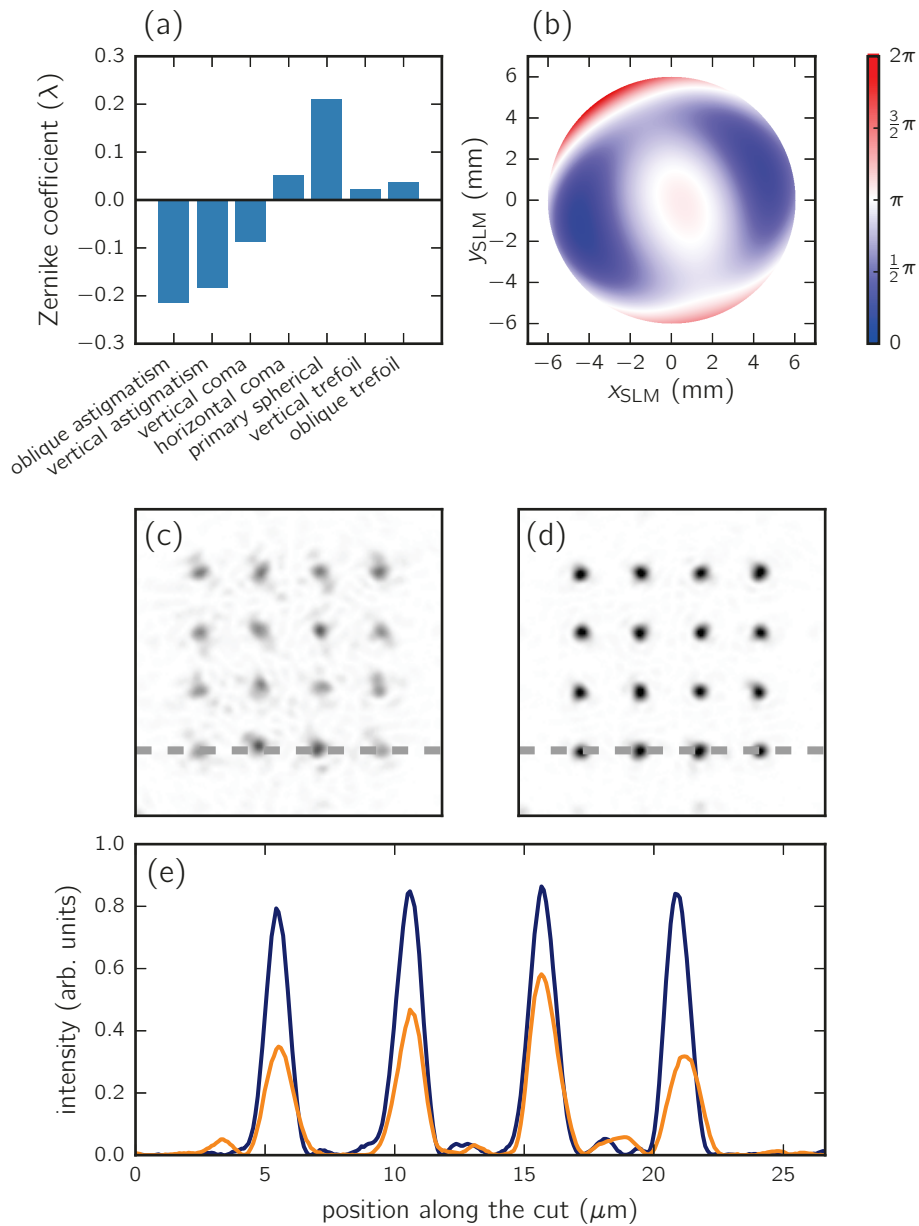


Figure 3.11: Aberration correction with the Shack-Hartmann. (a) The Zernike coefficients of the wavefront of the trap beam as measured with the Shack-Hartmann. Tilt and focus are ignored; higher-order coefficients are not shown, as they are much smaller than the ones that are shown. (b) The aberrations of the trap beam, reconstructed from the Zernike coefficients, with the beam dimension at the SLM. (c,d) Images of a 4×4 trap array taken with a CCD camera placed after the vacuum chamber, without (c) and with (d) the aberration correction phase pattern $\varphi_{\text{aberration}}$ displayed on the SLM. (e) Intensity profile along the bottom row of traps, integrated over a width of 3 pixels, as indicated by the grey dashed lines in (c,d), without (orange) and with (blue) the aberration correction. At the position of the Shack-Hartman, the rms deviation from a flat wavefront is reduced from $\delta_{\text{rms}} = 0.15 \lambda$ to $\delta_{\text{rms}} = 0.014 \lambda$.

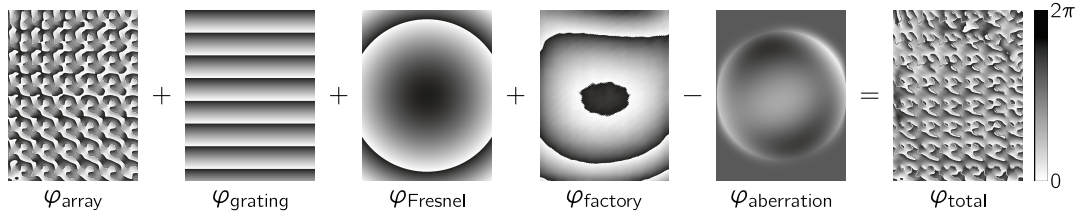


Figure 3.12: Composition of the final phase displayed on the SLM. The combined phase φ_{total} displayed on the SLM is made up of the phase patterns φ_{array} creating the actual array of traps, φ_{grating} and φ_{Fresnel} to move the pattern transversally and longitudinally respectively if needed, φ_{factory} to correct for the non-flatness of the SLM chip, and the measured $\varphi_{\text{aberration}}$ to correct for aberrations introduced by our optical elements. The sum is calculated modulo 2π .

shows the reconstructed wavefront using the Zernike polynomials, for a beam size corresponding to that at the SLM. We see that the main aberrations are astigmatism and spherical aberration, which we attribute to the viewports of the vacuum chamber.

When subtracting the correction pattern (from now on called $\varphi_{\text{aberration}}$) from the phase pattern displayed on the SLM the rms deviation from a flat wavefront after the vacuum chamber is reduced by about a factor ten to $\delta_{\text{rms}} = 0.014 \lambda$.

Ideally, we would like to correct the aberrations at the position of the atoms, in order to achieve the best trap quality. Unfortunately, we cannot access this position without opening the vacuum chamber and removing the second aspheric lens. We therefore place the Shack-Hartmann sensor and measure the wavefront directly after the beam has passed through the vacuum chamber.

However, correcting the aberrations that we measure *after* the vacuum chamber might *overcorrect* the aberrations at the focus of the aspheric lens, if significant aberrations are introduced by the optical elements after the focus. This is illustrated in the sketch shown in Figure 3.10: the aberration-correction phase pattern displayed on the SLM subtracts the aberrations detected by the Shack-Hartmann from the trap beam. The beam will therefore have a perfectly flat wavefront at the position of the Shack-Hartmann, but may still have aberrations in the focus of the aspheric lens. As we will see later, the aberration correction nevertheless improves the quality of the traps significantly. The final composition of the various phase patterns to create the trap array and correct for the aberrations is depicted in Figure 3.12.

We then replace the Shack-Hartmann sensor with a CCD camera in order to see the effect of subtracting $\varphi_{\text{aberration}}$ from a phase pattern creating a 4×4 trap array. We see that the quality of the trap array increases significantly (see Figure 3.11(c-e)).

When looking at a line profile along a row of the trap array, integrating over a width of 3 pixels, we see that the peak intensity of the traps increases by about a factor 2.

We thus showed that we could significantly reduce the aberrations *after* the vacuum chamber. This does not automatically imply that we actually improved the wavefront at the focus of the aspheric lens. An independent measurement of the wavefront before the vacuum chamber gives $\delta_{\text{rms}} = 0.05 \lambda$, showing that most of the aberrations are indeed introduced by the vacuum viewports and/or the aspheric lenses. We therefore used a single atom in the central trap of a 3×1 trap array with a $4 \mu\text{m}$ spacing, at the focus of the aspheric lens to directly investigate the effect of the aberration correction phase pattern $\varphi_{\text{aberration}}$ on the trap itself by measuring the trap depth and radial frequency of the atom in the trap.

3.3.2 Quantifying the effect of the aberration correction

The two important parameters here to characterise the microtrap are the trap depth U_0 and the frequencies (ω_r, ω_z) with which the atom oscillates in the trap in radial and longitudinal direction respectively. If we approximate the microtrap as an harmonic potential, then these parameters are related by

$$\omega_r = \sqrt{\frac{4U_0}{m w_0^2}} \quad \text{and} \quad \omega_z = \sqrt{\frac{2U_0}{m z_R^2}}, \quad (3.11)$$

with m the mass of the particle in the trap, w_0 the waist of the trap and $z_R = \pi w_0^2 / \lambda$ the Rayleigh length with λ the wavelength of the trapping light.

Measuring the trap depth seen by a single atom

We first measure the depth of the trap as seen by the ^{87}Rb atom. We follow the same procedure as in [Béguin, 2013] which relied on the method introduced in the thesis of G. Reymond [2002]. We make use of the fact that the excited state $|5P_{3/2}, F' = 3, m_{F'} = 3\rangle$ is only marginally shifted in energy by the trapping light. We can therefore quantify the light shift of the ground state caused by the microtrap by measuring the $|5S_{1/2}, F = 2, m_F = 2\rangle \rightarrow |5P_{3/2}, F' = 3, m_{F'} = 3\rangle$ transition frequency [Darquié, 2005; Tey *et al.*, 2008; Shih and Chapman, 2013], as all Zeeman sub-levels of the $5P_{1/2}$ state are shifted equally in energy for our π -polarised trapping light.

To measure the transition frequency, we shine σ^+ -polarised probe light on the atom

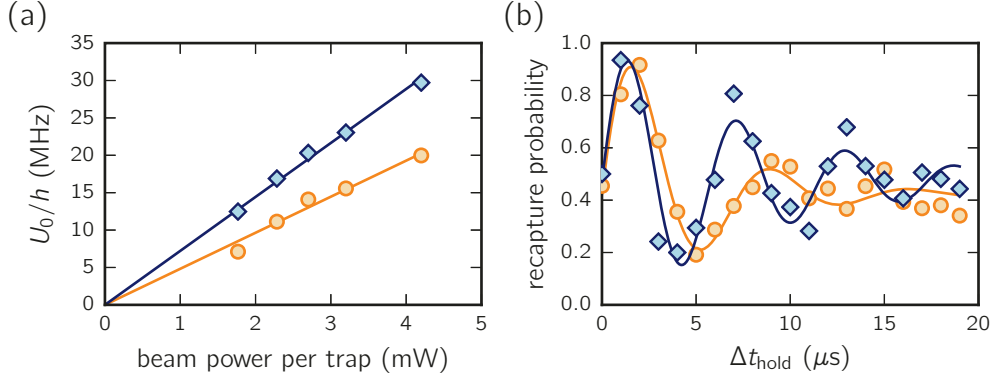


Figure 3.13: Microtrap characterisation with a single atom. We use a single atom trapped in a microtrap to verify that using the aberration correction phase pattern $\varphi_{\text{aberration}}$ (blue diamonds) actually improves the trap quality compared to the uncorrected beam (orange circles) at the focus of the aspheric lens. (a) The trap depth U_0/h as a function of the power in the trap beam. The aberration correction increases the trap depth by $\sim 50\%$. The solid lines are linear fits to the data through the origin. (b) We excite the atom to a higher monopole mode of the trap, let the atom oscillate for a variable time Δt_{hold} and measure the recapture probability after having switched the trap off again for a few μs . Solid lines are fits by the empirical function $y_0 + Ae^{-\Delta t_{\text{hold}}/\tau} \sin(2\omega_r \Delta t_{\text{hold}})$. The trap frequency increases by about 30% for the aberration corrected trap.

in the microtrap, and record the number of scattered photons as a function of the probe light frequency. The shift of the resonance of the atom in the trap compared to an atom in free space directly gives us the trap depth U_0/h . The measured trap depths are shown in Figure 3.13(a), for different trap beam powers per trap.

When fitting the measured light shifts by a linear function going through the origin, we find

$$\begin{aligned} \text{uncorrected:} \quad & U_0/P_{\text{trap}} = h \times 4.8 \frac{\text{MHz}}{\text{mW}} \\ \text{aberration corrected:} \quad & U_0/P_{\text{trap}} = h \times 7.2 \frac{\text{MHz}}{\text{mW}}. \end{aligned} \quad (3.12)$$

The trap depth as seen by the single atom thus improves by $\sim 50\%$ when correcting for the aberrations.

Measuring the trap oscillation frequencies

The second important trap parameter is the frequency with which the atom oscillates in the trap. The experiment to measure the transverse trap frequency [Reymond *et al.*, 2003] is explained in Figure 3.14 for the one dimensional case. We start the experiment with a single atom in the centre of the microtrap. We switch the trap off for a time

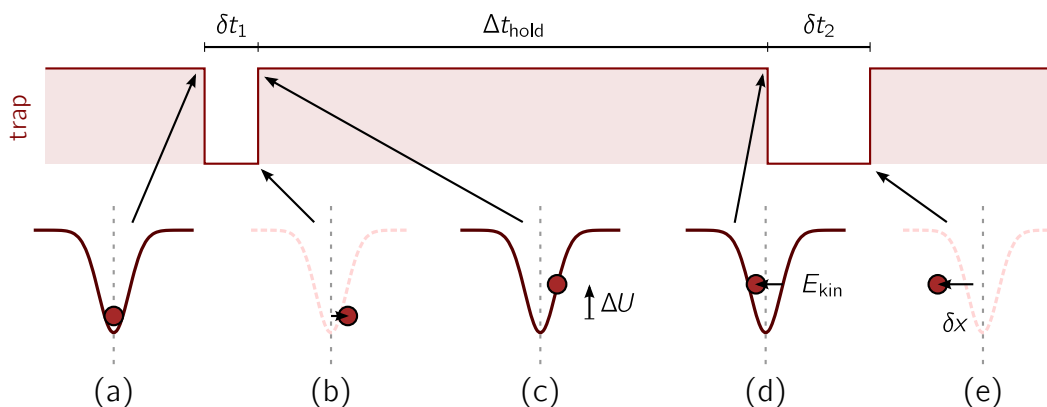


Figure 3.14: Sketch in 1D of the experiment to measure the trap frequency.

(a) We start the experiment with a single atom in the microtrap. (b) The trap is turned off for a time $\delta t_1 = 4 \mu\text{s}$. (c) In this time, the atoms moves away from the trap centre due to its finite initial velocity v_0 . When the trap is switched on again, the atom gains the potential energy $\Delta U = 1/2 m \omega^2 (v_0 \delta t_1)^2$ (with ω the trap frequency and m the mass of the atom). (d) We hold the atom for a variable time Δt_{hold} during which the atom will oscillate in the trap. When switching the trap off again, the atom has a kinetic energy $E_{\text{kin}} = (U_0 + \Delta U) (1 - \cos(2\omega \Delta t_{\text{hold}}))/2$. (e) After having turned the trap off a again for a time $\delta t_2 = 12 \mu\text{s}$, the atom will have moved away from the trap by $\delta x = \sqrt{2E_{\text{kin}}/m} \cdot \delta t_2$. The probability to recapture the atom will thus oscillate with twice the trap frequency ω .

$\delta t_1 = 4 \mu\text{s}$ to excite it to a higher monopole mode in the trap. We keep the trap on for a variable time Δt_{hold} , during which the atom will oscillate in the trap. We then probe the kinetic energy of the atom by looking at the probability to lose the atoms after switching the trap off again for a time $\delta t_2 = 12 \mu\text{s}$. The loss probability is related to the kinetic energy, and thus also oscillates with twice the trap frequency ω .

Here we can neglect the longitudinal motion of the atom, since with our trap beam parameters, according to Equation 3.11, the relation between the radial and transversal trap frequency is given by

$$\omega_z = \lambda / (\sqrt{2\pi} w_0) \cdot \omega_r \simeq 0.2 \omega_r. \quad (3.13)$$

For the chosen time $\delta t_1 = 4 \mu\text{s}$, the free expansion along the beam axis thus remains small, and we can assume that we mainly excite a radial oscillation in the trap.

The result of the measurement is shown in Figure 3.13(b). A fit to the data with a

damped sine gives the following radial trap frequencies:

$$\begin{aligned} \text{uncorrected:} \quad & \omega_r = 2\pi \times 68.0 \text{ kHz} \\ \text{aberration corrected:} \quad & \omega_r = 2\pi \times 86.5 \text{ kHz} \end{aligned} \tag{3.14}$$

This corresponds to a 30 % increase in the trap frequency, but is still almost 20 % smaller compared to sending the trap beam directly to the aspheric lens without the SLM, as found by Lucas Béguin [2013] on the same setup with a single trap without the SLM. This hints that the more complex setup with the SLM slightly increases the waist of the microtraps.

Together with Equation 3.11 the measured increase in trap depth and frequency shows that the trap waist w_0 does not change when applying the aberration correction. We however significantly increased the diffraction efficiency of the SLM, giving us deeper traps for the same amount of light power, which in turn also increases the trap frequency.

In principle, we could use the single atom measurements as a quality measure to try to improve the trap quality even further, e.g. by using an evolutionary algorithm [Weise, 2009] on the Zernike coefficients. But as every data point in Figure 3.13 takes about 15 minutes to record, such an optimisation would be very time consuming and very sensitive to possible slow drifts of experimental parameters as the excitation beam intensity.

We tried however to use an aberration correction pattern which was constructed using only half of the measured value of each Zernike coefficient, which would be the ‘correct’ correction if the two viewports would introduce equal aberrations. The result was marginally worse than taking the full value of the measured Zernike coefficients measured with the Shack-Hartmann.

For all the results shown in this thesis from here on, the aberration correction phase pattern is subtracted from the phase displayed on the SLM.

3.4 Feedback for intensity homogeneity

Even when taking care when calculating the phase for a given target intensity distribution, and taking into account the non-flatness of the SLM chip and the aberrations introduced by the optics, the trap depths in the resulting trap array can vary quite significantly from one trap to another, which is detrimental to the experiment. Having traps that are too deep leads to a light shift so large that the

trapped atom is shifted too far off-resonant from the MOT-light, and no longer scatters enough photons to be detected efficiently. In too shallow traps on the other hand it is no longer possible to trap atoms reliably over the duration of the experiment. It is therefore important when creating trap arrays that all the microtraps have very similar trap depths.

As an example we run the Gerchberg-Saxton algorithm for a 10×10 square trap array with a trap spacing of $4 \mu\text{m}$, where all traps have the same target intensity I_t . The resulting trap intensities as measured with the CCD camera are shown in Figure 3.15(b). We measure a rather large dispersion of trap intensities of $\pm 19\%$ rms, with the most shallow trap having 61% and the deepest trap having 148% of the mean intensity of the traps in the array.

The inhomogeneities in the trap depths that we see when measured with a CCD camera after the vacuum chamber (see Figure 3.6) can have various causes:

1. The Gerchberg-Saxton algorithm fails to calculate a phase which gives exactly equal trap intensities.
2. An imperfect diffraction of the light by the calculated phase pattern, e.g. due to remaining aberrations in the optics setup.

Both of the above mentioned points occur in our experiment. The first point we could easily correct for by adapting the target intensity in the numerical calculation of the phase pattern. The second point can also be corrected for by measuring the actual depth of the trap created by a given pattern with the CCD camera behind the vacuum chamber, and adapting the pattern accordingly⁵.

We thus equalise the trap intensities measured on the CCD camera in the following way (see Figure 3.15(a)). We run the Gerchberg-Saxton algorithm with the desired trap array as the target intensity, starting out with a random phase in the calculation. After a given number of loops, when the calculation has converged, we pause the algorithm and display the current calculated phase on the SLM. We then measure the trap intensity I_i of each trap i in the image recorded with the CCD camera, and adjust its intensity in the target trap array as

$$I'_i = \frac{\bar{I}}{1 - G(1 - I_i/\bar{I})}, \quad (3.15)$$

⁵Again, we could in principle also measure the trap depths by using single atom measurements, but as the measurement of the homogeneity of trap depths would take in the order of 15-20 minutes, the total duration of the optimisation would become intractable in day to day experiments.

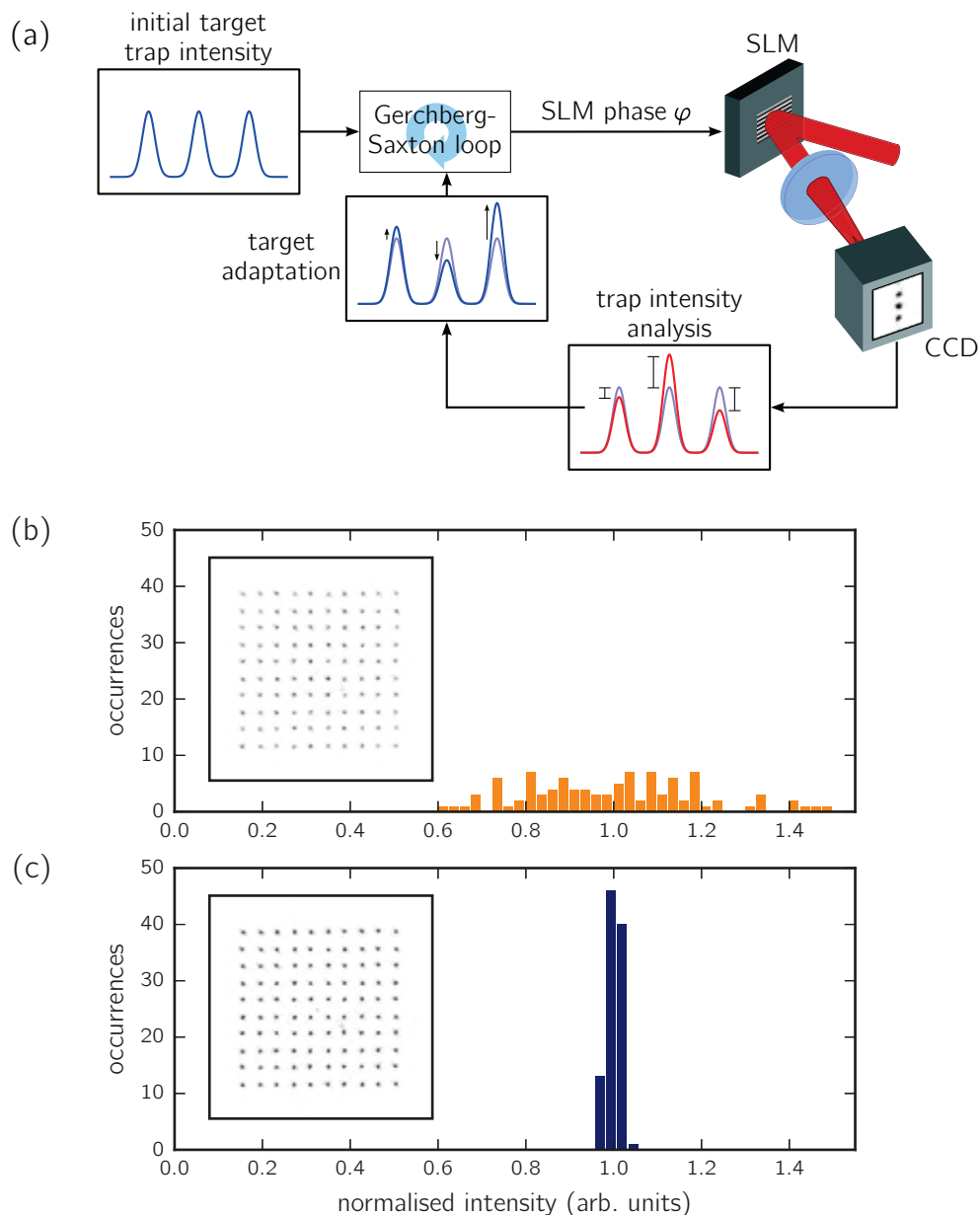


Figure 3.15: Feedback loop for trap intensity homogeneity. (a) For a given target image, we run the Gerchberg-Saxton algorithm, pause it and display the current phase on the SLM. We then analyse the trap intensities from this phase pattern as measured on the CCD camera, and adapt the target trap intensities accordingly, making deep traps shallower and shallow traps more intense in the target image. We then continue the Gerchberg-Saxton algorithm with the updated target image. We repeat the intensity feedback until the coefficient of variation of trap intensities has reached a satisfying level ($\sim 2\%$), typically after 5-10 feedback iterations. (b) The array after running the Gerchberg-Saxton algorithm once. The histogram shows that the intensities as measured on the CCD camera have a large spread, with a standard deviation of 19% of the mean. (c) The same array, this time using the intensity feedback in the Gerchberg-Saxton. The standard deviation of the trap intensities is reduced to 1.4%. The insets show the respective images recorded with the CCD camera.

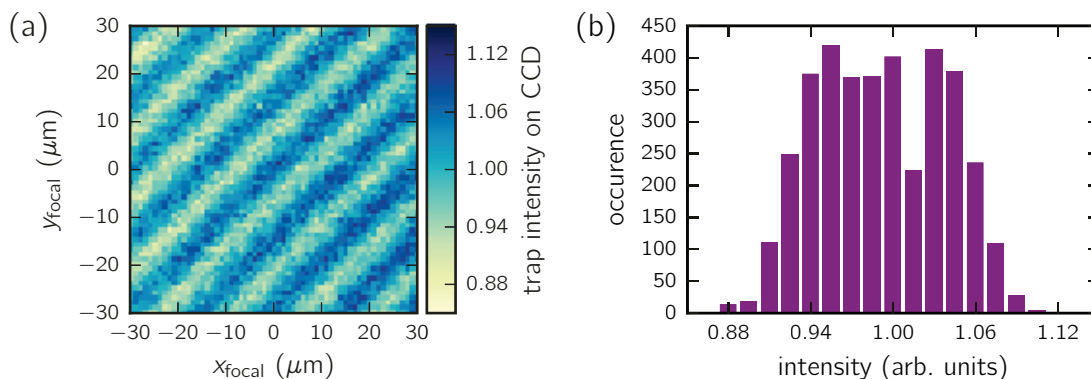


Figure 3.16: Intensity variations on the trap-imaging CCD camera. (a) Intensity of a single microtrap with constant power as measured on the CCD camera, scanned in steps of $1 \mu\text{m}$ in an area of $60 \times 60 \mu\text{m}^2$ in the focal plane of the aspheric lens. We see intensity fringes with a period of about $10 \mu\text{m}$ and an rms around the mean of 5%. (b) Histogram of the measured trap intensities in (a).

where \bar{I} is the mean intensity of all traps in the CCD image and G an adjustable gain factor in the feedback. This means that traps that are too weak get enhanced in the target image, while traps that are too deep get dimmed, proportionally to their ratio with the mean of the trap intensities. We then continue the Gerchberg-Saxton algorithm with the updated target image⁶. The entire process of taking an image with the CCD camera, measuring all individual trap depths, and adjusting the respective trap intensities in the phase calculation, is done in an automated way by a computer.

After typically ~ 5 intensity feedback iterations the standard deviation of the trap intensities is reduced significantly to $\sim 1\%$, with the fastest improvement typically achieved with $G \simeq 0.7$. A larger gain overshoots the correction, leading to oscillations of the trap intensities with the trap feedback iterations, while a smaller gain increases the convergence time. Figure 3.15(c) again shows the 10×10 trap array, this time after having run the Gerchberg-Saxton including 20 intensity feedback iterations. The standard deviation could be reduced to 1.4%, with the most shallow trap now having 96% and the deepest trap having 103% of the mean trap depth.

We recently became aware of spatial variation of the light intensity measured on the CCD camera, which results in a spatial variations of the measured trap depths, even for a homogeneous trap array. The spatial intensity dependence of our CCD camera⁷

⁶After the implementation of the intensity feedback loop we realised that a similar technique was already discussed in [Matsumoto *et al.*, 2012].

⁷We use a [The Imaging Source DMK 41BU02](#) monochrome industrial CCD camera with 8 bit A/D dynamic range.

is shown in Figure 3.16(a). We scan a single microtrap with constant total power in the transversal plane around the optical axis of the aspheric lens, and measure its intensity on the CCD camera. We see an oscillating intensity variation of the microtrap, with a period of about $10\ \mu\text{m}$ and an rms about the mean of about 5% (see Figure 3.16(b)). The origin of these intensity variations is most likely due to an internal interference of the trap beam in the microlens array in front of the CCD chip (personal communication, The Imaging Source, 10/07/2015). However, the 5% intensity variations only slightly broaden the detected distribution of trap depths of Figure 3.15(b).

All the results presented in this chapter, the careful implementation of the SLM in the setup, the aberration correction and the feedback loop for homogeneous trap intensities were crucial to achieve high quality trap arrays with $\gtrsim 5$ traps for experiments presented in the following Chapters of this thesis.

3.5 Gallery of trap arrays

With the methods described in this chapter, one can arrange single neutral atoms in arbitrary geometries, and change the order with a simple click of the mouse on the computer. We are able to generate trap arrays with spacings as low as $3\ \mu\text{m}$, containing up to ~ 100 traps⁸.

Figure 3.5 shows a selection of trap arrays that we are able to generate in the lab. We can simply arrange the atoms in one-dimensional chains, which we have used in [Barredo *et al.*, 2015], or in a ring (Figure 3.5(b)), realising a quasi-one-dimensional system with periodic boundary conditions, to study transport [Heidrich-Meisner, Honecker, and Brenig, 2007], thermalisation [Olmos, Müller, and Lesanovsky, 2010], or phase transitions [Mattioli, Glätzle, and Lechner, 2015] in one-dimensional systems.

For experiments in 2D, we can generate large non-trivial lattices, from square to triangular (Figure 3.5(d)), to hexagonal, kagome (3.5(e)) and ‘squagome’ (3.5(f)) lattices, e.g. to study the physics of graphene [Castro Neto *et al.*, 2009] and phenomena as frustration [Santos *et al.*, 2004; Glaetzle *et al.*, 2014] and topological spin liquids [Yan, Huse, and White, 2011; Peter *et al.*, 2015; Yao *et al.*, 2015].

It is even possible to put the atoms in aperiodic or completely random positions (Figure 3.5(c,g)), something that is intrinsically non-trivial for optical lattices [Weitenberg *et al.*, 2011], potentially allowing the study of phenomena as many-body

⁸The number of traps is limited by the total light power that can be sent on the SLM, and the field of view of the aspheric lens.

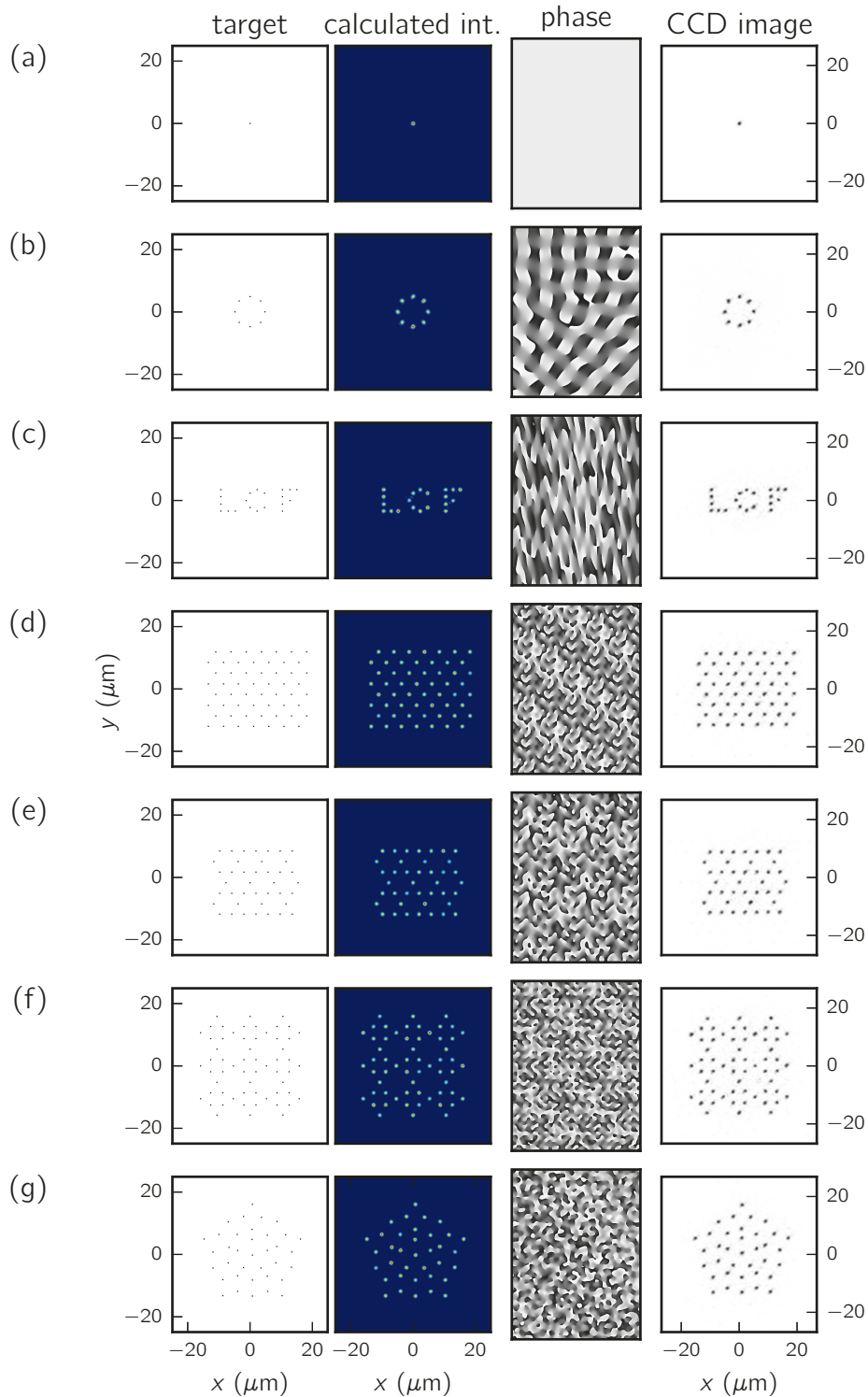


Figure 3.17: Examples of generated trap patterns. From left to right: the target pattern used as I_t in the Gerchberg-Saxton algorithm, the calculated intensity of the light field in the focal plane, the obtained phase pattern, and the trap intensities as measured with the CCD camera. (a) single trap, (b) circle of 8 traps, (c) arbitrary arrangement, (d) triangular lattice, (e) kagome lattice, (f) 'squagome' lattice, (g) quasi-periodic (Penrose) pattern.

localisation [Anderson, 1958; Hauke and Heyl, 2015] and transport in disordered networks [Bässler, 1993; Scholak *et al.*, 2011].

3.6 Conclusion

We have shown how we use a spatial light modulator to shape the spatial phase of our optical dipole trap beam to ‘clone’ the single microtrap. Using this technique, we are able to create arbitrary 2D geometries of up to ~ 100 single atoms traps, with trap spacings as low as $3 \mu\text{m}$, and array sizes up to $\sim 50 \times 50 \mu\text{m}^2$. We calculate an appropriate phase pattern for a given trap arrangement using the Gerchberg-Saxton algorithm. In order to create high-quality trap array, we have measured the aberrations in the dipole trap beam, and correct for them using the SLM. In order to create traps of equal depth, we employ a feedback which measures the depths of the traps, and automatically corrects the target intensity in the Gerchberg-Saxton algorithm.

Spatially resolved state detection and manipulation in arrays of single atoms

In the previous chapter we have seen how we can create arbitrary arrays of microtraps by manipulating the spatial phase of a single trap beam using a Spatial Light Modulator. In this chapter we will see how we detect the state of the atoms by recording their scattered photons, spatially resolving each individual atom, on a CCD camera.

Furthermore, we demonstrate our ability to locally address an arbitrary site in the array to block or uniquely enable the Rydberg excitation of the addressed atom, and how we can use this addressing capability to manipulate the phase of an entangled two-atom state.

4.1 Determination of the state of the atoms in the microtraps

The reliable determination of the state of the atoms is crucial for our experiments. Before launching an experimental sequence, we need to continuously monitor the state of the microtraps of a given array, in order to launch an experiment as soon as a certain trigger condition is fulfilled, e.g. having a minimum number of loaded traps. In addition, at the end of a sequence, we need to detect whether a given atom has been excited to a Rydberg state or not. In this section, we present the simple but efficient detection method that we use in the experiment to achieve this.

4.1.1 Detection of the atomic fluorescence

We detect the presence of an atom in a given microtrap by measuring the scattered light from the 780 nm MOT cooling beams at the position of the traps. We collect the light via the same aspheric lens which focuses the trap beam (see Figure 4.1), separating it from the trap light with a dichroic mirror. We then image the trap plane

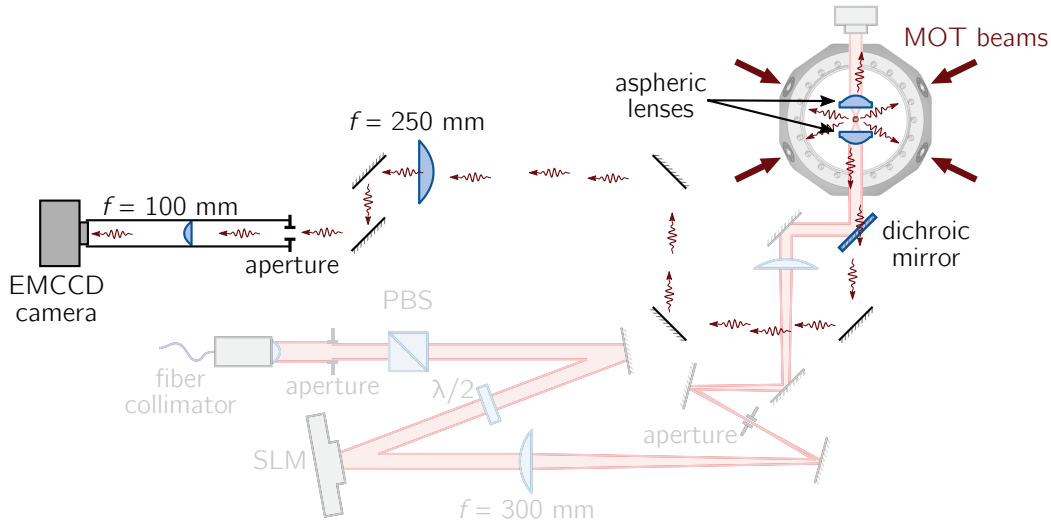


Figure 4.1: Overview of the single atom imaging system. We collect the MOT cooling light scattered by the atoms via the same aspheric lens which focuses the trap beam. A dichroic mirror separates the fluorescence light from the trap light. An $f = 250$ mm lens focuses the light at an aperture which reduces slightly the depth of field, and a second $f = 100$ mm lens images the atoms on the EMCCD chip, with total magnification of 16. The pixel separation of the EMCCD camera corresponds to $1 \mu\text{m}$ in the trap plane due to the magnification.

on a 16 bit electron multiplying CCD (EMCCD) camera¹, thermoelectrically cooled to -80°C in order to reduce the noise on the chip. We currently do not use the electron multiplying mode, as the photon yield from the single atoms at the EMCCD camera is high enough at about 6 photons/ms, detecting about 2% of photons scattered by an atom (see [Béguin, 2013] for an estimate of the detection efficiency).

The EMCCD camera has a 512×512 pixel resolution, with a pixel size of $16 \times 16 \mu\text{m}^2$. We calibrated the magnification of the imaging system to be 16, meaning that every pixel images a $1 \times 1 \mu\text{m}^2$ area in the trap plane. The fluorescence of each atom thus impinges on an area between 1×1 and 2×2 pixel, depending on whether it falls in the centre or on the edge of a pixel.

For all of the experiments presented in this thesis, we used the following parameters for the EMCCD camera. In order to increase the readout speed of the camera we used a 100×100 pixel subset of the CCD chip, and set the exposure time to 50 ms, giving us about 12 frames per second (fps), which we found to be a good trade-off between a high signal-to-noise ratio of the single atom signal and a high frame rate. A

¹We use a [Andor iXon Ultra 897](#) camera.

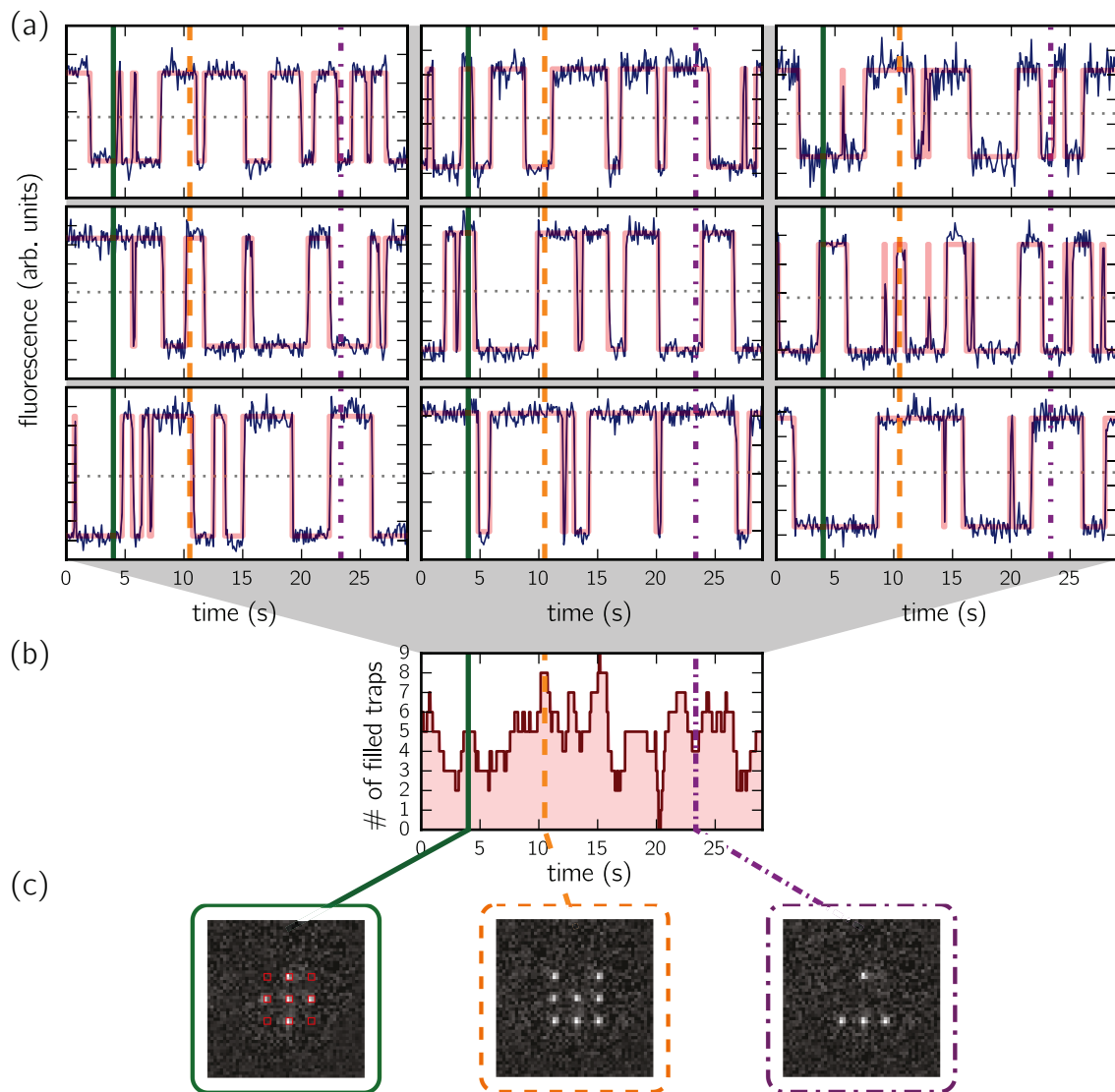


Figure 4.2: Fluorescence signal of atoms in a 3×3 trap array. (a) We monitor the mean fluorescence levels of the pixels indicated by the red squares in the frame in the bottom left during a 50 ms exposure, taking a frame about every 100 ms. For each trap, we see the typical telegraph-like fluorescence signal, with the low and high levels corresponding to 0 and 1 atoms in the trap respectively. We define a threshold (horizontal grey dashed lines) separating the two states, in order to create a binary signal (red curves on top of the fluorescence signal). (b) Number of filled traps obtained from the fluorescence traces. (c) Frames from the CCD camera taken at the times indicated by the green, orange and purple line respectively.

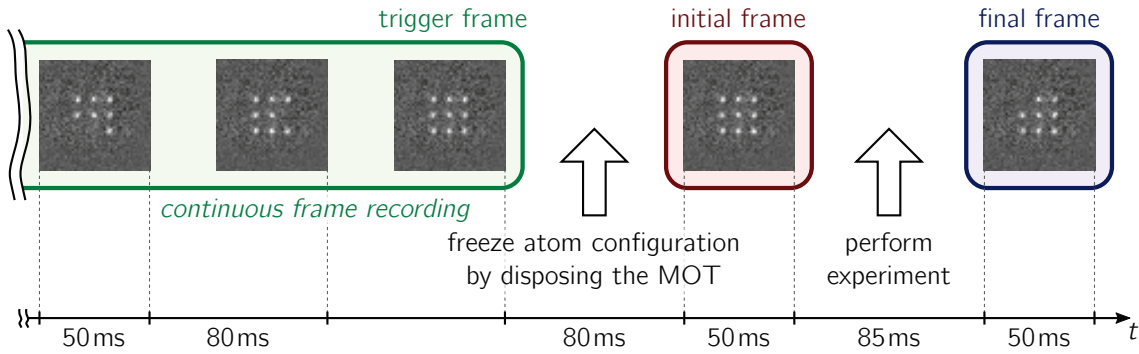


Figure 4.3: Timings of the EMCCD camera frames. We continuously record the fluorescence of the atoms on the EMCCD camera. When a predefined trigger condition is fulfilled, in this example the presence of 9 atoms in a 3×3 trap array, the configuration is frozen by turning of the MOT, thus stopping the loading process of the traps. We record another frame to get the initial atom configuration, perform a given experiment, e.g. a Rydberg excitation, and lastly record the final frame to see which atoms were lost during the experiment. The delays between the *trigger*, *initial* and *final* frames are set by the experimental sequence.

high frame rate is desirable, as we want to quickly launch an experiment once a given triggering condition has been fulfilled, before one of the traps loses its atoms again.

To display and analyse the detected atomic fluorescence on a computer, we developed a custom software based on the Python library `pyqtgraph`². It allows the real time display of the frames captured by the EMCCD camera, and automatically checks for the presence of atoms in predefined regions of interest (ROIs). The typical fluorescence signals for nine ROIs placed at the trap positions in a 3×3 trap array are shown in Figure 4.2. For each fluorescence signal we define a threshold which we use to binarise the signal to having either zero or one atom in the trap. The Python program continuously analyses the traces and can trigger an experiment once a pre-chosen condition, e.g. a minimum number of filled traps, is fulfilled (see Figure 4.3).

We then remove the MOT atoms by switching off the MOT cooling beams for ~ 40 ms. The loading process of the microtraps is therefore frozen. Without the MOT around, the lifetime of an atom in a microtrap was measured to be $\tau_{\text{lat}} \approx 10$ s. The lifetime of any given configuration in an N trap array is thus $\tau_{N\text{at}} = \tau_{\text{lat}}/N$.

Before we perform the actual experiment with the single atoms, we acquire an *initial frame*, giving us the initial atom configuration. It is not sufficient to just take

²`pyqtgraph` is a pure-python graphics and GUI library built on PyQt4 / PySide and numpy, aimed at fast data visualisation, distributed under the MIT open-source license.

the triggering frame for the initial atom configuration, as there is a finite probability for the atom configuration to change while disposing of the MOT. For the 3×3 array taken as an example here, in about 50 % of the experiments at least one of the atoms is lost between the triggering and the initial frame for trap loading rates of $R_{\text{load}} \approx 1$ atom/s. Of these 50 % ‘failed triggers’, 10 % are accounted for by the finite vacuum lifetime of the configuration. The remaining 40 % are accounted for by the 35 ms dead time between the end of the *trigger* frame exposure and the launch of an experimental sequence, and the ~ 20 ms to remove the MOT atoms.

We then record the *final frame* after having performed an experiment, from which we see which atoms were lost during the experiment. As will be shown later, this allows us to determine the internal state of each single atom individually, whether it was in the ground or Rydberg state.

We typically see a background on the single atom signal on the EMCCD camera, which is about 3 to 5 times larger than the fluorescence from a single atom. This background is due to MOT cooling light being scattered off components inside the vacuum chamber. The intensity of this speckle field varies in time on each pixel on the EMCCD camera. In order to still be able to define a threshold to automatically detect the presence of an atom in the trap, we ‘shake’ the pointing direction of five of the MOT beams with a few hundred Hz, by placing piezoelectric actuators underneath one of the mirrors of each of the five beams. This drastically improved the stability of the background on each pixel of the EMCCD camera, without leading to any noticeable increase of temperature for the trapped single atoms.

For any remaining fluctuations of the background, the Python program recording the camera frames can automatically adjust the threshold along with the background fluctuations in a very reliable way, by monitoring the average ‘high’ and ‘low’ values of the atomic fluorescence.

4.1.2 Loading statistics

The physics behind our single atom trapping was already briefly explained in Section 2.2.2. If a trap is empty, an atom can enter at any random time and stay in the trap, where it is continuously cooled by the MOT light. If an atom enters into an already filled trap, the two atoms will undergo a fast inelastic light assisted collision and will both be expelled from the trap [Schlosser *et al.*, 2001].

Since these two processes, loading an atom into the trap and removing the atom from the trap, rely on the same cause, namely an atom entering the trap, the expected

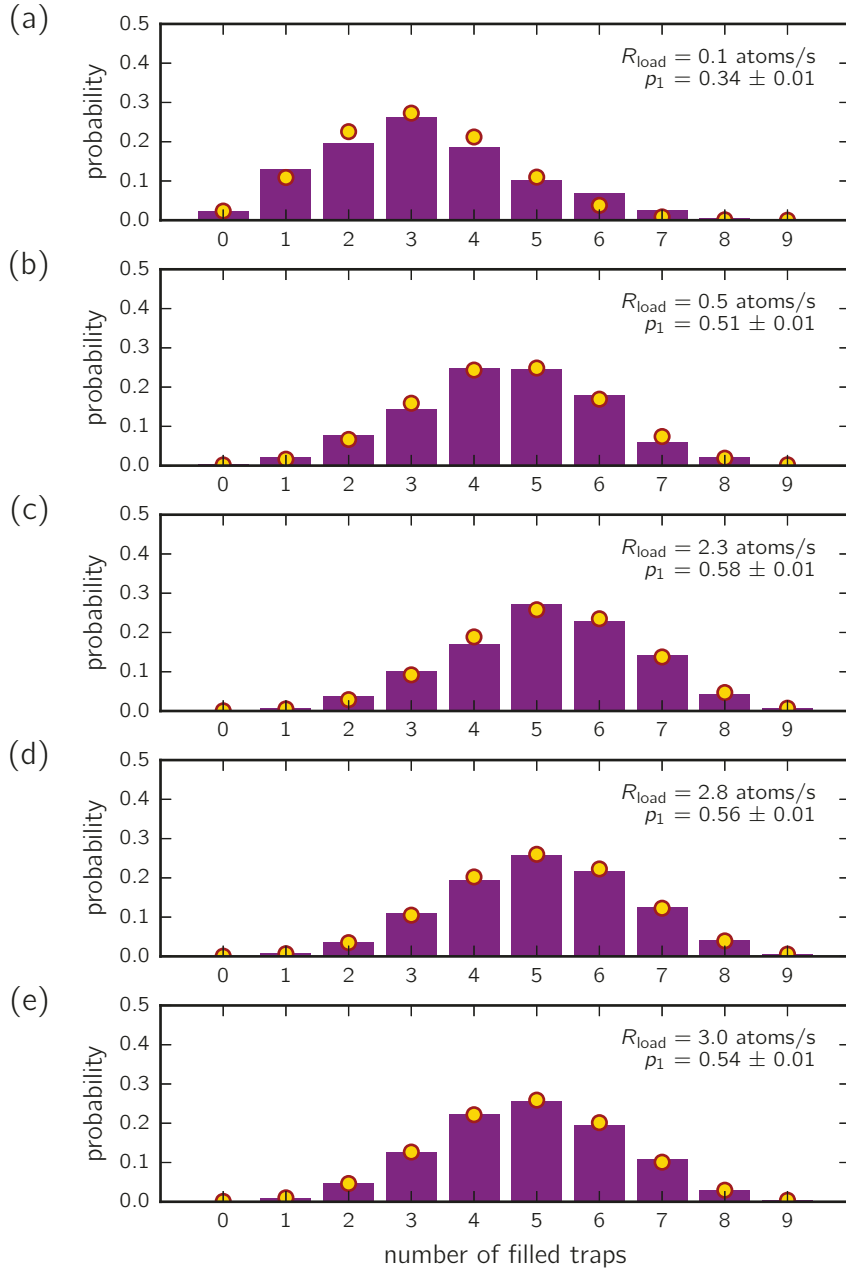


Figure 4.4: Counting statistics of filled traps in a 3×3 trap array. We measure the distribution of the number of filled traps for an array of nine traps for different rates R_{load} to load atoms into the trap (purple bars). We fit the distributions by a binomial distribution to get the occupation probability p of the traps (yellow points). The occupation probability saturates slightly above $p_1 = 0.5$ for loading rates $R_{\text{load}} \gtrsim 0.5$ atoms/s.

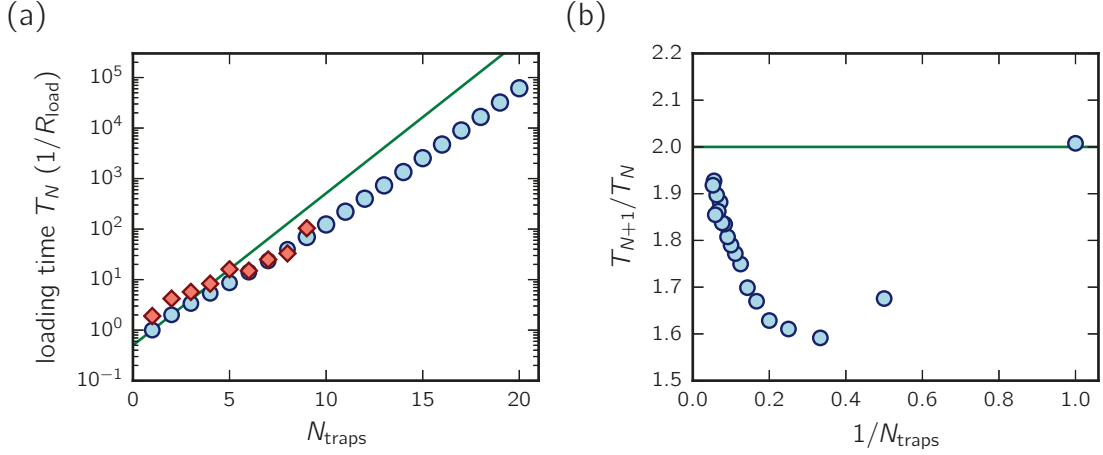


Figure 4.5: Times needed to completely fill an N-trap array. (a) Measured (red squares) and simulated (blue circles) average times T_N to fill an N trap array, in inverse trap loading rate R_{load} . The data is the result of a Monte-Carlo simulation. The green line shows the function $T_N = T_1 2^{N_{\text{traps}}-1}$. (b) Same simulated data as in (a), shown as the ratio of loading times versus the inverse of the trap number, to find the large- N scaling of the loading times. For large trap numbers, the scaling goes towards $T_N \approx 2^{N_{\text{traps}}}/R_{\text{load}}$.

probability to find an atom in the trap at a given time is 50%, if there were no other loss mechanism present.

Analysing the mean single atom occupation probability p_1 for 3×3 trap array, we find that above a loading rate of $R_{\text{load}} \gtrsim 0.5$ atoms/s into the microtrap we indeed find $p \simeq 0.5$ (see Figure 4.4). For very low loading rates the single-atom loss, e.g. due to background gas collisions, is non-negligible, whereas for high loading rates a occupation probability larger than $p_1 = 0.5$ is prevented by the high two-body loss rate [Schlosser, Reymond, and Grangier, 2002]. The loading rate itself was determined by taking the rate with which the trap state changes, thus ignoring other sources of atom loss as the $R_{\text{loss}}^{(\text{vac})} \simeq 0.1 \text{ s}^{-1}$ vacuum loss rate. Further increasing the loading rate R_{load} to be larger than the light-assisted-collision rate $\beta'^{-1} \approx 1 \text{ ms}$ [Fuhrmanek *et al.*, 2012] would lead to having more than one atom per trap on. Nevertheless, as our imaging scheme uses the same MOT beams that are responsible for the light assisted collisions, it will act as a parity projection of the atom number, again leaving on average half of the microtraps filled with a single atom.

The fact that we actually see occupation probabilities slightly larger than 0.5 can be explained by a finite probability $p_{2 \rightarrow 1}$ that when two atoms undergo a light-assisted collision in the microtrap, only one is expelled and the other one remains in the trap. It is even possible to significantly increase this probability $p_{2 \rightarrow 1}$ to dominate over the

two-body loss probability $p_{2 \rightarrow 0}$ by carefully choosing the frequency and power of the ‘collisional beam’ of Figure 2.2. Occupation probabilities of up to 90% have been achieved this way [Fung and Andersen, 2015; Lester *et al.*, 2015]. Very recently, a first preliminary test of this technique on our experiment gave occupation probabilities of $p_1 \gtrsim 80\%$.

With a single atom occupation probability of $p_1 \simeq 50\%$ we are limited to either work with trap arrays which are only partially loaded, or to work with small trap arrays and wait until all traps are occupied by a single atom at the same time.

For the latter, we measured the time to fully charge an array with N_{traps} traps both in the experiment and by doing a Monte-Carlo simulation (Figure 4.5(a)). On the experiment, waiting for a fully charged array is feasible only for up to $\simeq 9$ traps. For 9 traps the time to fully load the array is already about one minute for $R_{\text{load}} \simeq 1$ atom/s. For higher trap numbers this rapidly increases to several minutes, rendering the total duration even of a simple experiment challenging. Even with higher loading rates this time cannot be much improved, as then the lifetime of a given atom configuration gets too short, and the probability to have the same atom configuration in the trigger and the initial frame (see Figure 4.3) gets too low.

For the Monte-Carlo simulation of the trap loading times, we start with an empty trap array. During each time step δt we add an atom to each trap with a probability $\delta t \cdot R_{\text{load}}$. If a trap contains more than one atom, it is reset to zero. We then measure the time until all traps are filled at the same time. We average on 10 000 runs, with $\delta t = 0.01$ and $R_{\text{load}} = 1$, for arrays between 1 and 20 traps.

We see a N_{traps}^η power-law scaling, with $\eta \approx 2$ when extrapolating to large trap numbers (see Figure 4.5(b)), and $\eta \approx 1.7$ for $N_{\text{traps}} < 7$. Note that this kind of problem is mathematically speaking equivalent to that of a continuous random walk in a hypercube, a common problem studied in mathematics [Volkov and Wong, 2008]

4.1.3 Detection of Rydberg excitations

Various techniques exist that aim at the number or position resolved detection of Rydberg atoms. One can make use of the low binding energy of Rydberg atoms by either applying a strong static electric field [Schwarzkopf, Sapiro, and Raithel, 2011], or an ionising laser [Lothead *et al.*, 2013] or ion beam [Manthey *et al.*, 2014] and then detecting the resulting Rydberg ions. Another approach lies in detecting the change of the optical response of a cold atomic gas due to the strong Rydberg-Rydberg interactions [Gunter *et al.*, 2013]. We use a ‘negative’ detection scheme to determine if

an atom has been excited to a Rydberg state, since Rydberg atoms are not trapped by the microtraps and lost at the end of an experiment. We can thus deduce from the loss of an atom that it has been excited to the Rydberg state [Johnson *et al.*, 2008; Miroshnychenko *et al.*, 2010], with a single atom resolution and a $> 95\%$ detection efficiency.

Since the trap laser frequency is far detuned from any transitions involving the Rydberg state, we can approximate the polarisability α of the Rydberg atom by that of a free electron [Saffman and Walker, 2005]:

$$\alpha = -\frac{e^2}{m_e \varepsilon_0 \omega^2}, \quad (4.1)$$

where e and m_e are the charge and mass of the electron respectively, ε_0 the vacuum permittivity and $\omega/2\pi$ the frequency of the trap laser. Thus, since the polarisability for Rydberg states is negative, and the AC Stark shift proportional to $-\alpha$ [Friedrich, 1991], Rydberg states will be repelled by our 850 nm wavelength microtraps, as long as the trap light frequency is far away from all atomic resonances of the atom in the Rydberg state [Miroshnychenko *et al.*, 2010]. A trap with a typical depth of 20 MHz for ground state atoms will lead to an ‘anti-trap’ potential for the Rydberg states with a ‘height’ of 1 MHz, expelling the Rydberg atoms from the trapping region.

Thus, if the Rydberg atom has moved far enough away from the trap region before it decays back to the ground state, such that it will no longer be detected, we can use the loss of the atom from the trap during the experiment as a mean to check if the atom has been excited to a Rydberg state. For Rydberg states with $n > 50$ the lifetime is well above $50 \mu\text{s}$ [Branden *et al.*, 2010]. In $50 \mu\text{s}$, the force on the Rydberg atoms due to the repulsive potential of the microtraps leads to a displacement of about $3 \mu\text{m}$ [Béguin, 2013]. Adding this to the finite initial velocity of the atoms (typically $\sim 60 \text{ nm}/\mu\text{s}$ for $T = 30 \mu\text{K}$), the atoms will be far enough away when decaying to the ground state to not be recaptured by the trap.

We can therefore use the loss of an atom during the experiment as a signal that it has been successfully excited to a Rydberg state³. The maximum detected contrast of a single atom Rydberg Rabi oscillation suggests that this detection efficiency is larger than 95%. The loss of ground state atoms during the experiment is the most detrimental effect to the detection efficiency, as will be detailed in the following

³In addition we have a micro-channel plate (MCP) installed in the vacuum chamber to allow e.g. positive Rydberg detection, but we have not used this in experiments yet, as its detection efficiency would be much lower than by loss detection, and would not offer a spatially resolved Rydberg detection.

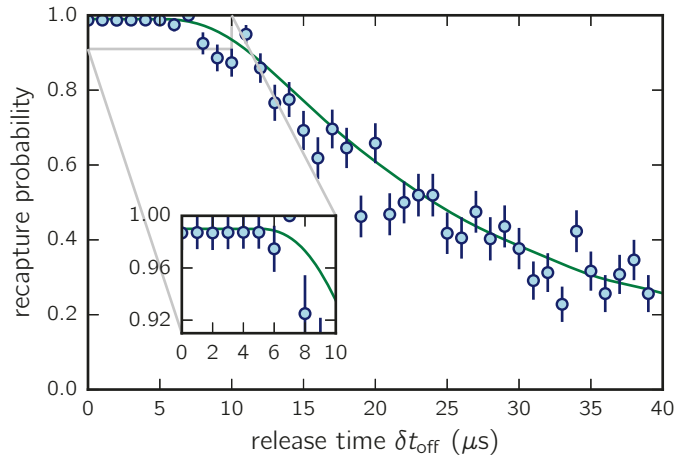


Figure 4.6: Release-and-recapture experiment of a single atom. We measure the recapture probability of a single atom after having switched the trap off for a time δt_{off} . The longer we switch off the trap, the higher the probability ε to lose the atom. The green solid line shows the best fit of the result of a Monte-Carlo simulation, giving a single atom temperature of $(30 \pm 2) \mu\text{K}$.

subsection.

4.1.4 Impact of detection errors

Due to the finite temperature of the single atom in the microtrap, the atoms have a small but finite probability to leave the trap region during the time that the trap is switched off for the Rydberg excitation, even if they remain in the ground state. We have measured the temperature of the atoms by a release-and-recapture experiment in a single trap. We switch the trap off for various durations and measure the probability to recapture the atom when turning the trap on again. We then fit the the data to the result of a Monte-Carlo simulation for various temperatures of the atom [Tuchendler *et al.*, 2008], and get a best fit for a temperature of the single atom of $(30 \pm 2) \mu\text{K}$ (see Figure 4.6).

For typical experiments we switch the traps off for a few μs , where we have a probability of $\varepsilon = (3 \pm 1) \%$ to lose any given atom from its trap without performing any Rydberg excitation (see inset in Figure 4.6). As we detect the Rydberg atoms by the absence of fluorescence from its trap, ε thus gives us the probability to falsely identify a ground state atom as a Rydberg atom due to its loss from the trap.

One can show by a relatively simple mathematical induction that if P_q is the *detected*

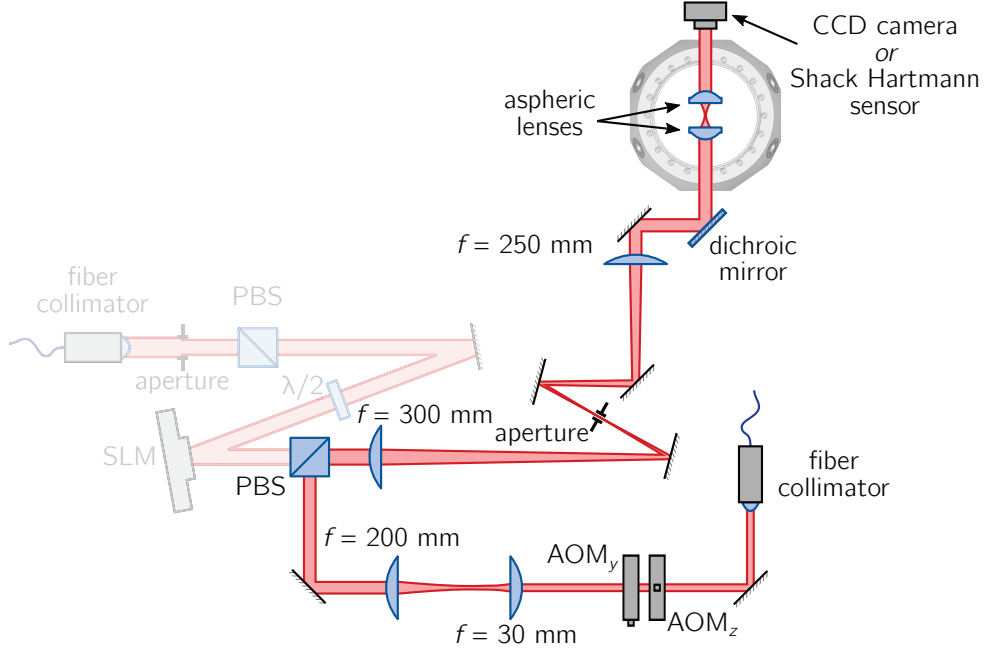


Figure 4.7: Setup of the single site addressing beam. For single site addressability we use a far red-detuned 850 nm laser beam which induces a light shift on the ground state of the addressed atom. We use two crossed AOMs for precise transverse positioning of the addressing beam (the undiffracted light is blocked by the aperture). We switch the beam using an electro-optic modulator (EOM) before the optical fiber (not shown). In the focal plane of the aspheric lens, the addressing beam has a measured $1/e^2$ radius of $w_0^{\text{add}} = 1.3 \mu\text{m}$, slightly bigger than the waist of the microtraps.

probability to have excited q Rydberg atoms in an N atom array, and \tilde{P}_p the *actual* probability to have p Rydberg excitations, then

$$P_q = \sum_{p=0}^q \binom{N-p}{q-p} \varepsilon^{q-p} (1-\varepsilon)^{N-q} \tilde{P}_p. \quad (4.2)$$

In principle we could correct our data for these detection error by inverting the above system of equations. In this thesis we nevertheless present only the uncorrected raw data.

4.2 Single site resolved addressing

An important feature in experiments for quantum simulation with cold atoms or ions is the local manipulation of individual qubits. This can either be done by directly

manipulating the qubit, e.g. by focusing an excitation laser on the chosen qubit [Nägerl *et al.*, 1999; Kruse *et al.*, 2010; Maller *et al.*, 2015], or by using global operations that are off-resonant for all but the selected qubit, e.g. by using electric [Lundblad *et al.*, 2009] or magnetic field gradients [Schrader *et al.*, 2004], or off-resonant laser fields [Weitenberg *et al.*, 2011; Lee *et al.*, 2013].

This section is based on our publication [Labuhn *et al.*, 2014]. As our Rydberg excitation beams are larger than the single atom arrays (see Section 2.4.3), it is not possible to selectively excite individual atoms to the Rydberg state using the excitation light only. Instead, we implemented the last of the above mentioned approaches, shining a tightly focused, far red-detuned 850 nm laser beam with a $1.3 \mu\text{m}$ $1/e^2$ -radius, on a targeted site. Compared to the microtraps the addressing beam has a $\sim 30\%$ larger waist to reduce the sensitivity to alignment errors, and a 200 MHz frequency difference and an orthogonal polarisation in order to minimise the interference between the two.

Just like the 850 nm light field used for trapping the atom, the addressing beam induces a frequency shift on the ground state of the addressed atom, due to the AC Stark effect.

It is not possible for us to dynamically change the trapping light field with the SLM to address individual sites of the trap array, as in our experiments we need switching times in the order of a μs , whereas the the switching times of the SLM are in the order of 100 ms (see Figure 3.4). We thus installed an additional beam path for the single site addressing, which is superimposed with the trap beam with a PBS. Figure 4.7 shows the optics setup of the single site addressing. We used two crossed acousto-optic modulators (AOMs) for precise transverse positioning of the beam in the trap plane. The zero order of the AOMs is blocked by the aperture in the focus of the SLM telescope. The addressing beam is superimposed on the trap beam with a PBS, having a slightly smaller collimated waist than the latter to give a slightly larger spot in the focal plane of the aspheric lens.

In order to characterise the addressing beam, we measure its waist in the trap plane with a single atom. For this we keep the addressing beam fixed, and place a single atom at various positions along a line profile through the intensity maximum of the addressing beam. We then measure the light shift of the Rydberg excitation frequency compared to a free atom, while the trap is off and the addressing beam is on (Figure 4.8(a)). We fit a Gaussian curve to the measured light shifts from which yields a $1/e^2$ radius of the addressing beam of $w_0^{\text{add}} = (1.3 \pm 0.1) \mu\text{m}$ (Figure 4.8(b)).

Theoretically, for an ideal Gaussian beam with the measured beam parameters, we expect that if an atom is addressed with a 10 MHz light shift, another atom $3 \mu\text{m}$

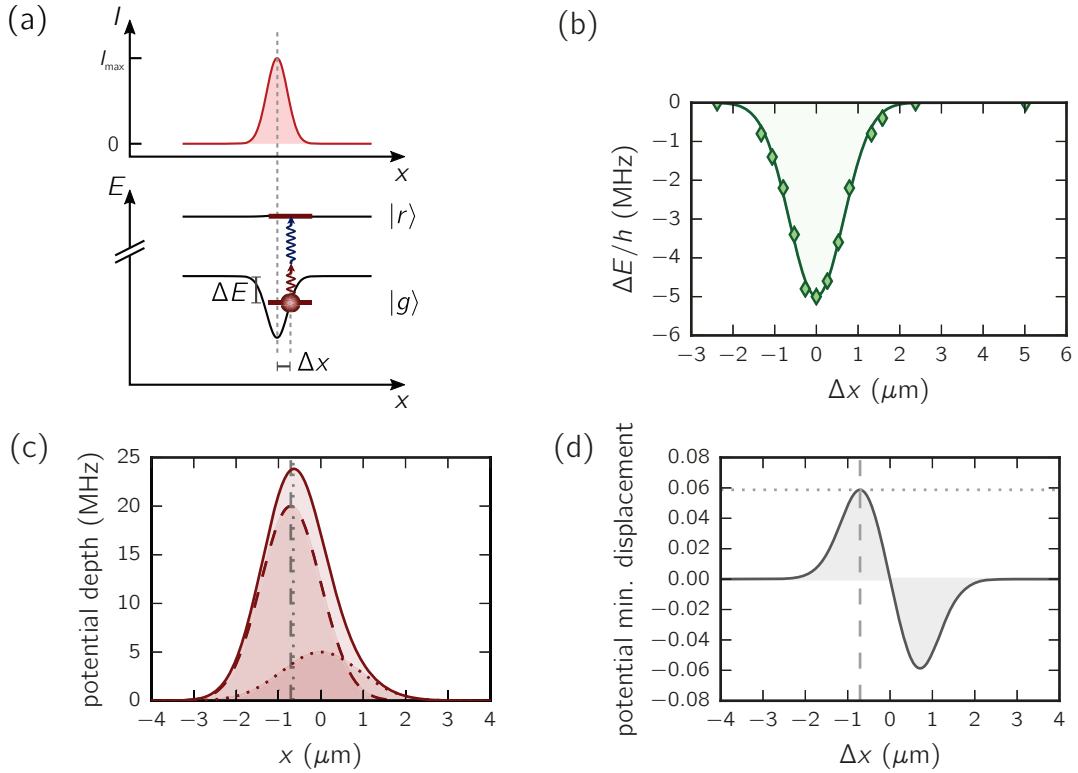


Figure 4.8: Measurement of the addressing beam profile in the trap plane. (a) We measure the addressing beam profile of the along the vertical (x) axis, by keeping the beam position fixed, while moving the position of the microtrap. We measure the light shift ΔE between $|g\rangle$ and the Rydberg state $|r\rangle = |82D_{3/2}\rangle$ at the position of the microtrap for several distances Δx from the addressing beam axis, giving us the local intensity of the addressing beam at this position. (b) Measured light shifts vs. Δx . Fitting a gaussian to the data yields a $1/e^2$ radius of $w_0 \simeq 1.3 \mu\text{m}$. (c) The depths of the trap potential (dashed red curve), the addressing beam potential (red dotted curve), and the sum of the two (red solid curve). (d) The displacement of the potential minimum from the centre of the trap as a function of the distance Δx between the trap and the addressing focus. Even at the ‘worst’ distance (grey dashed line), the potential minimum displacement is at most 60 nm and is thus negligible for the measurement of the addressing beam profile.

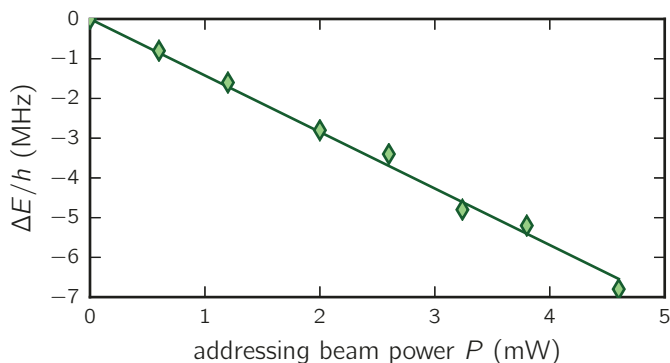


Figure 4.9: Light shift of the single atom due to the addressing beam. For different powers P in the addressing beam we measure the light shift on the transition between the ground state $|g\rangle$ and the Rydberg state $|r\rangle = |82D_{3/2}\rangle$ compared to the atom in free space. The fit gives a slope of -1.4 MHz/mW.

away would experience a light shift of merely 0.2 kHz, which is negligible compared to all other relevant frequencies in our experiment. When measured, the light shift at a $3\ \mu\text{m}$ distance is below the experimental resolution.

In this particular experiment to measure the profile of the addressing beam, the trap and the addressing beam are on at the same time before and after the Rydberg excitation. The atom thus sees the combined potential of the two spots (Figure 4.8(c)). Nevertheless the influence of the addressing beam on the motional state of the atom is negligible for our experiments. For example, for potential depths of 20 MHz and 5 MHz for the trap and the addressing potential, the minimum of the combined potential is only shifted by 60 nm with respect to the original trap position (Figure 4.8(d)).

As we switch off the trap during the Rydberg excitation, the force on the atom due to the potential created by the addressing beam might also displace the atom. Here the trap is off for $3\ \mu\text{s}$. Even if we assume that the atom experiences the force at the maximum slope of the addressing beam potential during this time, it will only be displaced by ~ 100 nm. Therefore, the influence of the addressing beam can be neglected on the external state of the atom even when the trap is off, as long as the atoms does not see only the addressing potential for more than a few μs .

We do however see an increase of probability to lose the atom during an experiment when significantly increasing the addressing beam intensity, thus increasing the force exerted on the atom and pushing the atoms further away from the trapping region. However, for light shifts below 40 MHz, this loss probability remains below 1 %, and is thus negligible.

We also measured the light shift induced by the addressing beam on the ground-Rydberg transition as a function of the total power in the addressing beam, without moving the addressing beam between the measurements. We indeed measure the expected linear dependence on the beam power, with a slope of -1.4 MHz/mW. Note that the slope depends strongly on the alignment of the addressing beam with respect to the addressed microtrap. The measured slope can thus be used as a rough guide, but it is advisable to measure the exact light shift for each new alignment of the addressing beam.

4.2.1 Locally blocking Rydberg excitations

As a first application of the single-site addressability, we perform a Rydberg blockade experiment between two single atoms. This is similar to the experiment done by [Urban *et al.* \[2009\]](#), who used site-resolving excitation beams to demonstrate the Rydberg blockade with two atoms separated by $10\ \mu\text{m}$. Here, we use our global excitation beams together with the single-site addressability to achieve similar results, for two atoms separated by only $3\ \mu\text{m}$.

We tune the excitation lasers resonant to the free-space, two-photon transition between the ground state $|g\rangle$ and the Rydberg state $|r\rangle = |59D_{3/2}\rangle$, with a single atom Rabi frequency $\Omega = 2\pi \times 1$ MHz, without addressing any atom (see [Figure 4.10\(a\)](#)). The Rydberg-Rydberg interaction between two atoms in the $59D_{3/2}$ state, separated by $3\ \mu\text{m}$, is $V_{\text{vdW}} \simeq h \times 300$ MHz. Since $V_{\text{vdW}} \gg \hbar\Omega$, the doubly excited state $|rr\rangle$ is shifted out of resonance. We thus only excite the symmetric superposition state

$$|s\rangle = \frac{|gr\rangle + |rg\rangle}{\sqrt{2}}, \quad (4.3)$$

with the coupling strength to this state being $\sqrt{2}\Omega$ [[Urban *et al.*, 2009](#); [Gaëtan *et al.*, 2009](#)]. The probability ($P_{\text{gr}} + P_{\text{rg}}$) to find either atom in the Rydberg state thus oscillates between 0 and 1 with a frequency $\sqrt{2}\Omega$. The probability P_{rr} to have both atoms in the Rydberg state on the other hand is strongly suppressed (left [Figure 4.10\(c\)](#)).

If we now address atom 2 with a light shift $\Delta E \simeq 10$ MHz, it will no longer be resonant to the Rydberg excitation light (see [Figure 4.10\(b\)](#)). Atom 1 will therefore behave like an independent particle, oscillating between $|g\rangle$ and $|r\rangle$ with the single atom Rabi frequency Ω ([Figure 4.10\(d\)](#)). The remaining excitation probability of atom 2 is accounted for by detection errors [[Labuhn *et al.*, 2016](#)], falsely detecting a

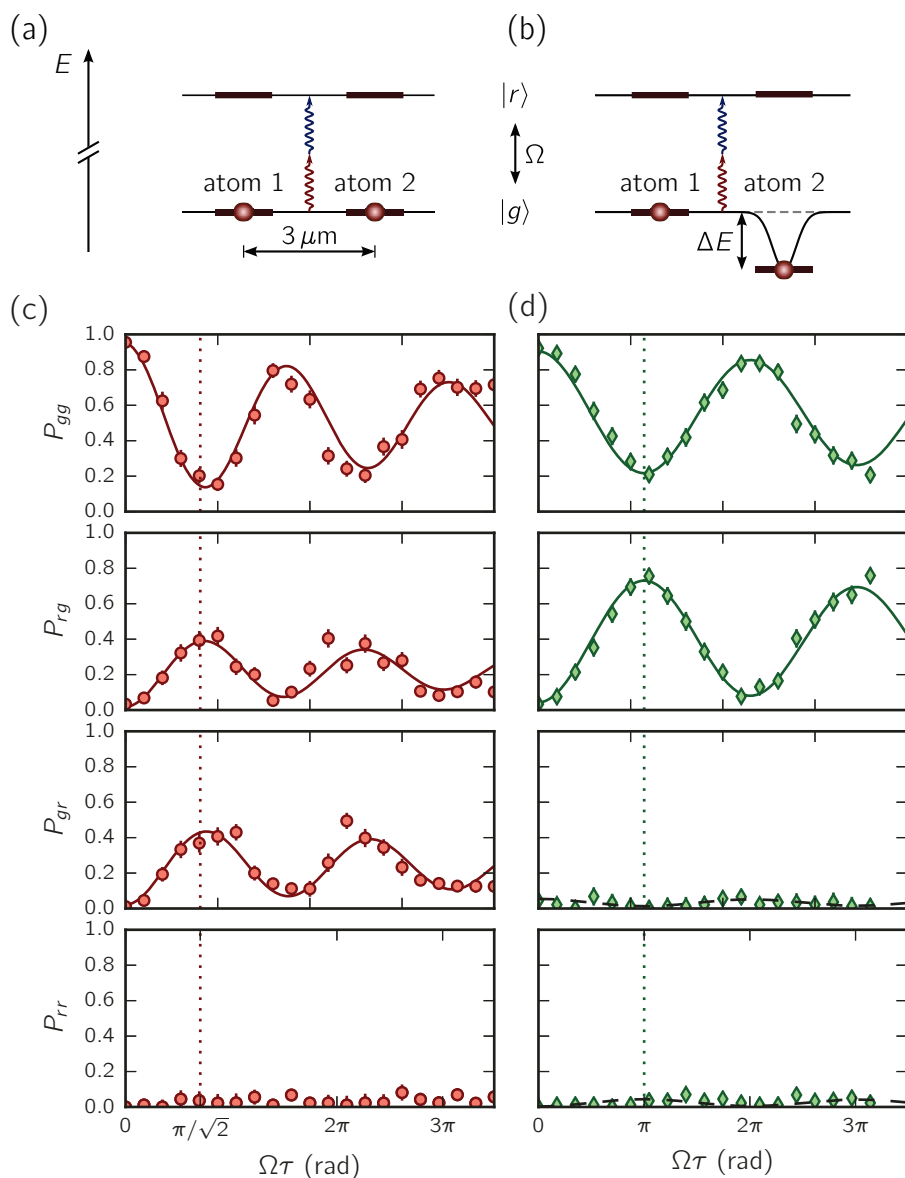


Figure 4.10: Using the addressing beam to exclude one atom from a global Rydberg excitation. Two atoms, separated by $3\ \mu\text{m}$, are illuminated by light which resonantly couples the ground state $|g\rangle$ to the Rydberg state $|r\rangle = |59D_{3/2}\rangle$ with a single atom Rabi frequency Ω , with (a) both atoms in free space, and (b) atom 2 addressed with a light shift of $\Delta E = 10\ \text{MHz}$, shifting it off-resonant from the Rydberg excitation.

The time evolution of the populations in the two-atoms states $|gg\rangle$, $|rg\rangle$, $|gr\rangle$ and $|rr\rangle$ is shown, (c) for both atoms in free space, and (d) for atom 2 addressed. The solid lines are fits of damped sines to the data, the black dashed lines show the expected probability from an $\varepsilon = 3\%$, the dotted red and green lines indicate excitation pulses of $\pi/\sqrt{2}$ and π respectively.

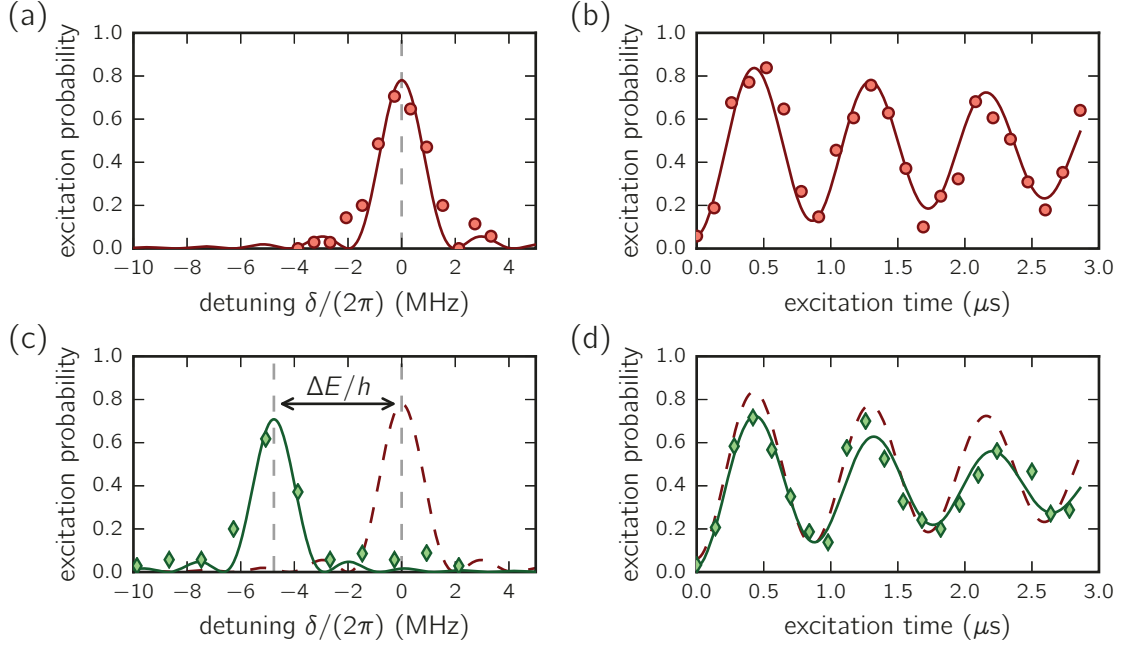


Figure 4.11: Rydberg excitation inside the addressing beam. We measure the spectrum and the Rabi frequency for the $|g\rangle \leftrightarrow |R\rangle = |100D_{3/2}\rangle$ transition, for the atom in free space (a,b), and while the atom is trapped by the addressing beam (c,d), leading to light shift of $\Delta E = -4.8$ MHz (fit results of the free space measurement are shown as dashed light red curves for comparison).

ground state atom as a Rydberg atoms with a $\varepsilon = 3\%$ probability. We can therefore claim that we efficiently block atom 2 from being excited to the Rydberg state, without any measurable cross-talk.

4.2.2 In-trap Rydberg excitation

For certain experiments it may be required to use the addressing beam as an additional microtrap that can be switched independently from the holographically created traps. For example, for some experiments we would like to create a state of the form $|\psi(0)\rangle = |rgggg\dots\rangle$ [Olmos, Lesanovsky, and Garrahan, 2012; Schempp *et al.*, 2014]. Such a state can be prepared by switching only switching off the addressing beam ‘trap’ during the excitation, with the excitation beams resonant to the free-space transition. Another possibility is to switch off the holographically created traps, and tune the excitation beam resonant to the atom trapped in the addressing beam.

For comparison, we first perform a single-atom Rydberg excitation to the $|r\rangle = |100D_{3/2}\rangle$ state, only using the addressing beam as a trap with a depth of $U_0/h \simeq 20$ MHz,

and as usual switching off the trap during the Rydberg excitation. In a second experiment, we first ramp the addressing-beam trap down to a trap depth of $U_0/h \simeq 5$ MHz, but then leave it on during the Rydberg excitation. When measuring the spectrum of the trapped atom, we see the expected light shift $\Delta E/h \simeq -4.8$ MHz of the transition frequency (see Figure 4.11(a,c)). When measuring the Rabi oscillation between $|g\rangle$ and $|r\rangle$ (Figure 4.11(b,d)), we notice that the measured single atom Rabi frequency Ω remains the same, but the contrast of the oscillation decreases and the damping gets more pronounced for the in-trap oscillation. We attribute this to the changing light shift which the atom sees in the trap. Due to the finite temperature of the atom the exact position of the atom in the trap is different in each realisation of the experiment, leading to an inhomogeneous broadening of the Rydberg transition. It is therefore preferable to perform the Rydberg excitation in free space whenever possible.

4.2.3 Local manipulation of a two-body wave function

Besides locally shifting the Rydberg transition into or out of resonance, it is also possible to use the addressing beam to manipulate the many-body wave function. We demonstrate this by again taking two atoms, $3\ \mu\text{m}$ apart, in the Rydberg blockade regime ($V_{\text{dd}} \gg \hbar\Omega$). We shine in an excitation pulse of duration $\pi/(\sqrt{2}\Omega)$ (see Figure 4.12(a)), preparing the atoms in the symmetric ‘bright’ state

$$|\psi(T=0)\rangle = \frac{1}{\sqrt{2}}(|gr\rangle + |rg\rangle). \quad (4.4)$$

We then turn on the addressing beam on atom 2, shifting the ground state energy by an amount ΔE (here we neglect the light shift on the Rydberg state). The states $|gr\rangle$ and $|rg\rangle$ therefore also differ in energy by ΔE , leading to a different phase evolution of the two parts in the wave function in Equation 4.4. After a time T , the two-atom state will therefore have evolved to

$$|\psi(T)\rangle = \frac{1}{\sqrt{2}}(|gr\rangle + e^{-i\Delta ET/\hbar} |rg\rangle). \quad (4.5)$$

After a time $T_\pi = \pi\hbar/\Delta E$ the system will have evolved to the antisymmetric ‘dark’ state

$$|\psi(T=T_\pi)\rangle = \frac{1}{\sqrt{2}}(|gr\rangle - |rg\rangle), \quad (4.6)$$

which is no longer coupled to the ground state $|gg\rangle$ by the excitation lasers. The

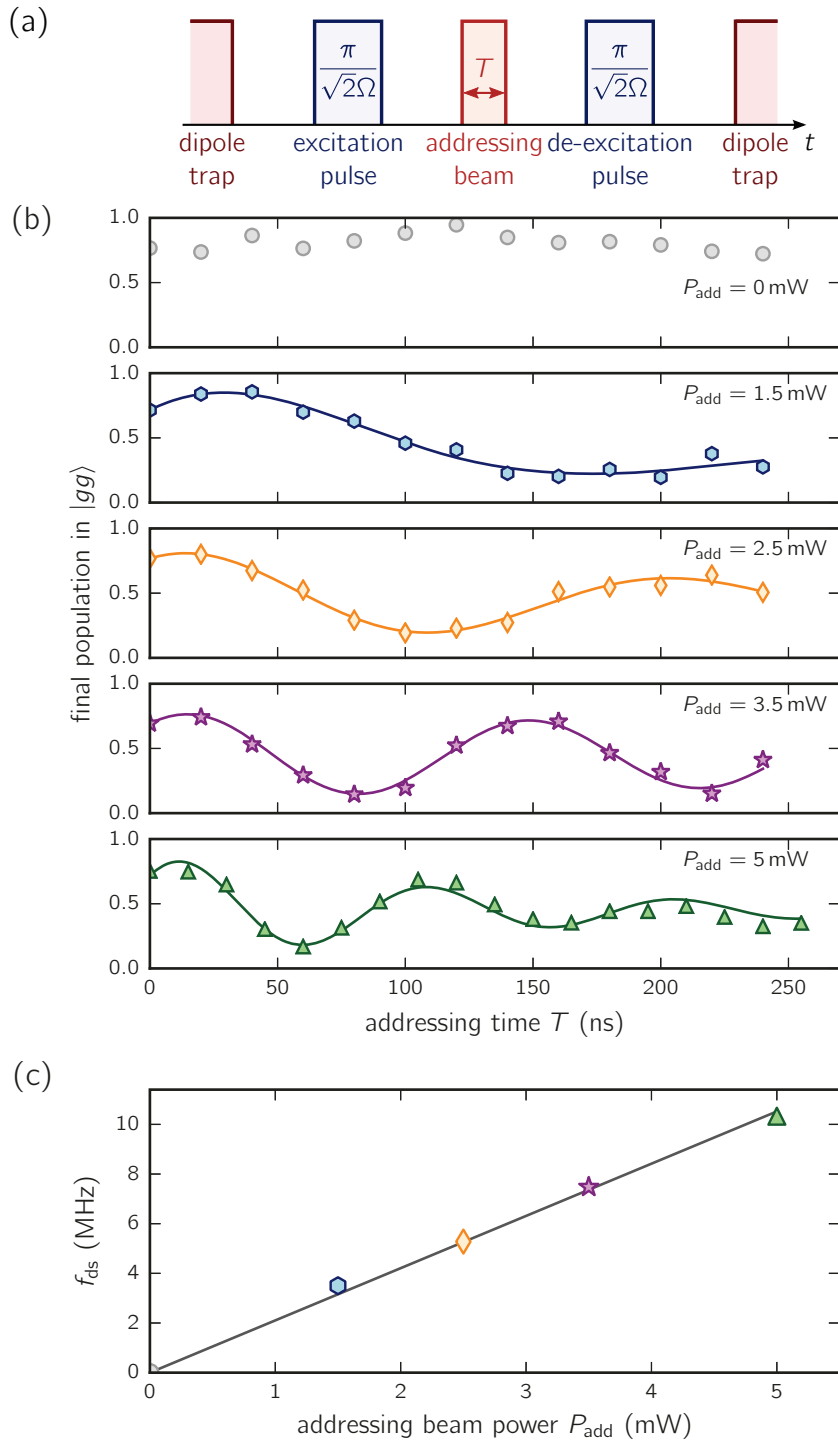


Figure 4.12: Dark state oscillations. (a) Experimental sequence: we prepare two atoms, separated by $3\ \mu\text{m}$, in the state $(|gr\rangle + |rg\rangle)/\sqrt{2}$ with $|r\rangle = |82D_{3/2}\rangle$. We then illuminate atom 2 with the addressing beam for a time T to induce a light shift ΔE , thus changing the relative phase evolution between $|gr\rangle$ and $|rg\rangle$. (b) We measure the population in the ground state $|gg\rangle$ after shining a de-excitation pulse on the atoms, for different addressing beam powers P_{add} , fitting by a damped sine with a phase offset. (c) The oscillation frequency scales linearly with the addressing beam power, with a slope of $2.1\ \text{MHz/mW}$.

probability of de-exciting the atoms to $|gg\rangle$ is thus expected to oscillate between 0 and 1 with a frequency $f_{\text{ds}} = \Delta E/h$.

Figure 4.12(b) shows the probabilities P_{gg} to de-excite the atoms back to the ground state $|gg\rangle$ after having addressed atom 2 for a duration T . We indeed observe that the system oscillates between the bright and the dark state. We extract the oscillation frequencies by fitting the data with the function $y_0 + A \sin(2\pi f_{\text{ds}}T + \phi)e^{-T/\tau_{\text{ds}}}$, and see the expected linear dependence of f_{ds} on the magnitude of the addressing beam power P_{add} , i.e. the induced light shift ΔE , shown in Figure 4.12(c).

We see a constant phase offset of the oscillation of $\phi \simeq -0.1\pi$, which we cannot account for. The imperfect contrast of the oscillation is due to the finite Rydberg excitation efficiency, the finite detection efficiency, and the finite temperature of the atoms. The latter has the effect that on one hand atom 2 sees a slightly different light shift in each experiment, which leads to a slightly different phase evolution between the two components of the wave function between the excitation and de-excitation pulse.

On the other hand, also the movement of the atoms between the excitation and de-excitation leads to dephasing. We actually prepare the initial state $|\psi(T=0)\rangle = \frac{1}{\sqrt{2}}(|gr\rangle + e^{i\xi(T)}|rg\rangle)$, with $\xi(T) = \mathbf{k}(\mathbf{r}_1(T) - \mathbf{r}_2(T))$, \mathbf{k} being the wave vector of the excitation light and \mathbf{r}_i the position of atom i [Wilk *et al.*, 2010]. Due to the change of \mathbf{r}_1 and \mathbf{r}_2 during the experiment this additional phase is not entirely cancelled out during the de-excitation. The movement of the atoms thus introduced a small, random phase between $|gr\rangle$ and $|rg\rangle$ in each experiment, also leading to some additional dephasing of the measured oscillation.

4.3 Conclusion

We have demonstrated our ability to measure the fluorescence of single atoms in the microtraps in real-time with a sensitive CCD camera. The spatially resolved detection lets us start experiments on a predefined atom configuration, allowing us to work with filling fractions of the traps arrays higher than 50 % despite the random trap loading process. We deduce the successful excitation of an atom to a Rydberg state by the loss of the atom during the experiment, as we know the initial and final atom configuration of a Rydberg experiment with a fidelity of nearly 100 %. The Rydberg detection efficiency itself is limited by the small probability $\varepsilon = 3\%$ to lose a ground-state atom from its trap during an experiment, thus being falsely identified as a Rydberg atom.

An additional addressing beam lets us selectively excite a chosen atoms to a Rydberg

state while leaving all other atoms in the array in the ground state.

In future work, we hope to reduce the false Rydberg detections by cooling the single atoms to lower temperatures, for example using Raman sideband cooling [Kaufman, Lester, and Regal, 2012], and to implement a scheme to achieve loading probabilities of the microtraps reaching up to 90%, which can be achieved by optimising the light-assisted collisions [Fung and Andersen, 2015; Lester *et al.*, 2015], or rearranging the atoms in the traps with the movable addressing beam [Beugnon *et al.*, 2007; Lengwenus *et al.*, 2010]

In the following two chapters we will use the presented techniques to probe both the collective enhancement and the spatial correlation of Rydberg excitations in array of single atoms.

The collective enhancement of the Rydberg excitation in fully blockaded ensembles

As explained in the introductory chapter, the strong interaction among Rydberg states can lead to a situation where only atom can be excited to a Rydberg state within a certain volume at the same time. This mechanism is called Rydberg blockade. The simultaneous excitation of two atoms to a Rydberg state is prohibited if the Rydberg-Rydberg interaction V_{vdW} between the atoms leads to an energy shift of the state $|rr\rangle$, which is larger than the bandwidth of the atomic transition. A characteristic length scale for Rydberg atoms is the interatomic distance for which the interaction and the transition linewidth are equal. This length is called the Rydberg blockade radius. On our experiment, the bandwidth of the ground-Rydberg transition is given by the single atom Rabi frequency Ω_1 , so that the blockade radius can be defined as

$$R_b = \sqrt[6]{\frac{C_6}{\hbar\Omega_1}}, \quad (5.1)$$

with the van der Waals interaction $V_{\text{vdW}} = C_6/R^6$ being the dominant interaction here. The blockade radius thus scales as $n^{11/6}$ with the principal quantum number n .

The concept of the Rydberg blockade is not only valid for two atoms but also for larger ensembles of atoms, as long as all the atoms in the ensemble are *pairwise blockaded*. If this condition is fulfilled, then it is only possible to excite one single atom in the ensemble to the Rydberg state at the same time. As a consequence, the Hilbert space reduces from 2^N states to just two states. These are the ground state

$$|g^{(N)}\rangle = |g_1 g_2 \dots g_N\rangle, \quad (5.2)$$

and the state with a single Rydberg excitation, which, since we do not know *which*

atom has been excited, is the N -atom superposition state

$$\left| \psi_{1r}^{(N)} \right\rangle = \frac{1}{\sqrt{\sum_{i=1}^N |\Omega_i|^2}} \sum_{i=1}^N \Omega_i e^{i\mathbf{k} \cdot \mathbf{R}_i} |g_1 g_2 \dots r_i \dots g_N\rangle, \quad (5.3)$$

with the Rydberg excitation shared among all the atoms. Here, Ω_i is the local Rabi frequency of atom i , \mathbf{R}_i its position and \mathbf{k} the wavevector of the excitation laser.

Due to the collectivity of the single Rydberg excitation, the coupling strength between the ground state $|g^{(N)}\rangle$ and the collectively excited state $|\psi_{1r}^{(N)}\rangle$ is enhanced compared to that of a single atom, now being

$$\Omega_N = \sqrt{\sum_{i=1}^N |\Omega_i|^2}. \quad (5.4)$$

If we assume that all atoms in the blockade sphere have the same single atom Rabi frequency, i.e. $\Omega_i = \Omega_1$ for all atoms i , then this enhancement¹ is exactly \sqrt{N} :

$$\Omega_N = \sqrt{N} \Omega_1. \quad (5.5)$$

In addition, if one can ignore the phase factors $e^{i\mathbf{k} \cdot \mathbf{R}_i}$ in Equation 5.3, i.e. the interatomic distances are small compared to the wavevector \mathbf{k} of the excitation light, we excite the highly symmetric $|W\rangle$ -state

$$|W^{(N)}\rangle = \frac{1}{\sqrt{N}} \sum_{i=1}^N |g_1 g_2 \dots r_i \dots g_N\rangle, \quad (5.6)$$

with a multi-partite entanglement among the atoms [Wilk *et al.*, 2010; Haas *et al.*, 2014; Zeiher *et al.*, 2015]. In the experiments presented in this thesis, the phase factors do not vanish, since the atomic separations of several micrometer is much larger than the effective two-photon wavevector $\mathbf{k} = \mathbf{k}_R + \mathbf{k}_B$ of the red and the blue excitation light. However, we could in principle map the Rydberg states to a different hyperfine level of the ground state with a separate optical de-excitation pulse, thus cancelling out the excitation and de-excitation wavevectors [Wilk *et al.*, 2010]. For ^{87}Rb , the wavevector of the 6.835 GHz hyperfine splitting of the ground state is then negligible compared to the interatomic spacings.

¹Due to the enhanced coupling strength to the collectively excited state, the N atom blockade radius slightly decreases to $R_b^{(N)} = \sqrt[6]{\frac{C_6}{\hbar \sqrt{N} \Omega}} = R_b / \sqrt[12]{N}$. As the effect is quite small – R_b decreases by 25% for 30 atoms – we assume Eq. 1.1 also to be valid for multiple atoms.

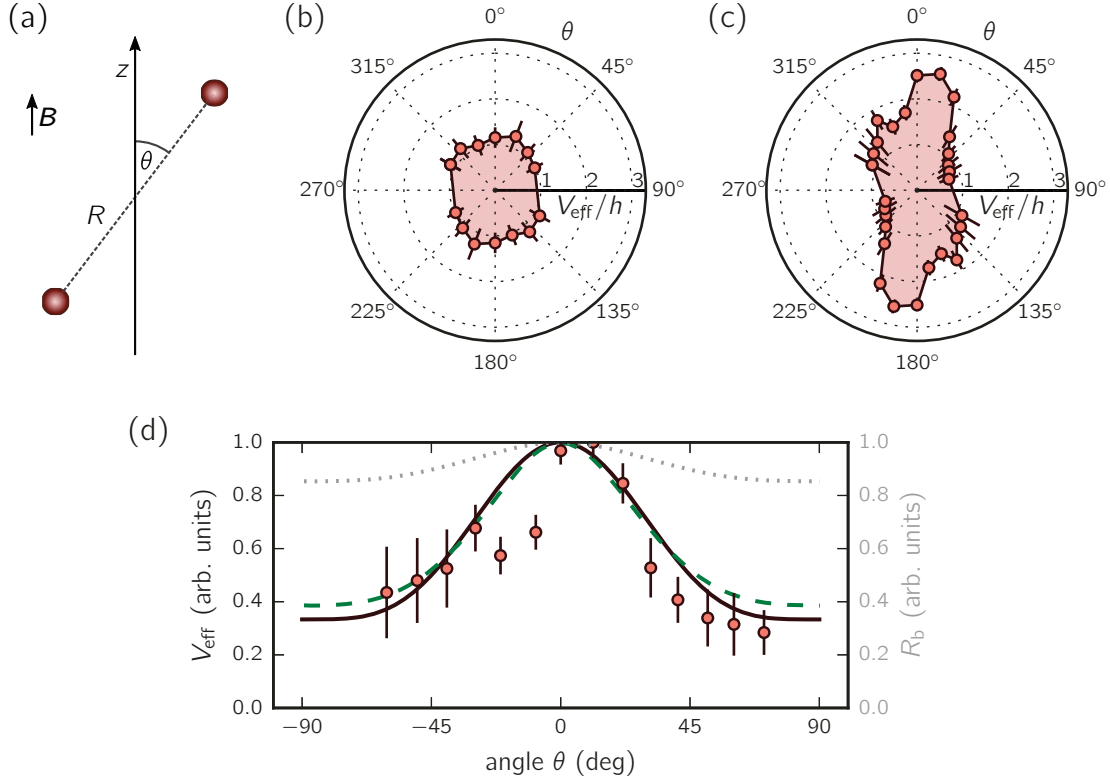


Figure 5.1: Anisotropy of the van der Waals interaction. Effective interaction strength $V_{\text{eff}}(\theta)/h$ measured for two atoms, with interatomic distance $R = 12.4 \mu\text{m}$, as a function of the angle θ between the internuclear axis and the quantisation axis (a), for the Rydberg states (b) $|82S_{1/2}, m_j = 1/2\rangle$, and (c) $|82D_{3/2}, m_j = 3/2\rangle$ (radial axes in MHz). (d) *Green dashed line*: Calculated effective potential $V_{\text{eff}}(\theta)$ for the $|nD_{3/2}, m_j = 3/2\rangle$ state, adapted from Figure 6(b) in [Vermersch, Glaetzle, and Zoller, 2015]. *Red solid line*: Approximation of the calculated effective potential by $V_{\text{eff}}(\theta) = V_{\text{eff}}(0) \cdot [1 + 2 \cos(\theta)^4]/3$ (data points the same as in (c)). *Grey dotted line*: Blockade radius R_b (see Equation 5.1).

5.1 The role of the anisotropy of the interaction

The van der Waals interaction among Rydberg states is not necessarily isotropic [Carroll *et al.*, 2004; Reinhard *et al.*, 2007; Vermersch, Glaetzle, and Zoller, 2015], and therefore also the blockade volume can deviate from a spherical shape. While the van der Waals interaction for S Rydberg states is fairly isotropic, D states can show strong anisotropy in their interaction.

Furthermore, if the angle θ between the interatomic axis and the quantisation axis is non-zero, the van der Waals interaction can couple all Zeeman sublevels of the Rydberg state. In our case of Rydberg states $j = 3/2$, thus describing the van der

Waals interaction for all Zeeman-sublevel pairs leads to a 16×16 interaction matrix. Although the full numerical calculation of the interaction for non-zero angles taking into account all Zeeman sublevels poses no difficulty for two atoms, it quickly becomes intractable for an increasing number of atoms. It is therefore helpful to introduce an effective, anisotropic van der Waals potential $V_{\text{eff}}(R, \theta)$, which is defined as the weighted average of the various interaction channels for a given angle θ , reducing the previous interaction matrix again to a single scalar [Vermersch, Glaetzle, and Zoller, 2015]. Since there exists no analytical solution for $V_{\text{eff}}(\theta)$, we use for the sake of simplicity an heuristic formula

$$V_{\text{eff}}(R, \theta) = \frac{C_6(0)}{R^6} \cdot \frac{1 + 2 \cos^4(\theta)}{3} \quad (5.7)$$

to describe the anisotropy of the interaction, which reproduces well the numerical curve, as shown in Figure 5.1(d). We see that changing θ from 0 to 90° reduces the effective interaction by a factor 3. The anisotropy of the Rydberg blockade radius is much smaller than for the interaction strength, due to the dominating effect of the $1/R^6$ scaling of the van der Waals interaction. The blockade volume defined by $V_{\text{eff}}(\theta) = \hbar\Omega_1$ can be well approximated by a prolate spheroid with an aspect ratio of about $3^{1/6} \simeq 1.2$.

We have measured the angular dependence of both S and D Rydberg states, shown in Figure 5.1(b,c), by looking at the coherent excitation dynamics of two atoms separated by $R \simeq R_b$, as we have described in [Barredo *et al.*, 2014]. The slight asymmetry observed for the D -state is most likely due to a systematic error: The effective potential V_{eff} is defined for a vanishing double-excitation probability. However, to be able to determine the interaction V , we need $V \approx \hbar\Omega_1$ (see [Béguin *et al.*, 2013]), leading to non-negligible double excitation probability. The exact magnitude of these double excitations was different for positive and negative angles θ , resulting in slightly different values of the obtained V_{eff} . More details on the anisotropy of the van der Waals interaction can be found in the thesis of Sylvain Ravets [2014].

We will see later in this chapter that for large number of atoms, the approach of an effective potential to describe the van der Waals interaction at non-zero angles becomes questionable in some cases, as the blockade seems to be no longer perfect when we increase the number of atoms inside the blockade volume.

5.2 Experimental observation of the Rydberg blockade in a fully blockade ensemble

The collective enhancement of the Rabi frequency in fully blockaded ensembles of cold atoms have been reported on in a dilute cloud [Heidemann *et al.*, 2007], an optical dipole trap [Ebert *et al.*, 2014], one-dimensional [Dudin *et al.*, 2012] and two-dimensional [Zeihner *et al.*, 2015] optical lattices. However, all of these experiment suffer from uncertainties or spreads in the prepared atom numbers.

Here we present our experimental results on the collective Rydberg excitation of a fully blockaded ensemble of atoms, with negligible uncertainties in the prepared atom numbers and complete counting statistics of the Rydberg excitations.

Our measurement was divided into two parts. For the first series experiments with up to nine atoms, we prepared a trap array with the respective number of traps and waited until all traps contained exactly one atom before launching the experiment. We placed the traps on a 3×3 square grid with a lattice spacing of $a = 3 \mu\text{m}$. Depending on the desired atom number of the experiment, we put between one and nine traps on the grid, arranged as shown in the fluorescence images in Figure 5.2. Since there is a finite probability for the atom configuration to change *after* the experiment has been triggered, as described in Section 4.1.1, we *post-selected* the experiments on those where the initial frame shows a fully loaded arrays.

For more than nine traps, waiting for all traps in the array to contain one atom is no longer feasible as mentioned in Section 4.1.2, since the probability to have a fully loaded array gets too low and the experimental cycle time thus too long². To probe the collective enhancement for more than nine atoms, we thus used a 19 trap array in triangular geometry, which we triggered on having between 8 and 15 atoms in the traps³. We post sorted the experiments according to the number of atoms in the trap array in the initial atom configuration. The triangular lattice has a lattice spacing of $3.6 \mu\text{m}$, as shown in top right of Figure 5.3. The distance between any pair of traps in the array is smaller than $15 \mu\text{m}$. We slightly increased the principal quantum number of the used Rydberg state to $n = 100$ to ensure full blockade among all atoms. All important experimental parameters used in each experiment are given in Table 5.1.

Once the experiment has been triggered, the atoms are prepared in the ground state

²For a fully loaded 9-trap array the cycle time of the experiment is around one minute.

³For the experiments on the partially loaded array with 8 and 9 atoms we removed two traps, one on the very left and one on the very right of the triangular array.

Table 5.1: Experimental parameters used for the experiments. Parameters of the trap array and the used Rydberg state for the fully loaded square array on the 3×3 grid (Figure 5.2), and the partially loaded triangular trap array (Figure 5.3). The C_6 coefficients are obtained using second-order perturbation theory, as described in [Béguin, 2013].

experiment	trap array parameters			Rydberg state parameters			
	spacing a (μm)	N_t	N	n	C_6/h (MHz μm^6)	$\Omega_1/(2\pi)$ (MHz)	R_b (μm)
fully loaded	3.0	1–9	N_t	82	-8.9×10^6	1.5	14
partially loaded	3.6	19	8–15	100	-7.3×10^4	1.1	20

(see Section 2.4)

$$|g^N\rangle = |g_1 g_2 \dots g_N\rangle. \quad (5.8)$$

We then switch off the traps for $3 \mu\text{s}$, and shine in an excitation pulse of duration τ which is resonant to the single atom transition $|g\rangle \leftrightarrow |r\rangle$, with a single atom Rabi frequency $\Omega_1 \simeq 1.5 \text{ MHz}$, and finally count the number of detected Rydberg atoms.

The measured probabilities to have 0, 1 and 2 Rydberg excitations are shown in Figure 5.2 for the fully loaded arrays, and in Figure 5.3 for the various atom numbers of partially loaded array. To extract the collective Rabi frequency Ω_N , we fit an asymmetrically damped sine of the form

$$P(\tau) = ae^{-\gamma\tau} (\cos^2(\Omega_N\tau/2) + b) + c \quad (5.9)$$

where a , b , c , γ and Ω_N are adjustable parameters of the fit. This functional form was chosen to account in a simple way for the observed asymmetry in the damping of the oscillation. We observe a speedup of the oscillation with increasing atom number, as well as an increase of the damping rate. We also see an increase of the double excitation probably with excitation time, which seems to depend on the geometry of the trap array. We will discuss these observations later in this chapter.

We extract the collective N -atom Rabi frequencies between $|g^N\rangle$ and $|\psi_{1r}^{(N)}\rangle$ from the fits to the zero excitation probabilities, i.e. the left panels in Figures 5.2 and 5.3, and normalise them to the respective single atom Rabi frequencies Ω_1 , measured on a single atom in the centre of the array. The obtained enhancement, shown in Figure 5.4(a), follows quite closely the expected \sqrt{N} behaviour. It appears that the enhancement is slightly lower than expected for the fully loaded array.

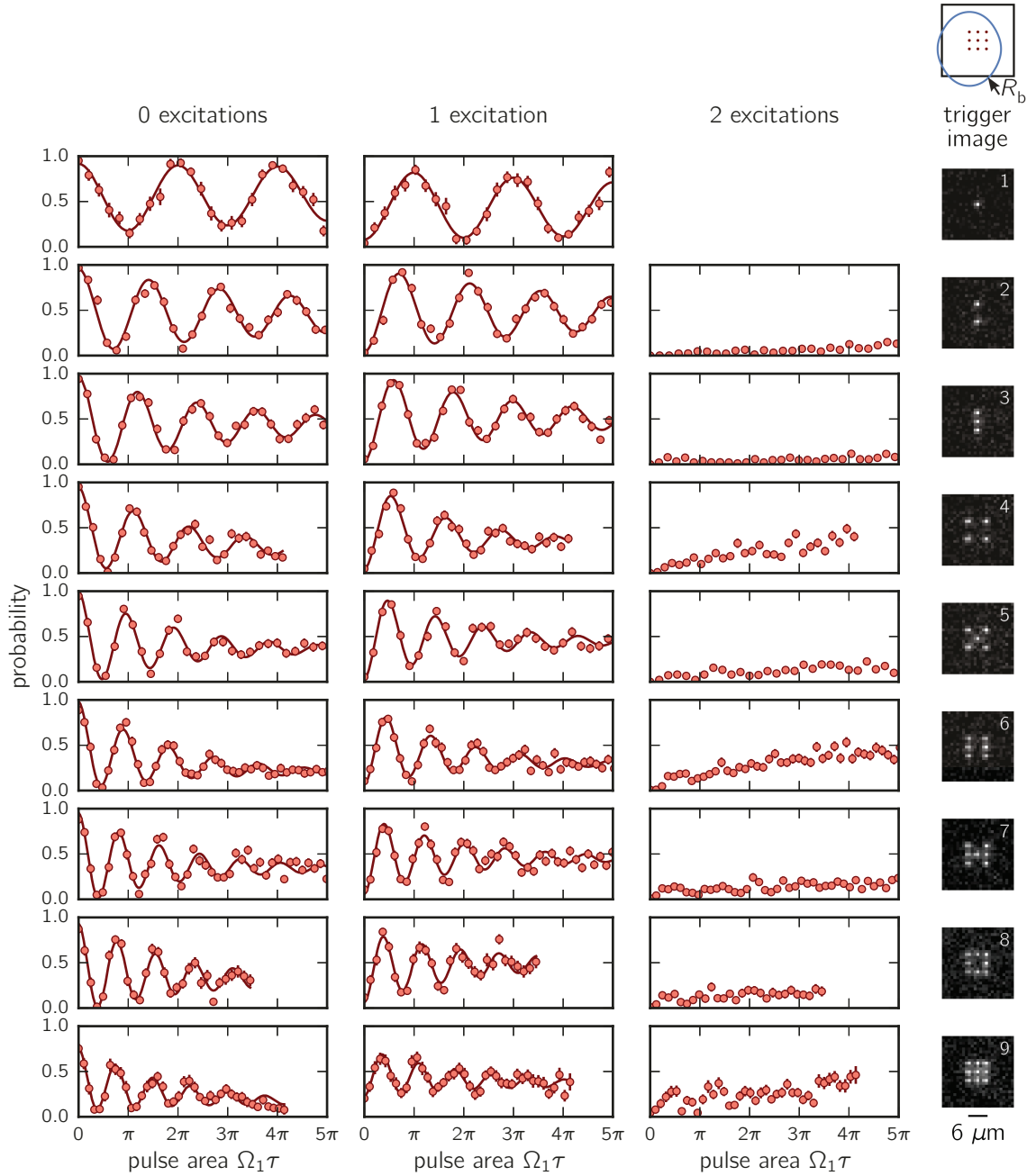


Figure 5.2: Rydberg excitation dynamics in fully loaded trap arrays with one to nine traps. We show the probabilities to have zero (left), one (middle), or two Rydberg excitations (right) for fully loaded trap arrays, with one (top) to nine (bottom) traps, on a 3×3 grid with a $3 \mu\text{m}$ lattice constant. The images at the very right show examples of trigger images for the respective atom numbers. We use the Rydberg state $|r\rangle = |82D_{3/2}\rangle$, giving a calculated blockade radius of $R_b > 10 \mu\text{m}$ in all directions (see fluorescence image for $N_{\text{at}} = 8$ atoms). The x-axes are the product of the excitation time τ and the single atom Rabi frequency $\Omega_1 \simeq 2\pi \times 1.5 \text{ MHz}$. The solid lines are fit of asymmetrically exponentially damped sines (see text). The error bars show the quantum projection noise for the ~ 100 repetitions of each experiment.

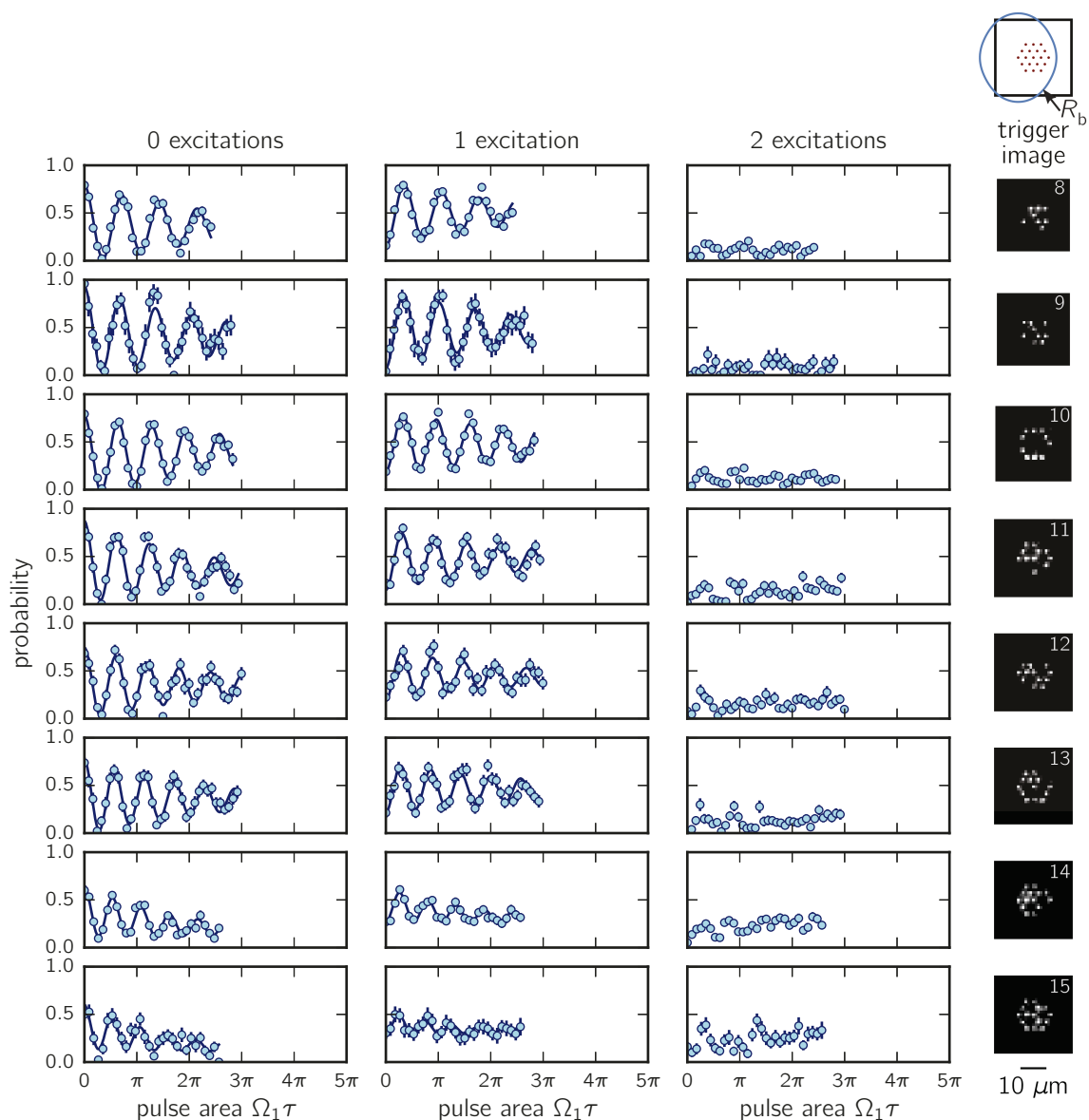


Figure 5.3: Rydberg excitation dynamics in a partially loaded 19 trap array. We show the same plots as in Figure 5.2, for a triangular lattice with 19 traps with a $3.6 \mu\text{m}$ nearest neighbour spacing, containing between 8 and 15 atoms (top to bottom). We use the Rydberg state $|r\rangle = |100D_{3/2}\rangle$, giving a calculated blockade radius of $R_b > 14 \mu\text{m}$ in all directions (see fluorescence image for $N_{\text{at}} = 15$ atoms). The x-axes are the product of the excitation time τ and the single atom Rabi frequency $\Omega_1 \simeq 2\pi \times 1.1 \text{ MHz}$. The solid lines are fit of asymmetrically exponentially damped sines (see text). The error bars show the quantum projection noise for the ~ 100 repetitions of each experiment.

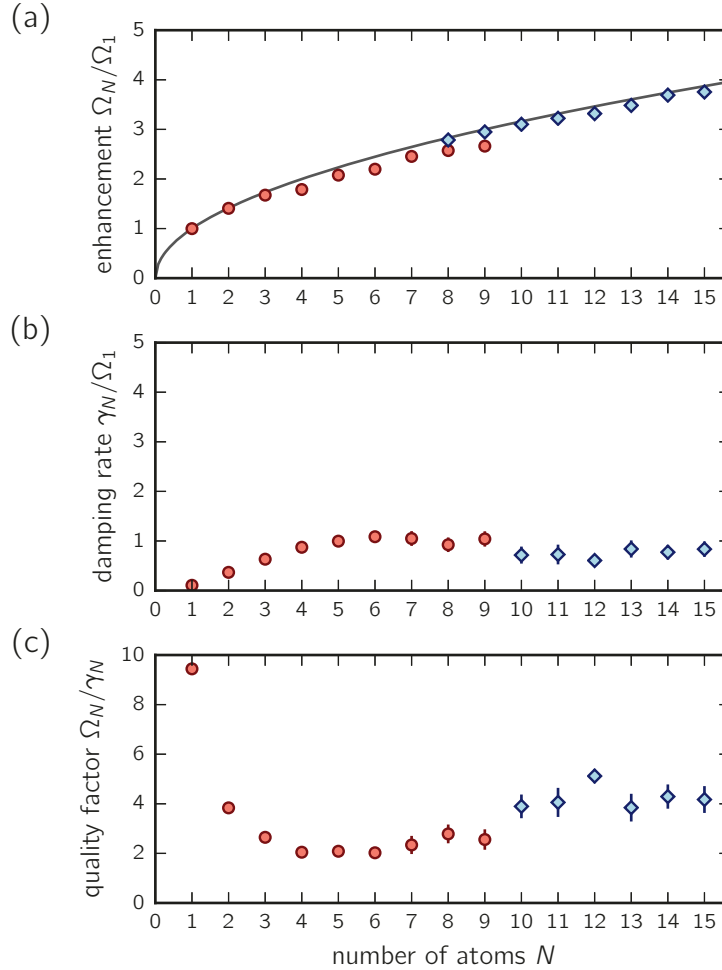


Figure 5.4: Rabi frequency and damping rate of the multi-atom Rabi oscillation.

Parameters extracted from zero excitation dynamics of the fully loaded (red circles) and partially loaded (blue squares) trap arrays in Figures 5.2 and 5.3. (a) Enhancement of the collective Rabi frequency Ω_N compared to the single atom Rabi frequency Ω_1 of an atom in the centre of the array. The solid line shows the expected \sqrt{N} behaviour. (b) Exponential damping rates in units of the respective single atom Rabi frequencies. (c) The ratio of the Rabi frequency and the damping rate, showing that the quality of the oscillations gets worse for more than one atom, but then stays roughly constant. Error bars (sometimes smaller than the data points) are 1σ statistical uncertainties from the fits.

Figure 5.4(b) shows the damping rates γ_N obtained from the fits. One sees that γ_N first increases with the number of atoms, although slower than Ω_N . This becomes more apparent when looking at the quality factor of the oscillation, given by the ratio of the Rabi frequency and the damping rate Ω_N/γ_N , shown in Figure 5.4(c). We see that the quality factor first decreases for more than one atom, and then seems to remain constant for larger atoms numbers.

5.3 Analysis of the experimentally observed imperfect blockade

We will now look at various possible sources of noise to account for the increase of the damping with increasing atom number, and the non-zero double excitation probability.

5.3.1 Analysis of the possible sources of noise

In order to quantify the effect of some of our imperfections, we numerically solve the time-dependent Schrödinger equation with the Hamiltonian of N two-level atoms

$$\hat{H} = \sum_i \frac{\hbar|\Omega_i|}{2} (e^{i\mathbf{k}\cdot\mathbf{R}_i} \hat{\sigma}_{rg}^{(i)} + e^{-i\mathbf{k}\cdot\mathbf{R}_i} \hat{\sigma}_{gr}^{(i)}) + \sum_{i<j} V_{ij} \hat{\sigma}_{rr}^{(i)} \hat{\sigma}_{rr}^{(j)} + \sum_i \hbar\delta_i \hat{\sigma}_{rr}^{(i)}, \quad (5.10)$$

with \mathbf{R}_i the position of atom i , $\hat{\sigma}_{rg}^{(i)} = |g\rangle\langle r|$ and $\hat{\sigma}_{gr}^{(i)} = |r\rangle\langle g|$ the transition operator, $\hat{\sigma}_{rr}^{(i)} = |r\rangle\langle r|$ the projection operator on the Rydberg state, and $V_{ij} = C_6/|\mathbf{R}_i - \mathbf{R}_j|^6$ the van der Waals interaction. In order to keep the calculation tractable, we truncate the Hilbert space removing all states containing more than 4 Rydberg excitations, and limit the maximum strength of a pairwise van der Waals interaction⁴ to $\max\{|V_{\text{vdW}}|\} = h \times 300$ MHz.

Inhomogeneous laser couplings: Experimentally we measure slightly different single atom Rabi frequencies Ω_1 for the trap positions in the arrays. For the 3×3 array, we measure variations of $\pm 5\%$ with respect to the mean Rabi frequency. For the 19 trap triangular lattice we observe variations of $\pm 10\%$. These inhomogeneities are due to the Gaussian intensity profile of the excitation laser beams, as explained

⁴Very large interactions will shift the respective state far off-resonant. This may cause very fast oscillations of the population of the state, but with negligible amplitude. Those oscillations have no contribution to the evolution of the states, but can significantly slow down the numerical differential equation solver, as it will drastically reduce the time step size to follow those fast oscillations.

in Section 2.4.3. According to Equation 5.4, this leads to a small reduction of the collectively enhanced coupling strength Ω_N , but does not increase the probability to create multiple excitations. For fully loaded arrays, an Ω_i varying from site to site will not introduce any damping or reduce the contrast of the oscillation. For partially loaded trap arrays however, the sites i participating in an experiment changes for each realisation of the experiment, and thus also the involved Ω_i . The collective Rabi frequency Ω_N will therefore also vary slightly from shot to shot, leading to a small effective damping of the measured oscillation, which is too small to notice for our experimental parameters.

Inhomogeneous detunings: Spatial variations of the red and blue Rabi frequencies Ω_R and Ω_B among the atoms may lead to variations of the effective detunings $\delta_i = (|\Omega_B^{(i)}|^2 - |\Omega_R^{(i)}|^2)/(4\Delta)$ of the ground-Rydberg transition. They result in the different components of $|\Psi_{1r}\rangle_N$ having different energies, leading to a beating of several frequencies in the collective Rabi oscillation, which may be interpreted as damping on the data. A numerical evaluation of the N -atom Schrödinger equation, with the Hamiltonian from 6.1 and $\Omega_i = \Omega_1$, shows that this only becomes significant for $\langle |\delta_i| \rangle \gtrsim 0.2 \langle \Omega_i \rangle$. We measured the individual detunings from $|r\rangle$ to be $\langle |\delta_i| \rangle < 0.05 \langle \Omega_i \rangle$, which leads to no noteworthy modification of the collective Rabi oscillation.

Motion of the atoms: The finite temperature of the atoms of $T \approx 30 \mu\text{K}$ leads to a residual motion of the atoms during the excitation, with $v_{\text{th}} = \sqrt{k_B T/m} \simeq 0.06 \mu\text{m}/\mu\text{s}$. The associated Doppler effect yields a distribution of frequency shifts $\sigma_\delta = |\mathbf{k}_R + \mathbf{k}_B| v_{\text{th}} \simeq 2\pi \times 0.15 \text{ MHz}$. This appears to be similar to the above mentioned inhomogeneous detunings due to the excitation light shifts. However, the velocity of the atoms is different in each realisation of the experiment, and thus each time every atom will see a slightly different Doppler shift. This will show as a true dephasing of the collective Rabi oscillation over multiple realisations of the experiment.

To numerically simulate the effect of the atomic motion, we modify the Hamiltonian in Equation 6.1 to include the finite velocity, changing the phase factor⁵ $e^{i\mathbf{k}\cdot\mathbf{R}_i} \rightarrow e^{i\mathbf{k}\cdot(\mathbf{R}_i + \mathbf{v}_i t)}$, the interaction $V_{ij} = C_6/|\mathbf{R}_i - \mathbf{R}_j|^6 \rightarrow V_{ij} = C_6/|\mathbf{R}_i + \mathbf{v}_i t - \mathbf{R}_j - \mathbf{v}_j t|^6$, and adding a detuning $\delta_i = |(\mathbf{k}_R + \mathbf{k}_B) \cdot \mathbf{v}_i|$, with \mathbf{v}_i being the velocity, for each atom i . Here we set $\varepsilon = 0$, and $\Omega_i = \Omega_1$ for all i . We average over 100 realisations of the simulation, each time drawing different velocities for the atoms according to the velocity distribution given by the respective temperature. The small variations in \mathbf{R}_i

⁵The change of \mathbf{k} due to the Doppler effect is negligible for the phase factor.

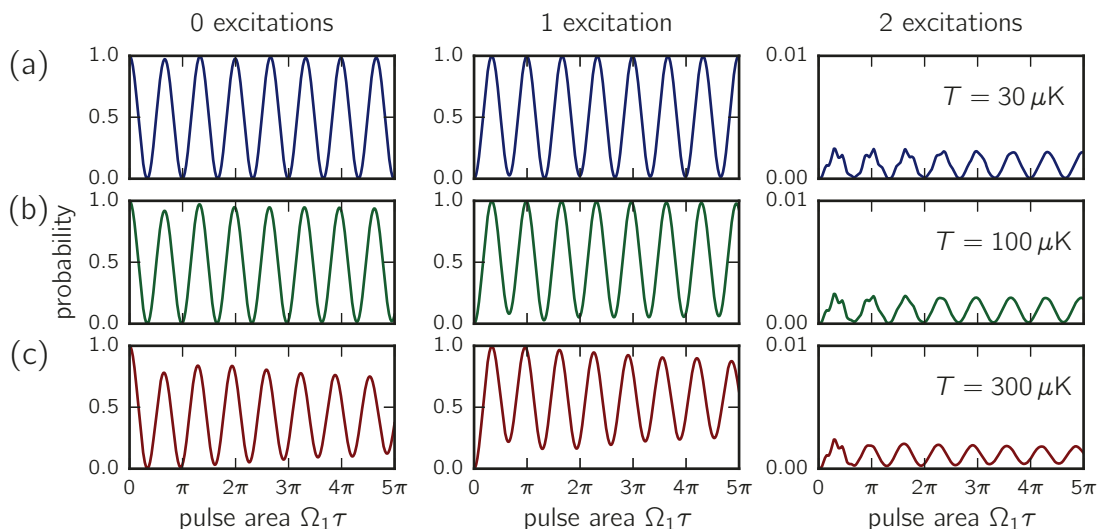


Figure 5.5: Effect of a finite temperature on the collective oscillation of 9 atoms.

We solve the time dependent Schrödinger equation for a 3×3 atom array, taking the same parameters as in the experiment and including the movement of the atoms, for three different temperatures of the atom, $30 \mu\text{K}$, $100 \mu\text{K}$ and $300 \mu\text{K}$ (a, b and c). We average over 100 realisations of the simulation, each time drawing different velocities of the atoms according to the distribution given by the respective temperature, and taking an $\varepsilon = 0$. We see that for $30 \mu\text{K}$, the temperature of the atoms in our experiment, we hardly see any effect on the collective oscillation. The probability to excite states with multiple Rydberg excitations is negligible (note the different y-axis of the plots in the right column).

in the order of $\sim 100 \text{ nm}$ has no effect on the dynamics, and is not taken into account here.

The result of the simulation for 9 atoms in the 3×3 trap array is show in Figure 5.5. We see that for the temperature of our atoms of $T = 30 \mu\text{K}$ the influence of the motion is hardly visible. The oscillation starts to show some damping only if the temperature exceeds $\sim 100 \mu\text{K}$. In addition, we do not see any significant population in the multiple-excitation states. The same observations also holds true for the other atoms numbers in the 3×3 array.

False Rydberg detections: As we have mentioned in Section 4.1.3, there is a finite probability of falsely detecting a ground state atom as a Rydberg atom. This is caused by a ground state atom leaving the trapping region during the excitation, thus being lost from the trap and falsely registered as a Rydberg atom. To picture the effect of these detection errors, we assume to have no imperfection in the experiment, including a perfect Rydberg blockade. The probabilities to have 0 or 1 excitation would

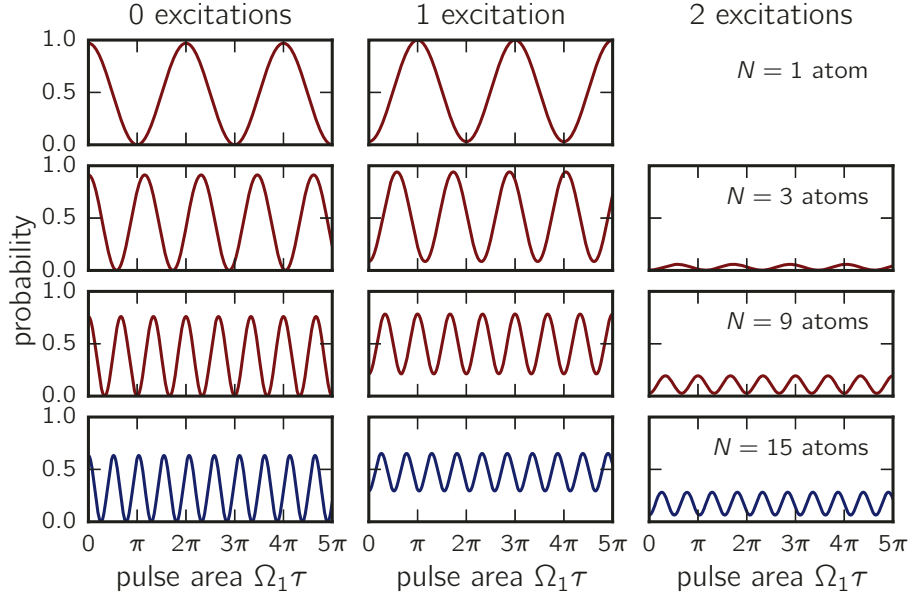


Figure 5.6: Effect of the false Rydberg detection on an ideal collective Rabi oscillation. Theoretically obtained curves for $N = 1, 3, 9$ and 15 atoms (top to bottom), assuming a *perfect blockade*, i.e. $P_{1r}^{(N)}(\tau) = \sin(\sqrt{N}\Omega_1\tau/2)^2$, for a false Rydberg detection probability $\varepsilon = 3\%$. We show the probability to have 0, 1 or 2 excitations (from left to right). For $\varepsilon = 0$, P_{2r} would be zero in all cases.

then be $P_{0r}^{(N)}(\tau) = \cos(\sqrt{N}\Omega_1\tau/2)^2$ and $P_{1r}^{(N)}(\tau) = \sin(\sqrt{N}\Omega_1\tau/2)^2$, respectively. All populations of multiple-excitation states would be zero.

If we now add a finite false Rydberg detection probability, the observed probabilities will be modified according to the set of Equations in 4.2, and are shown in Figure 5.6 for $N = 1, 3, 9$ and 15 atoms, for $\varepsilon = 3\%$ as on the experiment. We notice a decrease of the oscillation amplitude of P_{0r} and P_{1r} , which in first order of ε is proportional to the number of atoms. We see and a significant population of the doubly excited state P_{2r} for larger atom numbers, which in first order of ε is given by $P_{2r} \simeq (N - 1)\varepsilon P_{1r}$. The effect is constant though for all excitation times τ .

We therefore conclude that we can account for the most part of the decreasing contrast of the oscillation with the false Rydberg detection, but we so far do not fully understand the increase of the damping rate when going from one to a few atoms, nor the increase of P_{2r} with τ , which we observed for some trap configurations. Overall, the observed damping is comparable to that observed by *Zeiher et al.* [2015] on single atoms in an optical lattice, who claim that it “might be due to phase noise and slow frequency drifts of the laser”, or an incoherent coupling to nearby Rydberg

states [Ebert *et al.*, 2015]. More work is needed to clarify the imperfect Rydberg blockade when using Rydberg D -states.

5.3.2 Double-excitation analysis

In the following section we will investigate the observed double excitation events in the full Rydberg blockade regime.

The non-perfect contrast of the Rabi oscillations between $|g^{(N)}\rangle$ and $|\psi_{1r}^{(N)}\rangle$ in Figure 5.2 and 5.3 is mostly attributed to our imperfect optical detection, losing ground state atoms during the excitation and falsely detecting them as Rydberg atoms with an $\varepsilon \simeq 3\%$ probability. However, since the time during which we switch off the trap was the same with $3\mu\text{s}$ in all experiments, it cannot account for the increased damping and the increase of double Rydberg excitation probability with time. The only parameter varying with time in the experiment are the excitation pulses. One could argue that the excitation pulses might increase the atom loss probability, for instance due to off-resonant single-photon scattering. We verified that this is not the case however, by repeating the same experiments as in Figures 5.2 and 5.3, now with a detuning of $\delta = 100\text{ MHz}$. Here, we observed no change of the atom loss probability with the duration of the excitation pulse.

We now take a look at the blockade conditions. For the 3×3 trap array the distance between the traps is $a \simeq 3\mu\text{m}$, and the smallest pairwise interaction is about 12 MHz [Béguin *et al.*, 2013], much larger than the Rabi frequency $\Omega_1/2\pi = 1.5\text{ MHz}$, thus being well in the Rydberg blockade regime.

For the 19 trap array, the smallest calculated pairwise interaction is $V_{\text{vdW}} \simeq 3\text{ MHz}$, only slightly larger than the single atom Rabi frequency $\Omega_1/2\pi = 1.1\text{ MHz}$. Nevertheless, solving the Schrödinger equation with the Hamiltonian given in Equation 6.1 gives double excitation probabilities below 5% .

If the assumption of an ideal two-level system with an interaction given by the effective van der Waals potential $V_{\text{eff}}(\theta)$ were correct, the only other cause to observe population in the doubly excited states would be the detection efficiency ε . As we have seen in Figure 5.6, this is not enough to account for the double excitation probabilities observed in Figures 5.2 and 5.3.

The assumption of ε being the only source of double excitation events is further refuted if we look at *where* in the array the double excitations occur (see Figure 5.7). For this we take all the events, for all excitation times τ , where we detected *exactly* two excitation events, and sort them by the distance between the two excitations. We

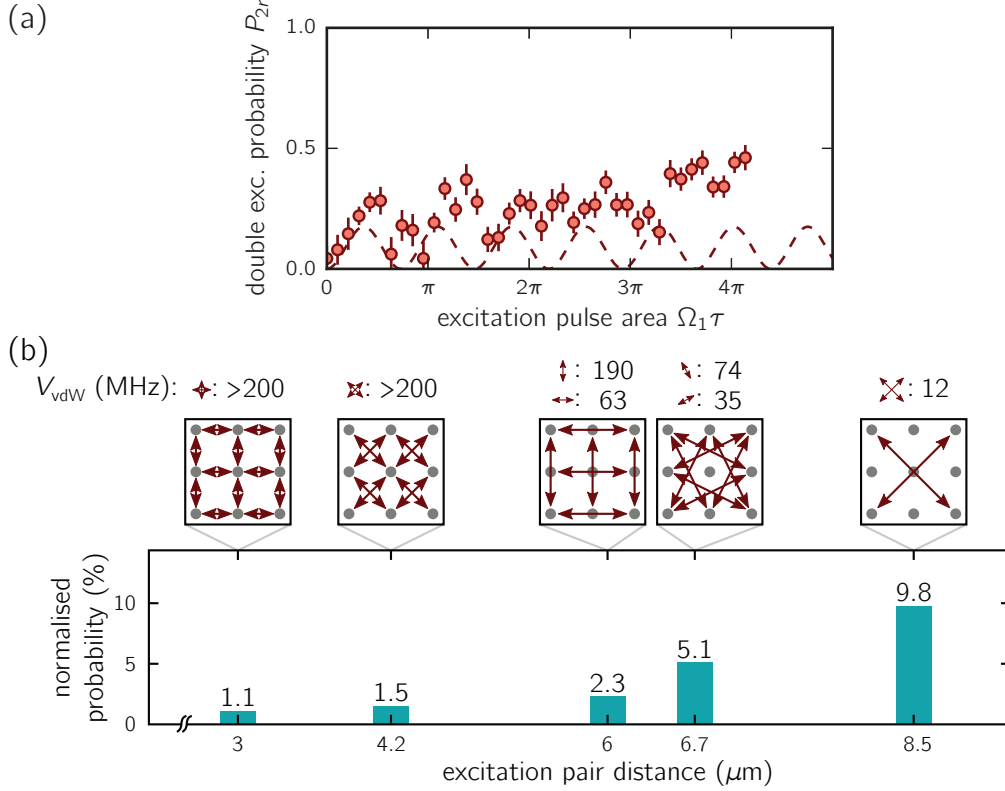


Figure 5.7: Spatial correlations of the double excitation events in the 3×3 array.

(a) Detected probabilities of double excitations in a 3×3 atom array (red points), as shown in Figure 5.2. The dashed line shows the expected probability of detected double excitation for a perfect oscillation $P_{2r}(\tau) \simeq \varepsilon \cdot \sin(\sqrt{9}\Omega_1\tau/2)^2$, due to the finite detection efficiency $\varepsilon = 3\%$. (b) Normalised pair distance of the excitations. The histogram shows the probability to find the double excitation at a given distance, normalised by the number of configurations containing that distance, as indicated in the insets above the plot. The values above the distance plots give the respective calculated van der Waals interaction in MHz. For uncorrelated excitation pairs, all probabilities would be equal.

plot the relative occurrences of each Rydberg pair distance, normalised by the number of configurations containing the given distance. Thus, if the finite detection efficiency ε were the only cause for double excitations, all excitation distances would show up with equal probabilities. We notice however that this is not the case, and see a strong favouring of large separations of the excitation pair. Even if we consider the enhanced coupling strength to the singly excited state $\Omega_9 = \sqrt{9}\Omega_1 = 2\pi \times 4.5$ MHz, we should still be well blocked, as confirmed by numerical simulations. Very similar behaviour is seen for all experiments with both the fully loaded 3×3 grid and the partially loaded 19 trap grid.

We thus believe that the assumed Rydberg-Rydberg interaction is slightly weaker than expected. This might be caused by the large number of interacting Zeeman sublevels [Vermersch, Glaetzle, and Zoller, 2015] of the Rydberg D states. For all atom pairs not aligned with the quantisation axis, all 16 pair state Zeeman sublevels are coupled together by the van der Waals interaction. For a large number of atoms, this may lead to a weak excitation of multiple-excitation states, and hence to a gradual increase of population of the Rydberg manifold. This assumption is supported by observations made in Rydberg D -state polaritons [Tresp *et al.*, 2015].

Another possible explanation might be the excitation of Rydberg molecules comprised of neighbouring Rydberg states, described by Derevianko *et al.* [2015]. However, for the molecular state to be resonant with the excitation laser, the distance between the atoms needs to be precise within a small fraction of a nanometer, which is unlikely to have happened just by chance on our experiments.

To gain a more quantitative insight into the effect of the large Zeeman manifold of the blockade will be an important task in view of future applications of the Rydberg blockade in quantum simulation and quantum computing experiments.

5.4 Conclusion

We have probed the collective enhancement of the Rabi oscillation between the ground state and a state with a single Rydberg excitation shared among all atoms, in the full Rydberg-blockaded regime. We observe well-contrasted, coherent collective oscillations, and measure the expected \sqrt{N} -scaling with the atom number N .

The double excitation probabilities seen in the experiments are larger than what can be explained by our false Rydberg detections. This may be due to an over-estimation of the van der Waals interaction strength, although in previous experiments our calculated C_6 coefficients were well confirmed by the data [Béguin *et al.*, 2013; Barredo *et al.*, 2014]. Another explanation could be the weak coupling to Rydberg pair-states involving the various Zeeman sub-levels of the Rydberg D -states used in this experiment [Vermersch, Glaetzle, and Zoller, 2015], for atom pairs that are not aligned along the quantisation axis.

A further investigation of the efficiency of the Rydberg blockade is necessary in view of using the blockade in high-fidelity quantum-gate operations for quantum information protocols [Saffman, Walker, and Mølmer, 2010].

Realisation of the Quantum Ising model in 1D and 2D arrays of Rydberg atoms

One aim of a quantum simulator is to give access to microscopic local observables, that can neither be accessed in the simulated material nor on a classical computer. In order for a particular quantum simulator to be credible, it needs to be benchmarked, which may be accomplished by various means. One can simulate a system with an analytically known behaviour, or compare the results of a quantum simulation on different systems. This is why realising a quantum simulator of a given Hamiltonian using different physical platforms is important. The promising results presented in the previous chapter thus motivated us to study the quantum Ising model on our experiment.

Here, we realise the Quantum Ising model on a system with between 8 and ~ 30 spins, and compare it to the numerical solution of the Schrödinger equation with the Quantum-Ising Hamiltonian whenever possible. For spin numbers $N > 15$, the numerical treatment of the full Hilbert space becomes difficult. The *ab initio* numerical simulation of our system was done by Tommaso Macrì from the Universidade Federal do Rio Grande do Norte, and International Institute of Physics (Brazil), based on a pseudo-spin 1/2 model with anisotropic, long-range interactions, and a finite Rydberg detection efficiency ε . In order to keep the numerical calculation tractable, we truncate the Hilbert space to a given maximum number of spin excitations. More details of the numerical simulations of this chapter can be found in the supplementary material in [Labuhn *et al.*, 2016].

We probe the Rydberg excitation dynamics for the case where the blockade radius extends between one and a few nearest neighbours, for various 1D and 2D geometries of atom arrays. Our apparatus allow the detection of the exact location of the Rydberg excitations, giving us direct access to the spatial correlations occurring in cold Rydberg media. The emergence of spatial correlations of Rydberg excitations in atomic media

due to their strong interactions has been suggested a decade ago [Robicheaux and Hernández, 2005]. The theoretical study of such Rydberg systems suggested that the spatial ordering undergoes phase transitions when changing the excitation laser parameters [Weimer *et al.*, 2008], even leading to a dynamic crystallisation of the Rydberg excitations [Pohl, Demler, and Lukin, 2010].

Those spatial correlations have since been indirectly observed experimentally, by looking at counting statistics and the temporal evolution of the total Rydberg excitation number [Viteau *et al.*, 2011; Dudin, Bariani, and Kuzmich, 2012; Schempp *et al.*, 2014; Urvoy *et al.*, 2015]. Only recently the spatial ordering has been observed directly by a spatially resolved detection of Rydberg atoms by field ionisation [Schwarzkopf, Sapiro, and Raithel, 2011], and on a quantum gas microscope [Schauss *et al.*, 2015], even allowing the adiabatic preparation of the crystalline¹ ground state [Schauss *et al.*, 2015].

Our new setup not only allows us to pinpoint the exact positions of the Rydberg excitation, but also lets us choose the initial ordering of the ground state atoms, in almost any arbitrary 2D geometry.

We can describe the internal dynamics of a system with N atoms with a ground state $|g\rangle$ and a Rydberg state $|r\rangle$, which are coupled by the Rabi frequency Ω , by the Hamiltonian

$$\hat{H} = \frac{\hbar\Omega}{2} \sum_i^N (\hat{\sigma}_{rg}^{(i)} + \hat{\sigma}_{gr}^{(i)}) + \sum_{i<j} V_{ij} \hat{\sigma}_{rr}^{(i)} \hat{\sigma}_{rr}^{(j)} + \hbar\delta \sum_i^N \hat{\sigma}_{rr}^{(i)}. \quad (6.1)$$

Here $\hat{\sigma}_{rg}^{(i)} = |g\rangle\langle r|$ and $\hat{\sigma}_{gr}^{(i)} = |r\rangle\langle g|$ are the transition operators between the ground and the Rydberg state of atom i , $\hat{\sigma}_{rr}^{(i)} = |r\rangle\langle r|$ the projection operator on the Rydberg state, $V_{ij} = C_6/|\mathbf{R}_i - \mathbf{R}_j|^6$ the van der Waals interaction between atoms i and j , and δ the detuning of the excitation lasers from the single atom resonance.

We can now introduce the two spin states $|\downarrow\rangle \equiv |g\rangle$ and $|\uparrow\rangle \equiv |r\rangle$. Following the spin-1/2 notation, we can map [Schauss *et al.*, 2015] the Hamiltonian in Eq. 6.1 to an Ising-type Hamiltonian of the form

$$\hat{H} = \frac{\hbar\Omega}{2} \sum_i^N \hat{\sigma}_x^{(i)} + \sum_{i,j,i\neq j} \frac{V_{ij}}{2} \hat{\sigma}_z^{(i)} \hat{\sigma}_z^{(j)} + \sum_i^N [B_i - \hbar\delta] \hat{\sigma}_z^{(i)}, \quad (6.2)$$

with $\hat{\sigma}_\alpha^{(i)}$ ($\alpha = x, y, z$) being the Pauli spin matrices and $B_i = \sum_{j,j\neq i} V_{ij}/2$. The

¹However, as recent pre-print rebuts the claim of a true crystalline state [Petrosyan, Mølmer, and Fleischhauer, 2016]

first and the last term of the Hamiltonian describe a transverse and a longitudinal magnetic field respectively. There is a large interest in such Ising-type Hamiltonians both theoretically [Weimer *et al.*, 2008; Weimer and Büchler, 2010; Lesanovsky, 2011] and experimentally [Richerme *et al.*, 2014; Jurcevic *et al.*, 2014; Schauss *et al.*, 2015]. On our experiment, we can realise such a Hamiltonian by simply shining the Rydberg excitation light on an array of ground state atoms, with a given single atom Rabi frequency Ω and detuning δ from the single atom resonance.

In all of the results presented in this chapter, we choose $\delta = 0$. The spin-Hamiltonian thus simplifies to

$$\hat{H} = \frac{\hbar\Omega}{2} \sum_i^N \hat{\sigma}_x^{(i)} + \sum_{i<j} V_{ij} \hat{n}^{(i)} \hat{n}^{(j)}, \quad (6.3)$$

with $\hat{n} = (\mathbb{1} + \hat{\sigma}_z)/2$ counting the number of Rydberg excitations on a given site, being either 0 or 1. The spin-spin coupling is given by the van der Waals interaction $V_{ij} = C_6(\theta)/|\mathbf{R}_i - \mathbf{R}_j|^6$ between atoms i and j is anisotropic, as we are still using Rydberg D -states (see Section 5.1).

6.1 A ring of 8 atoms

We first probe the spatial correlations and dynamics of Rydberg excitations on a system consisting of eight atoms arranged on a ring. This relatively small system size allows us to prepare the ring in a deterministic way, so that we can generate an eight-trap pattern, and trigger the experiment as soon as all the traps are filled². Furthermore, we can still numerically solve the time-dependent Schrödinger equation with the Hamiltonian of Equation 6.3 with the full Hilbert space including all 256 basis states. Despite the anisotropy of the van der Waals interaction of the Rydberg D -states, we assume translational invariance along the ring, thus realising a quasi-1D spin chain with periodic boundary conditions.

We can easily investigate different regimes of the range of the blockade radius by either tuning the interatomic spacing a in the ring, or the blockade radius R_b via the C_6 coefficient by changing the principal quantum number of the used Rydberg state. Intuitively, we expect independent Rabi oscillations if $R_b < a$, a Rabi oscillation to a state with a collective single excitation with an enhanced Rabi frequency if R_b exceeds the system size as seen in Chapter 5, and a more complicated behaviour for $R_b \approx a$.

²This way, the full data acquisition for the intermediate blockade regime in Figure 6.1(b) took about 24 hours.

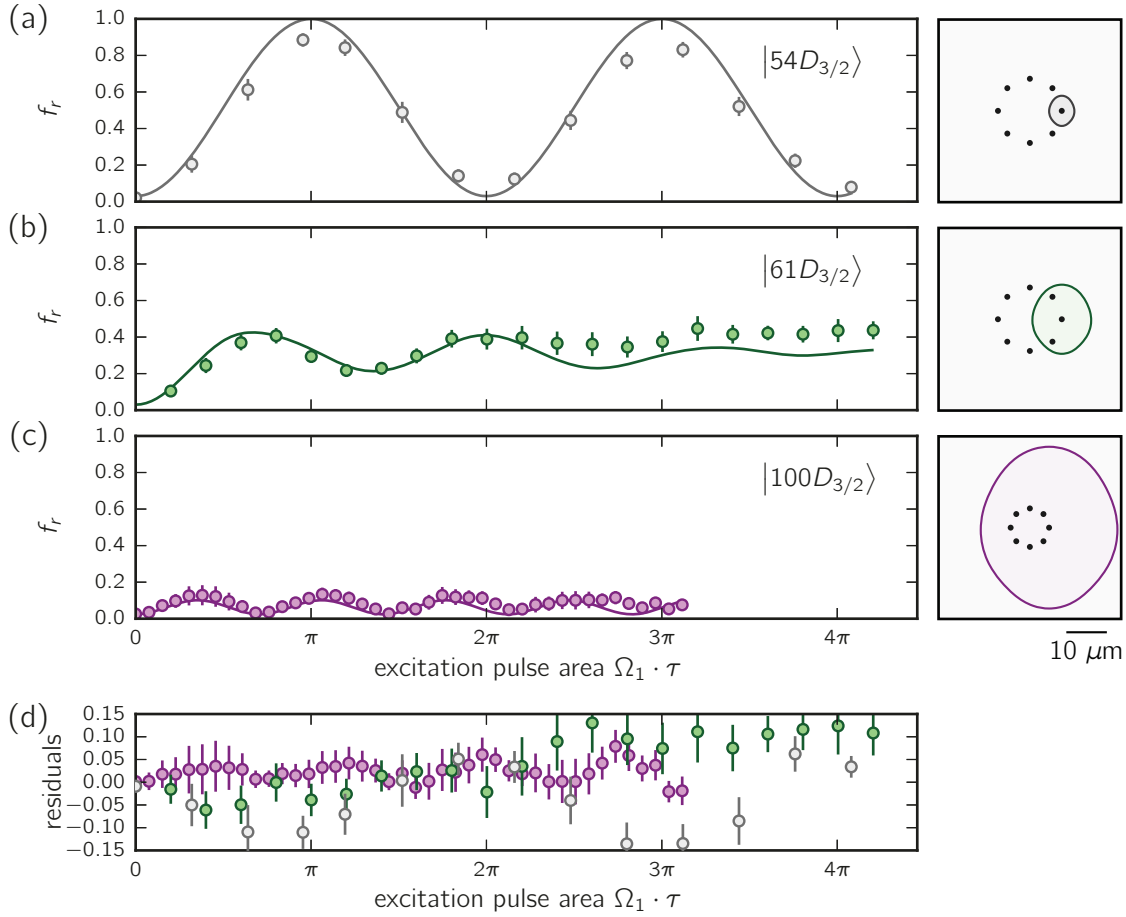


Figure 6.1: Rydberg excitation dynamics for an 8 atom ring. We probe the temporal evolution of the Rydberg fraction f_r for three different regimes of the blockade radius R_b , and compare it to the solution of the Schrödinger equation with the quantum Ising Hamiltonian of Equation 6.3 including a finite detection efficiency $\varepsilon = 3\%$ (solid lines). The sketches on the right show the positions of the atoms and the respective radii. (a) For R_b smaller than the atomic separation a the atoms behave independently, and each atom oscillates between the ground and Rydberg state with the single atom Rabi frequency Ω_1 . (b) For $R_b \simeq 1.5a$ the Rydberg fraction shows a damping which we attribute to the beating of several incommensurate frequencies of the interacting system. (c) For R_b larger than the trap array, multiple Rydberg excitations are blockaded, and f_r oscillates between 0 and $1/8$ with a frequency $\sqrt{8}\Omega_1$. (d) Residuals between the data points and the model.

Table 6.1: Experimental parameters used for the experiments. Parameters of the three different experiments shown in Figure 6.1).

interaction regime of Figure 6.1		trap array parameters		Rydberg state parameters				
		spacing a (μm)	N_{at}	n	calculated C_6/h ($\text{GHz } \mu\text{m}^6$)	$\Omega_1/(2\pi)$ (MHz)	R_b (μm)	α
independent	(a)	6.3	8	54	6.7×10^3	1.6	4	0.63
intermediate	(b)	6.3	8	61	7.6×10^5	1.3	9.1	1.4
fully loaded	(c)	3.8	8	100	8.0×10^7	0.95	21	5.5

We experimentally realise these three regimes by choosing the experimental parameters given in Table 6.1. We probe the global excitation dynamics by measuring the Rydberg fraction f_r , i.e. the average number of Rydberg excitations divided by the total number of atoms N . In the non-interacting regime, with $R_b < a$, the atoms behave independently of each other, and thus each atom will undergo Rabi oscillations between $|g\rangle$ and $|r\rangle$ with the same single atom Rabi frequency³ Ω_1 . Thus also the Rydberg fraction oscillates between 0 and 1 with frequency Ω_1 , as seen in Figure 6.1(a). The deviation from the expected f_r , plotted in Figure 6.1(d), stems from the finite Rydberg excitation efficiency.

For the other extreme case, the blockade radius R_b being larger than the system size, we use the Rydberg state to $n = 100$, and reduce the interatomic spacing to $a = 3.8 \mu\text{m}$, yielding a calculated $R_b \simeq 21 \mu\text{m}$ with an $\Omega_1 = 2\pi \times 0.95 \text{ MHz}$. All the atoms are now pairwise blockaded, leading to an oscillation of the system between the collective ground state and a strongly correlated state, with a single excitation symmetrically shared among all eight atoms. Equivalent to the results presented in Chapter 5, the Rydberg fraction now oscillates with an enhanced frequency $\sqrt{8}\Omega_1$ between 0 and $1/8$, as shown in Figure 6.1(c).

In the intermediate regime, where the blockade radius is comparable to the interatomic spacings, the dynamics becomes less intuitive. We now chose $n = 62$, giving a calculated $R_b = 9.1 \mu\text{m}$ with an $\Omega_1 = 2\pi \times 1.3 \text{ MHz}$, and again taking an interatomic spacing of $a = 6.3 \mu\text{m}$. We expect a ratio $\alpha = R_b/a \simeq 1.4$, so nearest neighbour excitations should now be blockaded, whereas next-nearest neighbours only show a van der Waals interaction strength of about 0.26 MHz and should behave nearly independently. The observed dynamics of the Rydberg fraction is shown in

³We have measured the Rabi frequencies to be equal within 4% along the ring.

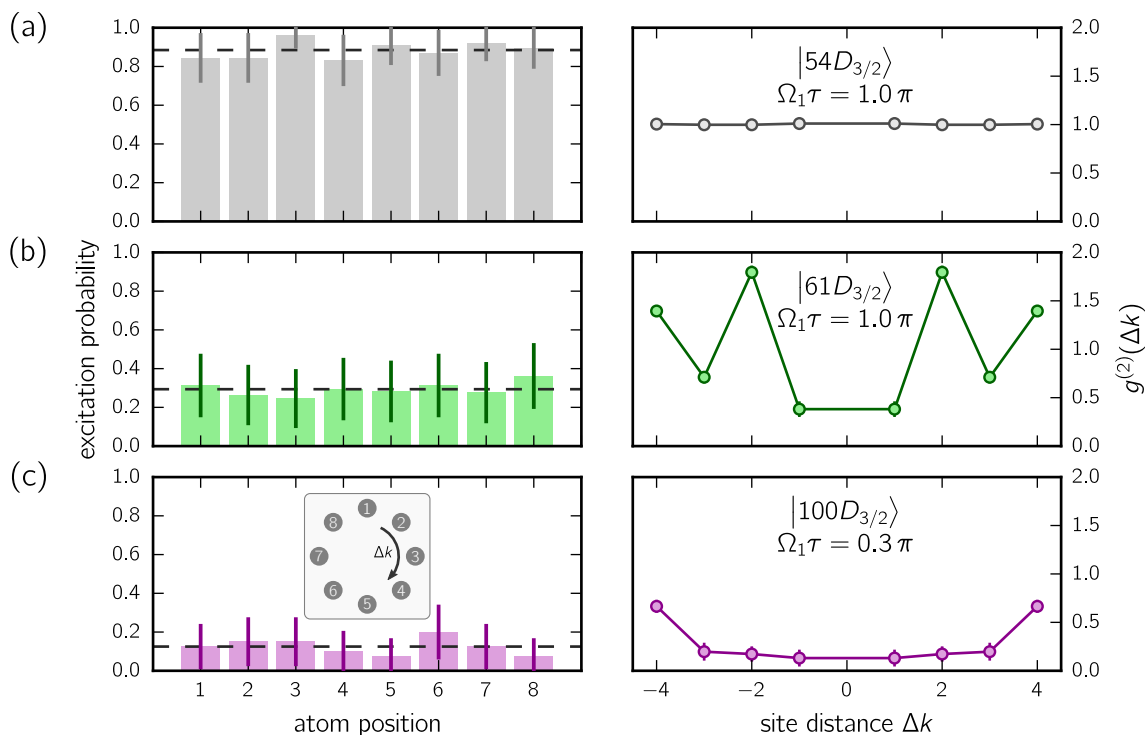


Figure 6.2: Site-resolved Rydberg excitation probability. The single-site resolved mean Rydberg excitation probabilities (left), and the pair correlation function $g^{(2)}(\Delta k)$ (right), for the data shown in Figure 6.1, with (a) $\alpha \simeq 0.63$, (b) $\alpha \simeq 1.4$, and (c) $\alpha \simeq 5.5$, for excitation times given in the right panels. The excitation probabilities are homogeneous among all sites within the error bars. The dashed lines in the left panels show the respective means, the solid lines in the right panels are guides to the eye. The site numbering is shown in the inset in (c).

Figure 6.1(b). It shows the beating of the incommensurate frequencies of the several resonantly or near-resonantly coupled eigenstates of the system, which looks as an effective damping (for long excitation times, the simulation does show a revival of the oscillation). We again compare the data to the full numerical solution of the Schrödinger equation of the spin-1/2 model of Equation 6.3, including an $\varepsilon = 3\%$. The measured data values agree quite well with the model. Only for the second half of the dataset, with excitation pulse areas $> 2\pi$, they start to deviate. This might be a sign of the limits of the simple two level model for our D -state Rydberg atoms, especially since the interacting atom pairs are not aligned with the quantisation axis, thus possibly leading to more involved interaction dynamics, as described in the previous chapter.

We see that we can easily vary the interaction regime of the system by strongly

tuning $\alpha = R_b/a$, the important parameter in this kind of experiment, by almost one order of magnitude, from a non-interacting $\alpha = 0.6$ to $\alpha = 5.5$.

As we measure the *atom resolved* Rydberg excitation probability, we can directly probe the spatial Rydberg-Rydberg pairs correlations. Due to the anisotropy of the interaction the system is not rotationally invariant. However, the important parameter here is not the interaction strength directly, but the blockade radius R_b . As the range of the blockade of the varies very little along the ring, we expected the system to behave translationally invariant. This assumption is supported by the mean Rydberg excitation probability per site, shown in Figure 6.2, for all three values of α presented above. We measure an excitation probabilities which are homogeneous on all sites within the error bars (the same holds true for other excitation times, which are not shown here).

A structured excitation pattern only becomes visible when computing the Rydberg-Rydberg pair correlation function

$$g^{(2)}(\Delta k, t) = \frac{1}{N_{\text{traps}}} \sum_i \frac{\langle n_i(t) n_{i+\Delta k}(t) \rangle}{\langle n_i(t) \rangle \langle n_{i+\Delta k}(t) \rangle}, \quad (6.4)$$

averaged over all sites Here, $n_i(t)$ is the Rydberg excitation probability of a ground state atom at site i , for an excitation time t . The results are shown in the right panels of Figure 6.2, for the same excitation times as in the site-resolved excitation probabilities.

In the non-interacting regime with $\alpha \simeq 0.63$, we as expected do not see any correlations of the Rydberg excitations, as all atoms behave independently, showing nearest neighbour interactions of only $V_{\text{vdW}} \simeq h \times 0.1$ MHz.

In the intermediate regime with $\alpha \simeq 1.4$, we see strong antiferromagnetic-like or crystal-like correlations, with a strong suppression of nearest neighbour excitations ($\Delta k = \pm 1$), and a nearly doubled excitation probability for next-nearest neighbours pairs ($\Delta k = \pm 2$).

In the fully blockaded regime with $\alpha \simeq 5.5$, we again expect a completely flat correlation function if the assumption of perfect blockade holds true, as there should always be at most one single excitation present in the system. The false Rydberg detection probability ε should only lead to a global offset from zero, as ε was measured to be equal among all site. However, we notice an increase of $g^{(2)}$ at $\Delta k = \pm 4$, i.e. for Rydberg pairs created at opposing sites of the ring. This means that for the occurrence of double Rydberg excitations, the excitations arrange themselves as far apart as possible. The occurrence of double excitation in the system is surprising, as even the

smallest calculated effective interaction strength in the system is $V_{eff} \gtrsim h \times 20$ MHz. Again this might hint that the effective interaction strength might be an over-simplified model.

We finally compare the measured pair correlation function $g^{(2)}(\Delta k, \Omega\tau)$ for the intermediate regime of $\alpha \simeq 1.4$ with that obtained from the solution of the Schrödinger with the quantum Ising model of Equation 6.3, including the anisotropic interaction, with and without including ε . In order to take into account a false positive detection probability of $\varepsilon = 3\%$, a standard Monte-Carlo algorithm was run, ‘exciting’ each ground state atom to the Rydberg state with a probability obtained from the solution of the time dynamics of the Schrödinger equation. The remaining ground state atoms are then converted to ‘Rydberg’ atoms with a probability $\varepsilon = 3\%$.

As the Rydberg fraction f_r in Figure 6.1(b) starts to deviate from the model for $\Omega_1\tau \gtrsim 2\pi$, we also expect the correlation function to show the ‘correct’ behaviour of a true spin-1/2 system only up to this point. The results for excitation pulse areas between 0.2π and 4.2π are shown in Figure 6.3. Overall we notice that the false detection probability ε only leads to a small reduction of the contrast of the pair correlations. For small excitation pulse areas of up to $\Omega_1\tau \simeq 1\pi$ we see a remarkable agreement between the data and the theory, except for the shortest excitation pulse of 0.2π , where the Rydberg excitation probability of multiple atoms is still too low to have sufficient events for the calculation of $g^{(2)}$. For excitation pulse areas between 1π and 2π the data no longer follows the model exactly, but the same pattern of the correlation is still visible. Only for excitation times larger than 2π the disagreement becomes more pronounced. Most notably the suppression of next-nearest neighbours weakens significantly, again suggesting that the idea of the effective van der Waals potential in Equation 5.7 to model the angular dependence of the interaction begins to fail. We attribute this deviation to the Zeeman structure of Rydberg D -states, which is not taken into account in our spin-1/2 model. It may lead to a reduced Rydberg-Rydberg interaction due to the van der Waals interaction coupling to other Zeeman sublevels for $\theta \neq 0$, i.e. atomic pairs not aligned along the quantisation axis, yielding a decreased efficiency of the Rydberg blockade, as we have already observed in Chapter 5.

To understand the origin of these increasing deviation from the model, we look at the time evolution of $g^{(2)}$ for each value of Δk separately. We see in Figure 6.4 that for all Δk the correlations oscillate with time. This is due to the still relatively small system size, which does not conceal the coherent nature of the Rydberg excitation. For $\Delta k = 1$ there is a roughly linear increase of $g^{(2)}$ on top of the oscillating behaviour.

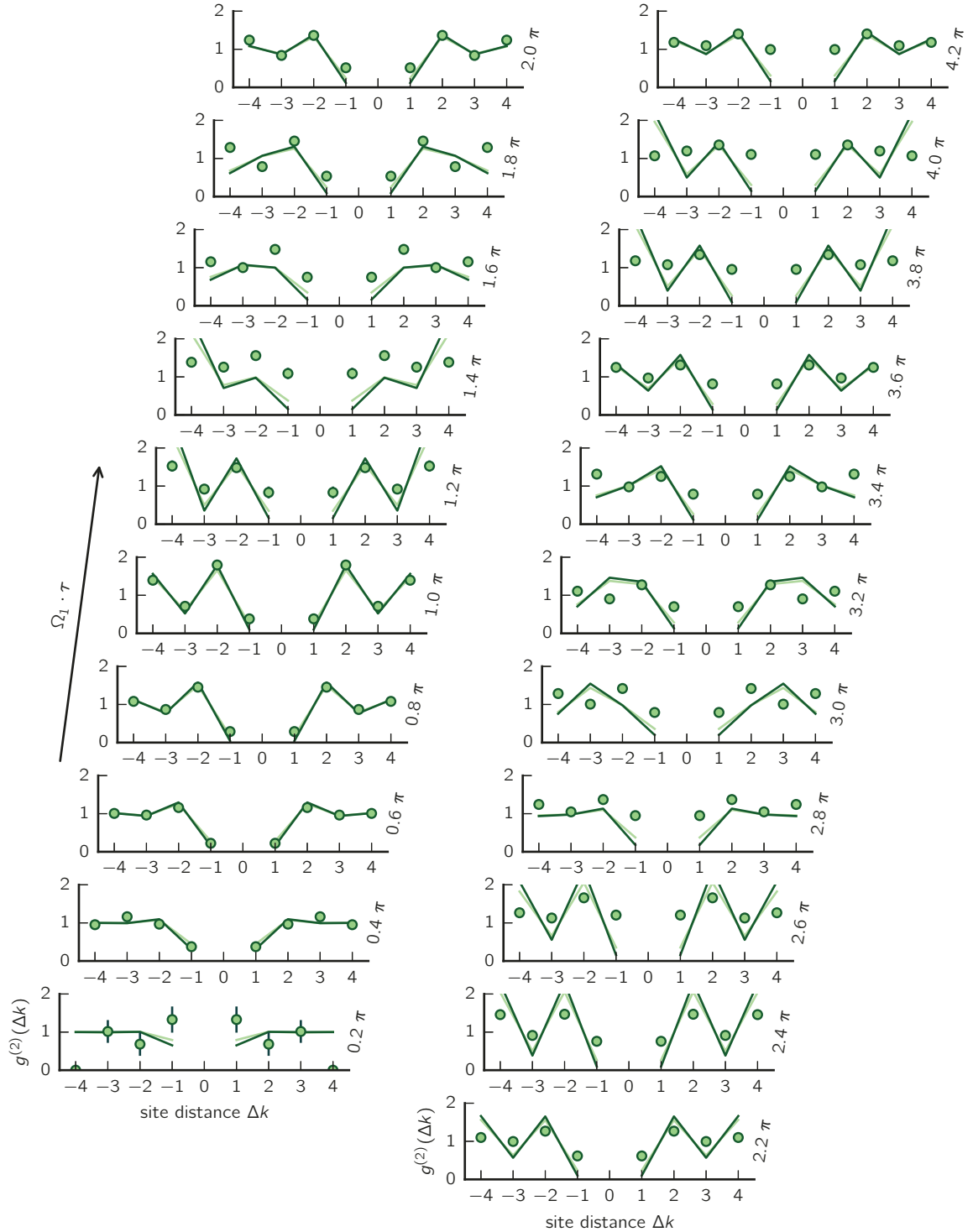


Figure 6.3: The Rydberg-Rydberg pair correlation function for the 8 atom ring.

We compare the measured Rydberg-Rydberg pair correlation function to the correlations obtained from the spin-1/2 model, for the parameters of Figure 6.1(b), as a function of the excitation pulse length $\Omega_1 \tau$. The solid lines are obtained by numerically solving the time-dependent Schrödinger equation with the Hamiltonian of Equation 6.3, for perfect detection (dark green), and including a detection error of $\varepsilon = 3\%$ (light green).

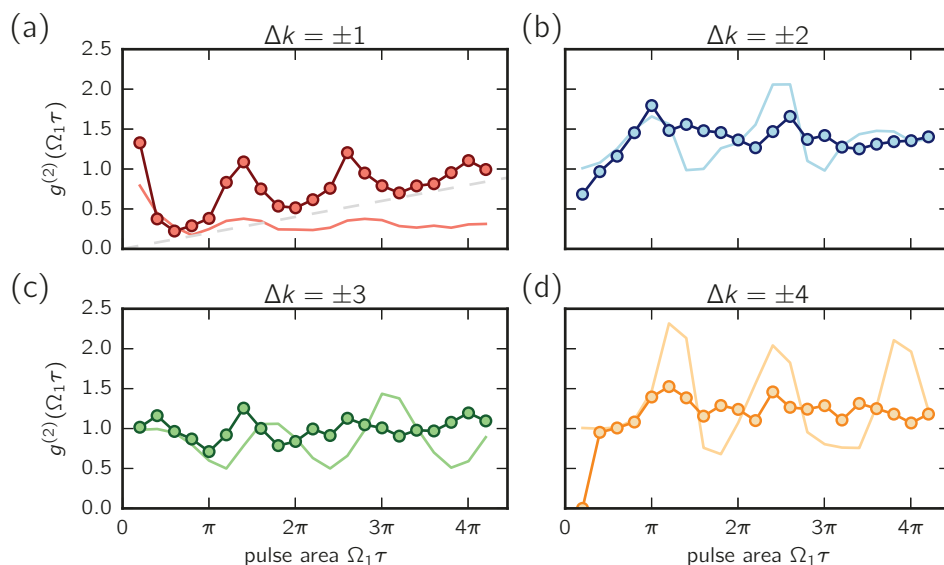


Figure 6.4: Time evolution of the pair-correlations. We show $g^{(2)}(\tau)$ for Δk ranging from ± 1 to ± 4 (a to b). Due to the coherent coupling and the still relatively small system size $g^{(2)}$ oscillates with the excitation time. For $\Delta k = \pm 1$ the pair correlations increase with time. The dashed grey line in (a) shows a slope of $0.2/\pi$.

This observation supports the assumption of an imperfect Rydberg blockade, since even for an interatomic axis perpendicular to the quantisation axis the nearest-neighbour interaction is still $V_{\text{vdW}}(\theta = 90^\circ) \simeq h \times 4.9 \text{ MHz}$, sufficiently larger than the Rabi frequency $\Omega_1 = 2\pi \times 1.3 \text{ MHz}$, thus nearest neighbour excitations should still be blocked.

As a possible extension to the experiment presented here, one could perform a sweep of the laser detuning and Rabi frequency as demonstrated by [Schauss *et al.* \[2015\]](#). If the translational invariance holds true, then due to the periodic boundary conditions and the even atom number one could adiabatically follow the ground state of the system to reach the antiferromagnetic state, producing a state of the form

$$|\Psi_{\text{af}}\rangle = \frac{|\uparrow\downarrow\uparrow\downarrow\uparrow\downarrow\rangle + |\downarrow\uparrow\downarrow\uparrow\downarrow\rangle}{\sqrt{2}}. \quad (6.5)$$

After local rotations this state is equivalent to the GHZ state [[Greenberger, Horne, and Zeilinger, 1989](#)]

$$|\text{GHZ}\rangle = \frac{|\uparrow\uparrow\uparrow\uparrow\uparrow\uparrow\rangle + |\downarrow\downarrow\downarrow\downarrow\downarrow\downarrow\rangle}{\sqrt{2}}. \quad (6.6)$$

We measure an overlap of the experimentally produced state after an excitation pulse of $\Omega_1\tau = 1.0\pi$ with the antiferromagnetic state of $|\langle\Psi_{\text{af}}|\Psi_{\text{exp}}(1.0\pi)\rangle|^2 = 0.4$.

6.2 Partially filled quasi-1D array

In the previous section we have probed the Rydberg-Rydberg pair correlations of eight atoms arranged along a fully loaded ring. In the intermediate regime of the interaction we observed strong correlations of the Rydberg excitations, which for excitation times up to $\Omega_1\tau \simeq 1\pi$ is very well described by a quantum-Ising type Hamiltonian. We attribute the increasing deviation from the model for longer excitation times to a more complex interaction mechanism for atom pairs whose interatomic axis is not aligned with the quantisation axis.

We therefore modify the trap geometry to a ‘racetrack’-shaped array of $N_t = 30$ traps, as shown in Figure 6.5(a). We chose this geometry to (i) have as many atom-pairs as possible aligned along the quantisation axis while keeping a quasi-1D chain with periodic boundary conditions, and (ii) to have Rabi frequencies as homogeneous as possible throughout the array, where the main constraint is the finite extent of the the 474 nm excitation laser along the y -axis.

With our stochastic trap loading we cannot wait until all traps in the array are filled with a single atom. However, as explained in Section 4.1, we can monitor the state of each trap in real time, allowing us to trigger the experiment on a minimum number of present atoms. In order to nevertheless improve the atom number statistics in the experiment from a binomial distribution centred around $N_t/2 = 15$ atoms, we set the trigger condition for the experiment to the presence of ≥ 20 atoms, yielding a short experimental cycle time of ≈ 2.5 s. Figure 6.5(b) shows the thereby obtained atom number distribution. We observe a narrow distribution centred around 20 atoms, corresponding to a filling fraction of 67%. We do not always obtain 20 atoms in the initial atom configuration, since there is a finite probability for trap to lose or catch an atom between the triggering frame and the initial frame, as explained in Section 4.1.1. For very slow trap loading rates, we would observe an atom number distribution with a sharp peak at $N = 20$ atoms. In the data presented in this section, we chose *not to* post-select on the atom number.

In order to observe strong Rydberg pair correlations despite the partial loading, we now use the $|79D_{3/2}\rangle$ Rydberg state, with a calculated $C_6/h = 6.0 \times 10^6$ GHz μm^6 . Using a single atom Rabi frequency $\Omega_1 \simeq 2\pi \times 1.0$ MHz, we expect a blockade radius of $R_b \simeq 13.5 \mu\text{m}$. Compared to the lattice spacing $a = 3.1 \mu\text{m}$, we obtain a ratio

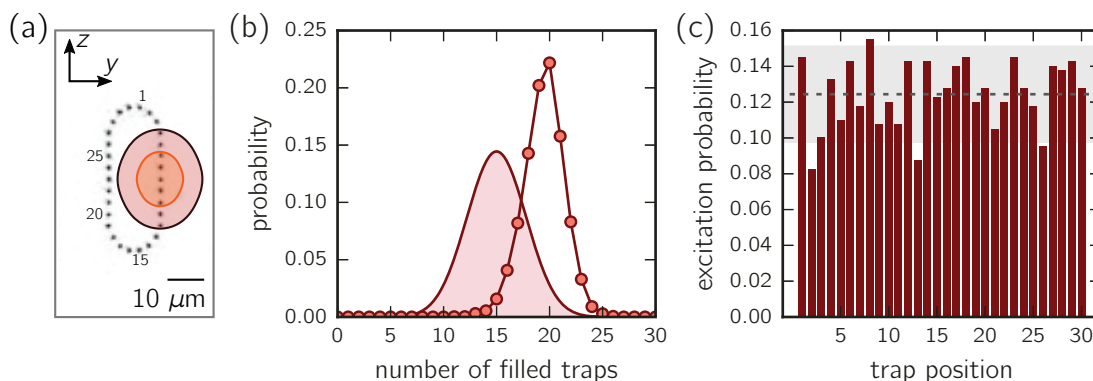


Figure 6.5: Parameters of the partially loaded Racetrack-like trap array. (a) CCD image of the trap intensities, with an inter-trap distance $a = 3.1 \mu\text{m}$. The numbers indicate the site labelling, the shaded areas the blockade radii of $R_b \simeq 13.5 \mu\text{m}$ for the $|79D_{3/2}\rangle$ (red) and $R_b \simeq 7.4 \mu\text{m}$ for the $|57D_{3/2}\rangle$ (orange) state. The array has an extent along the y -axis of $14 \mu\text{m}$ compared to the $1/e^2$ -radius of the blue excitation beam of $w_B^{(y)} = 47 \mu\text{m}$, and an extent along the z -axis of $39 \mu\text{m}$ compared to $w_R^{(z)} = 230 \mu\text{m}$ of the red beam. (b) The experiment is triggered by the presence of $N \geq 20$ atoms in the 30 traps. The points show the relative occurrences of obtained number of ground state atoms in the initial atom configurations. The shaded area shows the expected distribution for random triggering. (c) Site dependent excitation probability of a ground state atom to the $|79D_{3/2}\rangle$ state, for an excitation time $\Omega_1\tau = 0.64\pi$. The dashed line gives the mean excitation probability, the shaded grey area the statistical uncertainty.

$\alpha = R_b/a \simeq 4.3$, which should be sufficient to observe strong correlation even for a half-filling of the traps.

Along the racetrack, the measured light shifts seen by the atoms due to variations the excitation light intensity differ by less than 0.06 % of the mean Rabi frequency Ω_1 , the Rabi frequencies by less than 0.09 %. We measure again the site-resolved excitation probability for a present single atom, for an excitation time of $\Omega_1\tau = 0.64\pi$, shown in Figure 6.5(c). Almost all excitation probabilities are equal within the error bars. Due to the limited sample size, exciting on average ~ 3.7 out of the 20 atoms, for 400 realisations at $\Omega_1\tau = 0.64\pi$, the statistical uncertainty is relatively large.

The measured Rydberg fraction f_r as a function of excitation time is shown in Figure 6.6(a). We observe initial oscillations which are damped out for longer excitation times. We compare the data to the theoretical expected dynamics of the Rydberg fraction, obtained by again numerically solving the Schrödinger equation for the spin-1/2 Hamiltonian of Equation 6.3 and including an $\varepsilon = 3\%$ for all sites. The agreement between the model and the experimentally observed dynamics is remarkable,

with the residuals (see Figure 6.6(b)) smaller than ± 0.02 .

We again compute the experimentally observed, time dependent Rydberg-Rydberg pair correlation function given in Equation 6.4, here with Δk being the absolute site distance in either direction. In the case of a partially loaded array, both n_i and $n_{i+\Delta k}$ are computed from only those experiments where a ground state atom is present in the initial atom configuration both at site (i) and at site ($i + \Delta k$) at the same time. The result is shown in Figure 6.6(c). We see a strong suppression of $g^{(2)}(\Delta k)$ for short distances $\Delta k \leq 3$. The correlations emerge already at very short times, after which they show some small dynamics, but reach a quasi-steady state after $\Omega_1 \tau \approx 2\pi$.

To further assess the validity of the spin-1/2 model in this system, we want to again compare the measured pair correlations to the ones obtained from the model. For the calculation, carried out by Tommaso Macrì, the Schrödinger equation for the Hamiltonian of Equation 6.3 was solved numerically. The pair correlation function was computed for various random initial ground state distribution according to the ones observed experimentally. After several hundred realisations the computed pair correlation function is well converged.

The comparison between data and theory, shown in Figure 6.7 for a selection of excitation times, shows a remarkably good agreement. Also the apparently high value of $g^{(2)}$ for small Δk is reproduced by the theory. For these small distances $\Delta k < \alpha$, the small ε actually has a strong influence on the correlation function. In case of perfect blockade, i.e. $\varepsilon = 0$, $g^{(2)} = 0$ for small distances. Including a finite ε modifies the pair correlation computed with Equation 6.4 in the following way. To lowest order in ε , the numerator $\langle n_i n_{i+\Delta k} \rangle$ gives a non-zero value in the blocked regime only if atom i is in the Rydberg state (with a probability f_r), and atom $i + \Delta k$ is lost as a ground state atom (with probability $\varepsilon = 3\%$), or vice versa, giving $2\varepsilon f_r$. The denominator $\langle n_i \rangle \langle n_{i+\Delta k} \rangle$ gives f_r^2 , thus yielding a $g^{(2)} \simeq 2\varepsilon / f_r$, which experimentally can be as large as 0.5. Our observations show that the interaction induces spatial correlations in the system on a length scale R_b . The damped quasi-oscillatory behaviour of $g^{(2)}$ is typical of a that of a liquid. It has also been observed in Rydberg excitations on a 2D optical lattice [Schauss *et al.* \[2015\]](#).

The improved agreement to the spin-1/2 model compared to the eight-atom ring presented in the last section is likely due to the fact that many atom pairs are aligned along the quantisation axis, and only a single excitation in the ‘bend’ of the racetrack is allowed at the same time, thus making the effects of the anisotropy small.

In order to intentionally increase the effect of the anisotropy by allowing several excitations in the bend, we would ideally increase the lattice spacing by factor

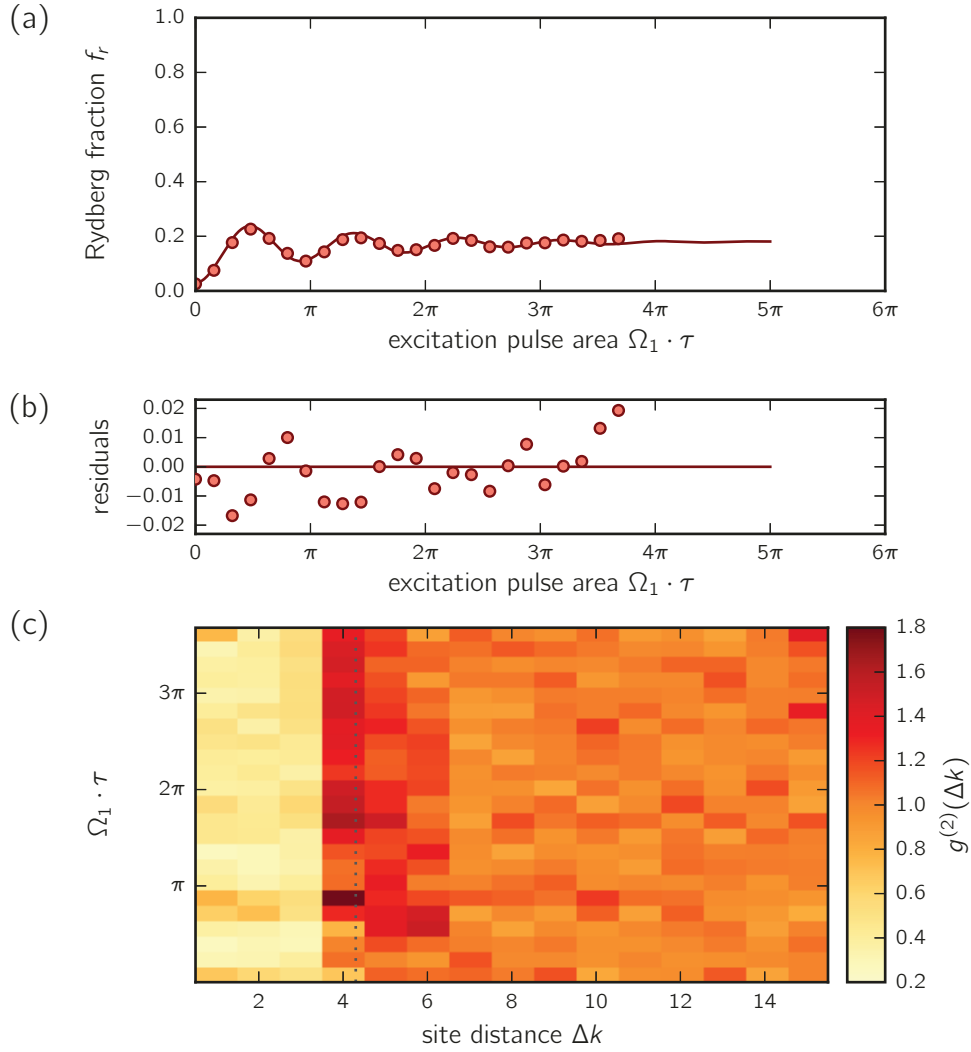


Figure 6.6: Excitation dynamics and correlations for large α . (a) The Rydberg excitation fraction in the racetrack for the $|79D_{3/2}\rangle$ Rydberg state (circles) and the numerical calculation using the spin-1/2 model (solid line), taking into account a false detection probability of $\varepsilon = 3\%$. (b) The residuals between the data and the model (error bars are smaller than the symbol size). (c) The Rydberg-Rydberg pair correlation $g^{(2)}(\Delta k)$ of Equation 6.4, the dotted line indicates $R_b(\theta = 0)$. The dynamics seems to reach a quasi-steady state after $\Omega_1 \tau \approx 2\pi$.

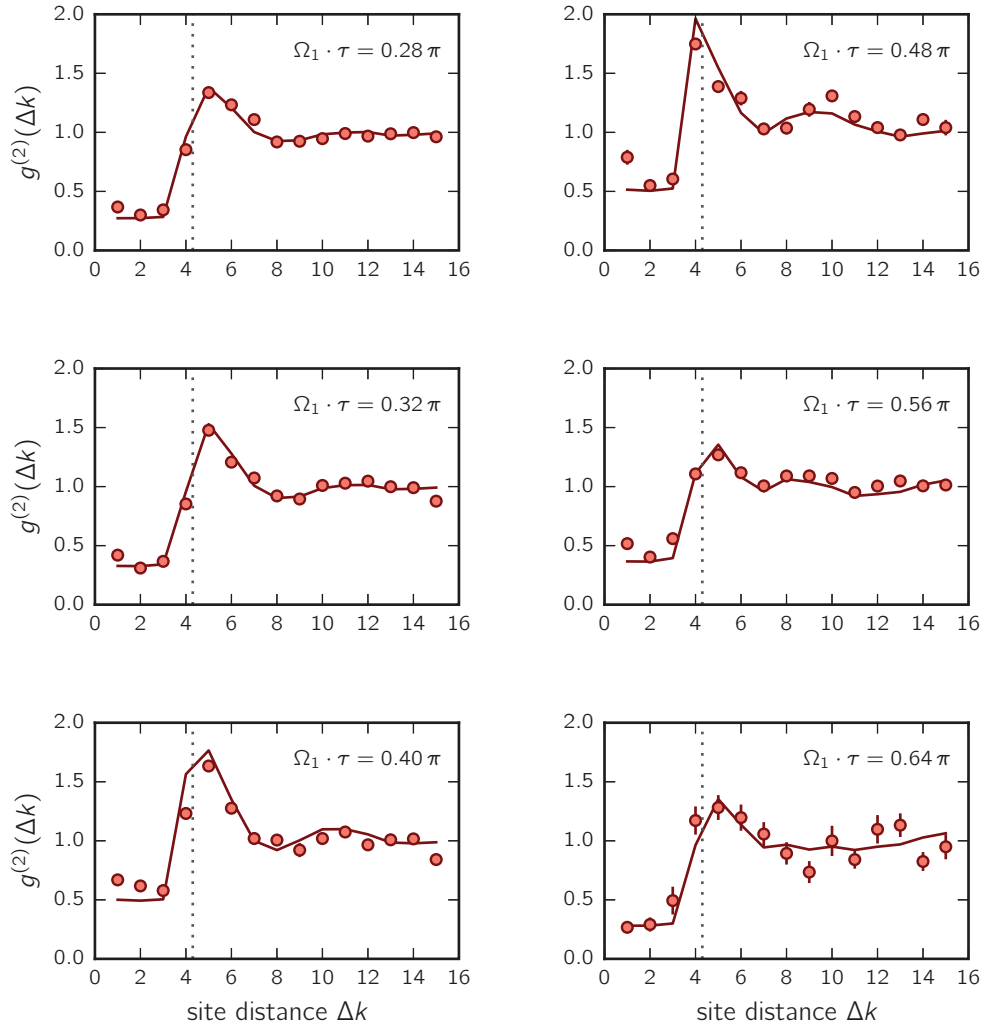


Figure 6.7: Comparison of the measured pair correlations to the spin-1/2 model. We compare, for a selection of excitation times, the measured Rydberg-Rydberg pair correlations for the $|79D_{3/2}\rangle$ state of Figure 6.6, with the numerically obtained pair correlations of the spin-1/2 model, taking into account a false detection probability of $\varepsilon = 3\%$. The dashed line indicates $\alpha = 4.3$.

~ 2 . Unfortunately this is unpractical for us, since then the array size would be comparable to the spatial extend of the excitation lasers, and Rabi frequencies would vary significantly among the trap sites. We therefore keep the array size fixed, and reduce the blockade radius R_b instead, by reducing the principal quantum number to $n = 57$. With $\Omega_1 \simeq 2\pi \times 1.7$ MHz and a calculated $C_6/h = 2.7 \times 10^5$ MHz μm^6 , we get $R_b = 7.4 \mu\text{m}$, giving $\alpha = 2.4$. As before, we again trigger on the presence of 20 atoms in the 30 traps.

We perform the same experiment as before with the $n = 79$ state, shown in Figure 6.8. Until an excitation time of $\Omega_1\tau \approx 1\pi$ the Rydberg fraction f_r follows the course predicted by the spin-1/2 model. For longer excitation times, the measured Rydberg fraction lies systematically above the calculated curve, meaning that we again measure more Rydberg excitations than predicted by the model. Finally, the pair correlations $g^{(2)}$ for the $|57D_{3/2}\rangle$ state as a function of excitation time is shown in Figure 6.8(b). The contrast is reduced compared to the previously presented one, and again a quasi-steady state seems to be reached after a time $\Omega_1\tau \approx 2\pi$. A numerical calculation of $g^{(2)}$ has not been carried out so far, as the Hilbert space is now significantly larger compared to the racetrack with the $n = 79$ Rydberg state, due to the increased number of possible Rydberg excitations in the system. While the calculation of f_r is still relatively simple by solving once the time dependent Schrödinger Equation, the calculation of $g^{(2)}$ including the finite ε in Monte-Carlo simulation requiring ~ 100 realisation to converge, becomes much more involved.

We have seen a clear distinction between the two realisations of the experiment. For the larger $\alpha = 4.3$ the agreement with the spin-1/2 model is exceptional, whereas with a smaller $\alpha = 2.4$ a deviation of the Rydberg fraction from the model becomes quickly visible. Which we attribute to a more pronounced influence of the anisotropy when decreasing α .

6.3 Partially filled 7x7 square lattice

In the previous section we investigated the Rydberg-Rydberg pair correlations along a partially loaded, quasi-1D chain of 30 traps with periodic boundary conditions. When comparing the experimental results to the spin-1/2 model of Equation 6.3, we observe an excellent agreement for $\alpha = R_b/a = 4.3$, whereas for $\alpha = 2.4$ we notice an increasing discrepancy of the Rydberg fraction for larger excitation times, which may be caused by a larger influence of the anisotropy of the interaction for atomic pairs not aligned with the quantisation axis.

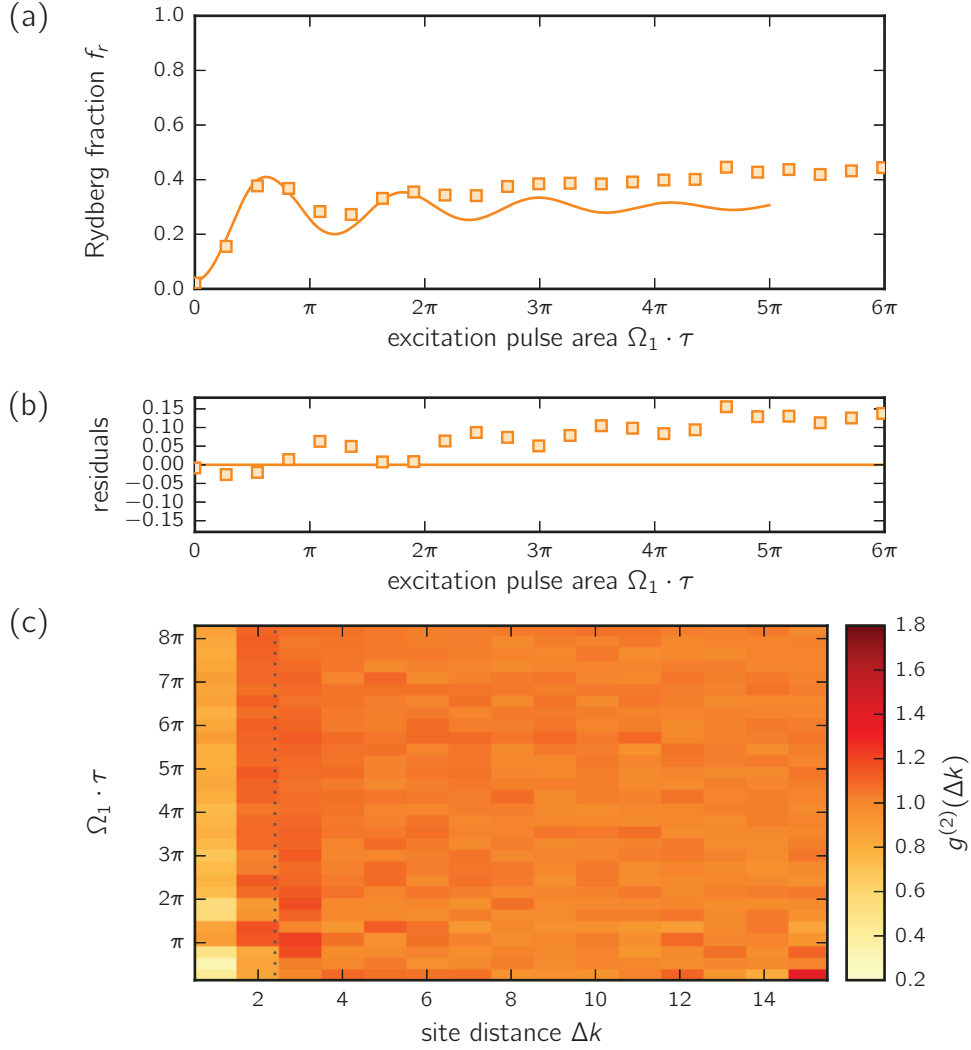


Figure 6.8: Excitation dynamics and correlations for small α . (a) The Rydberg excitation fraction in the racetrack for the $|57D_{3/2}\rangle$ Rydberg state (squares) and the numerical calculation using the spin-1/2 model (solid line), taking into account a false detection probability of $\varepsilon = 3\%$. (b) The residuals between the data and the model. (c) The Rydberg-Rydberg pair correlation $g^{(2)}(\Delta k)$ of Equation 6.4, the dotted line indicates $R_b(\theta = 0)$. Compared to the experiment with large α the correlation function is less contrasted, but also seems to reach a quasi-steady state after $\Omega_1\tau \approx 2\pi$.

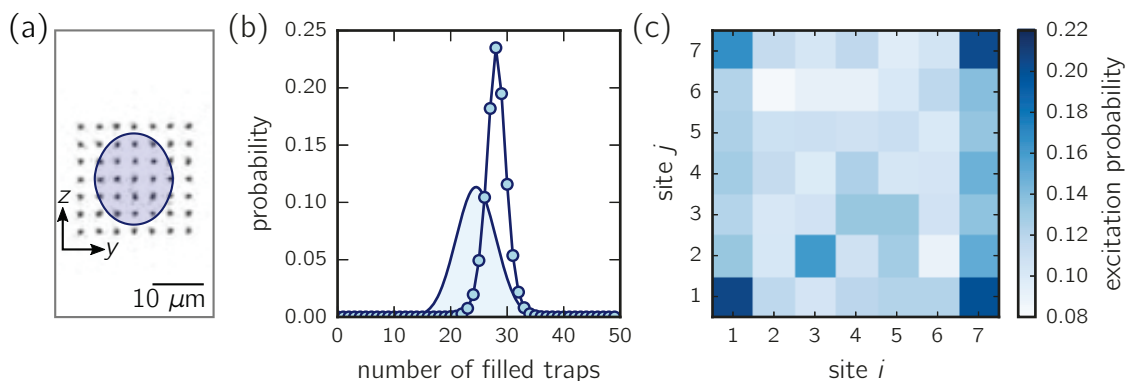


Figure 6.9: Parameters of the partially loaded 7×7 square trap array. (a) CCD image of the trap intensities, with a lattice spacing $a = 3.5 \mu\text{m}$. The blue shaded area shows the blockade radius of $R_b \simeq 9.1 \mu\text{m}$ for the $|61D_{3/2}\rangle$ state, with $\alpha = 2.6$. (b) The experiment is triggered on the presence of $N \geq 30$ atoms in the 49 traps. The points show the relative occurrences of obtained numbers of ground state atoms in the initial atom configurations. The shaded area shows the expected distribution for random triggering. (c) Single-site resolved Rydberg excitation probability of a ground state atom at position $(i, j) = (\frac{x}{a}, \frac{z}{a})$ in the array, for an excitation time $\Omega_1 \tau = 0.90\pi$. Due to finite size effects the excitation probability is slightly higher at the edges and corners of the array.

In order to further probe the influence of the angular dependence on the dynamics of the Rydberg fraction and the Rydberg-Rydberg pair correlations, we now prepare a two-dimensional 7×7 square trap array, with a lattice spacing $a = 3.5 \mu\text{m}$. We use the Rydberg state $|61D_{3/2}\rangle$ with a calculated $C_6/h = 7.6 \times 10^5 \text{ MHz } \mu\text{m}^6$. With a single atom Rabi frequency $\Omega_1 \simeq 2\pi \times 1.4 \text{ MHz}$ we expect a blockade radius $R_b = 9.1 \mu\text{m}$, giving a ratio $\alpha = 2.6$.

We trigger the experiment on the presence of $N \geq 30$ atoms present in the 49 traps, narrowing and shifting the atom number distribution to higher atom numbers compared to random triggering (see Figure 6.9(b)). Again we do not post-select the experiments on the initial atom number. In Figure 6.9(c) we show the Rydberg excitation probability for each site in the array, for an excitation time $\Omega_1 \tau = 0.90\pi$. We see the effect of the finite size of the system, leading to a higher excitation probability along the edges and in the corners of the array, as those sites have fewer neighbours than the sites in the bulk, and thus are less often blocked. Even though the false positive detection probability ε varies between 2% and 4% among the trap sites, those variations do not contain any pattern, and would be too small to explain the variation in excitation probability.

The measured dynamics of the Rydberg fraction f_r for the square array, shown in

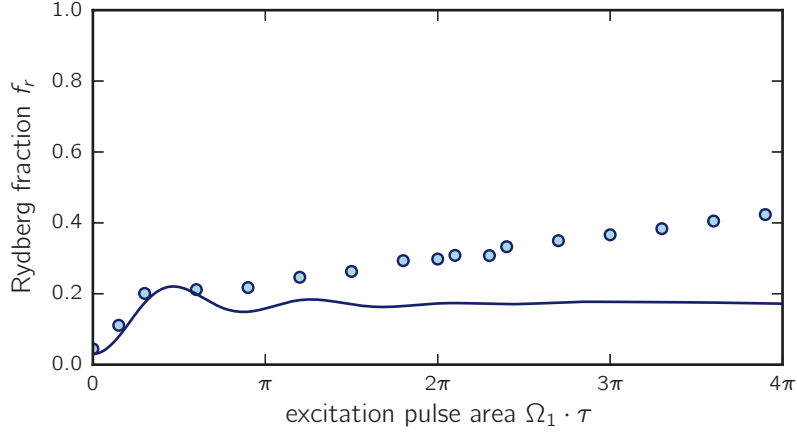


Figure 6.10: Time evolution of the Rydberg fraction in the 7x7 square trap array. Measured Rydberg fraction f_r (points) and solution of the Schrödinger equation with the spin-1/2 Hamiltonian of Equation 6.3 (solid line), taking into account a false detection probability of $\varepsilon = 3\%$.

Figure 6.10, agrees with the spin-1/2 model only for short excitation times below $\Omega_1\tau = \pi$, then monotonously increases with the excitation time without showing any further oscillations. This suggests that already with $N_{\text{at}} \sim 30$ atoms, the observed excitation dynamics resembles that of a many-body system observed in large ensembles (see e.g. [Löw *et al.*, 2009]), with an initial fast rise followed by a saturation of the Rydberg fraction. However, if the magnitude of the van der Waals interaction would just be smaller than expected, the saturation of the Rydberg fraction would occur at a slightly higher value, but we would not see a slow continuous increase as observed in the experiment. We thus again attribute the seemingly linear increase of f_r for $\Omega_1\tau > \pi$ to multilevel effects, which are indeed expected to be strong in this array where the internuclear axis of many pairs lies at a large angle θ to the quantisation axis.

In order to study the effect of the finite size of the system and the angular dependence of the interaction on the Rydberg-Rydberg correlations, we now compute the two-dimensional pair correlation function

$$g^{(2)}(\Delta k, \Delta l) = \frac{1}{N_{\text{traps}}} \sum_{i,j} \frac{\langle n_{i,j} n_{i+\Delta k, j+\Delta l} \rangle}{\langle n_{i,j} \rangle \langle n_{i+\Delta k, j+\Delta l} \rangle}, \quad (6.7)$$

where $n_{i,j}$ refers to the excitation probability at position $(i, j) = (y/a, z/a)$ of the array, and the site distances $\Delta k, \Delta l$ each ranging from -6 to 6 . Both $n_{i,j}$ and $n_{i+\Delta k, j+\Delta l}$ are computed from only those experiments where a ground state atom is present in the

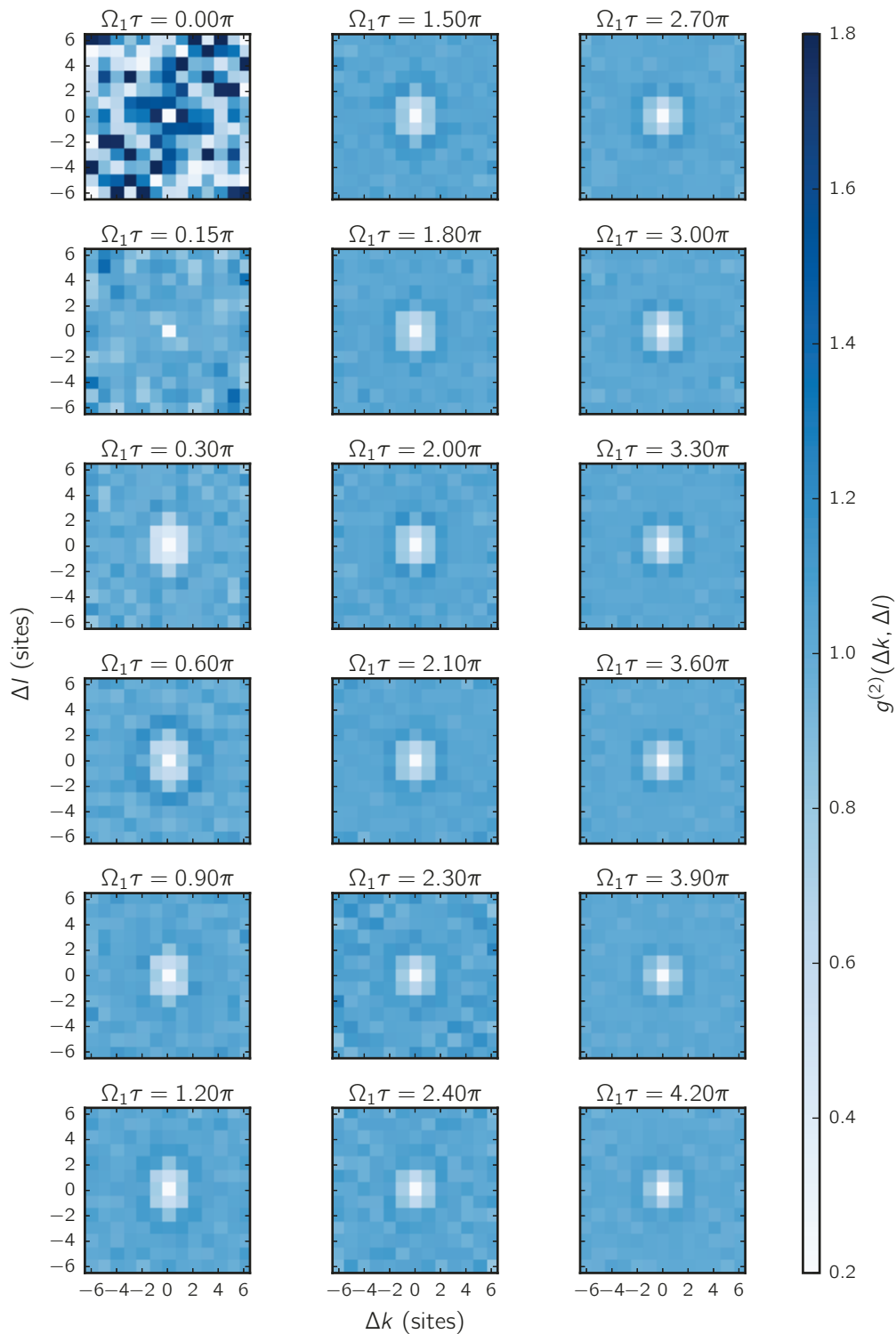


Figure 6.11: Time evolution of the pair correlation function in the 7×7 array. Already after very short excitation times a strong suppression of neighbouring Rydberg pairs emerges in the correlation function, becoming slightly weaker for long excitation times. Note the unevenly spaced excitation times of the experiment.

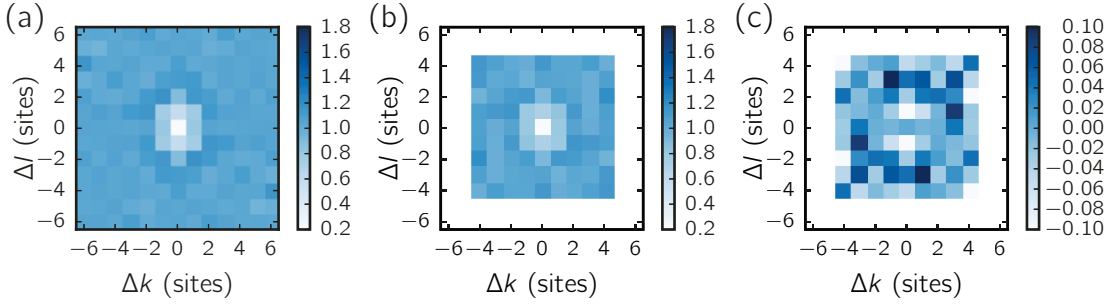


Figure 6.12: Influence of the edge atoms on the pair correlations. Pair correlation function $g^{(2)}(\Delta k, \Delta l)$ of the 7×7 array, for a excitation time of $\Omega_1 \tau = 1.5\pi$, (a) taking into account all sites on the array, as shown in Figure 6.11, (b) ignoring correlations where one atom sits on the edge of the array, and (c) the difference for the two. The same behaviour is observed for other excitation times.

initial atom configuration both at site (i, j) and at site $(i + \Delta k, j + \Delta l)$ at the same time. Here we omit the explicit time dependence of $g^{(2)}$ for better readability.

The measured Rydberg-Rydberg pair correlations are shown in Figure 6.11. Despite the finite size of the array, we clearly see the fast emergence of a strong depletion around each excitation. We already see strong correlations after an excitation pulse area of only $\Omega_1 \tau = 0.3\pi$. For excitation times up to $\Omega_1 \tau \approx 2\pi$ we see an isotropy in the pair correlations which resembles that of the effective van der Waals potential of Equation 5.7, which then seems to disappear at later times. This is not yet understood.

Lastly, in order to probe the effect of the finite size of the system, we again compute the pair correlation function according to Equation 6.7, this time neglecting the sites which are on the edge of the 7×7 array, i.e letting i and j only run from 2 to 6 thus and Δk and Δl from -4 to 4 . The obtained $g^{(2)}$, together with that of Figure 6.11 using the full array, are shown in Figure 6.12 for an excitation time $\Omega_1 \tau = 1.5\pi$. Except for a slightly increased noise, the results are qualitatively equivalent. The same holds true for all other measured excitation times. The finite size of the arrays therefore does not seem to have a large impact on the pair correlations, which is not surprising as the blockade radius is small compared to the size of the array.

6.4 Conclusion

We have realised the quantum Ising model of a spin-1/2 system both in effective one-dimensional atom arrays with periodic boundary conditions and in a two-dimensional atom array. We have benchmarked our implementation of a spin system by comparing

both the Rydberg fraction f_r and the Rydberg-Rydberg pair correlation function $g^{(2)}$ against a numerical simulation of the quantum Ising model for the experiments where a numerical treatment was still practical.

We observed an overall good agreement for short excitation times. For long excitation times, we notice an increase of nearby Rydberg pair-excitations for most cases, which is not reproduced by the spin-1/2 model. For the racetrack-shaped trap array with a large blockade radius, where most of the interacting atom pairs are aligned along the quantisation axis, we observe an exceptional agreement between our experiment and the spin-1/2 model.

The obtained results are promising in view of the quantum simulation of spin systems with single Rydberg atoms. Additional work is necessary to e.g. clarify the role of the Zeeman level-structure of Rydberg D -states as pointed out in Chapter 5, in order to better understand the cause of the discrepancy between the experiment and the spin-1/2 model.

The Rydberg blockade in the resonant dipole-dipole regime

The Rydberg blockade is predominantly studied in the van der Waals regime [Comparat and Pillet, 2010]. However, a similar type of blockade can be observed for resonant dipole-dipole interactions [Vogt *et al.*, 2007; van Ditzhuijzen *et al.*, 2008; Reinhard, Younge, and Raithel, 2008; Maxwell *et al.*, 2013; Gunter *et al.*, 2013; Ravets *et al.*, 2014].

Although the van der Waals and the resonant dipole-dipole interaction are two regimes of the same atomic interaction, the characteristics of the blockade can be somewhat different. In the van der Waals regime, the strong interaction shifts all states with more than a single excitation out of resonance within a certain blockade volume, as we have seen in Chapter 5. In the resonant dipole-dipole regime, the blockade mechanism is a bit more involved, due to the off-diagonal nature of the interaction.

We have previously studied the resonant dipole-dipole blockade by tuning two different atomic pair states into resonance by applying a specific electric field [Ravets *et al.*, 2014, 2015], a so-called Förster resonance [Walker and Saffman, 2005].

Here, we present a slightly different approach to observe the Rydberg blockade between two single atoms in the resonant-dipole regime, by driving coherent Rydberg-Rydberg transitions using microwaves. By scanning the frequency of the microwave field, we can excite a symmetric ‘superradiant’ state with a coupling strength enhanced by the expected factor $\sqrt{2}$, while seeing no coupling to the antisymmetric ‘dark’ state.

7.1 Theoretical description

The principle of the experiment is depicted in Figure 7.1. Two atoms in the $|d\rangle = |nD_{3/2}\rangle$ Rydberg state are placed along the quantisation axis, with an interatomic distance R . We then shine in a microwave field resonant to the single atom $|d\rangle \leftrightarrow |p\rangle = |(n+1)P_{1/2}\rangle$ transition with a coupling strength given by the single atom microwave

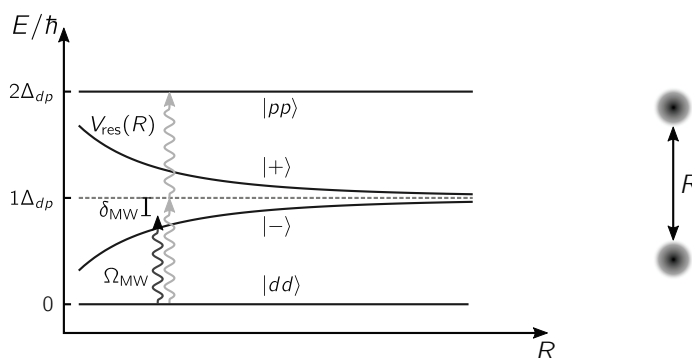


Figure 7.1: Illustration of the Rydberg blockade in the resonant dipole-dipole regime. Due to the resonant dipole-dipole interaction, the two-atom state $|dp\rangle$ is split into the bright state $|+\rangle = (|dp\rangle + |pd\rangle)/\sqrt{2}$ and the dark state $|-\rangle = (|dp\rangle - |pd\rangle)/\sqrt{2}$. For small distances, the microwave transfer is thus blocked at the single atom resonance $\delta_{\text{MW}} = 0$ (dark grey wiggly line). The state $|pp\rangle$ may still be excited via a two-photon excitation (light grey wiggly line), albeit with a reduced coupling strength. (The van der Waals interaction is neglected here.)

Rabi frequency Ω_{MW} . With the resonant dipole-dipole interaction, the new eigenstates of the system are now

$$\begin{aligned}
 &|dd\rangle \\
 &|+\rangle = \frac{|dp\rangle + |pd\rangle}{\sqrt{2}} \\
 &|-\rangle = \frac{|dp\rangle - |pd\rangle}{\sqrt{2}} \\
 &|pp\rangle,
 \end{aligned} \tag{7.1}$$

where the superposition states $|\pm\rangle$ are shifted by an amount $\pm V_{\text{res}} = \pm \langle dp | \hat{V}_{\text{dd}} | pd \rangle = \pm C_3/R^3$. With the microwave field tuned to the single atom resonance, i.e. $\delta_{\text{MW}} = 0$, the states $|\pm\rangle$ are thus shifted out of resonance if $C_3/R^3 \gg \Omega_{\text{MW}}$, and the microwave transfer of one of the two atoms to the $|p\rangle$ state is thus blocked. On the other hand, the microwave field can still transfer both atoms at the same time, to the doubly excited state $|pp\rangle$, without populating the states $|dp\rangle$ or $|pd\rangle$. However, since this is an off-resonant two photon transition, it has a reduced coupling strength $\Omega_{2\text{ph}} \approx \hbar\Omega_{\text{MW}}^2/V_{\text{res}}$ when $\Omega_{\text{MW}} \ll V_{\text{res}}$.

7.2 Microwave spectroscopy of a resonantly interacting two-atom system

In order to perform this experiment, we need to be able to efficiently excite the atoms to the initial $|dd\rangle$ state, meaning that the van der Waals interaction of this state should be small compared to the optical Rabi frequency. At the same time, we want the resonant dipole-dipole interaction of the $|pd\rangle$ state to be large, in order to shift the $|\pm\rangle$ states off-resonant to the microwave field.

We therefore choose an interatomic distance of $R \simeq 10.3 \mu\text{m}$, and the Rydberg states $|d\rangle = |62D_{3/2}\rangle$ and $|p\rangle = |63P_{1/2}\rangle$. In this case, the van der Waals interaction of the $|dd\rangle$ state $V_{\text{vdW}}(10.3 \mu\text{m}) \simeq h \times 0.7 \text{ MHz}$ can be neglected compared to the optical Rabi frequency $\Omega_1 \simeq 2\pi \times 7.8 \text{ MHz}$ used to prepare the initial $|dd\rangle$ state. We have previously measured a $C_3 = 7950 \pm 130 \text{ MHz } \mu\text{m}^3$ for the resonant dipole-dipole interaction of the $|pd\rangle$ state [Barredo *et al.*, 2015]. The expected interaction strength at the chosen distance $V_{\text{res}}^{(\text{theo})}(10.3 \mu\text{m}) = h \times 7.3 \pm 0.1 \text{ MHz}$ is large compared to the chosen microwave Rabi frequency $\Omega_{\text{MW}} \simeq 2\pi \times 0.87 \text{ MHz}$. The van der Waals interaction of the $|pp\rangle$ state is $V_{\text{vdW}}(10.3 \mu\text{m}) < h \times 0.1 \text{ MHz}$ and is negligible compared to all other relevant frequencies. As explained in Section 2.5, we measure the final population in $|d\rangle$ at the end of an experiment by coherently coupling it back to the ground state $|g\rangle$.

We first use one single atom to calibrate the transition frequency between the $|d\rangle$ and $|p\rangle$ state, and find¹ $\Delta_{dp}/2\pi \simeq 9132.50 \text{ MHz}$, shown in Figure 7.2(a). We then use two atoms as mentioned above. Figure 7.2(b) shows the probability to find the atoms in $|dd\rangle$ after sending a microwave pulse with a $\tau_{\text{MW}} = 0.4 \mu\text{s}$ duration, when scanning the microwave detuning δ_{MW} . We see a depletion of the population in the $|dd\rangle$ state for $\delta_{\text{MW}}/2\pi = V_{\text{res}}^{(\text{exp})}/h = -7.45 \text{ MHz}$, corresponding to the excitation of the $|+\rangle$ state, close to the expected value of $V_{\text{res}}^{(\text{theo})}/h = 7.3 \pm 0.1 \text{ MHz}$. The width of the resonance is about 1.8 times the width of the single atom resonance, larger than the expected factor $\sqrt{2} \simeq 1.414$. This broadening is explained by the shot-to-shot fluctuations of the interatomic distance of $\approx 100 \text{ nm}$ due to the finite temperature of the atoms, which in turn can lead to variations in interaction strength of up to 0.5 MHz.

Changing the microwave frequency by the same absolute value but with a positive detuning should tune the field resonant to the $|-\rangle$ state. However, we do not observe any transfer away from the $|dd\rangle$ state, since the microwave coupling to this ‘dark’ state

¹We still apply a +6 G magnetic field along the z axis to define a quantisation axis.

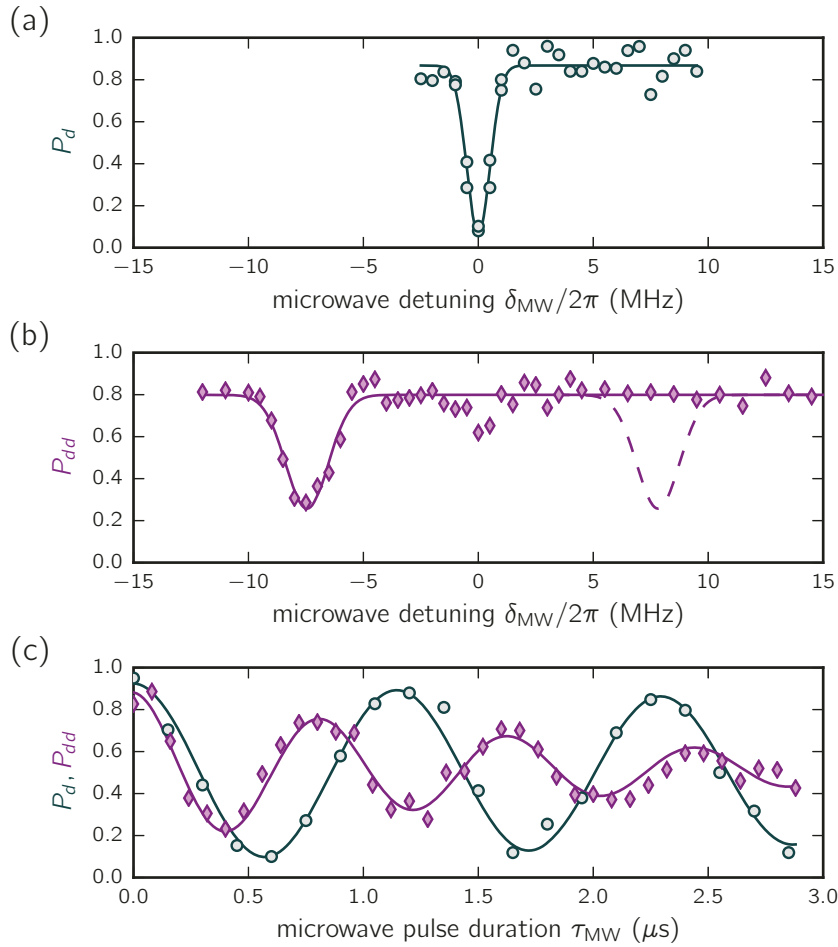


Figure 7.2: Spectroscopy and Rabi oscillation of the p-d microwave transition for one and two atoms. (a) Spectroscopy of a single atom. We show the probability P_d to find the atom in the $|d\rangle$ state after sending a 400 ns microwave pulse of frequency $(\Delta_{dp} + \delta_{MW})$, with $\Delta_{dp}/2\pi = 9\,132.50$ MHz. (b) Spectroscopy of two atoms with an interatomic distance of $R = 10.3\,\mu\text{m}$. We measure the probability P_{dd} to find the atoms in the $|dd\rangle$ state after sending the 400 ns microwave pulse. We find a shift of the superradiant $|+\rangle$ state of $\delta_+/2\pi \simeq -7.45$ MHz, whereas we find no population transfer at the expected position of the subradiant $|-\rangle$ state (dashed purple line). The small dip of P_{dd} at $\delta_{MW} = 0$ is caused by the imperfect state preparation (see text). (c) Microwave driven Rabi oscillations. We measure a single atom Rabi oscillation (grey circles) of $\Omega_{MW} = 2\pi \times 0.87$ MHz for a detuning $\delta_{MW} = 0$. For two atoms and the microwave field tuned resonant to the $|dd\rangle \leftrightarrow |+\rangle$ transition, i.e. $\delta_{MW} = \delta_+$ (purple diamonds), we measure an enhanced Rabi frequency $\Omega_+ \simeq 1.41\Omega_{MW}$.

is zero. With the microwave field tuned to the single atom resonance, i.e. $\delta_{\text{MW}} = 0$, we observe a small dip in the $|dd\rangle$ population. One might think that this is caused by a two-photon transition to the $|pp\rangle$ state. This not the case however, as the two-photon Rabi frequency $\Omega_{2\text{ph}} \approx \hbar\Omega_{\text{MW}}^2/V_{\text{res}} \simeq 0.1$ MHz is very weak, and with the $\tau_{\text{MW}} = 0.4 \mu\text{s}$ microwave pulse we only expect a population in $|pp\rangle$ of $P_{pp} < 0.02$ according to Equation 2.10². The dip is actually caused by an imperfect initial Rydberg state preparation. As in some cases only one of the two ground state atoms is excited, thus preparing the state $|gd\rangle$, the microwave pulse is now resonant again for the single Rydberg atom, resulting in the final state $|gp\rangle$ and thus a reduced observed population in $|dd\rangle$.

We now tune the microwave field resonant to the $|dd\rangle \leftrightarrow |+\rangle$ transition, i.e. $\delta_{\text{MW}}/2\pi = -7.45$ MHz, to drive a coherent Rabi oscillation between the two states. We measure a collective Rabi frequency of $\Omega_{\text{MW}}^{(2)} = 2\pi \times 1.2$ MHz $= 1.4\Omega_{\text{MW}}$, perfectly matching the expected $\sqrt{2}$ enhancement. We notice a significant increase of damping for the two-atom oscillation compared to the single-atom oscillation. Again, this is due to the shot-to-shot fluctuations of the interatomic separation, which can lead to a slightly off-resonant excitation of the $|+\rangle$ state. Note that for the collective Rabi oscillation in the van der Waals regime these fluctuations do not play a role. They do change the exact interaction strength between the atoms from shot to shot, they do not play any role however, since the exact magnitude of the interaction is not important here, as long as it is larger than optical Rabi frequency.

7.3 A possible extension to many atoms

We have seen that here, different to the van der Waals Rydberg blockade, there is interaction between the atoms even if there is only one ‘excitation’ present in the system. In view of extending the above experiment from two to many atoms, analogous to the van der Waals regime in Chapter 5, and to further illustrate the difference of the two regimes, we consider the following ‘gedankenexperiment’. We take a system of 9 atoms all in the $|d\rangle$ state, arranged in a 3×3 array, with the quantisation axis parallel to the plane of the atoms, such that the resonant dipole-dipole interaction is isotropic in the plane of the atoms. We want to see what to expect when we couple this state $|d^{(9)}\rangle = |d_1d_2\dots d_N\rangle$ to a state with a single $|p\rangle$ excitation.

The eigenenergies of a system whose basis consists of the nine states containing one

²This is confirmed by a numerically solving the Schrödinger equation of the 4-level system, showing a negligible population of the $|pp\rangle$ state for experimental parameters used here.

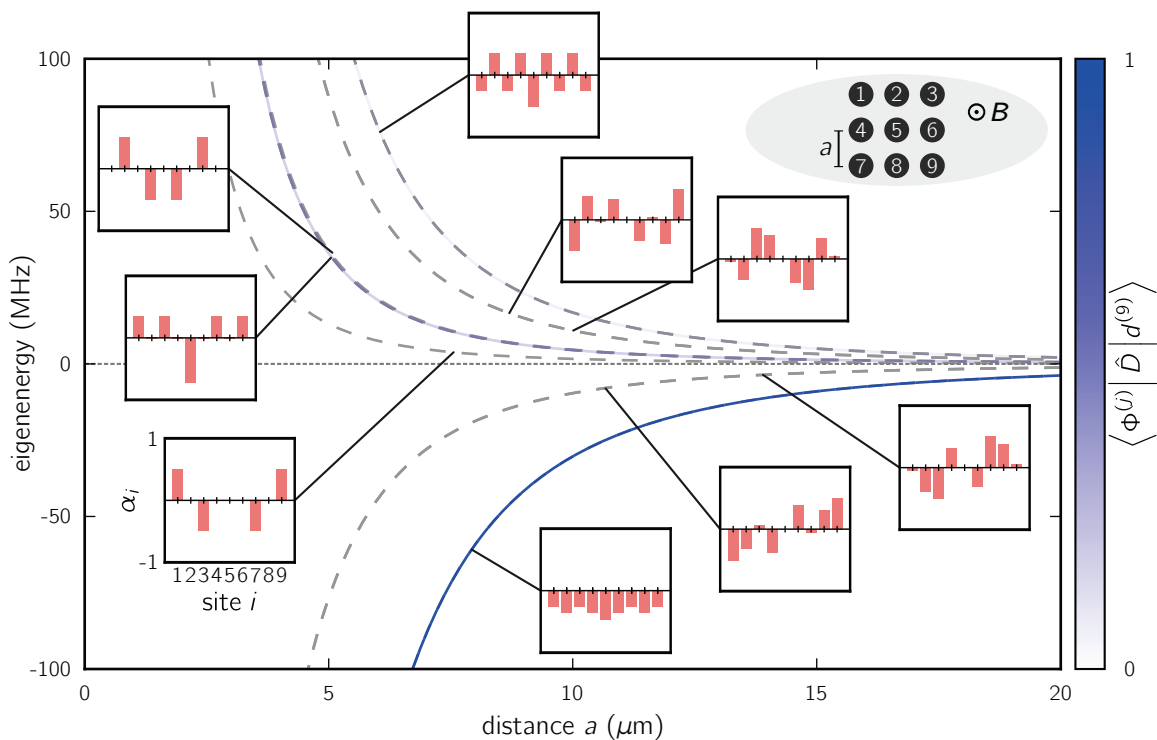


Figure 7.3: Calculated energy spectrum of a 3×3 atom array with a single P excitation in the resonant dipole-dipole regime. We calculate the eigenenergies of a 3×3 array of Rydberg atoms, with 8 atoms in the $|d\rangle = |62D_{3/2}\rangle$ state, and a single $|p\rangle = |63P_{1/2}\rangle$ excitation, with a $C_3 = 7965 \text{ MHz } \mu\text{m}^3$, and isotropic in-plane interactions. The grey dashed lines indicate the eigenenergies of the nine eigenstates $|\Phi^{(j)}\rangle$, $j \in [1, 9]$, as the function of the lattice spacing. The strength of the blue shading indicates the relative microwave coupling strength to the state $|d^{(9)}\rangle = |d_1 d_2 \dots d_9\rangle$. The insets show for each eigenstate the probability amplitudes $\alpha_i^{(j)} = \langle \phi_i | \Phi^{(j)} \rangle$ to find the $|p\rangle$ excitation at atom i for each eigenstate, with $|\phi_i\rangle = |d_1 d_2 \dots p_i \dots d_N\rangle$ (atom labelling indicated in the top right).

single excitation $|\phi_i\rangle = |d_1 d_2 \dots p_i \dots d_N\rangle$, with $i \in [1, 9]$, are shown in Figure 7.3. Due to the resonant dipole-dipole interaction between the single $|p\rangle$ excitation and the remaining $|d\rangle$ state atoms, the absolute values of the eigenenergies become large for small lattice spacings.

We now compute the microwave coupling strength to the various singly excited eigenstates $|\Phi^{(j)}\rangle = \frac{1}{\sqrt{N}} \sum_{i=1}^N \alpha_i^{(j)} |\phi_i\rangle$. The coefficients α_i are shown in the insets in Figure 7.3 for all eigenstates j . We assume that the microwave coupling is equal for all atoms, i.e. $\langle d_i | \hat{d} | p_i \rangle = c$ for all i , with \hat{d} being the transition dipole operator, and c a constant. The coupling strength $\langle \Phi^{(j)} | \hat{D} | d^{(9)} \rangle$ is shown as the strength of the blue shading on the eigenenergies in Figure 7.3, with $\hat{D} = \sum_i \hat{d}_i$. We see one

strongly superradiant state with an enhanced coupling, although showing a smaller enhancement than the $\sqrt{9}$ in the van der Waals regime. A second eigenstate is still weakly coupled, whereas the coupling to all other states is zero. It should therefore be possible, if one were to spectroscopically probe such a 3×3 atom array, to find 2 resonances for the microwave transition.

For a fully symmetric system, e.g. all atoms arranged on a ring, all states $|\phi_i\rangle = |d_1 d_2 \dots p_i \dots d_N\rangle$ would have the same energy, since it makes no difference at which site the $|p\rangle$ excitation is. One finds that in this case, there is only one superradiant state with a \sqrt{N} enhanced coupling (N being the number of atoms), the remaining eigenstates all being dark states. The difficulty in this type of microwave experiment remains the reliable excitation of the array of ground state atoms to the Rydberg $|d\rangle$ states, i.e. overcoming the van der Waals interaction, while at the same time being fully blockaded in the resonant dipole-dipole regime.

7.4 Conclusion

We observed the Rydberg blockade in the resonant dipole-dipole regime by shining a microwave pulse on two single Rydberg atoms. Unlike the van der Waals interaction, which only acts perturbatively on interacting pair states, the resonant dipole-dipole interaction changes the eigenstates of the interacting system, due to its off-diagonal nature.

By tuning the microwave field resonant to the symmetric ‘bright’ superposition state we could observe its $\sqrt{2}$ -enhanced coupling to the initially prepared Rydberg pair-state.

Using the resonant dipole-dipole interaction between Rydberg atoms we can implement an XY spin-Hamiltonian of the form [Barredo *et al.*, 2015]

$$H = \frac{1}{2} \sum_{i \neq j} V_{ij} (\sigma_i^+ \sigma_j^- + \sigma_i^- \sigma_j^+), \quad (7.2)$$

allowing the study of dipolar energy transport, which plays for example an important role in photosynthesis [Collini *et al.*, 2010] and organic semiconductors [Najafov *et al.*, 2010].

Conclusion and outlook

In this thesis I presented my work on probing the dynamics and pair correlations of Rydberg excitations in 2D arrays of single neutral atoms. Two main technical advancements of the existing experimental setup [Béguin, 2013; Ravets, 2014] were necessary to realise such kind of experiments. First, the implementation of a spatial light modulator to shape the spatial phase of our optical dipole trap beam now allows us to arrange as many as ~ 100 single atom traps in any desired 2D pattern, with trap separations as low as $\sim 3 \mu\text{m}$, and array sizes as large as $\sim 50 \times 50 \mu\text{m}^2$. Second, using a sensitive CCD camera to detect the atomic fluorescence provides the real-time, single-site resolved monitoring of the filling of the traps.

The combination of these two techniques lets us to perform Rydberg experiments with any chosen two-dimensional arrangement of ground state atoms, measuring the site-resolved Rydberg excitation efficiency with an unprecedented $\gtrsim 95\%$ efficiency. The real-time monitoring of the fluorescence from the traps allows us to trigger and / or post-sort experiments on any atom configuration, e.g. a given number of present atoms. We can perform experiments with fully loaded trap arrays with up to nine traps. For larger trap numbers, we are as of now constrained to partially loaded arrays, due to the randomness of loading single atoms in the microtraps, which results in a probability of about 0.5^{N_t} to have a fully loaded N_t -trap array.

Techniques leading to single-trap occupation probabilities up to 90% have been successfully demonstrated recently by optimising the light-assisted collision process [Fung and Andersen, 2015; Lester *et al.*, 2015]. This is comparable to the filling fraction of single atoms in an optical lattice in the Mott-insulator regime for a defined pattern [Weitenberg *et al.*, 2011]. A preliminary implementation of this technique in our experiment gave trap loading probabilities of about 80% (see Figure 8.1).

We measured the collective enhancement of a single Rydberg excitation for up to $N = 15$ atoms, in the full blockade regime of the van der Waals interaction, observing the expected \sqrt{N} -scaling. Our single-site resolved atom detection lets us determine the initially prepared number states with a fidelity close to unity. We measure a double excitation probability higher than expected from both the simple blockade picture and

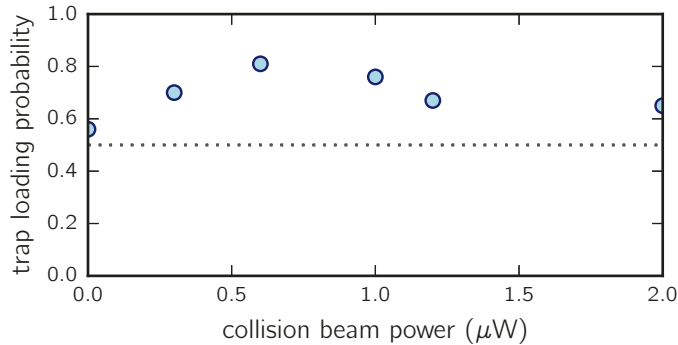


Figure 8.1: Enhanced single atom loading. By adjusting the parameters of the collision beam, the laser beam photo-associating the atom pair in the inelastic collision, collisions where only one atom leaves the trap become more probable. In a preliminary test, we achieve trap loading probabilities up to 80 %.

the numerical simulation of the Schrödinger equation. We suggest that this is caused by the Zeeman-substructure of the used Rydberg D -states, which are coupled by the van der Waals interaction for atom pairs not aligned with the quantisation axis.

We have measured a similar Rydberg blockade in the regime of resonant dipole-dipole interactions for two single atoms, using microwave transitions in the Rydberg manifold. When tuning the microwave field resonant to the superradiant symmetric superposition state, we again measure the expected $\sqrt{2}$ -enhancement of the microwave coupling.

Finally, demonstrating the versatility of the presented setup, we have implemented the quantum Ising model of a spin-1/2 system, in various one- and two-dimensional geometries, for up to 30 atoms. We probed the excitation dynamics and Rydberg-Rydberg pair correlations in the partial blockade regime of the van der Waals interaction, and compared the results to numerical simulations of the quantum Ising model wherever possible. We observe a good agreement to the model especially for short excitation times. If the effect of the anisotropy of the van der Waals interaction is small, the agreement to the spin-1/2 model is exceptional.

Apart from achieving a higher filling fraction of the traps by optimising the light-assisted collisions, reducing the temperature of the single atom, e.g. by Raman sideband cooling [Kaufman, Lester, and Regal, 2012], will be an important task in view of future experiments. Lower atom temperatures will improve the false Rydberg detection probability, which will be important when working with even larger atom numbers, and reduce the Doppler effect during the Rydberg excitation.

The results presented in this thesis are an important step towards the realisation of Rydberg quantum simulator for spin-1/2 system, of both the quantum Ising model

presented in this thesis, and the XY -model, which we have already realised in a chain of three atoms [Barredo *et al.*, 2015].

This experiment will allow to probe strongly correlated mesoscopic quantum systems with single particle resolution, ranging from the study of topological insulators by effective spin-orbit coupling [Peter *et al.*, 2015], exotic states of matter [Glaetzle *et al.*, 2014], thermalisation in closed quantum systems [Ates, Garrahan, and Lesanovsky, 2012], to the dynamical emergence of entanglement following a quantum quench [Hazzard *et al.*, 2014].

Following the path of quantum information with Rydberg atoms [Saffman, Walker, and Mølmer, 2010; Wilk *et al.*, 2010; Isenhower *et al.*, 2010], we can put to test protocols such as the CNOT-gate [Maller *et al.*, 2015], or creating strongly entangled GHZ states [Greenberger, Horne, and Zeilinger, 1989; Müller *et al.*, 2009].

Publications

Single-Atom Trapping in Holographic 2D Arrays of Microtraps with Arbitrary Geometries

F. Nogrette, H. Labuhn, S. Ravets, D. Barredo, L. Béguin, A. Vernier, T. Lahaye, and A. Browaeys

*Laboratoire Charles Fabry, UMR 8501, Institut d'Optique, CNRS, Univ Paris Sud 11,
2 avenue Augustin Fresnel, 91127 Palaiseau cedex, France*

(Received 21 February 2014; revised manuscript received 24 March 2014; published 23 May 2014)

We demonstrate single-atom trapping in two-dimensional arrays of microtraps with arbitrary geometries. We generate the arrays using a spatial light modulator, with which we imprint an appropriate phase pattern on an optical dipole-trap beam prior to focusing. We trap single ^{87}Rb atoms in the sites of arrays containing up to approximately 100 microtraps separated by distances as small as $3\ \mu\text{m}$, with complex structures such as triangular, honeycomb, or kagome lattices. Using a closed-loop optimization of the uniformity of the trap depths ensures that all trapping sites are equivalent. This versatile system opens appealing applications in quantum-information processing and quantum simulation, e.g., for simulating frustrated quantum magnetism using Rydberg atoms.

DOI: [10.1103/PhysRevX.4.021034](https://doi.org/10.1103/PhysRevX.4.021034)

Subject Areas: Atomic and Molecular Physics, Optics

I. INTRODUCTION

The optical trapping of cold atoms [1] allows for a variety of applications, from the study of quantum gases [2] to the manipulation of single atoms [3]. Impressive achievements in the engineering of quantum systems have been obtained using relatively simple configurations of light fields, such as single-beam traps [4], crossed optical dipole traps [5], arrays of microtraps obtained by microlens arrays [6,7] or holographic plates [8], optical lattices [9,10], or speckle fields [11].

In the last few years, an interest in more advanced tailoring of optical potentials has arisen. Several technical approaches can be considered. A first solution consists of “painting” arbitrary patterns of light using a time-dependent light deflector [12,13], over time scales that are fast compared to the typical oscillation frequency in the trap. Ultracold atoms then experience an optical potential corresponding to the time-averaged light intensity. Another approach relies on the generation of reconfigurable light patterns using spatial light modulators (SLMs), either in amplitude or in phase [14–17].

Single atoms held in arrays of microtraps with a spacing of a few μm are a promising platform for quantum-information processing and quantum simulation with Rydberg atoms [18–22]. The realization of an array of approximately 50 microtraps for single atoms using an elegant combination of fixed diffractive optical elements and polarization optics was recently demonstrated in Ref. [23].

Here, we report on the trapping of single atoms in reconfigurable 2D arrays of microtraps, separated by distances down to $3\ \mu\text{m}$, with almost arbitrary geometries. We create not only mesoscopic arrays of a few traps but also regular 2D lattices with up to approximately 100 sites, with geometries ranging from simple square or triangular lattices to more advanced ones, such as kagome or honeycomb structures. Using a closed-loop optimization of the uniformity of the trap depths allows us to obtain very uniform lattices. As compared to previous approaches using SLMs, this novel feature opens appealing prospects for quantum simulation with neutral atoms [24] and eliminates a source of complication in the theoretical modeling of these systems. For that, we use a phase-modulating SLM, which has the advantage of being versatile and easily reconfigurable. Another major asset of the system lies in the fact that, in combination with wave-front analysis, the SLM can also be used to correct *a posteriori* for aberrations that are inevitably present in the optical setup, thus improving considerably the optical quality of the traps.

This article is organized as follows. After giving an overview of the principles behind our setup, we give a detailed account of the obtained results. We present a gallery of examples of microtrap arrays in which we trap single atoms, and we study the single-atom loading statistics of a 3×3 square array. In a second part, we give details about the implementation of the optical setup and the calculation of the phase holograms. We then explain how we optimize the obtained traps using a Shack-Hartmann (SH) wave-front sensor and present a closed-loop improvement of the uniformity of the trap intensities.

II. MAIN RESULTS

In this section, after briefly describing our experimental setup, we demonstrate the trapping of single atoms in microtrap arrays with various geometries.

Published by the American Physical Society under the terms of the Creative Commons Attribution 3.0 License. Further distribution of this work must maintain attribution to the author(s) and the published article's title, journal citation, and DOI.

A. Overview of the experimental setup

Figure 1 shows a sketch of the setup we use to trap single ^{87}Rb atoms [25]. It is based on a red-detuned dipole trap at a wavelength $\lambda = 850$ nm, with a $1/e^2$ radius $w_0 \approx 1$ μm . For a power of 3 mW, the trap has a typical depth $U_0 = k_B \times 1$ mK, with radial (respectively, longitudinal) trapping frequencies around 100 kHz (respectively, 20 kHz). To load atoms into the microtrap, we produce a cloud of cold atoms at approximately 50 μK in a magneto-optical trap (MOT). The dipole-trap beam is focused in the cloud with a custom-made high-numerical-aperture (NA) aspheric lens with focal length $f_{\text{asph}} = 10$ mm [26]. We detect single atoms by measuring their fluorescence signal at 780 nm (collected by the same aspheric lens) using a cooled, 16-bit electron-multiplying CCD (EMCCD) camera [27]. We separate the fluorescence signal from the trapping beam with a dichroic mirror (DM). A second aspheric lens, facing the first one in a symmetrical configuration, is used to recollimate the trapping beam. An 8-bit CCD camera, placed after the vacuum chamber, is conjugated with the plane of the single atoms for diagnostic purposes.

We generate arrays of microtraps with arbitrary geometries using a phase-modulating SLM [28], which imprints a calculated phase pattern $\varphi(x, y)$ onto the trapping beam of initial Gaussian amplitude $A_0(x, y)$. The intensity distribution in the focal plane of the aspheric lens is then given by the squared modulus of the 2D Fourier transform of

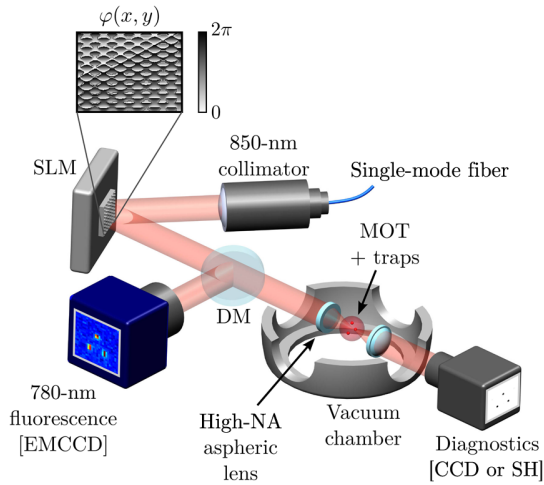


FIG. 1. Generation of an array of microtraps for single-atom trapping. The SLM imprints the calculated phase pattern $\varphi(x, y)$ on the 850-nm dipole-trap beam. A high-numerical-aperture aspheric lens under vacuum focuses it at the center of a MOT. The intensity distribution in the focal plane is $\propto |\text{FT}(A_0 e^{i\varphi})|^2$, where A_0 is the initial Gaussian amplitude profile of the 850-nm beam and FT stands for Fourier transform. The atomic fluorescence at 780 nm is reflected off a DM and detected using an EMCCD camera. A second aspheric lens (identical to the first one) recollimates the 850-nm beam. This transmitted beam is used for trap diagnostics (either with a diagnostics CCD camera or a SH wave-front sensor).

$A_0 \exp(i\varphi)$. The phase pattern φ needed to obtain the desired intensity distribution is determined by the iterative algorithm described in Sec. III B.

B. Gallery of microtrap arrays

Figure 2 presents a selection of 2D trap arrays that we have created with the setup described above. For each array, we show the phase pattern $\varphi(x, y)$ used to create it, an image of the array obtained with the diagnostics CCD camera behind the chamber, and the average of approximately 1000 images of the atomic fluorescence of single atoms in the traps (imaged with the EMCCD camera). The figure illustrates strikingly the versatility of the setup. We can create small clusters containing approximately 10 traps, useful for the study of mesoscopic systems [Figs. 2(a)–2(h)]. It is also possible to create larger, regular lattices of up to approximately 100 traps with varying degrees of complexity, from simple square [Fig. 2(i)] or triangular [Fig. 2(j)] lattices to honeycomb [Fig. 2(k)] or kagome [Fig. 2(l)] structures, which opens, for instance, the possibility to simulate frustrated quantum magnetism with Rydberg-interacting atoms. The typical nearest-neighbor distance a in those arrays is 4 to 5 μm . We have also created arrays with spacings as small as $a \approx 3$ μm without observing a significant degradation in the quality of the arrays. Other configurations, e.g., aperiodic structures, can be generated easily.

The total power needed to create an array of N microtraps with a depth $U_0/k_B \approx 1$ mK necessary for single-atom trapping is about $3N$ mW on the atoms. Because of the finite diffraction efficiency of the SLM and losses on various optical components, we find that this needed power requires us to have slightly below $5N$ mW at the output of the fiber guiding the 850-nm light to the experiment, which remains a very reasonable requirement even for $N = 100$ traps.

C. Single-atom trapping in the arrays

We now demonstrate directly single-atom trapping in a 3×3 square array [see Fig. 3(a)]. Figure 3(b) shows a series of snapshots obtained with the EMCCD camera (the exposure time being 50 ms), showing fluorescence images of single atoms. As each of the $N = 9$ traps has a probability $p \sim 1/2$ of containing one atom, we observe that most images correspond to a sparsely loaded array, with an average number of atoms present close to $Np = 9/2$ and fluctuations corresponding to atoms randomly entering and leaving each trap. To confirm that these images do correspond to single-atom trapping, we plot the photon counts per 50 ms in the pixels corresponding to the positions of each of the nine traps as a function of time [see Fig. 3(c)]. One observes the characteristic random telegraphlike signal, with only two fluorescence levels, which is the hallmark of single atoms loaded into the microtraps by the collisional blockade mechanism [3,25].

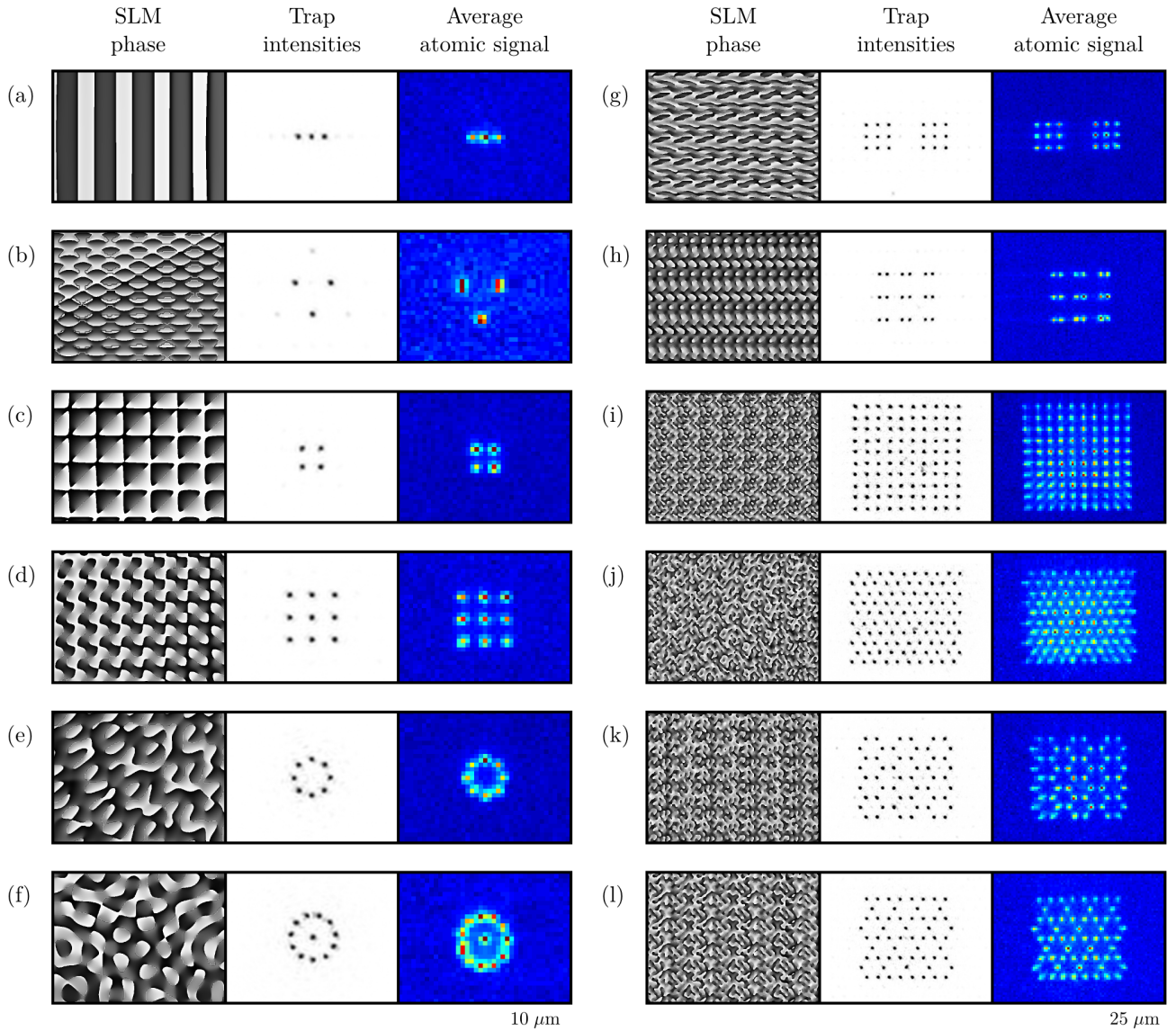


FIG. 2. A gallery of microtrap arrays with different geometries. For each panel, we show the calculated phase pattern φ used to create the array (left), an image of the resulting trap arrays taken with the diagnostics CCD (middle), and the average of approximately 1000 fluorescence images of single atoms loaded into the traps (right).

By analyzing each of the nine traces, we find that the occupation probability p_i of each trap i is close to $1/2$. (We find probabilities p_i ranging from 0.43 to 0.57, with an average $\bar{p} = 0.53$.)

Figure 3(d) is a histogram of the number of atoms trapped in the 3×3 array, obtained by analyzing approximately 2500 images [23]. For an array of N independent traps, if each trap has the same probability p to be filled, the probability P_n to have n atoms in the array is given by the binomial distribution

$$P_n = \frac{N!}{n!(N-n)!} p^n (1-p)^{N-n}. \quad (1)$$

The dots in Fig. 3(d) correspond to Eq. (1) with $N = 9$ and $p = \bar{p}$ and show good agreement with the data. Therefore, the assumption that all traps are loaded with the same probability is a good approximation for estimating the probability of a given configuration to occur.

III. DETAILED IMPLEMENTATION

In the preceding section, we focused on giving a detailed presentation of the results obtained. However, obtaining arrays of traps with as high a quality as what is demonstrated in Figs. 2 and 3 requires some care in the implementation of the setup. In this section, we detail the implementation of both the hardware and the software parts of the system.

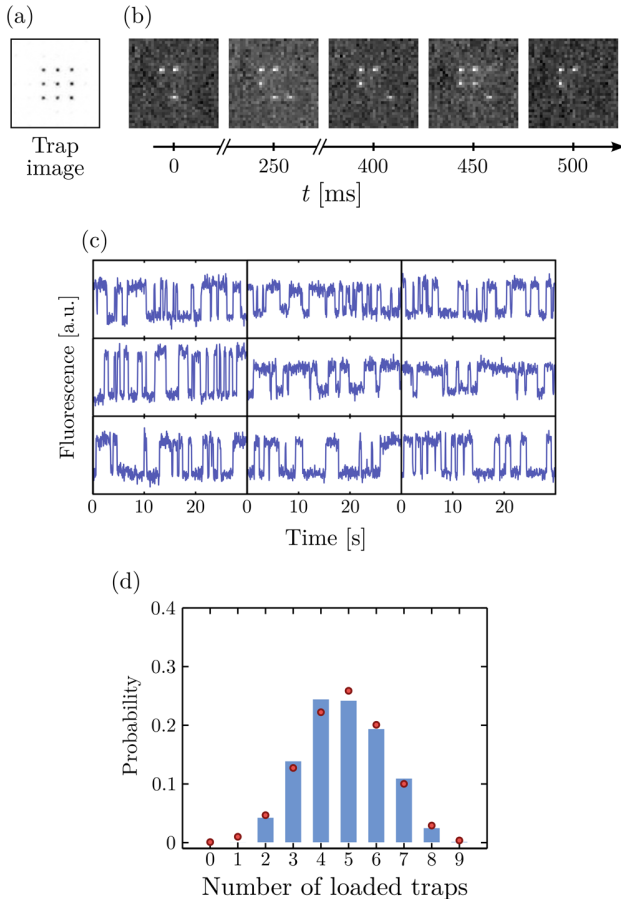


FIG. 3. Single-atom trapping in a 3×3 array. (a) Image of the traps, separated by $4 \mu\text{m}$, obtained with the diagnostics CCD camera. (b) Sample fluorescence images of single atoms trapped in the array. The exposure time is 50 ms. (c) Photon counts per 50 ms at the pixels corresponding to each of the nine trap positions, as a function of time. The random, telegraphlike signal with only two fluorescence levels is the signature of single-atom trapping. (d) Histogram of the occurrences of images with n atoms trapped (with $0 \leq n \leq 9$) over a set of approximately 2500 images. The red dots correspond to the binomial distribution [Eq. (1)] with $p = 0.53$.

A. Optical layout

Our SLM has an active area of $12 \times 18 \text{ mm}^2$, with a resolution of 600×800 pixels. It is illuminated by a collimated Gaussian beam with a 6.7-mm $1/e^2$ radius coming from a polarization-maintaining, single-mode fiber connected to a collimator with a focal length $f = 75 \text{ mm}$. As diffraction-limited operation of the aspheric lens is obtained for an infinite-to-focus conjugation, with a pupil diameter $D = 10 \text{ mm}$, we use an afocal telescope with a transverse magnification $m_y = -0.8$ to adapt the SLM active area to the aspheric lens aperture, while maintaining the collimation of the beam.

The implementation of the full system (vacuum chamber, dichroic mirror for fluorescence detection, components for generating the microtrap array) results in a relatively long

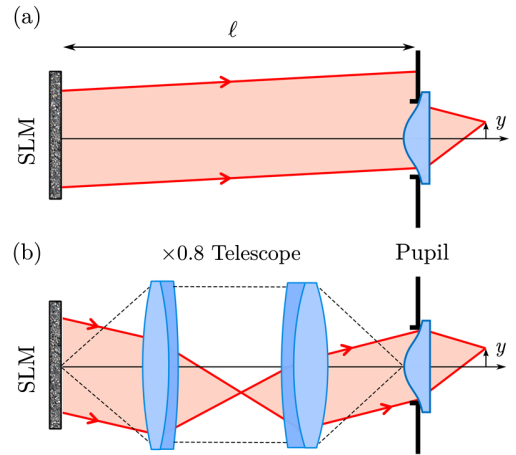


FIG. 4. Pupil conjugation. (a) Without a telescope, for a given field $y \neq 0$, the dipole-trap beam is clipped and not centered on the aspheric lens. (b) The implemented telescope adapts the size of the beam to the aspheric lens pupil; by conjugating the SLM aperture to the entrance pupil of the aspheric lens, the beam is well centered, whatever the field.

distance ($\ell \approx 500 \text{ mm}$) between the SLM and the aspheric lens. This leads to the following problem [see Fig. 4(a)]: When generating off-axis traps, the beam diffracted by the SLM impinges on the lens off center, giving rise to clipping and field aberrations. These effects decrease the quality of arrays with a large number of microtraps. We circumvent this problem using pupil conjugation: We take advantage of the extra degree of freedom given by the position of the telescope to conjugate the plane of the SLM with the aspheric lens, as shown in Fig. 4(b).

The optimization of the system is done with an optical design software. The simulation includes all the components from the optical fiber to the focal plane of the aspheric lens in the vacuum chamber. The lenses of the telescope and the lens of the collimator are near-infrared achromatic doublets used at low numerical aperture and small fields. The performance of the system over a field of $30 \times 30 \mu\text{m}^2$ in the microtrap plane is satisfactory: The Strehl ratio, i.e., the ratio of the actual peak intensity over the theoretical peak intensity for a diffraction-limited system [29], is predicted to be $S \geq 0.88$ by the calculation.

For the phase-pattern calculation described below, we replace the telescope and the aspheric lens by a single equivalent lens with an effective focal length $f_{\text{eff}} = f_{\text{asph}}/|m_y| = 12 \text{ mm}$ and an effective pupil in the SLM plane with diameter $D_{\text{eff}} = 12 \text{ mm}$.

B. Gerchberg-Saxton algorithm

We use the Gerchberg-Saxton (GS) algorithm [30] to calculate the phase pattern $\varphi(x, y)$ required to obtain an intensity distribution in the lens focal plane close to a desired target intensity I_t . For the sake of completeness, we briefly recall below the essential steps of the algorithm (see Fig. 5).

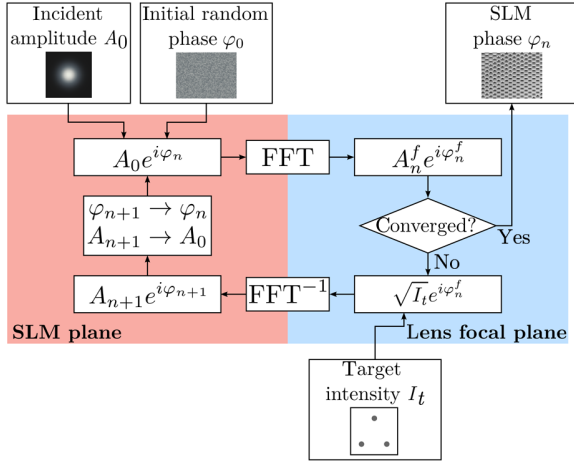


FIG. 5. The Gerchberg-Saxton algorithm. The field in the lens focal plane is calculated by the FFT of the complex field in the SLM plane. If the obtained intensity $|A_n^f|^2$ does not match the target intensity I_t , another iteration must be performed: The amplitude of the field in the focal plane is forced to the target amplitude $\sqrt{I_t}$, and this new field is propagated back to the pupil plane by the inverse FFT, resulting in a new amplitude and a new phase φ_{n+1} . This new phase is kept as the next SLM phase pattern, while the amplitude is forced to the incident one A_0 , giving a new input field $A_0 e^{i\varphi_{n+1}}$ for the next iteration.

We initialize the algorithm using a random phase pattern φ_0 in which each pixel value is given by a uniformly distributed random variate in the range $(0, 0.2) \times 2\pi$. The target image I_t is a superposition of Gaussian peaks with $1/e^2$ radii $w = 1 \mu\text{m}$ centered on the desired location of the microtraps. The amplitude of each Gaussian can be defined separately, which allows for correcting nonuniformities in the depths of the microtraps over the array (see Sec. III E).

The incident field on the SLM is modeled as having a uniform phase and an amplitude $A_0(x, y)$. At each iteration of the algorithm, we propagate the electric field in the SLM plane $A_0 e^{i\varphi_n}$ through the effective lens using a fast Fourier transform (FFT) to calculate the field $A_n^f e^{i\varphi_n^f}$ in the focal plane. If the difference between the calculated intensity $|A_n^f|^2$ and the desired target image I_t is small enough, the phase pattern φ_n is used to drive the SLM; otherwise, the amplitude of the field in the focal plane is replaced by the target amplitude $\sqrt{I_t}$. This new field $\sqrt{I_t} e^{i\varphi_n^f}$ is then propagated back to the SLM plane by an inverse FFT,

giving the field $A_{n+1} e^{i\varphi_{n+1}}$ in the SLM plane. The calculated phase φ_{n+1} is kept as the new phase pattern in the SLM plane, while the amplitude is replaced by the incident one A_0 , and another iteration is performed for the field $A_0 e^{i\varphi_{n+1}}$. For the patterns shown in Fig. 2, the algorithm converges (i.e., the calculated phase patterns do not evolve any more) toward an approximate solution, typically after a few tens of iterations [31]. The intensity distribution in the lens focal plane is then a good approximation of I_t . However, we can approach the target even closer, as described in Sec. III E.

C. Phase patterns displayed on the SLM

The phase pattern φ_{tot} used to drive the SLM includes several contributions beyond the calculated phase pattern φ and reads

$$\varphi_{\text{tot}} = \varphi + \varphi_{\text{blaze}} + \varphi_{\text{Fresnel}} + \varphi_{\text{factory}} + \varphi_{\text{SH}}, \quad (2)$$

where the sum is calculated modulo 2π . In this equation,

(i) φ_{blaze} is a blazed grating pattern, allowing us to block the zeroth-order reflection from the SLM arising from its nonperfect diffraction efficiency;

(ii) φ_{Fresnel} is a quadratic phase pattern acting as a Fresnel lens, which allows us to fine-tune the focusing of the microtraps;

(iii) φ_{factory} is the correction phase pattern provided by the SLM manufacturer to correct for the optical flatness defects of the SLM chip; and

(iv) φ_{SH} corrects for aberrations introduced by the setup and is obtained using a Shack-Hartmann wave-front sensor as described in Sec. III D below.

Figure 6 gives an example of the composition of the final phase pattern obtained by summing (modulo 2π) the various terms described above.

D. Improving the traps by analyzing the wave front and correcting for aberrations using the SLM

Without the last term of Eq. (2), we observe that the quality of the obtained microtrap arrays decreases when the number of traps increases. Indeed, the assumption of a perfect effective lens used in the calculation of the hologram is not valid. The imperfections of the optics (vacuum windows, aspheric lens, etc.) and the residual misalignments distort the wave front, thus reducing the depth of the microtraps.

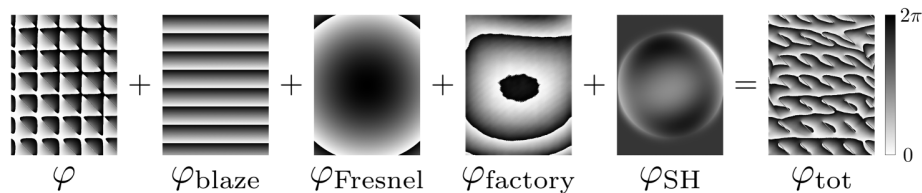


FIG. 6. Composition of the phase pattern φ_{tot} displayed on the SLM for generating the trap array of Fig. 2(c). The sum is calculated modulo 2π .

1. Wave-front measurement

In order to correct for the above-mentioned imperfections, we measure the wave front with a Shack-Hartmann sensor and use the resulting φ_{SH} to drive the SLM [32]. We perform this measurement at the exit of the vacuum chamber, where the trapping beam has been recollimated by the second aspheric lens (see Fig. 1). The wave-front sensor [33] analyzes the wave front corresponding to a single trap centered in the field where the phase pattern displayed on the SLM is $\varphi_{\text{blaze}} + \varphi_{\text{factory}}$. The measured rms deviation from a flat wave front is $\delta_{\text{rms}} = 0.15\lambda$ (tilt and focus terms being removed). After applying the correction phase φ_{SH} to the SLM, we measure $\delta_{\text{rms}} = 0.014\lambda$. Figure 7 illustrates the impact of the phase corrections on the trap pattern (as measured by the diagnostics CCD camera) for a 4×4 array: A comparison between Figs. 7(a) and 7(b) suggests that the correction increases the trap depth by a factor close to 2.

This wave-front measurement includes the aberrations induced by the recollimating aspheric lens and the second vacuum window (see Fig. 1). An independent wave-front measurement on the trapping beam before the chamber yields $\delta_{\text{rms}} = 0.05\lambda$ without correction, showing that the optics of the vacuum chamber account for most of the wave-front aberrations. Applying directly the measured φ_{SH} on the SLM thus “overcorrects” aberrations, and one might fear that at the location of the atoms, the effect of the correction is actually detrimental. It is therefore desirable to check directly the actual effect of the correction on the

atoms. For this purpose, we directly measure the trap depth and frequency with single atoms.

2. Impact on the trap depth

We measure the trap depth using light-shift spectroscopy with a single atom [34,35]. For that, we shine a σ^+ -polarized probe that is quasiresonant with the transition $|5S_{1/2}, F=2, m_F=2\rangle \rightarrow |5P_{3/2}, F=3, m_F=3\rangle$ on the atom and we record the number of fluorescence photons scattered by the atom as a function of probe detuning. The shift of the resonance with respect to its free-space value gives directly the trap depth U_0 [36]. Figure 8(a), obtained on the central trap of a 3×1 array with a $4\text{-}\mu\text{m}$ separation, shows that including the Shack-Hartmann correction actually increases the trap depth by about 50%.

3. Impact on the trap frequency

Another important parameter of the trap is the trapping frequency. In order to determine the transverse trapping frequency seen by the atoms, we excite the breathing mode, as in Refs. [25,37]. For that purpose, the microtrap is switched off for a few microseconds, during which the atom leaves the center of the trap. When the trap is switched on again for a time ΔT_{hold} , the atom oscillates in the trap, with a radial frequency ω_r [38]. If the trap is then switched off again for a short time, the probability to recapture the atom afterward depends on its kinetic energy at the time of the last switch-off, and thus oscillates at $2\omega_r$.

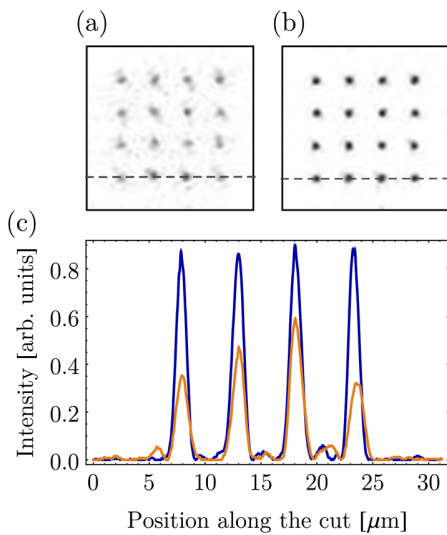


FIG. 7. Effect of the Shack-Hartmann correction pattern φ_{SH} . A CCD image of 4×4 microtraps is shown (a) only with the factory correction and (b) with both the factory and the Shack-Hartmann patterns applied. (c) Intensity profiles along the dashed lines on (a) and (b), with (blue curve) and without (orange curve) the correction φ_{SH} . The arrays are created with the same calculated phase φ . The laser power and the exposure time of the CCD camera are the same for both cases.

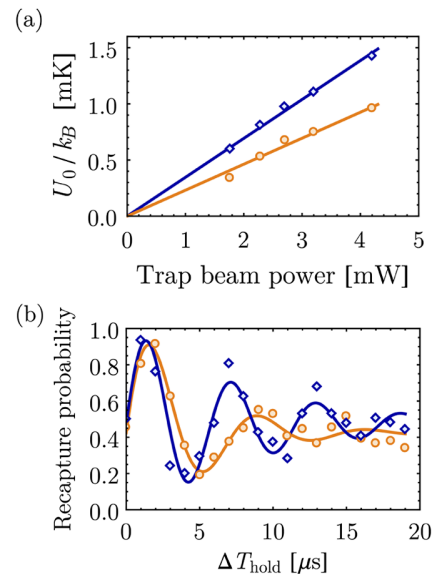


FIG. 8. (a) Trap depth U_0/k_B as a function of the trap power, with (blue diamonds) and without (orange disks) Shack-Hartmann correction. With the latter, the trap depth increases by about 50%. (b) Recapture probabilities for an atom oscillating in the trap as a function of the hold time ΔT_{hold} . The trap frequency increases by about 30% when the Shack-Hartmann correction pattern is added to the SLM.

Figure 8(b) shows the results of such a measurement, for a power of 2.8 mW per trap, again in the 3×1 array. The measured trap frequencies are $\omega_r = 2\pi \times 68.0$ kHz before correction and $\omega_r = 2\pi \times 86.5$ kHz with the Shack-Hartmann correction applied to the SLM. The increase in trapping frequency comes essentially from the increased depth of the corrected traps.

Using the single atom as a diagnostics tool, we could, in principle, test whether one can improve even further the trap quality by applying to the SLM a phase $\alpha\varphi_{\text{SH}}$ (where $0 \leq \alpha \leq 1$ is an adjustable parameter), in the hope of correcting only the aberrations “seen” by the atom, i.e., not the aberrations induced by the second lens and the second viewport. A test for $\alpha = 1/2$ (which would yield the best correction if both lenses and windows introduce equal aberrations) gives results slightly worse than for $\alpha = 1$, and in the following, we thus keep this choice.

E. Closed-loop optimization of the uniformity of the trap depths in the array

An important figure of merit to assess the quality of the arrays is the uniformity of the trap depths. Figure 9(a)

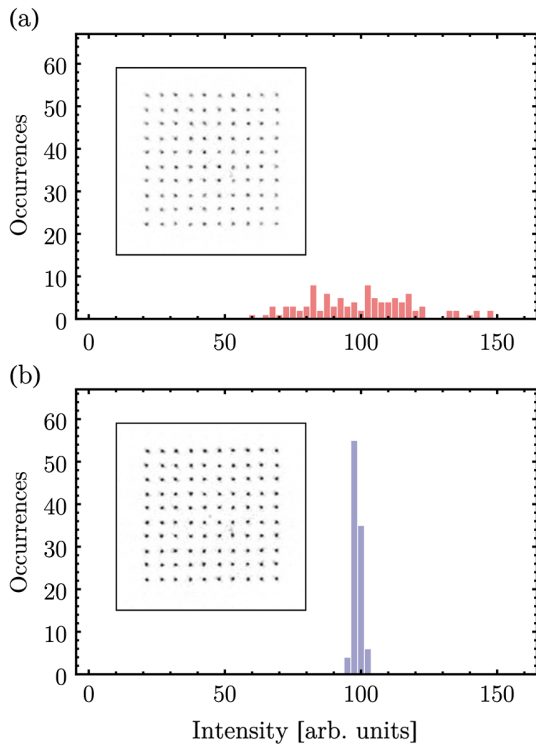


FIG. 9. Improving the uniformity of trap depths in a 10×10 square array. (a) Histogram of the maximal intensity levels of the microtraps I_i , measured with the diagnostics CCD camera (see the inset), for the trap array obtained after a single use of the GS algorithm and a target image where all traps have the same intensity. The standard deviation is 19%. (b) Same as (a) but after the closed-loop optimization of the uniformity of the trap intensities. The standard deviation is now 1.4%.

shows the distribution of the trap intensities, inferred from an analysis of an image of the array obtained with the diagnostics CCD camera, for a 10×10 square lattice with a spacing $a = 4 \mu\text{m}$. In this case, the phase applied to the SLM is obtained by running the GS algorithm with a target image I_t for which all traps have the same intensity. One observes a dispersion in the trap depths of $\pm 19\%$ rms (the minimal and maximal values being $I_{\min} = 61$ and $I_{\max} = 148$, where the average intensity of all traps is normalized to $\bar{I} = 100$). This variation in trap depths is detrimental for loading optimally the trap array with single atoms. Indeed, if the trap depth is too low, one still traps single atoms, but with a probability of occupancy significantly lower than $1/2$. Conversely, if the trap is too deep, one enters a regime in which the probability to have more than one atom is not negligible [36].

A way to compensate for this imperfection is to use the image of the trap array obtained with the diagnostics CCD to calculate a new target image where the new trap intensity I'_i of trap i is scaled according to the measured one I_i as

$$I'_i = \frac{\bar{I}}{1 - G(1 - I_i/\bar{I})}, \quad (3)$$

where \bar{I} is the average intensity of all traps and G an adjustable “gain.” In other words, traps that are too weak get enhanced in the new target image, while the brightest ones get dimmed. We then run again the GS algorithm with this new target image as an input and with the previously obtained phase pattern φ as the initial guess for the phase (see Fig. 10). We observe that the distribution of the trap intensities decreases quite drastically after a few iterations. Choosing $G \approx 0.7$ gives the best performance. (Lower values decrease the convergence speed, while higher values yield overshoots in the correction.) Figure 9(b) shows the

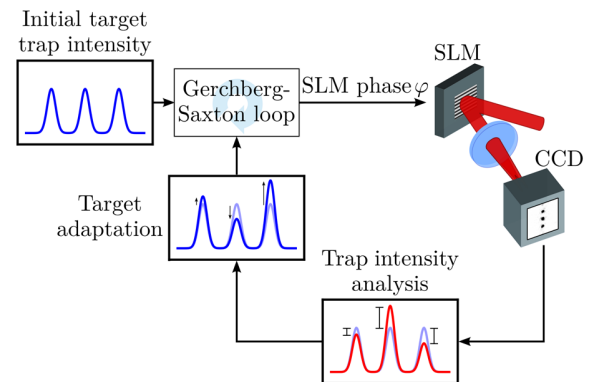


FIG. 10. Closed-loop algorithm used for improving the uniformity of trap depths. From the various trap intensities measured with the CCD camera (red profile), we calculate a new target intensity I_t following Eq. (3): The brightest traps are dimmed, while the dimmest ones are enhanced. We then use this adapted target as the input for a new iteration of the GS algorithm, with the previously calculated phase as the initial condition.

resulting histogram of trap intensities for the 10×10 square lattice, after 20 iterations. The array is now very uniform, with trap intensities varying between 96% and 103% of \bar{I} (peak to peak). This improvement corresponds to a 15-fold reduction in the dispersion of the trap depths.

The single-atom trapping demonstrated in the arrays of Figs. 2 and 3 could be achieved only after this closed-loop optimization is implemented and illustrates strikingly the efficiency of the method. We believe that such an optimization, which takes full advantage of the reconfigurable character of the SLM, could prove useful in order to create very uniform lattices with arbitrary structures for quantum simulation with ultracold atoms.

IV. CONCLUSION AND OUTLOOK

The simple setup described above is a versatile tool for creating arrays of microtraps with almost arbitrary geometries. We have demonstrated single-atom loading in such arrays, which opens exciting possibilities to engineer interesting few-atom entangled states using, e.g., a Rydberg blockade [39], especially in combination with dynamical addressability using moving optical tweezers [40].

For arrays with a large number of traps, a current limitation of the system is the nondeterministic character of the single-atom loading of the microtraps: As each trap has a probability $1/2$ of being filled with an atom, an N -trap array has, at any given time, only an exponentially small probability $1/2^N$ to be fully loaded. Implementing quasi-deterministic loading schemes will thus be needed to take full advantage of the setup, which implies increasing the loading probability p per trap beyond $1/2$. A first approach toward this goal consists in using the Rydberg blockade: Loading probabilities of $p \sim 60\%$ have been recently demonstrated in a single microtrap [41]. Alternatively, using a blue-detuned “collision beam,” relatively high loading probabilities, already in excess of 90%, have been achieved [42]. This scheme opens the possibility to fully load an array of 20 traps with a probability of more than 10%. Testing both approaches on our setup will be the subject of future work.

In combination with the recently demonstrated Raman-sideband cooling of single atoms trapped in optical tweezers [43,44], a similar system with smaller distances between microtraps—which could be achieved using high-numerical-aperture objectives such as the ones used in quantum-gas microscopes [45]—could then become an interesting alternative approach to study the many-body physics of ultracold atoms in engineered optical potentials, without using traditional optical lattices [46].

ACKNOWLEDGMENTS

We thank Yvan Sortais for invaluable advice about the optical design and for a careful reading of the manuscript, André Guilbaud for technical assistance, and Bruno Viaris,

Laurence Pruvost, and Zoran Hadzibabic for fruitful discussions. We are grateful to Lionel Jacubowicz, Thierry Avignon, and Samuel Bucourt for the loan of Imagine Optic Shack-Hartmann wave-front sensors. This work was supported financially by the EU [ERC Stg Grant ARENA, AQUOTE Integrating Project, FET-Open Xtrack Project HAIRS, and EU Marie-Curie Program ITN COHERENCE FP7-PEOPLE-2010-ITN-265031 (H. L.)], by the DGA (L. B.), and by Région Île-de-France (LUMAT and Triangle de la Physique, LAGON Project).

-
- [1] R. Grimm, M. Weidemüller, and Yu. B. Ovchinnikov, *Optical Dipole Traps for Neutral Atoms*, *Adv. At. Mol. Opt. Phys.* **42**, 95 (2000).
 - [2] M. Lewenstein, A. Sampera, and V. Ahufinger, *Ultracold Atoms in Optical Lattices: Simulating Quantum Many-Body Systems* (Oxford University Press, Oxford, England, 2012).
 - [3] N. Schlosser, G. Reymond, I. Protsenko, and P. Grangier, *Sub-Poissonian Loading of Single Atoms in a Microscopic Dipole Trap*, *Nature (London)* **411**, 1024 (2001).
 - [4] G. Cennini, G. Ritt, C. Geckeler, and M. Weitz, *Bose-Einstein Condensation in a CO₂-Laser Optical Dipole Trap*, *Appl. Phys. B* **77**, 773 (2003).
 - [5] M. D. Barrett, J. A. Sauer, and M. S. Chapman, *All-Optical Formation of an Atomic Bose-Einstein Condensate*, *Phys. Rev. Lett.* **87**, 010404 (2001).
 - [6] R. Dumke, M. Volk, T. Müther, F. B. J. Buchkremer, G. Birkl, and W. Ertmer, *Micro-optical Realization of Arrays of Selectively Addressable Dipole Traps: A Scalable Configuration for Quantum Computation with Atomic Qubits*, *Phys. Rev. Lett.* **89**, 097903 (2002).
 - [7] M. Schlosser, S. Tichelmann, J. Kruse, and G. Birkl, *Scalable Architecture for Quantum Information Processing with Atoms in Optical Microstructures*, *Quantum Inf. Process.* **10**, 907 (2011).
 - [8] R. Newell, J. Sebby, and T. G. Walker, *Dense Atom Clouds in a Holographic Atom Trap*, *Opt. Lett.* **28**, 1266 (2003).
 - [9] I. Bloch, *Ultracold Quantum Gases in Optical Lattices*, *Nat. Phys.* **1**, 23 (2005).
 - [10] K. D. Nelson, X. Li, and D. S. Weiss, *Imaging Single Atoms in a Three-Dimensional Array*, *Nat. Phys.* **3**, 556 (2007).
 - [11] J. Billy, V. Josse, Z. Zuo, A. Bernard, B. Hambrecht, P. Lugan, D. Clément, L. Sanchez-Palencia, P. Bouyer, and A. Aspect, *Direct Observation of Anderson Localization of Matter Waves in a Controlled Disorder*, *Nature (London)* **453**, 891 (2008).
 - [12] F. K. Fatemi, M. Bashkansky, and Z. Dutton, *Dynamic High-Speed Spatial Manipulation of Cold Atoms Using Acousto-optic and Spatial Light Modulation*, *Opt. Express* **15**, 3589 (2007).
 - [13] K. Henderson, C. Ryu, C. MacCormick, and M. G. Boshier, *Experimental Demonstration of Painting Arbitrary and Dynamic Potentials for Bose-Einstein Condensates*, *New J. Phys.* **11**, 043030 (2009).
 - [14] A. L. Gaunt and Z. Hadzibabic, *Robust Digital Holography for Ultracold Atom Trapping*, *Sci. Rep.* **2**, 721 (2012).

- [15] A. L. Gaunt, T. F. Schmidutz, I. Gotlibovych, R. P. Smith, and Z. Hadzibabic, *Bose-Einstein Condensation of Atoms in a Uniform Potential*, *Phys. Rev. Lett.* **110**, 200406 (2013).
- [16] V. Boyer, C. M. Chandrashekar, C. J. Foot, and Z. J. Laczik, *Dynamic Optical Trap Generation Using FLC SLMs for the Manipulation of Cold Atoms*, *J. Mod. Opt.* **51**, 2235 (2004).
- [17] S. Bergamini, B. Darquié, M. Jones, L. Jacubowicz, A. Browaeys, and P. Grangier, *Holographic Generation of Microtrap Array for Single Atoms by Use of a Programmable Phase Modulator*, *J. Opt. Soc. Am. B* **21**, 1889 (2004).
- [18] M. Saffman, T. Walker, and K. Mølmer, *Quantum Information with Rydberg Atoms*, *Rev. Mod. Phys.* **82**, 2313 (2010).
- [19] E. Urban, T. A. Johnson, T. Henage, L. Isenhower, D. D. Yavuz, T. G. Walker, and M. Saffman, *Observation of Rydberg Blockade between Two Atoms*, *Nat. Phys.* **5**, 110 (2009).
- [20] A. Gaëtan, Y. Miroshnychenko, T. Wilk, A. Chotia, M. Viteau, D. Comparat, P. Pillet, A. Browaeys, and P. Grangier, *Observation of Collective Excitation of Two Individual Atoms in the Rydberg Blockade Regime*, *Nat. Phys.* **5**, 115 (2009).
- [21] L. Béguin, A. Vernier, R. Chicireanu, T. Lahaye, and A. Browaeys, *Direct Measurement of the van der Waals Interaction between Two Rydberg Atoms*, *Phys. Rev. Lett.* **110**, 263201 (2013).
- [22] D. Barredo, S. Ravets, H. Labuhn, L. Béguin, A. Vernier, F. Nogrette, T. Lahaye, and A. Browaeys, *Demonstration of Strong Rydberg Blockade in Three-Atom Systems with Anisotropic Interactions*, *Phys. Rev. Lett.* **112**, 183002 (2014).
- [23] M. J. Piotrowicz, M. Lichtman, K. Maller, G. Li, S. Zhang, L. Isenhower, and M. Saffman, *Two-Dimensional Lattice of Blue-Detuned Atom Traps Using a Projected Gaussian Beam Array*, *Phys. Rev. A* **88**, 013420 (2013).
- [24] I. Bloch, J. Dalibard, and S. Nascimbène, *Quantum Simulations with Ultracold Quantum Gases*, *Nat. Phys.* **8**, 267 (2012).
- [25] Y. R. P. Sortais, H. Marion, C. Tuchendler, A. M. Lance, M. Lamare, P. Fournet, C. Armellin, R. Mercier, G. Messin, A. Browaeys, and P. Grangier, *Diffraction Limited Optics for Single Atom Manipulation*, *Phys. Rev. A* **75**, 013406 (2007).
- [26] We use a D-ZLaF52LA aspheric lens from LightPath technologies. It is optimized at 780 nm for an infinite-to-focus conjugation with a numerical aperture $NA = 0.54$. When used at 850 nm, its performance is maintained for a reduced aperture $NA = 0.44$, i.e., $D = 10$ mm.
- [27] We use a Andor iXon Ultra, which can be used in an EMCCD mode. However, due to the relatively high photon yield (approximately 300 photons per 50-ms time bin), here, we do not need to use the electron multiplier to detect single atoms.
- [28] Reflective liquid crystal on silicon, Hamamatsu X10468-02.
- [29] H. Gross, *Handbook of Optical Systems* (Wiley-VCH, Weinheim, 2007), Vol. 3.
- [30] R. W. Gerchberg and W. O. Saxton, *A Practical Algorithm for the Determination of Phase from Image and Diffraction Plane Pictures*, *Optik (Stuttgart)* **35**, 237 (1972).
- [31] We have implemented the algorithm using MATLAB. Without any attempt to optimize the code, convergence takes less than one minute on a personal computer.
- [32] C. López-Quesada, J. Andilla, and E. Martín-Badosa, *Correction of Aberration in Holographic Optical Tweezers Using a Shack-Hartmann Sensor*, *Appl. Opt.* **48**, 1084 (2009).
- [33] We use a HASO4 First from Imagine Optic.
- [34] M. K. Tey, Z. Chen, S. A. Aljunid, B. Chng, F. Huber, G. Maslennikov, and C. Kurtsiefer, *Strong Interaction between Light and a Single Trapped Atom without the Need for a Cavity*, *Nat. Phys.* **4**, 924 (2008).
- [35] C. Y. Shih and M. S. Chapman, *Nondestructive Light-Shift Measurements of Single Atoms in Optical Dipole Traps*, *Phys. Rev. A* **87**, 063408 (2013).
- [36] L. Béguin, Ph.D. thesis, Institut d'Optique Graduate School, 2013.
- [37] H. Engler, T. Weber, M. Mudrich, R. Grimm, and M. Weidemüller, *Very Long Storage Times and Evaporative Cooling of Cesium Atoms in a Quasielectrostatic Dipole Trap*, *Phys. Rev. A* **62**, 031402 (2000).
- [38] The longitudinal confinement is much weaker than in the radial direction, so for short switch-off times, the longitudinal motion of the atom is only weakly excited.
- [39] M. Müller, I. Lesanovsky, H. Weimer, H. P. Büchler, and P. Zoller, *Mesoscopic Rydberg Gate Based on Electromagnetically Induced Transparency*, *Phys. Rev. Lett.* **102**, 170502 (2009).
- [40] J. Beugnon, C. Tuchendler, H. Marion, A. Gaëtan, Y. Miroshnychenko, Y. R. P. Sortais, A. M. Lance, M. P. A. Jones, G. Messin, A. Browaeys, and P. Grangier, *Two-Dimensional Transport and Transfer of a Single Atomic Qubit in Optical Tweezers*, *Nat. Phys.* **3**, 696 (2007).
- [41] M. Ebert, A. Gill, M. Gibbons, X. Zhang, M. Saffman, and T. G. Walker, *Atomic Fock State Preparation Using Rydberg Blockade*, *Phys. Rev. Lett.* **112**, 043602 (2014).
- [42] A. V. Carpentier, Y. H. Fung, P. Sompert, A. J. Hilliard, T. G. Walker, and M. F. Andersen, *Preparation of a Single Atom in an Optical Microtrap*, *Laser Phys. Lett.* **10**, 125501 (2013).
- [43] A. M. Kaufman, B. J. Lester, and C. A. Regal, *Cooling a Single Atom in an Optical Tweezer to Its Quantum Ground State*, *Phys. Rev. X* **2**, 041014 (2012).
- [44] J. D. Thompson, T. G. Tiecke, A. S. Zibrov, V. Vuletić, and M. D. Lukin, *Coherence and Raman Sideband Cooling of a Single Atom in an Optical Tweezer*, *Phys. Rev. Lett.* **110**, 133001 (2013).
- [45] W. S. Bakr, J. I. Gillen, A. Peng, S. Foelling, and M. Greiner, *A Quantum Gas Microscope for Detecting Single Atoms in a Hubbard Regime Optical Lattice*, *Nature (London)* **462**, 74 (2009).
- [46] A. M. Kaufman, B. J. Lester, C. M. Reynolds, M. L. Wall, M. Foss-Feig, K. R. A. Hazzard, A. M. Rey, and C. A. Regal, *Hong-Ou-Mandel Atom Interferometry in Tunnel-Coupled Optical Tweezers*, [arXiv:1312.7182](https://arxiv.org/abs/1312.7182).

Single-atom addressing in microtraps for quantum-state engineering using Rydberg atoms

Henning Labuhn, Sylvain Ravets, Daniel Barredo, Lucas Béguin, Florence Nogrette, Thierry Lahaye, and Antoine Browaeys

Laboratoire Charles Fabry, UMR 8501, Institut d'Optique, CNRS, Univ Paris Sud 11,

2 avenue Augustin Fresnel, 91127 Palaiseau cedex, France

(Received 19 June 2014; published 22 August 2014)

We report on the selective addressing of an individual atom in a pair of single-atom microtraps separated by $3\ \mu\text{m}$. Using a tunable light shift, we render the selected atom off-resonant with a global Rydberg excitation laser which is resonant with the other atom, making it possible to selectively block this atom from being excited to the Rydberg state. Furthermore we demonstrate the controlled manipulation of a two-atom entangled state by using the addressing beam to induce a phase shift onto one component of the wave function of the system, transferring it to a dark state for the Rydberg excitation light. Our results are an important step towards implementing quantum information processing and quantum simulation with large arrays of Rydberg atoms.

DOI: [10.1103/PhysRevA.90.023415](https://doi.org/10.1103/PhysRevA.90.023415)

PACS number(s): 37.10.Gh, 32.80.Ee, 03.67.Bg

Cold neutral atoms are a promising platform for quantum computation and quantum simulation [1]. Their weak interactions in the ground state lead to long coherence times. Using highly excited Rydberg states allows one to switch on and off the strong interactions that are necessary for engineering many-body quantum states [2]. For many of those experiments it is desirable to confine single atoms at well-defined positions separated by a few micrometers, which can be achieved, e.g., using arrays of optical tweezers [3]. Another requirement is the selective manipulation of individual atoms in the ensemble. This can be done by applying static field gradients, or a laser beam focused to one single trap site, which induces a frequency shift at the targeted site. Such techniques have been demonstrated with trapped ions [4–6] and neutral atoms in optical lattices [7–13].

In previous work [14,15], we have demonstrated quantum-state engineering with single atoms held in two and three optical microtraps, by using the Rydberg blockade mechanism with global excitation of the atoms. Extending these studies to a larger number of atoms and to wider classes of quantum states requires extra tools. A step towards this goal was our recent demonstration of single-atom trapping in large arrays of optical microtraps with arbitrary geometries [3]. Combined with global excitation, this already opens the possibility to generate interesting multiatom entangled states, such as the W state $|W\rangle = (|rgg\dots g\rangle + |grg\dots g\rangle + \dots + |ggg\dots r\rangle)/\sqrt{N}$, where $|g\rangle$ ($|r\rangle$) corresponds to the ground (Rydberg) state. However, single-site addressing is needed to engineer other classes of quantum states. For instance, the realization of the collective controlled-NOT (CNOT) gate of Ref. [16] that can be used to create the Greenberger-Horne-Zeilinger state $|GHZ\rangle = (|gg\dots g\rangle + |rr\dots r\rangle)/\sqrt{2}$, requires the singling out of one control atom whose state determines the state of the remaining, target, atoms.

Here we demonstrate the selective addressing of one single ^{87}Rb atom among two atoms held in microtraps separated by $3\ \mu\text{m}$, by shining a tightly focused, red-detuned 850-nm laser beam on it. This addressing beam induces a frequency shift on the ground state of the atom, while leaving its Rydberg states nearly unaffected. This differential light shift thus makes the addressed atom off-resonant with the Rydberg excitation laser, which is resonant for the other atom. This

article is organized as follows. We first briefly describe the implementation of the addressing beam, and characterize its size and depth *in situ* using a single atom. We then perform a global Rydberg excitation in the presence of the addressing beam, and observe nearly perfect suppression of excitations for the addressed atom. Finally, we use the addressing beam to perform a controlled local operation on one atom, coherently transferring the symmetric entangled state $(|rg\rangle + |gr\rangle)/\sqrt{2}$ to the antisymmetric, dark state $(|rg\rangle - |gr\rangle)/\sqrt{2}$.

Our experimental setup, schematically shown in Fig. 1(a), has been described previously [3,14,15]. We use a spatial light modulator (SLM) to create two microtraps, separated by a distance of $3\ \mu\text{m}$ in the focal plane of a high-numerical-aperture (NA) aspherical lens. The traps, each with a $1/e^2$ radius of about $1\ \mu\text{m}$ and a depth of $U_0 \approx h \times 20\ \text{MHz}$, are focused in an ^{87}Rb magneto-optical trap (MOT). Due to fast light-assisted collisions, we trap only either zero or one atom per trap [17], and trigger the experiment on the presence of one atom in each trap. The temperature of the atoms in the traps is approximately $50\ \mu\text{K}$. We coherently couple the ground state $|g\rangle = |5S_{1/2}, F=2, m_f=2\rangle$ to the Rydberg state $|r\rangle = |nD_{3/2}, m_j=3/2\rangle$ (with n in the range 50–100) via a two-photon transition, with the wavelengths of the excitation lasers being 795 and 474 nm. During the excitation, of duration τ , the traps are switched off to avoid extra broadening arising from the shot-to-shot fluctuation of the light shift due to the random positions of the atoms in the traps. The detuning from the intermediate state $|5P_{1/2}, F=2, m_f=2\rangle$ is $2\pi \times 740\ \text{MHz}$. After the excitation pulse, we measure the states of both atoms. Repeating the experiment about 100 times, we reconstruct the populations P_{ij} of the two-atom states $|ij\rangle$, where i and j can take the values g and r .

The $1/e^2$ radii of the lasers used for Rydberg excitation are $100\ \mu\text{m}$ for the 795-nm beam, and $18\ \mu\text{m}$ for the 474-nm beam. This configuration prevents the direct addressing of a single trap. To achieve single-site addressability, we thus induce an extra light shift on the ground state of the atom at the targeted site, to selectively control the Rydberg excitation. As a fast (i.e., on microsecond time scales) reconfiguration cannot be achieved with the SLM, we superimpose a second, independently controlled 850-nm laser beam onto the trapping beam. Orthogonal polarizations and a frequency difference of

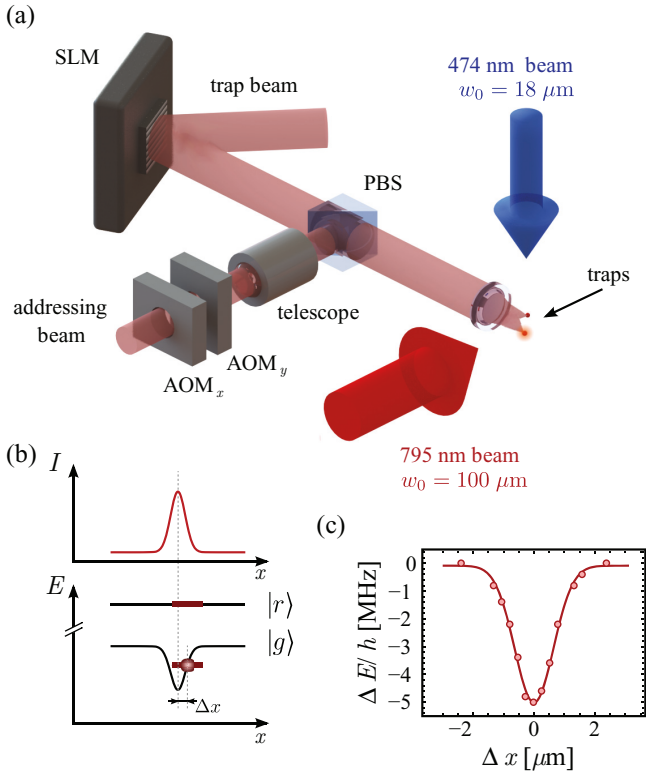


FIG. 1. (Color online) (a) Sketch of the experimental setup. The two microtraps are created by a red-detuned 850-nm laser beam on which an appropriate phase is imprinted using a spatial light modulator (SLM), and focused by a high-NA aspheric lens in a MOT. The addressing beam is superimposed onto the trap beam by a polarizing beam-splitter cube (PBS), and focused down on the targeted atom by the same aspheric lens. The two perpendicular AOMs can be used for precise dynamical x - y positioning of the addressing beam. A telescope is used to conjugate the AOM plane with the aspheric lens, to avoid clipping when the addressing beam is deflected. (b) The light shift ΔE of the ground state of the targeted single atom is directly proportional to the intensity I of the addressing beam at the position x of the atom. (c) Measured light shift ΔE as a function of the distance Δx between the addressing beam and the targeted trap, yielding a $1/e^2$ radius of the addressing beam of $w_0 \simeq 1.3 \mu\text{m}$.

about 200 MHz prevent interference between the trapping and addressing beams. The addressing beam has a $1/e^2$ radius of $w_0 \simeq 1.3 \mu\text{m}$ in the focus, slightly larger than the trap size. This choice results from a trade-off between two opposite requirements, namely, minimizing alignment sensitivity and inhomogeneous light shifts (which favors a large w_0) and minimizing cross-talk (which implies choosing a small w_0). For a perfectly Gaussian beam with $w_0 \simeq 1.3 \mu\text{m}$, one expects theoretically that if one atom is addressed by a light shift of 10 MHz, the second atom $3 \mu\text{m}$ away experiences a light shift of only 0.2 kHz, which is negligible as compared to the other relevant frequencies in the experiment. An electro-optic modulator enables fast (about 10 ns) switching of the addressing beam. In addition, two acousto-optic modulators (AOMs) can be used for dynamical x - y positioning of the addressing beam with respect to the targeted trap.

In a first experiment, we measure the intensity profile of the addressing beam *in situ* by performing Rydberg spectroscopy on a single atom. For different positions Δx of the addressing beam with respect to the targeted atom, we scan the frequency of the Rydberg excitation lasers. As mainly the ground state experiences a light shift ΔE proportional to the addressing beam intensity, the resonance frequency for Rydberg excitation is shifted by ΔE [see Fig. 1(b)]. Figure 1(c) shows the measured light shift as a function of Δx . A Gaussian fit gives a $1/e^2$ radius $w_0 = 1.3 \pm 0.1 \mu\text{m}$. The residual light shift experienced by the nearby atom $3 \mu\text{m}$ away is below the resolution of our experiment.

We observe that for large light shifts, the probability of losing an atom during the sequence increases. We attribute this effect to the following: due to the finite temperature, the atom never sits exactly at the intensity maximum of the addressing beam. The fast switching on and off of the addressing beam thus imparts kinetic energy to the atom. This increase in kinetic energy becomes more and more important as the intensity of the addressing beam gets larger. For large enough intensities in the addressing beam, this effect thus increases the probability for the atom to leave the trapping region during the experiment. However, for light shifts below 40 MHz, this loss probability remains below 1%, and is thus negligible.

We now perform a Rydberg blockade experiment with two single atoms in order to demonstrate single-site addressability (Fig. 2). In Ref. [18], site-resolving excitation beams were used to demonstrate blockade with two atoms separated by $10 \mu\text{m}$. Here, we use a global excitation scheme in combination with the addressing beam, and obtain similar results, albeit with a distance between the atoms of only $3 \mu\text{m}$. For both atoms, the ground state $|g\rangle$ is coupled to the Rydberg state $|r\rangle = |59D_{3/2}\rangle$ with a Rabi frequency $\Omega \simeq 2\pi \times 1 \text{ MHz}$ [Fig. 2(a)]. If the atoms were independent, they would both undergo Rabi oscillations between $|g\rangle$ and $|r\rangle$ with the Rabi frequency Ω . The strong dipole-dipole interaction U_{dd} between the Rydberg states forbids a double excitation of the atoms if $U_{dd} \gg \hbar\Omega$. This condition is largely fulfilled for the parameters chosen here: the interaction energy of two atoms in $|59D_{3/2}\rangle$, separated by $3 \mu\text{m}$, is approximately $\hbar \times 300 \text{ MHz}$. We thus excite only the superposition state $|s\rangle = (|rg\rangle + e^{i\mathbf{k}\cdot\mathbf{r}}|gr\rangle)/\sqrt{2}$, whose coupling to the two-atom ground state $|gg\rangle$ is $\sqrt{2}\Omega$ [18,19] (here, \mathbf{k} is the vector sum of the wave vectors of the excitation lasers, and \mathbf{r} is the position of atom 2 with respect to atom 1). This results in P_{rg} and P_{gr} oscillating between 0 and $1/2$ with a frequency $\sqrt{2}\Omega$, as can be seen in Fig. 2(b). Another signature of the blockade is the suppression of double excitation $P_{rr} \simeq 0$ [see bottom panel in Fig 2(b)].

If we shine the addressing beam on atom 2, we observe a strong suppression of the excitation probability for the states $|gr\rangle$ and $|rr\rangle$ [see Fig. 2(c)], as atom 2 is never excited to the Rydberg state $|r\rangle$. At the same time, atom 1 shows Rabi oscillations between $|g\rangle$ and $|r\rangle$ with the single-atom Rabi frequency Ω . The small residual excitation probability of atom 2 that we observe is fully accounted for by the errors in our state detection [15], meaning that cross-talk between the two traps is negligible.

Finally, we show that we can also use the addressing beam to directly manipulate a two-atom quantum state. Without any addressing, the excitation to the state $|rr\rangle$ is completely

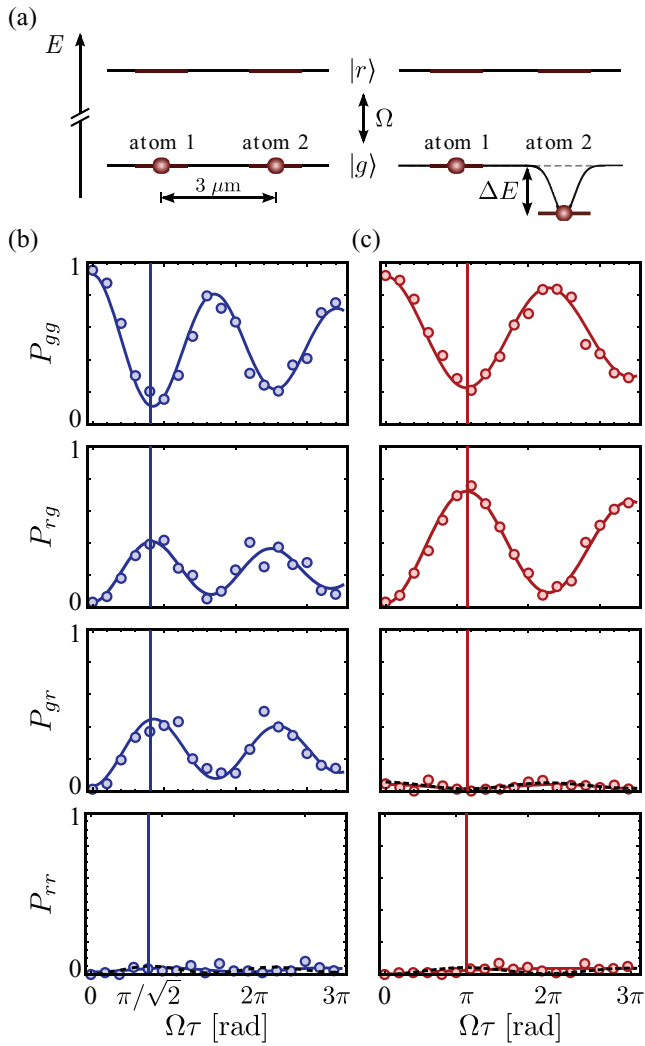


FIG. 2. (Color online) (a) Two atoms, separated by $3 \mu\text{m}$, are illuminated by light that resonantly couples the ground state $|g\rangle$ to $|r\rangle = |59D_{3/2}\rangle$ with the single-atom Rabi frequency Ω . The time evolution of the populations of the two-atom states $|gg\rangle$, $|gr\rangle$, $|rg\rangle$, and $|rr\rangle$ are shown, (b) without any addressing and (c) with atom 2 addressed with a light shift of $\Delta E \simeq h \times 10$ MHz. Solid lines are fits by damped sine curves. The vertical solid lines mark the pulse areas $\Omega\tau$ corresponding to a π pulse for the nonaddressed case (blue) and the addressed case (red). The black dashed lines show the expected measured populations for a perfect blockade of atom 2, taking into account state-detection errors.

suppressed in the Rydberg blockade regime ($U_{dd} \gg \hbar\Omega$). By applying an excitation pulse of duration $\pi/(\sqrt{2}\Omega)$ we thus prepare the atoms in the state $|\psi(0)\rangle = (|gr\rangle + e^{ik\cdot r}|rg\rangle)/\sqrt{2}$. We then illuminate atom 2 with the addressing beam [Fig. 3(a)]. Its energy is shifted by ΔE when in the ground state, while its Rydberg state remains unaffected [see Fig. 2(a)]. After a time T the state of the system has therefore evolved to

$$|\psi(T)\rangle = \frac{1}{\sqrt{2}}(|gr\rangle + e^{-i\Delta ET/\hbar} e^{ik\cdot r}|rg\rangle). \quad (1)$$

The antisymmetric dark state $|\psi(T_\pi)\rangle = (|gr\rangle - e^{ik\cdot r}|rg\rangle)/\sqrt{2}$ (with $T_\pi = \pi\hbar/\Delta E$) is not coupled to the ground state

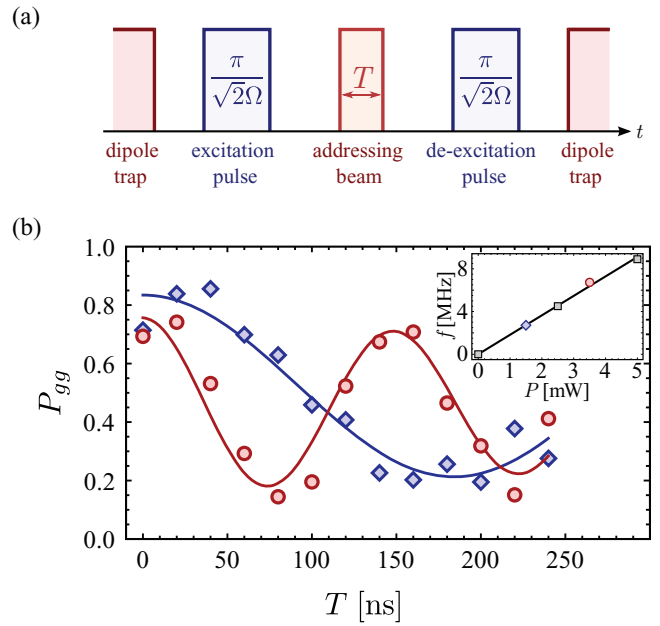


FIG. 3. (Color online) (a) Pulse sequence for the phase manipulation: while the dipole trap is switched off, the atoms are excited to the state $|\psi\rangle = (|gr\rangle + e^{ik\cdot r}|rg\rangle)/\sqrt{2}$. The addressing beam induces a light shift ΔE on the ground state of atom 2, thus changing the relative phase evolution between $|gr\rangle$ and $|rg\rangle$. This is followed by a global deexcitation pulse. (b) Population of the two-atom ground state $|gg\rangle$ after the deexcitation pulse, as a function of the addressing pulse length T , for a laser power in the addressing beam $P = 1.5$ mW (blue diamonds) and $P = 3.5$ mW (red circles). Solid lines are fits by damped sine curves of frequency f . Inset: oscillation frequency f as a function of the power P of the addressing beam, showing the expected linear dependence. For this experiment we use the Rydberg state $|82D_{3/2}\rangle$.

$|gg\rangle$. The probability of deexciting the atoms to $|gg\rangle$ is thus expected to oscillate between 0 and 1 with a frequency $f = \Delta E/h$.

Figure 3(b) shows the probability P_{gg} of deexciting the atoms back to $|gg\rangle$ versus the duration T of the addressing pulse. We observe the expected oscillation of the final ground-state population P_{gg} . Due to the finite Rydberg excitation efficiency (about 90% for our parameters), we measure a contrast of the oscillations that is lower than 1. In addition, the finite temperature of the atoms in the experiment leads to a small motion of the atoms during the sequence, implying that (i) the phase $\mathbf{k} \cdot \mathbf{r}$ imprinted by the excitation pulse is not exactly canceled out by the deexcitation pulse [20]; and (ii) the light shift ΔE experienced by atom 2 fluctuates from shot to shot. Averaged over many runs, both effects lead to a decreased contrast and a finite damping of the observed oscillations. To take these effects into account, we fitted the data with a damped sine curve of the form $P_{gg}(T) = A + B \exp(-\gamma T) \cos(2\pi f T)$, with the oscillation frequency f and the damping rate γ as adjustable parameters. Repeating the experiment for different powers of the addressing beam, we obtain the expected linear dependence of f with the applied light shift on the atom [see inset of Fig. 3(b)]. This demonstrates our ability to perform some controlled local operations on qubits in a quantum register.

In conclusion, we have shown that we can selectively prevent one single atom in a pair of single-atom traps from being resonant with Rydberg excitation lasers, with no measurable cross-talk with a neighboring atom as close as $3\ \mu\text{m}$. We also demonstrated the use of the addressing beam to perform a local operation in a system of two atoms. Our scheme is easily scalable to a larger number of traps. These techniques will prove useful for a variety of applications in quantum simulation and quantum information processing with Rydberg atoms. For instance, they open the possibility of selectively addressing a single qubit in a larger ensemble, e.g., as a control

atom for realizing collective quantum gates [16], or to excite a single atom to a different Rydberg state, allowing the study of the transfer of excitations along a Rydberg chain [21].

We thank Yvan Sortais for helpful advice about the optical design. We acknowledge financial support by the EU [ERC Stg Grant ARENA, AQUITE Integrating Project, FET-Open Xtrack Project HAIRS, and EU Marie-Curie Program ITN COHERENCE Grant No. FP7-PEOPLE-2010-ITN-265031 (H.L.)], by DGA (L.B.), and by Région Île-de-France (LUMAT and Triangle de la Physique, LAGON Project).

-
- [1] I. Bloch, J. Dalibard, and S. Nascimbène, *Nat. Phys.* **8**, 267 (2012).
- [2] M. Saffman, T. G. Walker, and K. Mølmer, *Rev. Mod. Phys.* **82**, 2313 (2010).
- [3] F. Nogrette, H. Labuhn, S. Ravets, D. Barredo, L. Béguin, A. Vernier, T. Lahaye, and A. Browaeys, *Phys. Rev. X* **4**, 021034 (2014).
- [4] H. C. Nägerl, D. Leibfried, H. Rohde, G. Thalhammer, J. Eschner, F. Schmidt-Kaler, and R. Blatt, *Phys. Rev. A* **60**, 145 (1999).
- [5] H. Häffner, W. Hänsel, C. F. Roos, J. Benhelm, D. Chek-al-kar, M. Chwalla, T. Körber, U. D. Rapol, M. Riebe, P. O. Schmidt, C. Becher, O. Gühne, W. Dür, and R. Blatt, *Nature* **438**, 643 (2005).
- [6] C. Monroe and J. Kim, *Science* **339**, 1164 (2013).
- [7] R. Dumke, M. Volk, T. Müther, F. B. J. Buchkremer, G. Birkel, and W. Ertmer, *Phys. Rev. Lett.* **89**, 097903 (2002).
- [8] M. Saffman, *Opt. Lett.* **29**, 1016 (2004).
- [9] M. Karski, L. Förster, J.-M. Choi, A. Steffen, N. Belmechri, W. Alt, D. Meschede, and A. Widera, *New J. Phys.* **12**, 065027 (2010).
- [10] C. Weitenberg, M. Endres, J. F. Sherson, M. Cheneau, P. Schauß, T. Fukuhara, I. Bloch, and S. Kuhr, *Nature (London)* **471**, 319 (2011).
- [11] M. Schlosser, S. Tichelmann, J. Kruse, and G. Birkel, *Quantum Inf. Process.* **10**, 907 (2011).
- [12] T. Fukuhara, A. Kantian, M. Endres, M. Cheneau, P. Schauß, S. Hild, D. Bellem, U. Schollwöck, T. Giamarchi, C. Gross, I. Bloch, and S. Kuhr, *Nat. Phys.* **9**, 235 (2013).
- [13] J. H. Lee, E. Montano, I. H. Deutsch, and P. S. Jessen, *Nat. Commun.* **4**, 2027 (2013).
- [14] L. Béguin, A. Vernier, R. Chicireanu, T. Lahaye, and A. Browaeys, *Phys. Rev. Lett.* **110**, 263201 (2013).
- [15] D. Barredo, S. Ravets, H. Labuhn, L. Béguin, A. Vernier, F. Nogrette, T. Lahaye, and A. Browaeys, *Phys. Rev. Lett.* **112**, 183002 (2014).
- [16] M. Müller, I. Lesanovsky, H. Weimer, H. P. Büchler, and P. Zoller, *Phys. Rev. Lett.* **102**, 170502 (2009).
- [17] Y. R. P. Sortais, H. Marion, C. Tuchendler, A. M. Lance, M. Lamare, P. Fournet, C. Armellin, R. Mercier, G. Messin, A. Browaeys, and P. Grangier, *Phys. Rev. A* **75**, 013406 (2007).
- [18] E. Urban, T. A. Johnson, T. Henage, L. Isenhourer, D. D. Yavuz, T. G. Walker, and M. Saffman, *Nat. Phys.* **5**, 110 (2009).
- [19] A. Gaëtan, Y. Miroshnychenko, T. Wilk, A. Chotia, M. Viteau, D. Comparat, P. Pillet, A. Browaeys, and P. Grangier, *Nat. Phys.* **5**, 115 (2009).
- [20] T. Wilk, A. Gaëtan, C. Evellin, J. Wolters, Y. Miroshnychenko, P. Grangier, and A. Browaeys, *Phys. Rev. Lett.* **104**, 010502 (2010).
- [21] S. Wüster, C. Ates, A. Eisfeld, and J. M. Rost, *Phys. Rev. Lett.* **105**, 053004 (2010).

Demonstration of a Strong Rydberg Blockade in Three-Atom Systems with Anisotropic Interactions

D. Barredo, S. Ravets, H. Labuhn, L. Béguin, A. Vernier, F. Nogrette, T. Lahaye, and A. Browaeys

Laboratoire Charles Fabry, Institut d'Optique, CNRS, Univ Paris Sud,

2 avenue Augustin Fresnel, 91127 Palaiseau cedex, France

(Received 17 February 2014; published 8 May 2014)

We study the Rydberg blockade in a system of three atoms arranged in different two-dimensional geometries (linear and triangular configurations). In the strong blockade regime, we observe high-contrast, coherent collective oscillations of the single excitation probability and an almost perfect van der Waals blockade. Our data are consistent with a total population in doubly and triply excited states below 2%. In the partial blockade regime, we directly observe the anisotropy of the van der Waals interactions between $|nD\rangle$ Rydberg states in the triangular configuration. A simple model that only uses independently measured two-body van der Waals interactions fully reproduces the dynamics of the system without any adjustable parameter. These results are extremely promising for scalable quantum information processing and quantum simulation with neutral atoms.

DOI: 10.1103/PhysRevLett.112.183002

PACS numbers: 32.80.Ee, 03.67.Bg, 34.20.Cf

Engineering quantum many-body systems with a high degree of control and tunable interactions is an active field of research as it is a prerequisite for quantum information processing [1] and quantum simulation [2]. Recently, significant achievements have been obtained towards this goal, e.g., using trapped ions for simulating quantum magnetism [3–5]. Another platform considered for such tasks consists of systems of neutral Rydberg atoms interacting via the strong and controllable long-range dipole-dipole interaction, which is responsible for the Rydberg blockade [6–9]. Through this mechanism, multiple excitations with a resonant narrow-band laser are inhibited within a blockade sphere by Rydberg-Rydberg interactions. The dipole blockade provides a way to realize fast quantum gates and to entangle particles, as demonstrated for two atoms [10,11]. This mechanism can in principle be extended to an ensemble of N atoms, with fascinating applications in quantum state engineering [12].

Although the picture of a blockade sphere has been remarkably successful at describing many recent experiments [13–22], some theoretical works question this simple approach. Even for the case of $N = 3$, some situations have been identified where nearly resonant dipole-dipole interactions [23], the nonadditivity of the van der Waals potentials [24], or the anisotropy of the interactions [25] lead to the breakdown or reduction of the blockade.

In this Letter, we show that, for experimentally relevant parameters, the Rydberg blockade is robust in ensembles of three atoms. In particular, we consider two different arrangements, namely, a line and an equilateral triangle. We observe an almost perfect van der Waals blockade and the coherent collective behavior of Rydberg excitations in both configurations. To go beyond this observation and understand the dynamics of the system in detail, we

measure the angular dependence of the effective interaction energy V_{eff} between two single-atoms excited to $|r\rangle \equiv |nD_{3/2}, m_j = 3/2\rangle$ Rydberg states. Using the measured two-body interaction strength we demonstrate that it is possible to fully reproduce the three-atom excitation dynamics in both the full and partial blockade regimes, with a model based on a master equation with no adjustable parameters. With the degree of experimental control demonstrated here, many theoretical proposals envisioning quantum simulation using Rydberg atoms become realistic.

We consider three atoms, with ground $|g_i\rangle$ and Rydberg $|r_i\rangle$ states coupled with Rabi frequencies Ω_i , and interacting via pairwise interactions V_{ij} . The system is thus described by the Hamiltonian [26]

$$\hat{H} = \sum_{i=1}^3 \frac{\hbar\Omega_i}{2} (\hat{\sigma}_{rg}^{(i)} + \hat{\sigma}_{gr}^{(i)}) + \sum_{i<j} V_{ij} \hat{\sigma}_{rr}^{(i)} \hat{\sigma}_{rr}^{(j)}, \quad (1)$$

where $\hat{\sigma}_{rg}^{(i)} = |r_i\rangle\langle g_i|$, $\hat{\sigma}_{gr}^{(i)} = |g_i\rangle\langle r_i|$, and $\hat{\sigma}_{rr}^{(i)} = |r_i\rangle\langle r_i|$. All parameters of the Hamiltonian can be tuned by a proper choice of the experimental settings. In particular, choosing $|r\rangle = |nD_{3/2}\rangle$ gives an extra degree of freedom to tune V_{ij} due to the anisotropy of the interaction. In what follows all Rabi couplings $\Omega_i \equiv \Omega$ are equal within 5%.

A strong blockade is obtained if the interaction strengths V_{ij} between atom pairs are much greater than the atom-light coupling $\hbar\Omega$ [Fig. 1(a)]. In this regime, the states carrying double and triple Rydberg excitations are off-resonant with the light field and the system can be described as a two-level model involving the collective states $|ggg\rangle$ and $|\Phi_{1r}\rangle = (|ggr\rangle + |grg\rangle + |rgg\rangle)/\sqrt{3}$, coupled by an effective Rabi frequency $\sqrt{3}\Omega$. Here, $|ijk\rangle \equiv |i_1\rangle|j_2\rangle|k_3\rangle$ stands

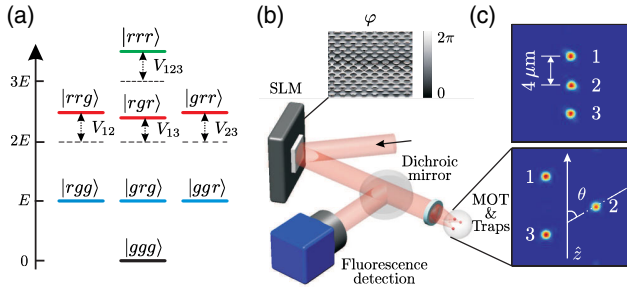


FIG. 1 (color online). (a) Relevant energy levels of a three-atom system with van der Waals interactions V_{ij} . In the blockade regime, the ground state $|ggg\rangle$ is resonantly coupled to the symmetric collective state $(|ggr\rangle + |grg\rangle + |rgg\rangle)/\sqrt{3}$. (b) Scheme of the experimental setup. Arbitrary geometries of two-dimensional arrays of dipole traps are obtained by imprinting a phase map φ with the SLM. (c) Trap geometry. Three single-atoms are trapped in microscopic optical tweezers separated by $R = 4 \mu\text{m}$ in a linear (top) and by $R = 8 \mu\text{m}$ in a triangular arrangement (bottom). The quantization axis \hat{z} is set by a 3G external magnetic field.

for products of the single-atom ground $|g\rangle$, and Rydberg $|r\rangle$ states for atoms 1, 2, and 3.

Our apparatus, shown schematically in Fig. 1(b), was previously described in detail [27]. Three single ^{87}Rb atoms are loaded from a magneto-optical trap into three 1 mK-deep microscopic optical traps [28], formed by focusing down a 850 nm Gaussian beam to a waist of $1 \mu\text{m}$ ($1/e^2$ radius) using a high numerical aperture lens under vacuum [29]. Arbitrary patterns of traps are obtained by imprinting a calculated phase pattern on the beam with a spatial light modulator (SLM) [30]. CCD images of the two trap configurations used in this work are displayed in Fig. 1(c). In the first arrangement (top), the three traps are collinear (parallel to the quantization axis \hat{z}) and separated by $R = 4 \mu\text{m}$. In the second configuration (bottom), the traps form an equilateral triangle with $8 \mu\text{m}$ sides.

The same aspheric lens is used to collect the atom fluorescence from each trap. We trigger the experimental sequence as soon as one atom is detected in each of the three traps. The atoms are then optically pumped into $|g\rangle = |5S_{1/2}, F = 2, m_F = 2\rangle$. The quantization axis \hat{z} is set by a 3G external magnetic field. For Rydberg excitation from $|g\rangle$ to $|nD_{3/2}, m_j = 3/2\rangle$, we use a two-photon process [31]: a π -polarized laser beam at 795 nm, detuned from the $|5P_{1/2}, F = 2, m_F = 2\rangle$ intermediate state by $2\pi \times 740 \text{ MHz}$, and a σ^+ -polarized 474 nm laser beam. Both excitation lasers are frequency locked using an ultrastable cavity providing laser linewidths $\sim 10 \text{ kHz}$. During the Rydberg excitation, the dipole traps are switched off to avoid light shifts. After excitation for a duration τ , we switch on again the dipole traps and we look for the fluorescence of the three atoms. Excitation of an atom to the Rydberg state is inferred from its loss from the corresponding trap (and thus the absence of fluorescence),

as Rydberg states are not trapped. The eight different populations P_{ijk} of the three-atom states $|ijk\rangle$ are then reconstructed by repeating each sequence ~ 150 times [31].

We first consider a one-dimensional array of three individual atoms aligned along the quantization axis [see Fig. 1(c) top] and separated by $4 \mu\text{m}$. To obtain the single-atom Rabi frequencies Ω_i we measure the probability P_{r_i} to excite atom i to the Rydberg state, with the other two traps switched off, as a function of the excitation pulse area. We observe well-contrasted Rabi oscillations [Fig. 2(a)]. A fit of the data (solid line) gives the same Rabi frequencies $\Omega_i \approx 2\pi \times 0.8 \text{ MHz}$ for the three atoms (within 5%), as well as small damping rates $\gamma_i \approx 0.3 \mu\text{s}^{-1}$ (see below). In Fig. 2(b) a single atom is loaded in each of the three traps. In this configuration we expect full blockade, as the single-atom Rabi frequencies are much smaller than van der Waals interactions: even for the $R = 8 \mu\text{m}$ distance between the outermost atoms, extrapolation of the measurement of Ref. [27] gives $V_{13} \approx h \times 32 \text{ MHz}$. The three atoms are excited to the collective state $|\Phi_{1r}\rangle$ [Fig. 1(a)], and the single excitation probability $P_{1r} \equiv P_{r_{gg}} + P_{g_{rg}} + P_{g_{gr}}$ shows oscillations with a frequency of $(1.72 \pm 0.02)\Omega$, compatible with the expected $\sqrt{3}\Omega$. Clear blockade of multiple Rydberg

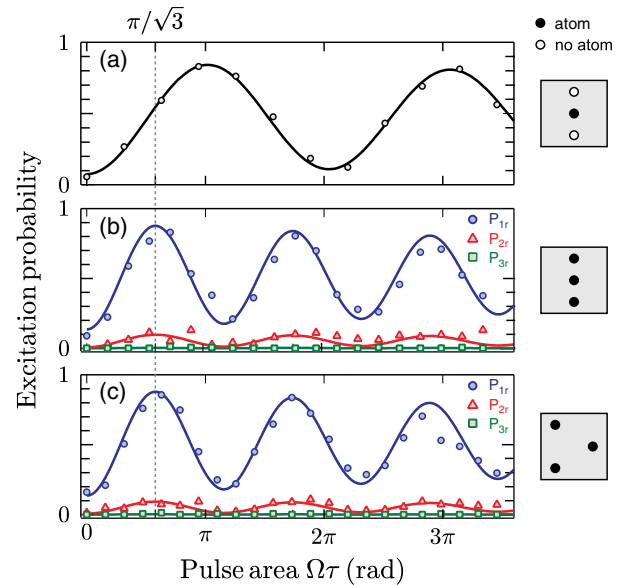


FIG. 2 (color online). (a) Representative single-atom Rabi flopping to the $|82D_{3/2}\rangle$ state for the central atom in the linear arrangement. Single-atom Rabi frequencies $\Omega \approx 2\pi \times 0.8 \text{ MHz}$, and damping rates $\gamma \approx 0.3 \mu\text{s}^{-1}$ for all three atoms are obtained from fits (solid lines) to the solution of the OBEs for a single two-level atom. (b) Probability of single (blue circles), double (red triangles), and triple (green squares) Rydberg excitation as a function of the excitation pulse area in the linear arrangement. The collective enhancement of the Rabi frequency by $\sqrt{3}$ clearly appears in the data. Solid lines are the result of the model described in the text without any adjustable parameter. (c) Same as (b) but for the triangular geometry.

excitations is observed in the data, as the populations $P_{2r} = P_{rrg} + P_{rgr} + P_{grr}$ ($P_{3r} = P_{rrr}$) of doubly (triply) excited states are almost totally suppressed in the system, with P_{2r} (P_{3r}) never exceeding 9% (1%).

We now show that the actual blockade is even better than suggested by these values. Indeed, each atom has a small probability ε to be lost during the sequence, independently of its internal state [32]. An independent measurement of the loss probability gives $\varepsilon = (5 \pm 1)\%$. Since in our detection scheme an atom loss is interpreted as an excitation to the Rydberg state, the *observed* double excitation P_{2r} differs from the *actual* one \tilde{P}_{2r} and, to first order in ε , it reads [32]

$$P_{2r} = (1 - \varepsilon)\tilde{P}_{2r} + 2\varepsilon\tilde{P}_{1r}. \quad (2)$$

If the blockade were perfect, one would have $\tilde{P}_{2r} = 0$, and the measured P_{2r} would thus oscillate between 0 and 2ε , in phase with P_{1r} . From the data on Fig. 2(b) we can extract an upper bound of $\sim 2\%$ on \tilde{P}_{2r} [32].

To gain more insight into the quality of the blockade for our experimental parameters, we simulate the dynamics of the system with Hamiltonian (1). A sum of independent single atom dissipators,

$$L[\rho] = \sum_i \frac{\gamma_i}{2} (2\hat{\sigma}_{gr}^{(i)}\rho\hat{\sigma}_{rg}^{(i)} - \hat{\sigma}_{rr}^{(i)}\rho - \rho\hat{\sigma}_{rr}^{(i)}), \quad (3)$$

is used to account for a small experimental damping γ_i of the oscillations (mainly due to off-resonant spontaneous emission through the intermediate state $|5P_{1/2}\rangle$; all the γ_i are equal within 10%). The results of the simulation, with no adjustable parameter, are represented by solid lines in Fig. 2(b), where the loss-error correction (2) is included. The very good agreement with the data further supports the quality of the blockade. Our results are compatible with the prediction of the model of double excitation probability $\tilde{P}_{2r}^{(\text{theo.})} \sim 10^{-3}$ for the same experimental parameters. Although proving experimentally that the double excitation is that low would require a more detailed study of systematic effects, this figure is very encouraging for high-fidelity generation of three-atom $|W\rangle$ states.

In the results discussed so far, we only considered a one-dimensional configuration. For scalability to a large number of atoms, however, two-dimensional arrays of traps are preferable. In this case, some atom pairs necessarily have an internuclear axis not aligned along the quantization axis and the anisotropy of the interaction comes into play, which might eventually prevent a perfect blockade [23–25]. To investigate this effect we study the blockade in an equilateral triangle configuration. Here, the anisotropic character of the D -state orbital plays a role and the interaction energies between atom pairs $V_{12} \approx V_{23}$ are weaker than V_{13} , although the atoms are equally separated. Despite this, Fig. 2(c) shows that the strength of the blockade is not reduced in the triangular geometry. Double and triple excitation probabilities are inhibited and the single

excitation probability oscillates at $\sim\sqrt{3}\Omega$. This result opens encouraging prospects for achieving strong blockade over two-dimensional arrays of atoms.

In order to observe directly the anisotropy of the interaction [33] we measured the interaction energy between atom pairs separated by $R = 12 \mu\text{m}$ as a function of the angle θ between the internuclear axis and the quantization axis \hat{z} . The procedure to extract the effective interaction energy V_{eff} is similar to the one introduced in Ref. [27]. Working in the partial blockade regime ($\hbar\Omega \sim V_{\text{eff}}$), we model the excitation dynamics through the solution of the optical Bloch equations (OBE) involving two-level atoms. Strictly speaking, to model two atoms in the $|nD_{3/2}\rangle$ state and $\theta \neq 0$, one would need to consider all 49 Zeeman sublevels with their different van der Waals couplings [34]. So as to keep the model tractable, even for large number of atoms, we model the system in the simplest nontrivial way, retaining only one single doubly excited state $|rr\rangle$ with an effective energy shift $V_{\text{eff}}(\theta)$. All input parameters are obtained from single-atom Rabi oscillation experiments. The measured dynamics of the two-atom system are then fitted with the solution of the OBEs with V_{eff} as the only fitting parameter. A more detailed study of the angular dependence of the van der Waals interaction, taking into account the full Zeeman structure of the atom pair, is beyond the scope of this Letter and will be the subject of future work.

The result of this approach is shown in Fig. 3 for the $|82D_{3/2}\rangle$ state. The anisotropy of the effective interaction is evident. The energy shift shows a maximum around $\theta = 0$

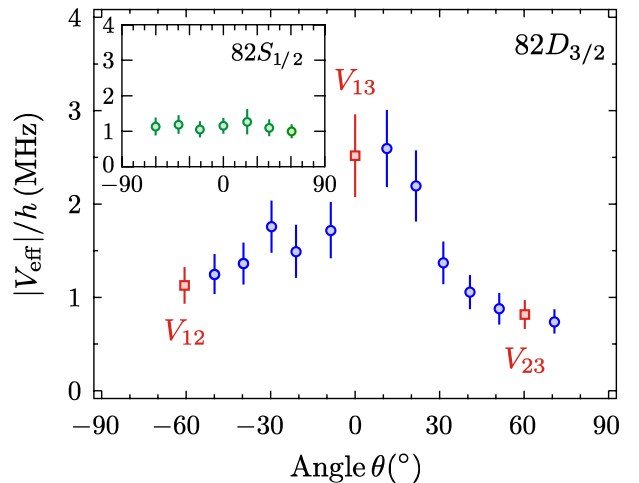


FIG. 3 (color online). Angular dependence of the effective interaction energy V_{eff} for two atoms in $|82D_{3/2}\rangle$ at $R = 12 \mu\text{m}$, with θ the angle between the internuclear axis and the quantization axis \hat{z} . Red squares indicate the measured energy shifts V_{13} , V_{23} , and V_{12} used for the simulation of three-atom dynamics in the partial blockade regime (see Fig. 4). In the inset, the angular dependence of the interaction for the spherically symmetric $|82S_{1/2}\rangle$ state is shown for comparison. Error bars represent one standard deviation confidence intervals in the fits.

and decreases for larger angles. A relative change of interaction strength by a factor ~ 3 is measured when θ varies from $\theta = 0$ to $\theta = 60^\circ$. In contrast, for a spherically symmetric S -Rydberg state, the interaction energy is isotropic (see inset of Fig. 3) [35]. For the D state, we observe an unexpected, slight asymmetry in the angular dependence of V_{eff} , probably due to small systematic effects [36].

The angular dependence of V_{eff} manifests itself in the interaction dynamics of the three atoms in the triangular configuration. By increasing the sides of the triangle to $R = 12 \mu\text{m}$, the effective interaction energies become $(V_{12}, V_{23}, V_{13}) \approx h \times (0.9, 1.1, 2.6)$ MHz (see red squares in Fig. 3), and the blockade is only partial for our chosen Rabi frequency Ω . In Fig. 4 we show the populations of doubly ($P_{rrg}, P_{rgr}, P_{grr}$) and triply (P_{rrr}) excited states for two different Rabi frequencies. In the first data set [Fig. 4(a)], $\Omega = 2\pi \times 0.8$ MHz and the anisotropy in the binary interaction ($V_{12} \neq V_{13}$) is directly observed in the dynamics: the probability P_{rgr} to detect double excitation of atoms 1 and 3 is almost totally suppressed, while it is appreciable for P_{rrg} and P_{grr} . Those two curves show almost the same dynamics, as expected. Triple excitations are totally blocked in this regime. For comparison, we show also the dynamics when a slightly higher Rabi frequency $\Omega = 2\pi \times 1.6$ MHz is used [Fig. 4(b)]. This corresponds to a partial blockade regime where $V_{13} > \hbar\Omega > V_{12}$. In this case, even triple excitations are not completely blocked. P_{rrg} and P_{grr} also exhibit similar behavior, while P_{rgr} shows different dynamics. The populations of states carrying only single excitations also show the anisotropy [32].

Many-body effects have largely been recognized to play a key role in the modeling of systems in physics and

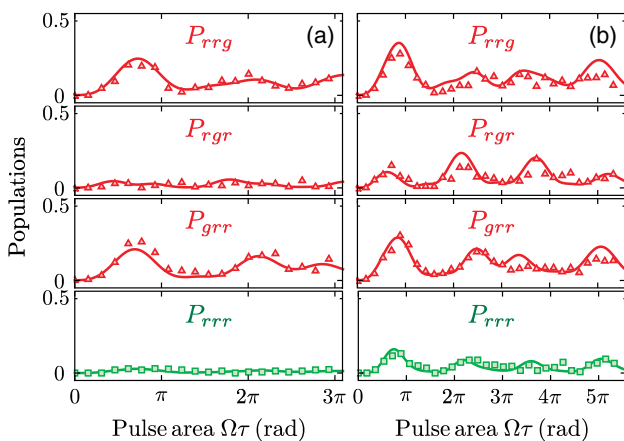


FIG. 4 (color online). Probabilities of detection of double Rydberg excitation P_{rrg} , P_{rgr} , P_{grr} , and triple excitation P_{rrr} versus excitation pulse area $\Omega\tau$ for driving Rabi frequencies $\Omega = 2\pi \times 0.8$ MHz (a), and $\Omega = 2\pi \times 1.6$ MHz (b) in the triangular configuration. The distance between the traps is $R = 12 \mu\text{m}$. The ratio between effective pairwise interaction energies is $V_{13}/V_{12} \sim 3$ for $\theta = 60^\circ$. Solid lines are the solution of the OBEs without any adjustable parameter.

chemistry [37]. In the case of Rydberg atoms they have been invoked to explain anomalous broadenings of Förster resonances [38,39]. To understand the evolution of the population of the states during excitation and to investigate to what extent few-atom many-body physics can be described from pairwise interactions we perform again a simulation using the OBEs for the three-atom system. In the model, with no adjustable parameters, the measured interaction energies at $\theta = 0$ and $\theta = 60^\circ$ (red squares in Fig. 3) are introduced. As shown by the solid lines in Fig. 4, the simulation (where atom loss correction is included) fully reproduces the experimental data. The fact that the simulation can accurately describe the evolution of the triply excited state P_{rrr} suggests that, for our choice of parameters, the pairwise addition of van der Waals level shifts $V_{123} = V_{12} + V_{13} + V_{23}$ is valid to a very good approximation. However, this additivity of the potential may not hold in the case of resonant dipole-dipole interactions. There, quantum interference between different many-body interaction channels can influence the dynamics [23]. All these processes can be studied for Rydberg atoms close to Förster resonance and will be the subject of future work. Another interesting line of research will consist in studying the recently predicted Borromean trimers bound by the dipole-dipole interaction [40].

In summary, we have investigated the dynamics of a system of three Rydberg atoms in both full and partial blockade regimes. We observe a strong van der Waals blockade of the excitations and coherent Rabi oscillations for two different spatial configurations. For the same experimental parameters in the equilateral triangle arrangement, the anisotropy of the interaction potential between $|nD\rangle$ states does not prevent the observation of a strong van der Waals blockade, which is a prerequisite for the scalability of quantum information processing proposals using two-dimensional arrays of dipole traps. The strong blockade achieved and the small damping of the oscillations pave the way for the generation of many-atom entanglement with high fidelity through the Rydberg blockade [12]. In the partial blockade regime, the angular dependence of the interaction energy shift between two atoms has been measured for the $|82D_{3/2}\rangle$ and $|82S_{1/2}\rangle$ Rydberg states. Furthermore, we have shown that with the measured effective energy shifts it is possible to reproduce the three-atom dynamics with high accuracy. This result demonstrates that one can confidently scale those studies for two-dimensional arrays of more than a few atoms, enabling the quantum simulation of large-size, long-range interacting spin systems.

We thank Daniel Cano for interesting discussions. This work was supported financially by the EU [ERC Stg Grant ARENA, AQUITE Integrating project, FET-Open Xtrack project HAIRS, EU Marie-Curie program ITN COHERENCE FP7-PEOPLE-2010-ITN-265031 (H.L.)], by the DGA (L.B.), and by Région Île-de-France (LUMAT and Triangle de la Physique, LAGON project).

- [1] M. A. Nielsen, I. L. Chuang, *Quantum Computation and Quantum Information* (Cambridge University Press, Cambridge, England, 2000).
- [2] R. Feynman, *Int. J. Theor. Phys.* **21**, 467 (1982).
- [3] B. P. Lanyon *et al.*, *Science* **334**, 57 (2011).
- [4] J. W. Britton, B. C. Sawyer, A. C. Keith, C.-C. Joseph Wang, J. K. Freericks, H. Uys, M. J. Biercuk, and J. J. Bollinger, *Nature (London)* **484**, 489 (2012).
- [5] R. Islam, C. Senko, W. C. Campbell, S. Korenblit, J. Smith, A. Lee, E. E. Edwards, C.-C. J. Wang, J. K. Freericks, and C. Monroe, *Science* **340**, 583 (2013).
- [6] H. Weimer, M. Müller, I. Lesanovsky, P. Zoller and H. P. Büchler, *Nat. Phys.* **6**, 382 (2010).
- [7] D. Jaksch, J. I. Cirac, P. Zoller, S. L. Rolston, R. Côté, and M. D. Lukin, *Phys. Rev. Lett.* **85**, 2208 (2000).
- [8] M. D. Lukin, M. Fleischhauer, R. Cote, L. M. Duan, D. Jaksch, J. I. Cirac, and P. Zoller, *Phys. Rev. Lett.* **87**, 037901 (2001).
- [9] D. Comparat and P. Pillet, *J. Opt. Soc. Am. B* **27**, A208 (2010).
- [10] T. Wilk, A. Gaëtan, C. Evellin, J. Wolters, Y. Miroshnychenko, P. Grangier, and A. Browaeys, *Phys. Rev. Lett.* **104**, 010502 (2010).
- [11] L. Isenhower, E. Urban, X. L. Zhang, A. T. Gill, T. Henage, T. A. Johnson, T. G. Walker, and M. Saffman, *Phys. Rev. Lett.* **104**, 010503 (2010).
- [12] M. Saffman, T. G. Walker, and K. Mølmer, *Rev. Mod. Phys.* **82**, 2313 (2010).
- [13] K. Singer, M. Reetz-Lamour, T. Amthor, L. G. Marcassa, and M. Weidemüller, *Phys. Rev. Lett.* **93**, 163001 (2004).
- [14] R. Heidemann, U. Raitzsch, V. Bendkowsky, B. Butscher, R. Löw, L. Santos, and T. Pfau, *Phys. Rev. Lett.* **99**, 163601 (2007).
- [15] J. D. Pritchard, D. Maxwell, A. Gauguet, K. J. Weatherill, M. P. A. Jones, and C. S. Adams, *Phys. Rev. Lett.* **105**, 193603 (2010).
- [16] Y. O. Dudin and A. Kuzmich, *Science* **336**, 887 (2012).
- [17] Y. O. Dudin, L. Li, F. Bariani, and A. Kuzmich, *Nat. Phys.* **8**, 790 (2012).
- [18] P. Schauss, M. Cheneau, M. Endres, T. Fukuhara, S. Hild, A. Omran, T. Pohl, C. Gross, S. Kuhr, and I. Bloch, *Nature (London)* **491**, 87 (2012).
- [19] E. Urban, T. A. Johnson, T. Henage, L. Isenhower, D. D. Yavuz, T. G. Walker, and M. Saffman, *Nat. Phys.* **5**, 110 (2009).
- [20] A. Gaëtan, Y. Miroshnychenko, T. Wilk, A. Chotia, M. Viteau, D. Comparat, P. Pillet, A. Browaeys, and P. Grangier, *Nat. Phys.* **5**, 115 (2009).
- [21] G. Günter, H. Schempp, M. Robert-de-Saint-Vincent, V. Gavryusev, S. Helmrich, C. S. Hofmann, S. Whitlock, and M. Weidemüller, *Science* **342**, 954 (2013).
- [22] A. M. Hankin, Y.-Y. Jau, L. P. Parazzoli, C. W. Chou, D. J. Armstrong, A. J. Landahl, and G. W. Biedermann, *Phys. Rev. A* **89**, 033416 (2014).
- [23] T. Pohl and P. R. Berman, *Phys. Rev. Lett.* **102**, 013004 (2009).
- [24] D. Cano and J. Fortágh, *Phys. Rev. A* **86**, 043422 (2012).
- [25] J. Qian, X.-D. Zhao, L. Zhou, and W. Zhang, *Phys. Rev. A* **88**, 033422 (2013).
- [26] I. Lesanovsky, *Phys. Rev. Lett.* **106**, 025301 (2011).
- [27] L. Béguin, A. Vernier, R. Chicireanu, T. Lahaye, and A. Browaeys, *Phys. Rev. Lett.* **110**, 263201 (2013).
- [28] N. Schlosser, G. Reymond, I. Protchenko and P. Grangier, *Nature (London)* **411**, 1024 (2001).
- [29] Y. R. P. Sortais *et al.*, *Phys. Rev. A* **75**, 013406 (2007).
- [30] F. Nogrette *et al.*, arXiv:1402.5329 [Phys. Rev. X (to be published)].
- [31] Y. Miroshnychenko, A. Gaëtan, C. Evellin, P. Grangier, D. Comparat, P. Pillet, T. Wilk, and A. Browaeys, *Phys. Rev. A* **82**, 013405 (2010).
- [32] See Supplemental Material at <http://link.aps.org/supplemental/10.1103/PhysRevLett.112.183002> for detailed error-loss analysis and full system dynamics.
- [33] T. J. Carroll, K. Claringbould, A. Goodsell, M. J. Lim, and M. W. Noel, *Phys. Rev. Lett.* **93**, 153001 (2004).
- [34] A. Reinhard, T. C. Liebisch, B. Knuffman, and G. Raithel, *Phys. Rev. A* **75**, 032712 (2007).
- [35] For excitation to the S state, the polarizations of the 795 nm (474 nm) lasers are π (σ^-).
- [36] However, the observed asymmetry has a negligible impact on the three-atom dynamics that we study in the rest of the Letter.
- [37] R. A. DiStasio, O. A. von Lilienfeld, and A. Tkatchenko, *Proc. Natl. Acad. Sci. U.S.A.* **109**, 14791 (2012).
- [38] W. R. Anderson, J. R. Veale, T. F. Gallagher, *Phys. Rev. Lett.* **80**, 249 (1998).
- [39] I. Mourachko, D. Comparat, F. de Tomasi, A. Fioretti, P. Nosbaum, V. Akulin, and P. Pillet, *Phys. Rev. Lett.* **80**, 253 (1998).
- [40] M. Kiffner, W. Li, and D. Jaksch, *Phys. Rev. Lett.* **111**, 233003 (2013).

Coherent Excitation Transfer in a Spin Chain of Three Rydberg Atoms

Daniel Barredo, Henning Labuhn, Sylvain Ravets, Thierry Lahaye, and Antoine Browaeys
*Laboratoire Charles Fabry, UMR 8501, Institut d'Optique, CNRS, Université Paris Sud 11,
2 avenue Augustin Fresnel, 91127 Palaiseau cedex, France*

Charles S. Adams

*Joint Quantum Centre (JQC) Durham-Newcastle, Department of Physics, Durham University,
Durham DH1 3LE, United Kingdom*

(Received 23 September 2014; revised manuscript received 21 November 2014; published 19 March 2015)

We study coherent excitation hopping in a spin chain realized using highly excited individually addressable Rydberg atoms. The dynamics are fully described in terms of an XY spin Hamiltonian with a long range resonant dipole-dipole coupling that scales as the inverse third power of the lattice spacing, C_3/R^3 . The experimental data demonstrate the importance of next neighbor interactions which are manifest as revivals in the excitation dynamics. The results suggest that arrays of Rydberg atoms are ideally suited to large scale, high-fidelity quantum simulation of spin dynamics.

DOI: 10.1103/PhysRevLett.114.113002

PACS numbers: 32.80.Ee, 03.67.Bg, 05.50.+q

Spin Hamiltonians, introduced in the early days of quantum mechanics to explain ferromagnetism, are widely used to study quantum magnetism [1]. Assemblies of interacting, localized spins are a paradigm of quantum many-body systems, where the interplay between interactions and geometry-induced frustration creates a wealth of intriguing quantum phases. Many other phenomena, such as coherent energy transfer, photochemistry, or photosynthesis [2], can also be described using spin Hamiltonians. However, despite this fundamental significance, exact analytical solutions are known only for the simplest cases, and numerical simulations of strongly correlated spin systems are notoriously difficult.

For those reasons, quantum simulation of spin Hamiltonians by controllable systems raises great interest. Recently, various approaches were followed to simulate spin systems using tools of atomic physics [3], such as cold atoms [4–6] or polar molecules [7] in optical lattices, interacting via weak exchange or dipole-dipole interactions, or trapped ions with engineered effective interactions [8–10]. As compared to their condensed-matter counterparts, the spin couplings can be long range, which gives rise to new properties [11–14].

Rydberg atoms are a promising alternative platform for quantum simulation [15,16]. In particular, they allow implementing various spin-1/2 Hamiltonians on two-dimensional lattices with strong couplings, in the MHz range [17,18]. Rydberg systems interacting through van der Waals interactions can be described by Ising-type

Hamiltonians $H = \sum_{ij} V_{ij} \sigma_i^z \sigma_j^z$ where σ^z is the z -Pauli matrix acting in the (pseudo-) spin Hilbert space, and $V_{ij} \sim |\mathbf{r}_i - \mathbf{r}_j|^{-6}$, where \mathbf{r}_i denotes the position of atom i [17–21]. On the other hand, spin-exchange, or XY , spin Hamiltonians of the form $H = \sum_{ij} V_{ij} (\sigma_i^+ \sigma_j^- + \sigma_i^- \sigma_j^+)$, where $\sigma^\pm = \sigma^x \pm i\sigma^y$ are spin-flip operators and $V_{ij} \sim |\mathbf{r}_i - \mathbf{r}_j|^{-3}$, can be realized by using two different Rydberg states, interacting directly via the resonant dipole-dipole interaction. However, in this case, only incoherent transfer of excitations has been observed so far, due to the random atomic positions in the ensembles used in experiments [22–27].

In this Letter, we study the coherent dynamics of a spin excitation in a chain of three Rydberg atoms. The dipole-dipole interaction between atoms is given by the XY Hamiltonian [28]

$$H = \frac{1}{2} \sum_{i \neq j} \frac{C_3}{R_{ij}^3} (\sigma_i^+ \sigma_j^- + \sigma_i^- \sigma_j^+), \quad (1)$$

where $R_{ij} = |\mathbf{r}_i - \mathbf{r}_j|$ is the distance between atoms i and j . We calibrate the spin-spin coupling between two Rydberg atoms by investigating the temporal evolution of two Rydberg atoms prepared in the state $|\uparrow\downarrow\rangle$, as a function of distance R between the atoms, up to $R \approx 50 \mu\text{m}$. We then use three Rydberg atoms prepared in $|\uparrow\downarrow\downarrow\rangle$ and study the propagation of the excitation through this minimalistic spin chain, observing the effect of long-range hopping of the excitation. The agreement between experimental data and the XY model without adjustable parameters validates our setup as a future quantum simulator for systems of many spins in arbitrary two-dimensional arrays.

The experimental setup, shown in Fig. 1(a), is detailed in Ref. [30]. Briefly, we focus a red-detuned trapping beam

Published by the American Physical Society under the terms of the Creative Commons Attribution 3.0 License. Further distribution of this work must maintain attribution to the author(s) and the published article's title, journal citation, and DOI.

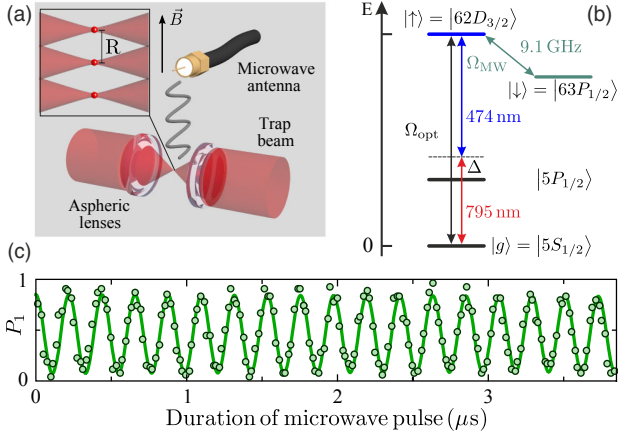


FIG. 1 (color online). (a) Individual ^{87}Rb atoms in microtraps aligned along the quantization axis, defined by a $B = 6$ G magnetic field. (b) Excitation lasers couple the ground state $|g\rangle = |5S_{1/2}, F=2, m_F=2\rangle$ and the Rydberg state $|\uparrow\rangle = |62D_{3/2}, m_J=3/2\rangle$ with an effective Rabi frequency Ω_{opt} . Microwaves couple $|\uparrow\rangle$ to $|\downarrow\rangle = |63P_{1/2}, m_J=1/2\rangle$, with Rabi frequency Ω_{MW} . (c) Microwave-driven Rabi oscillation of a single atom between $|\uparrow\rangle$ and $|\downarrow\rangle$, yielding $\Omega_{\text{MW}} = 2\pi \times 4.6$ MHz.

with an aspheric lens into a magneto-optical trap of ^{87}Rb , to a waist ≈ 1 μm . Multiple traps at arbitrary distances are created by imprinting an appropriate phase on the trapping beam with a spatial light modulator [31]. Because of fast light-assisted collisions in the small trapping volume, at most one atom is present in each trap. The temperature of the trapped atoms is approximately 50 μK . A 6 G magnetic field defines the quantization axis [32].

We encode the two spin states in the Rydberg states $|\uparrow\rangle = |62D_{3/2}, m_J=3/2\rangle$ and $|\downarrow\rangle = |63P_{1/2}, m_J=1/2\rangle$ [see Fig. 1(b)]. We trigger an experiment when an atom is detected in each trap. To prepare the atoms in a desired spin state, we first optically pump them in $|g\rangle = |5S_{1/2}, F=2, m_F=2\rangle$. We then switch off the traps to avoid inhomogeneous light shifts, and excite the atoms to $|\uparrow\rangle = |62D_{3/2}, m_J=3/2\rangle$ via a two-photon transition (wavelengths 795 and 474 nm, with polarizations π and σ^+ , respectively), detuned from the intermediate state $|5P_{1/2}, F=2, m_F=2\rangle$ by $\Delta \approx 2\pi \times 740$ MHz. From the $|\uparrow\rangle$ state the atom can be transferred to $|\downarrow\rangle = |63P_{1/2}, m_J=1/2\rangle$ using resonant microwaves at ≈ 9.131 GHz, emitted by an antenna outside the vacuum chamber.

To read out the state of an atom at the end of a sequence, we switch on the excitation lasers, coupling only $|\uparrow\rangle$ back to the ground state. We then turn on the dipole traps to recapture ground-state atoms, while atoms in Rydberg states remain untrapped, and detect atoms in $|g\rangle$ by fluorescence. Therefore if we detect an atom in its trap at the end of a sequence, we assume it was in $|\uparrow\rangle$, while a loss corresponds to the $|\downarrow\rangle$ state. We reconstruct all the 2^N

probabilities $P_{i_1 \dots i_k \dots i_N}$ of having i_k atom in trap k , with $i_k = 0$ or 1, for our N -trap system (with $N = 1, 2$, or 3) by repeating the experiment typically 100 times. For instance for $N = 3$, P_{100} is the probability to recapture an atom in trap 1, while recapturing none in traps 2 and 3. The statistical error on the determination of the probabilities is below 5%. Figure 1(c) illustrates the coherent spin manipulation for a single atom, by showing Rabi oscillations between $|\uparrow\rangle$ and $|\downarrow\rangle$: the probability P_1 to recapture the atom oscillates with a frequency $\Omega_{\text{MW}} \approx 2\pi \times 4.6$ MHz. In 4 μs , we induce more than 35 spin flips without observing noticeable damping.

We first use two atoms, aligned along the quantization axis, to directly measure the coupling between two spins as a function of their distance. The sequence is shown in Fig. 2(a). We illuminate atom 1 with an addressing beam [33] which induces a 20 MHz light shift, making it off resonant to the global Rydberg excitation. Atom 2 is excited to $|\uparrow\rangle$, and then transferred to $|\downarrow\rangle$ using microwaves. Subsequently, atom 1 is optically excited to the $|\uparrow\rangle$ state with the addressing beam switched off (atom 2 in $|\downarrow\rangle$ is not affected by the Rydberg excitation pulse). We let the system evolve for an adjustable time τ and read out the

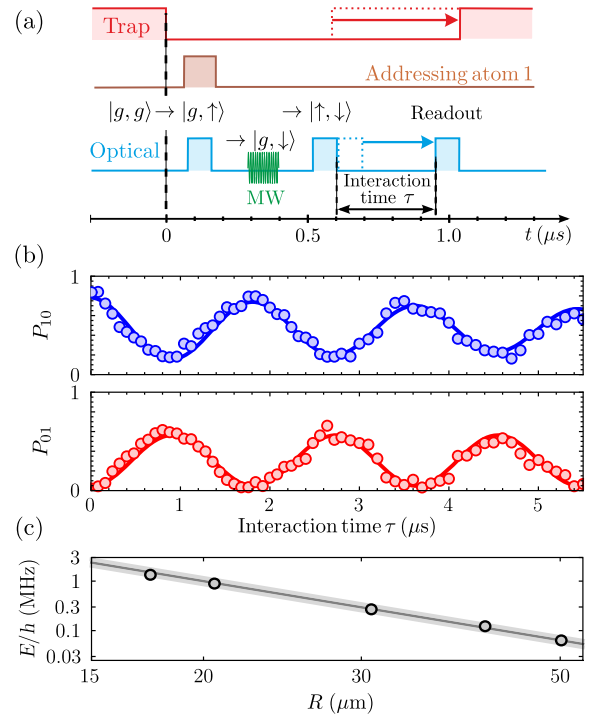


FIG. 2 (color online). (a) Sequence to observe spin exchange between two atoms. (b) Excitation hopping between states $|\uparrow\downarrow\rangle$ (blue disks) and $|\downarrow\uparrow\rangle$ (red disks) of two atoms separated by $R = 30$ μm . Solid lines are sinusoidal fits, with frequency $2E/\hbar$. (c) Interaction energy E (circles) versus R . Error bars are smaller than the symbols size. The line shows the theoretical prediction C_3/R^3 with $C_3^{\text{th}} = 7965$ $\text{MHz} \mu\text{m}^3$. The shaded area corresponds to our systematic 5% uncertainty in the calibration of R .

final state by deexciting $|\uparrow\rangle$ back to $|g\rangle$. In the absence of experimental imperfections (see [28], Sec. S.3), P_{10} (respectively, P_{01}) would give the population of $|\uparrow\downarrow\rangle$ (respectively, $|\downarrow\uparrow\rangle$).

The evolution of $P_{10}(\tau)$ and $P_{01}(\tau)$ for two atoms prepared in $|\uparrow\downarrow\rangle$ separated by $30\ \mu\text{m}$ is shown in Fig. 2(b). The spin excitation oscillates back and forth between the two atoms, with a frequency $2E/h \approx 0.52\ \text{MHz}$. The finite contrast is essentially due to spontaneous emission via the intermediate $|5P_{1/2}\rangle$ state during preparation and readout, which limits the oscillation amplitude to about 60%, and, to a lesser extent, to the onset of dipolar interactions during the second excitation pulse [28]. We then repeat the same experiment for several values of the distance R between the atoms, and observe spin-exchange oscillations for distances as large as $50\ \mu\text{m}$. Figure 2(c) shows the measured interaction energies as a function of R , together with the expected C_3/R^3 behavior (solid line) for the theoretical value $C_3^{\text{th}} = 7965\ \text{MHz}\ \mu\text{m}^3$ of the C_3 coefficient, calculated from the dipole matrix elements $\langle \uparrow|\hat{d}_{\pm 1}|\downarrow\rangle$ [30,34]. A power-law fit to the data (not shown) gives an exponent -2.93 ± 0.20 . Fixing the exponent to -3 gives $C_3^{\text{exp}} = 7950 \pm 130\ \text{MHz}\ \mu\text{m}^3$. The agreement between data and theory is excellent.

We now extend the system to a three-spin chain, with a distance $R = 20\ \mu\text{m}$ between the atoms. The sequence is similar to that in Fig. 2(a) for two atoms, except that we now use microwave transfer for atoms 2 and 3 to prepare $|g\downarrow\downarrow\rangle$. Here, the van der Waals interaction between the two atoms in $|\uparrow\rangle$ is only $\sim 10\ \text{kHz}$ for $R = 20\ \mu\text{m}$, and thus no blockade effect arises during excitation. We then excite atom 1 to prepare $|\uparrow\downarrow\downarrow\rangle$.

We first analyze theoretically the evolution of the system. Assuming that the initial state is $|\psi(0)\rangle = |\uparrow\downarrow\downarrow\rangle$, the dynamics induced by the XY Hamiltonian (1), which conserves the total magnetization $\sum_i \sigma_i^z$, occurs within the subspace spanned by $\{|\uparrow\downarrow\downarrow\rangle, |\downarrow\uparrow\downarrow\rangle, |\downarrow\downarrow\uparrow\rangle\}$. Figures 3(a) and 3(b) show the calculated dynamics of the spin excitation, which moves back and forth between the extreme sites. Figure 3(a) corresponds to the case where only nearest-neighbor interactions are retained in (1). Periodic, fully contrasted oscillations at a frequency $\sqrt{2}C_3/R^3$ are expected for the population of the extreme sites, while the population of $|\downarrow\uparrow\downarrow\rangle$ oscillates twice as fast between 0 and 1/2. In contrast, in Fig. 3(b), the full Hamiltonian (1) is simulated, including the interaction between extreme sites. One observes a clear signature of this long-range coupling, as the dynamics now becomes aperiodic for the populations of $|\uparrow\downarrow\downarrow\rangle$ and $|\downarrow\downarrow\uparrow\rangle$. The interplay of the couplings C_3/R^3 and $C_3/(8R^3)$ between nearest- and next-nearest neighbors makes the eigenvalues of (1) incommensurate. The back-and-forth exchange of excitation is thus modulated by a slowly varying envelope due to the beating of these frequencies.

Figure 3(c) shows the experimental results for P_{100} , P_{010} , and P_{001} (symbols). We observe qualitative agreement with Fig. 3(b), in particular the ‘‘collapse and revival’’ in the dynamics showing the effects of the long-range coupling. However, one notices differences with the ideal case: (i) the preparation is imperfect, as one starts with a significant population in $|\downarrow\uparrow\downarrow\rangle$, (ii) this, together with imperfect readout [28], reduces the overall amplitude of the oscillations, and (iii) the oscillations show some damping, which becomes significant for $\tau \geq 4\ \mu\text{s}$.

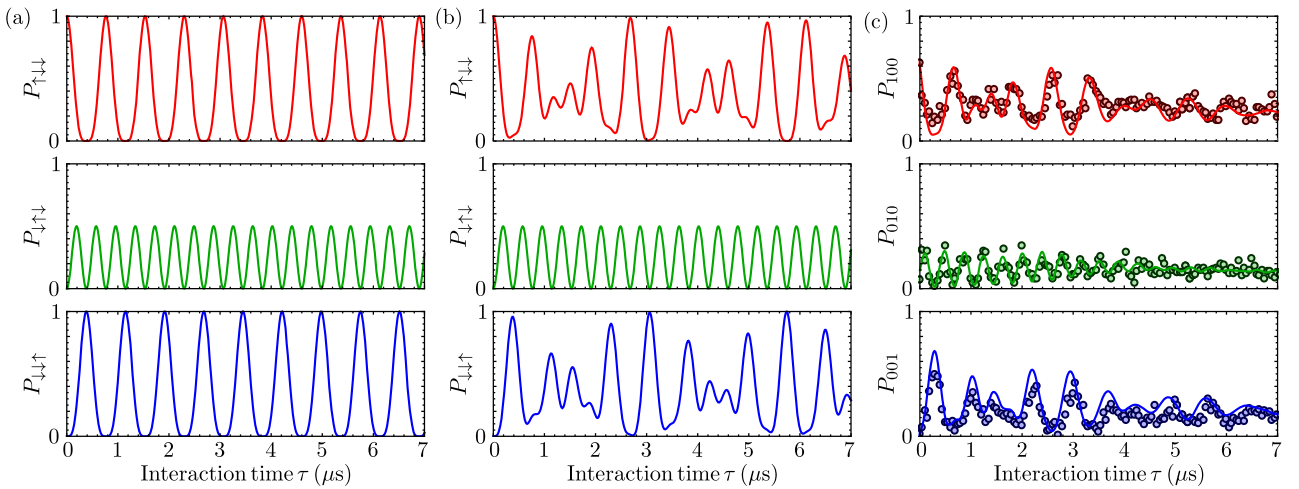


FIG. 3 (color online). Spin excitation transfer along a chain of three Rydberg atoms with nearest-neighbor separation of $20\ \mu\text{m}$. (a) Theoretical dynamics for a system initially prepared in $|\uparrow\downarrow\downarrow\rangle$, and evolving under a Hamiltonian similar to (1), but with only nearest-neighbor interactions. (b) The same as (a), but for the full Hamiltonian (1), including long-range interactions. (c) Experimental data (points) and prediction of the model taking into account experimental imperfections (see text), with no adjustable parameters. For perfect preparation and readout, the probabilities $P_{\uparrow\downarrow\downarrow}$ (respectively, $P_{\downarrow\uparrow\downarrow}$, $P_{\downarrow\downarrow\uparrow}$) and P_{100} (respectively, P_{010} , P_{001}) would coincide.

Imperfect preparation and readout stem from the fact that, in addition to the spontaneous emission via the intermediate state during the optical pulses, the Rabi frequency for optical excitation (≈ 5.3 MHz) of atom 1 from $|g\rangle$ to $|\uparrow\rangle$ is not much higher than the interaction (≈ 0.92 MHz for $R = 20 \mu\text{m}$). Thus, during the excitation of atom 1, the spin excitation already has a significant probability to hop to atom 2. The damping essentially arises from the finite temperature of the atoms, which leads to changes in the interatomic distances, and thus in the couplings.

To go beyond this qualitative understanding of the limitations of our “quantum simulator,” we add all known experimental imperfections to the XY model [28]. The result, shown by solid lines on Fig. 3(c) accurately reproduces the data with no free parameters. To obtain these curves, we simulate the full sequence, i.e., all three optical (de-) excitation pulses with or without the addressing beam, the microwave pulse, and evolution time, by solving the optical Bloch equations describing the dynamics of the internal states of the atoms, restricted to three states: $|g\rangle$, $|\uparrow\rangle$, and $|\downarrow\rangle$. Dissipation comes from both off-resonant excitation of the intermediate $|5P_{1/2}\rangle$ state during the optical excitation pulse, and from the finite lifetimes of the Rydberg states (101 and 135 μs for $|\uparrow\rangle$ and $|\downarrow\rangle$, respectively [35]). The former effect is treated as an effective damping of the $|g\rangle \leftrightarrow |\uparrow\rangle$ transition, present only during the optical pulses, and with a damping rate chosen to match the damping of single-atom Rabi oscillations performed to calibrate the excitation Rabi frequency Ω_{opt} [17].

We then account for the thermal motion of the atoms. A first consequence of the finite temperature ($T \approx 50 \mu\text{K}$) is that at the beginning of the sequence, the atoms have random positions (the transverse rms extension of the thermal motion in each microtrap, of radial frequency 90 kHz, is about 120 nm) and random velocities (70 nm/ μs rms). During the sequence, the traps are switched off and the atoms are thus in free flight with their initial velocity. When solving the optical Bloch equations, we thus first draw the initial positions \mathbf{r}_i^0 and velocities \mathbf{v}_i^0 of each atom i according to a thermal distribution, and use time-dependent dipolar couplings $C_3/|\mathbf{r}_i^0 + \mathbf{v}_i^0 t - (\mathbf{r}_j^0 + \mathbf{v}_j^0 t)|^3$ in Eq. (1) [36]. We then average the results over 100 realizations. This yields a dephasing of the oscillations, resulting in a significant contrast reduction at long times.

A second effect of the temperature is that an atom has a small probability $\varepsilon(t)$ to leave the trap region during the experiment. In this case, we mistakenly infer that it was in a Rydberg state at the end of the sequence. This leads to a small distortion of the measured populations P_{ijk} ($i, j, k = 0, 1$) [37], that we compute from the actual ones as described in [17]. We measure $\varepsilon(t)$ (which increases with the duration t of the sequence, from $\sim 1\%$ at $t = 0$ up to $\sim 20\%$ for $t = 7 \mu\text{s}$) in a calibration experiment, and then

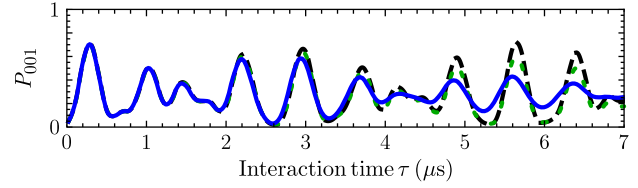


FIG. 4 (color online). Influence of the temperature on $P_{001}(\tau)$: simulated dynamics at zero temperature (black dashed line), and adding either only atom loss (green dotted line), or only atomic motion (blue solid line).

use it to calculate the expected populations from the simulated ones [28].

Figure 4 shows how those two consequences of the finite temperature contribute to the observed damping in the dynamics of P_{001} : both have sizable effects, but the dephasing due to fluctuations in the coupling dominates at long times. Reducing the atomic temperature using, e.g., Raman cooling [38,39] would render those effects negligible for our time scales, and allow the realization of a nearly ideal quantum simulator of spin dynamics.

In summary, we have measured the dynamics of a spin excitation in a minimal spin chain of three Rydberg atoms. The evolution of the system is accurately described by an XY Hamiltonian without any adjustable parameters. The obtained results are encouraging in view of scaling up the system to a larger number of spins. In particular, the residual motion of the atoms and the level of detection errors would already allow us to observe unambiguously the back-and-forth propagation of an excitation over a chain of ~ 20 atoms [28]. However, so far, experiments with more than ~ 5 atoms are hampered by the stochastic loading of the traps by single atoms [31]. In future work, we will thus explore various quasideterministic loading schemes that have been demonstrated at the level of a single [40,41] or a few [42,43] traps. Once this is achieved, our system will allow us to study the equivalent of an assembly of hard-core bosons on a 2D lattice with long-range, anisotropic hopping. We will also study dipolar interactions involving more than only two Rydberg states at an electrically tuned Förster resonance [44]. Our system will be ideal to study exotic phases and frustration in quantum magnetism, excitation hopping in complex networks [45,46], or quantum walks with long-range hopping [47].

We acknowledge financial support by the EU [ERC Stg. Grant ARENA, AQUOTE Integrating Project, FET-Open Xtrack Project HAIRS, and EU Marie-Curie Program ITN COHERENCE FP7-PEOPLE-2010-ITN-265031 (H. L.)], and by Région Île-de-France (LUMAT and Triangle de la Physique, projects LAGON and COLISCINA during the stay of C. S. A. at LCF). C. S. A. also acknowledges support from the U.K. EPSRC and Durham University.

- [1] A. Auerbach, *Interacting Electrons and Quantum Magnetism* (Springer-Verlag, New York, 1994).
- [2] E. Collini, *Chem. Soc. Rev.* **42**, 4932 (2013).
- [3] M. Lewenstein, A. Sanpera, and V. Ahufinger, *Ultracold Atoms in Optical Lattices: Simulating Quantum Many-Body Systems* (Oxford University Press, Oxford, U.K., 2012).
- [4] J. Simon, W. S. Bakr, R. Ma, M. E. Tai, P. M. Preiss, and M. Greiner, *Nature (London)* **472**, 307 (2011).
- [5] T. Fukuhara, P. Schauß, M. Endres, S. Hild, M. Cheneau, I. Bloch, and C. Gross, *Nature (London)* **502**, 76 (2013).
- [6] A. de Paz, A. Sharma, A. Chotia, E. Maréchal, J. H. Huckans, P. Pedri, L. Santos, O. Gorceix, L. Vernac, and B. Laburthe-Tolra, *Phys. Rev. Lett.* **111**, 185305 (2013).
- [7] B. Yan, S. A. Moses, B. Gadway, J. P. Covey, K. R. A. Hazzard, A. M. Rey, D. S. Jin, and J. Ye, *Nature (London)* **501**, 521 (2013).
- [8] K. Kim, M. S. Chang, S. Korenblit, R. Islam, E. E. Edwards, J. K. Freericks, G. D. Lin, L. M. Duan, and C. Monroe, *Nature (London)* **465**, 590 (2010).
- [9] P. Richerme, Z.-X. Gong, A. Lee, C. Senko, J. Smith, M. Foss-Feig, S. Michalakakis, A. V. Gorshkov, and C. Monroe, *Nature (London)* **511**, 198 (2014).
- [10] P. Jurcevic, B. P. Lanyon, P. Hauke, C. Hempel, P. Zoller, R. Blatt, and C. F. Roos, *Nature (London)* **511**, 202 (2014).
- [11] P. Hauke, F. M. Cucchietti, A. Müller-Hermes, M.-C. Bañuls, J. I. Cirac, and M. Lewenstein, *New J. Phys.* **12**, 113037 (2010).
- [12] D. Peter, S. Müller, S. Wessel, and H. P. Büchler, *Phys. Rev. Lett.* **109**, 025303 (2012).
- [13] K. R. A. Hazzard, M. van den Worm, M. Foss-Feig, S. R. Manmana, E. Dalla Torre, T. Pfau, M. Kastner, and A. M. Rey, *Phys. Rev. A* **90**, 063622 (2014).
- [14] M. Avellino, A. J. Fisher, and S. Bose, *Phys. Rev. A* **74**, 012321 (2006).
- [15] M. Saffman, T. G. Walker, and K. Mølmer, *Rev. Mod. Phys.* **82**, 2313 (2010).
- [16] H. Weimer, M. Müller, I. Lesanovsky, P. Zoller, and H.-P. Büchler, *Nat. Phys.* **6**, 382 (2010).
- [17] D. Barredo, S. Ravets, H. Labuhn, L. Béguin, A. Vernier, F. Nogrette, T. Lahaye, and A. Browaeys, *Phys. Rev. Lett.* **112**, 183002 (2014).
- [18] P. Schauß, J. Zeiher, T. Fukuhara, S. Hild, M. Cheneau, T. Macrì, T. Pohl, I. Bloch, and C. Gross, *arXiv:1404.0980*.
- [19] H. Weimer, R. Löw, T. Pfau, and H. P. Büchler, *Phys. Rev. Lett.* **101**, 250601 (2008).
- [20] T. Pohl, E. Demler, and M. D. Lukin, *Phys. Rev. Lett.* **104**, 043002 (2010).
- [21] I. Lesanovsky, *Phys. Rev. Lett.* **106**, 025301 (2011).
- [22] I. Mourachko, D. Comparat, F. de Tomasi, A. Fioretti, P. Nosbaum, V. M. Akulin, and P. Pillet, *Phys. Rev. Lett.* **80**, 253 (1998).
- [23] W. R. Anderson, J. R. Veale, and T. F. Gallagher, *Phys. Rev. Lett.* **80**, 249 (1998).
- [24] C. S. E. van Ditzhuijzen, A. F. Koenderink, J. V. Hernández, F. Robicheaux, L. D. Noordam, and H. B. van Linden van den Heuvell, *Phys. Rev. Lett.* **100**, 243201 (2008).
- [25] G. Günter, H. Schempp, M. Robert-de-Saint-Vincent, V. Gavryusev, S. Helmrich, C. S. Hofmann, S. Whitlock, and M. Weidemüller, *Science* **342**, 954 (2013).
- [26] S. Bettelli, D. Maxwell, T. Fernholz, C. S. Adams, I. Lesanovsky, and C. Ates, *Phys. Rev. A* **88**, 043436 (2013).
- [27] D. Maxwell, D. J. Szwer, D. Paredes-Barato, H. Busche, J. D. Pritchard, A. Gauguier, K. J. Weatherill, M. P. A. Jones, and C. S. Adams, *Phys. Rev. Lett.* **110**, 103001 (2013).
- [28] See Supplemental Material at <http://link.aps.org/supplemental/10.1103/PhysRevLett.114.113002>, which includes Ref. [29], for extra details about the simulation of the spin chain dynamics.
- [29] C. Tuchendler, A. M. Lance, A. Browaeys, Y. R. P. Sortais, and P. Grangier, *Phys. Rev. A* **78**, 033425 (2008).
- [30] L. Béguin, A. Vernier, R. Chicireanu, T. Lahaye, and A. Browaeys, *Phys. Rev. Lett.* **110**, 263201 (2013).
- [31] F. Nogrette, H. Labuhn, S. Ravets, D. Barredo, L. Béguin, A. Vernier, T. Lahaye, and A. Browaeys, *Phys. Rev. X* **4**, 021034 (2014).
- [32] The stray electric field is below 5 mV/cm. Note that as (1) conserves the excitation number, the system is quite immune to decoherence due to global fluctuations in electric or magnetic fields.
- [33] H. Labuhn, S. Ravets, D. Barredo, L. Béguin, F. Nogrette, T. Lahaye, and A. Browaeys, *Phys. Rev. A* **90**, 023415 (2014).
- [34] A. Reinhard, T. C. Liebisch, B. Knuffman, and G. Raithel, *Phys. Rev. A* **75**, 032712 (2007).
- [35] I. I. Beterov, I. I. Ryabtsev, D. B. Tretyakov, and V. M. Entin, *Phys. Rev. A* **79**, 052504 (2009).
- [36] Here, we neglect mechanical effects due to the interactions between Rydberg atoms during the interaction time. Using a classical model we estimate that these induce a displacement in R below 30 nm for $\tau \leq 7 \mu\text{s}$ and are therefore negligible.
- [37] C. Shen and L.-M. Duan, *New J. Phys.* **14**, 053053 (2012).
- [38] A. M. Kaufman, B. J. Lester, and C. A. Regal, *Phys. Rev. X* **2**, 041014 (2012).
- [39] J. D. Thompson, T. G. Tiecke, A. S. Zibrov, V. Vuletić, and M. D. Lukin, *Phys. Rev. Lett.* **110**, 133001 (2013).
- [40] T. Grünzweig, A. Hilliard, M. McGovern, and M. F. Andersen, *Nat. Phys.* **6**, 951 (2010).
- [41] M. Ebert, A. Gill, M. Gibbons, X. Zhang, M. Saffman, and T. G. Walker, *Phys. Rev. Lett.* **112**, 043602 (2014).
- [42] Y. Miroshnychenko, W. Alt, I. Dotsenko, L. Förster, M. Khudaverdyan, D. Meschede, D. Schrader, and A. Rauschenbeutel, *Nature (London)* **442**, 151 (2006).
- [43] M. Schlosser, J. Kruse, C. Gierl, S. Teichmann, S. Tichelmann, and G. Birkl, *New J. Phys.* **14**, 123034 (2012).
- [44] S. Ravets, H. Labuhn, D. Barredo, L. Béguin, T. Lahaye, and A. Browaeys, *Nat. Phys.* **10**, 914 (2014).
- [45] S. Wüster, C. Ates, A. Eisfeld, and J. M. Rost, *Phys. Rev. Lett.* **105**, 053004 (2010).
- [46] S. Mostarda, F. Levi, D. Prada-Gracia, F. Mintert, and F. Rao, *arXiv:1312.1833*.
- [47] R. Côté, A. Russell, E. E. Eyler, and P. L. Gould, *New J. Phys.* **8**, 156 (2006).

Coherent dipole–dipole coupling between two single Rydberg atoms at an electrically-tuned Förster resonance

Sylvain Ravets, Henning Labuhn, Daniel Barredo, Lucas Béguin, Thierry Lahaye and Antoine Browaeys*

Resonant energy transfers, the non-radiative redistribution of an electronic excitation between two particles coupled by the dipole–dipole interaction, lie at the heart of a variety of phenomena¹, notably photosynthesis. In 1948, Förster established the theory of fluorescence resonant energy transfer (FRET) between broadband, nearly-resonant donors and acceptors². The $1/R^6$ scaling of the energy transfer rate, where R is the distance between particles, enabled widespread use of FRET as a ‘spectroscopic ruler’ for determining nanometric distances in biomolecules³. The underlying mechanism is a coherent dipolar coupling between particles, as recognized in the early days of quantum mechanics⁴, but this coherence has not been directly observed so far. Here we study, spectroscopically and in the time domain, the coherent, dipolar-induced exchange of excitations between two Rydberg atoms separated by up to 15 μm , and brought into resonance by applying an electric field. Coherent oscillation of the system between two degenerate pair states then occurs at a frequency scaling as $1/R^3$, the hallmark of resonant dipole–dipole interactions⁵. Our results not only demonstrate, at the fundamental level of two atoms, the basic mechanism underlying FRET, but also open exciting prospects for active tuning of strong, coherent interactions in quantum many-body systems.

The possibility to tune at will coherent interactions in many-body systems by changing external parameters is one of the key tools enabling quantum simulation. For instance, in ultracold quantum gases, such tuning can be achieved by magnetically-induced Feshbach resonances^{6,7}. Rydberg atoms are another promising platform for the quantum simulation of complex many-body problems, owing to the strong interactions associated with their large principal quantum numbers⁸. They have proved to be an efficient tool for characterizing non-radiative exchange of energy in resonant collisional processes⁹, studying collective effects¹⁰ and engineering quantum states of matter¹¹. The observation of Rydberg blockade between individual atoms^{12,13}, where the strong interaction between Rydberg states inhibits multiple excitations within a blockade sphere, opens the way towards the development of Rydberg quantum simulators¹⁴. An appealing tool for those applications is the possibility to tune the strength of the interactions by external electric fields using Förster resonances^{15–23}. So far, owing to inhomogeneities in the atomic ensembles used in experiments, only indirect evidence for the coherent character of the interaction has been obtained^{24,25}.

Here, we study a system of two single atoms at a Förster resonance. We first perform a spectroscopic measurement of the energies of the two-atom states as a function of the applied electric field, and observe directly the avoided crossing between pair states induced by the dipole–dipole interaction. The splitting at resonance is observed to scale as $1/R^3$ as a function of the distance R between the atoms. In a second experiment, we prepare the system in a given pair state away from resonance, and switch to resonance for a controlled time, revealing the coherent oscillation between the two degenerate pair states induced by the dipolar interaction. These results open the way to real-time tuning of interactions for quantum simulation with Rydberg atoms^{11,14}.

Two atoms located at positions \mathbf{R}_1 and \mathbf{R}_2 interact through the dipole–dipole interaction

$$\hat{V}_{\text{dip}} = \frac{1}{4\pi\epsilon_0} \left(\frac{\hat{\boldsymbol{\mu}}_1 \cdot \hat{\boldsymbol{\mu}}_2 - 3(\hat{\boldsymbol{\mu}}_1 \cdot \mathbf{n})(\hat{\boldsymbol{\mu}}_2 \cdot \mathbf{n})}{R^3} \right)$$

where $\hat{\boldsymbol{\mu}}_i$ is the electric dipole moment of atom i ($i = 1, 2$), $\mathbf{R} = \mathbf{R}_2 - \mathbf{R}_1$ and $\mathbf{n} = \mathbf{R}/R$. When the two atoms are prepared in the same state, \hat{V}_{dip} usually has no effect to first order, as the average value of the dipole moment vanishes in an atomic eigenstate. Second-order perturbation theory gives rise to an energy shift of the atom pair, which results in the van der Waals interaction²⁶ $U_{\text{vdw}} \propto R^{-6}$. However, resonance effects between two Rydberg atoms can occur when two pair states are degenerate⁵, and in this case the dipolar interaction manifests itself at first order. Such a resonance, called a ‘Förster resonance’ in analogy with the FRET mechanism at work in photochemistry, can be achieved using small electric fields to Stark-tune the energy of the pair states.

In this work, we use the states $|p\rangle = |61P_{1/2}, m_J = 1/2\rangle$, $|d\rangle = |59D_{3/2}, m_J = 3/2\rangle$ and $|f\rangle = |57F_{5/2}, m_J = 5/2\rangle$ of ^{87}Rb . The pair states $|dd\rangle$, $|pf\rangle$ and $|fp\rangle$ are almost degenerate (Fig. 1a): their Förster defect $\Delta_0 = (E_{pf} - E_{dd})/h$, in the absence of an electric field, is only 8.5 MHz (h is Planck’s constant). Using the differential Stark effect between $|dd\rangle$ and $|pf\rangle$, they can be brought to exact resonance by applying an electric field $F_{\text{res}} \simeq 32 \text{ mV cm}^{-1}$ (Fig. 1b). The small electric fields at play ensure that we work in a regime of induced dipoles (even for the highly polarizable f state), as opposed to the rigid dipoles obtained for larger electric fields. At resonance, the eigenstates of the interacting system are $|\pm\rangle = (|dd\rangle \pm |p\tilde{f}\rangle)/\sqrt{2}$, where $|p\tilde{f}\rangle = (|pf\rangle + |fp\rangle)/\sqrt{2}$. If the system is initially prepared in $|dd\rangle$, it thus oscillates between the two degenerate electronic

Laboratoire Charles Fabry, UMR 8501, Institut d’Optique, CNRS, Univ Paris Sud 11, 2 avenue Augustin Fresnel, 91127 Palaiseau Cedex, France.

*e-mail: antoine.browaeys@institutoptique.fr

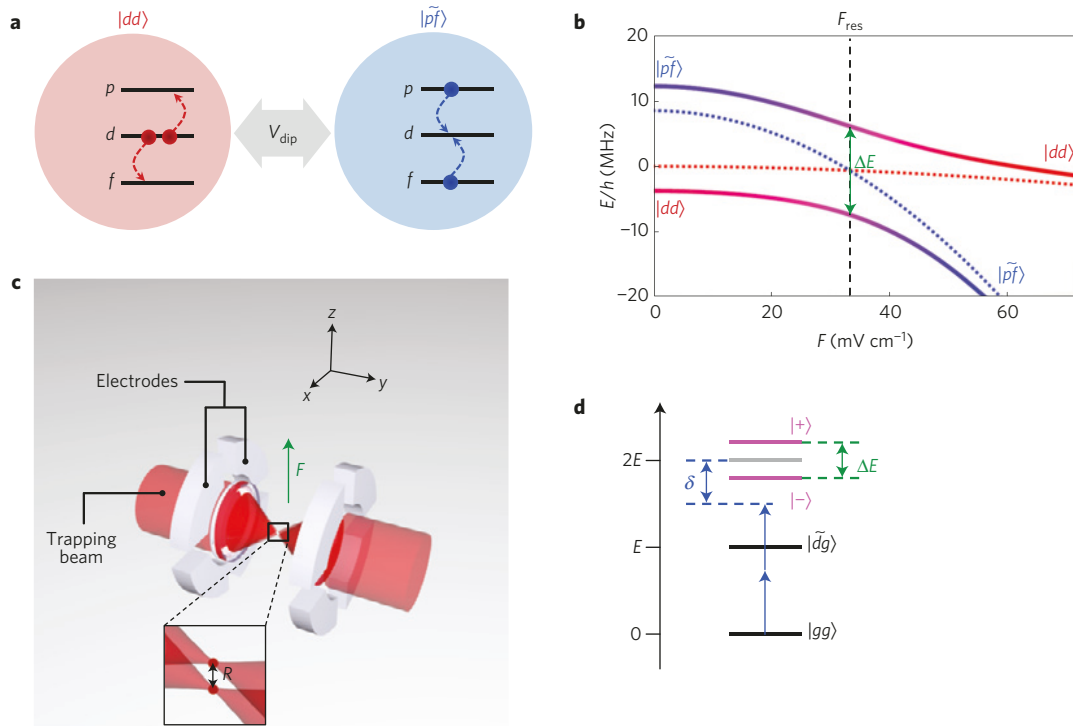


Figure 1 | Principle of the experiment. **a**, The pair states $|dd\rangle$ and $|\tilde{p}\tilde{f}\rangle$ are coupled by the dipolar interaction at a Förster resonance. **b**, Stark effect of the pair states. In the absence of coupling, the two pair-state energy levels (dotted lines) vary when an external electric field F is applied, and cross each other for $F = F_{\text{res}}$. The coupled system (solid lines) undergoes an avoided crossing at resonance (vertical dashed line). **c**, Experimental set-up. Two individual ^{87}Rb atoms are trapped in microscopic optical tweezers separated by a distance R . Eight independent electrodes allow the application of a tunable electric field F along the internuclear axis z . **d**, Structure of the coupled levels at resonance. We scan the excitation laser (blue arrow) to perform a two-atom excitation from $|gg\rangle$ to $|dd\rangle$ via the intermediate, one-excitation state $|\tilde{d}g\rangle = (|dg\rangle + |gd\rangle)/\sqrt{2}$. The detuning between the laser frequency and the position of $|dd\rangle$ in the absence of interactions (grey horizontal line) is denoted by δ .

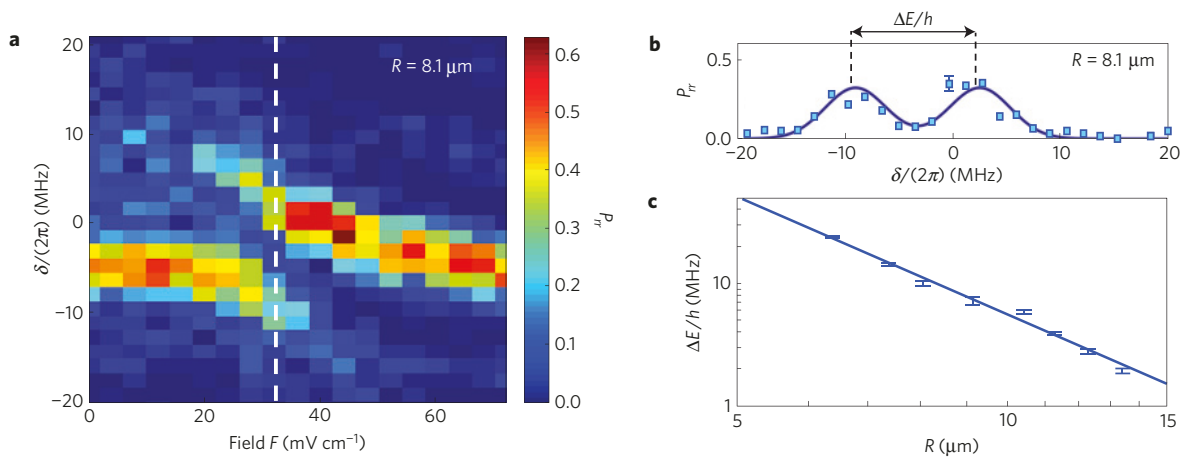


Figure 2 | Spectroscopy at the Förster resonance. **a**, Two-atom excitation spectrum where the population of doubly-Rydberg-excited states, P_{rr} , is plotted as a function of δ and F , showing the avoided crossing between the resonant pair states. The white dashed line indicates the position of the Förster resonance. **b**, Spectrum $P_{rr}(\delta)$ at resonance for $R = 8.1 \mu\text{m}$. A representative error bar (one standard error in the measurement of P_{rr}) is shown. A double Gaussian (solid line) is fit to the data. **c**, Double-logarithmic plot of the splitting ΔE between the peaks, at resonance, as a function of R . Error bars are one standard deviation in the determination of ΔE in the fit by a double Gaussian. The solid line shows a fit by a power law, giving an exponent -3.2 ± 0.2 .

configurations with a frequency given by the dipolar coupling $2\sqrt{2}C_3/R^3$ (where $C_3\sqrt{2}/R^3 = \langle dd|\hat{V}_{\text{dip}}|\tilde{p}\tilde{f}\rangle$). In particular, after half a period of interaction, the system has evolved to the entangled state $|\tilde{p}\tilde{f}\rangle$.

Our experimental set-up has been described previously^{26,27}. We trap two single laser-cooled atoms in optical tweezers separated by a controlled distance R of a few micrometres (Fig. 1c). A set of eight

independent electrodes allows us to apply a controlled electric field F aligned with the internuclear axis²⁸. A 3 G magnetic field, also aligned along z , is used to split the Zeeman sublevels. We optically pump the atoms in the ground state $|g\rangle = |5S_{1/2}, F = 2, m_F = 2\rangle$ (with an efficiency $>90\%$), which we couple, with an effective Rabi frequency Ω , to the Rydberg state $|d\rangle$ using a two-photon transition (using two lasers of wavelengths 795 nm and 474 nm, with π and σ^+

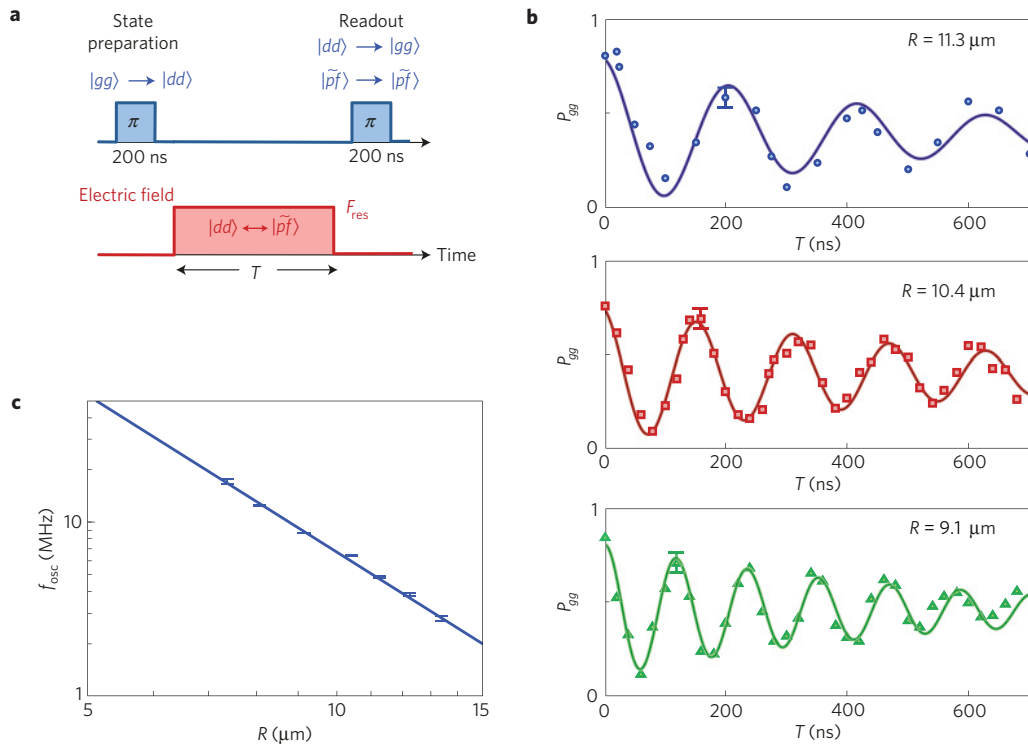


Figure 3 | Observation of the oscillation between the two pair states. **a**, Experimental sequence. After exciting the atoms to $|dd\rangle$ (first π -pulse, of duration 200 ns), we switch on the resonant interaction for a variable amount of time T by tuning the electric field to F_{res} . The system oscillates back and forth between the two pair states $|dd\rangle$ and $|\tilde{p}\tilde{f}\rangle$ for the duration T . A deexcitation pulse (second π -pulse) couples back the $|dd\rangle$ part of the resulting state to $|gg\rangle$. **b**, Evolution of P_{gg} as a function of the interaction time for several values of R . P_{gg} oscillates at a frequency f_{osc} which depends on R . A representative error bar (one standard error in the measurement of P_{gg}) is shown. The solid lines are fits by a damped sine wave with frequency f_{osc} . **c**, Double-logarithmic plot of the oscillation frequency f_{osc} as a function of R . Error bars correspond to one standard deviation in the determination of f_{osc} . The solid line shows a fit by a power law, giving an exponent -3.0 ± 0.1 .

polarizations, respectively). The readout of the states of the atoms is performed by shining resonant light at 780 nm on the atoms, giving a fluorescence signal only if the atom is in $|g\rangle$ (an atom in a Rydberg state, be it $|p\rangle$, $|d\rangle$, or $|f\rangle$, is lost from the trap during the sequence). Repeating the same sequence ~ 100 times allows us to reconstruct the four populations P_{gg} , P_{gr} , P_{rg} and P_{rr} (where r stands for any of the Rydberg states p , d and f , which we cannot discriminate directly with our loss-based detection scheme), with a typical uncertainty in the measurement of P_{ij} on the order of ± 0.05 (see representative error bars in Figs 2b and 3b).

We first fix $R = 8.1 \mu\text{m}$ and perform a spectroscopic measurement to find the electric field F_{res} corresponding to the Förster resonance. Our laser system couples $|gg\rangle$ to $|dd\rangle$ (but not to $|\tilde{p}\tilde{f}\rangle$ or $|\tilde{f}\tilde{p}\rangle$), via the states $|dg\rangle$ and $|gd\rangle$. Thus $|gg\rangle$ is partially coupled to the states $|+\rangle$ and $|-\rangle$ at resonance. For increasing values of F , we scan the laser detuning δ (defined with respect to the transition $|gg\rangle$ to $|dd\rangle$), see Fig. 1d) and measure the probability P_{rr} for both atoms to be in a Rydberg state (Fig. 2a). For $F = 0$, we observe a single line centred at $\delta/(2\pi) \approx -5$ MHz, corresponding to the attractive van der Waals interaction between the two atoms out of resonance. For $F \approx 20 \text{ mV cm}^{-1}$, a repulsive branch appears in the spectrum, a signature of the interaction between $|dd\rangle$ and $|\tilde{p}\tilde{f}\rangle$. Increasing the field even further allows scanning across the avoided crossing until only one peak is visible again. We reach the Förster resonance (smallest splitting between the two peaks) at $F_{\text{res}} = 32 \pm 4 \text{ mV cm}^{-1}$, where we observe two symmetric peaks corresponding to $|\pm\rangle$. The spectra also show further small structures in addition to the two main peaks. However, to extract the interaction energy in a simple way, we fit the spectra by two Gaussians with a splitting ΔE between the two peaks (Fig. 2b).

We then measure the evolution of the spectra at resonance when varying the distance R . When R increases, the splitting between the peaks decreases. Figure 2c is a double-logarithmic plot of ΔE versus R . The data show a power-law behaviour of exponent -3.2 ± 0.2 , consistent with the expected C_3/R^3 law. We measure $C_3 = 2.1 \pm 0.1 \text{ GHz } \mu\text{m}^3$, where the error is statistical. Systematic effects are an overall $\sim 5\%$ uncertainty in our calibration of R , a small bias in the determination of ΔE due to the choice of double Gaussian functions to fit the data and possible residual light-shifts in the two-photon spectroscopy. (To estimate the bias introduced by our choice of fit function, we fitted simulated spectra, obtained by solving the optical Bloch equations, by double Gaussians. The extracted splitting underestimates by $\approx 10\%$ the actual splitting ΔE .) Theoretical calculations²⁹ give $C_{3,\text{th}} \approx 2.54 \text{ GHz } \mu\text{m}^3$.

We now study the coherence properties of the system at resonance using a sequence (Fig. 3a) reminiscent of pump-probe spectroscopy. We prepare the system in the state $|dd\rangle$ using a π -pulse of 200 ns, which transfers each atom from $|g\rangle$ to $|d\rangle$. To start in a pure $|dd\rangle$ state, we perform the excitation in the van der Waals regime above resonance ($F \approx 64 \text{ mV cm}^{-1}$), where the Förster defect is $\Delta(F) \geq h \times 100$ MHz and where interactions are weak. We then turn on the resonant interaction for a variable duration T , by rapidly switching (risetime below 10 ns) the field to F_{res} . During this time, the two-atom system oscillates between $|dd\rangle$ and the entangled state $|\tilde{p}\tilde{f}\rangle$, with a frequency $f_{\text{osc}} = \Delta E/h = 2\sqrt{2}C_3/(hR^3)$ given by the dipolar coupling. We then apply a deexcitation π -pulse identical to the first one to read out the state of the system. The deexcitation pulse couples the $|dd\rangle$ component of the system back to $|gg\rangle$. At the end of the sequence we measure the probability P_{gg} to be back in $|gg\rangle$, thus indirectly measuring the population left in $|dd\rangle$ after the pulse

of electric field. We observe highly contrasted oscillations between $|dd\rangle$ and $|pf\rangle$, with a frequency depending on R (Fig. 3b).

The oscillations between two states are a direct proof of the coherent nature of the coupling underlying Förster energy transfer, and also allow a more accurate determination of the interaction energy than the spectroscopic method described above. We fit the oscillation by a damped sine wave to extract the oscillation frequency f_{osc} . Figure 3c shows a double-logarithmic plot of the values of f_{osc} as a function of R . The data shows a power-law behaviour of exponent -3.0 ± 0.1 , again in excellent agreement with the expected R^{-3} behaviour. The measured $C_3 = 2.39 \pm 0.03 \text{ GHz } \mu\text{m}^3$ is also close to the theoretical value.

The observed damping of the oscillations comes mainly from dephasing, arising from two effects. First, shot-to-shot fluctuations in the distance R (on the order of $\delta R \simeq 170 \text{ nm}$), due to the finite temperature of the atoms in the tweezers, give rise to dephasing, as the oscillation frequency $f_{\text{osc}} \propto 1/R^3$ is slightly different for each realization. This effect dominates at short distances: for instance, for $R \simeq 9 \mu\text{m}$, the corresponding spread $\delta f_{\text{osc}}/f_{\text{osc}} = 3\delta R/R$ in relative frequencies reaches $\sim 6\%$, which is enough to reduce the contrast of the oscillations by more than a factor of two after only four oscillation periods. Second, the voltages applied to the electrodes also fluctuate from shot to shot by a few mV, inducing fluctuations in F and thus in the detuning $\Delta(F)$ from resonance (by a fraction of a MHz for our parameters). This has negligible impact for small R , but appreciably contributes to the damping for large R , where the dipolar interaction is weaker. In principle, both sources of damping can be strongly decreased by technical improvements in the set-up, using colder atoms as demonstrated recently^{30,31} and more stable voltage sources.

Our results open exciting prospects for real-time tuning of interactions in systems of Rydberg atoms, in particular to switch on and off Rydberg blockade on nanosecond timescales. As an illustration, in the above experiment, when switching F from 64 mV cm^{-1} (away from resonance) to 32 mV cm^{-1} (right on resonance), the blockade shift between two atoms separated by $R = 10 \mu\text{m}$ varies from $U = U_{\text{vdW}} \sim h \times 0.2 \text{ MHz}$ (van der Waals regime) up to $U = \Delta E/2 \sim h \times 4 \text{ MHz}$ (C_3/R^3 regime). If the pair of atoms initially in $|gg\rangle$ were driven with a Rabi frequency $\Omega/(2\pi) \sim 1 \text{ MHz}$, one would observe a strong blockade in the second case, whereas blockade would be almost totally suppressed in the first situation. This means that, simply by changing the value of the electric field by a few mV cm^{-1} , we obtain a twenty-fold enhancement of the interaction, and the blockade radius is increased by a factor ~ 2 in real time, a feature hard to achieve by other means.

A natural extension of this work will consist in measuring the angular dependence of resonant interactions²⁹, in view of tailoring even further the interactions between two particles. Extending our results beyond two particles, to few-body³² and many-body systems^{15,16,23}, will enable the study of transport of excitations and generation of entanglement in fully controlled many-body systems.

Received 30 May 2014; accepted 8 September 2014;
published online 26 October 2014

References

- Andrews, D. L. & Demidov, A. A. *Resonance Energy Transfer* (Wiley, 1999).
- Förster, T. Zwischenmolekulare Energiewanderung und Fluoreszenz. *Ann. Phys.* **437**, 55–75 (1948).
- Stryer, L. & Haugland, R. P. Energy transfer: A spectroscopic ruler. *Proc. Natl Acad. Sci. USA* **58**, 719–726 (1967).
- Clegg, R. M. *Reviews in Fluorescence 2006* 1–45 (Springer, 2006).
- Walker, T. G. & Saffman, M. Zeros of Rydberg–Rydberg Förster interactions. *J. Phys. B* **38**, S309–S319 (2005).
- Inouye, S. *et al.* Observation of Feshbach resonances in a Bose–Einstein condensate. *Nature* **392**, 151–154 (1998).
- Chin, C., Grimm, R., Julienne, P. & Tiesinga, E. Feshbach resonances in ultracold gases. *Rev. Mod. Phys.* **82**, 1225–1286 (2010).
- Gallagher, T. F. *Rydberg Atoms* (Cambridge Univ. Press, 2005).
- Safinya, K. A., Delpech, J. F., Gounand, F., Sandner, W. & Gallagher, T. F. Resonant Rydberg-atom–Rydberg-atom collisions. *Phys. Rev. Lett.* **47**, 405–408 (1981).
- Comparat, D. & Pillet, P. Dipole blockade in a cold Rydberg atomic sample. *J. Opt. Soc. Am. B* **27**, A208–A232 (2010).
- Saffman, M., Walker, T. G. & Mølmer, K. Quantum information with Rydberg atoms. *Rev. Mod. Phys.* **82**, 2313–2363 (2010).
- Urban, E. *et al.* Observation of Rydberg blockade between two atoms. *Nature Phys.* **5**, 110–114 (2009).
- Gaëtan, A. *et al.* Observation of collective excitation of two individual atoms in the Rydberg blockade regime. *Nature Phys.* **5**, 115–118 (2009).
- Weimer, H., Müller, M., Lesanovsky, I., Zoller, P. & Büchler, H. P. A Rydberg quantum simulator. *Nature Phys.* **6**, 382–388 (2010).
- Anderson, W. R., Veale, J. R. & Gallagher, T. F. Resonant dipole–dipole energy transfer in a nearly frozen Rydberg gas. *Phys. Rev. Lett.* **80**, 249–252 (1998).
- Mourachko, I. *et al.* Many-body effects in a frozen Rydberg gas. *Phys. Rev. Lett.* **80**, 253–256 (1998).
- Anderson, W. R., Robinson, M. P., Martin, J. D. D. & Gallagher, T. F. Dephasing of resonant energy transfer in a cold Rydberg gas. *Phys. Rev. A* **65**, 063404 (2002).
- Mudrich, M., Zahzam, N., Vogt, T., Comparat, D. & Pillet, P. Back and forth transfer and coherent coupling in a cold Rydberg dipole gas. *Phys. Rev. Lett.* **95**, 233002 (2005).
- Vogt, T. *et al.* Electric-field induced dipole blockade with Rydberg atoms. *Phys. Rev. Lett.* **99**, 073002 (2007).
- Reinhard, A., Younge, K. C. & Raithel, G. Effect of Förster resonances on the excitation statistics of many-body Rydberg systems. *Phys. Rev. A* **78**, 060702(R) (2008).
- Van Ditzhuijzen, C. S. E. *et al.* Spatially resolved observation of dipole–dipole interaction between Rydberg atoms. *Phys. Rev. Lett.* **100**, 243201 (2008).
- Ryabtsev, I. I., Tretyakov, D. B., Beterov, I. I. & Entin, V. M. Observation of the Stark-tuned Förster resonance between two Rydberg atoms. *Phys. Rev. Lett.* **104**, 073003 (2010).
- Günter, G. *et al.* Observing the dynamics of dipole-mediated energy transport by interaction-enhanced imaging. *Science* **342**, 954–956 (2013).
- Nipper, J. *et al.* Highly resolved measurements of Stark-tuned Förster resonances between Rydberg atoms. *Phys. Rev. Lett.* **108**, 113001 (2012).
- Nipper, J. *et al.* Atomic pair-state interferometer: Controlling and measuring an interaction-induced phase shift in Rydberg-atom pairs. *Phys. Rev. X* **2**, 031011 (2012).
- Béguin, L., Vernier, A., Chicireanu, R., Lahaye, T. & Browaeys, A. Direct measurement of the van der Waals interaction between two Rydberg atoms. *Phys. Rev. Lett.* **110**, 263201 (2013).
- Nogrette, F. *et al.* Single-atom trapping in holographic 2D arrays of microtraps with arbitrary geometries. *Phys. Rev. X* **4**, 021034 (2014).
- Löw, R. *et al.* An experimental and theoretical guide to strongly interacting Rydberg gases. *J. Phys. B* **45**, 113001 (2012).
- Reinhard, A., Cubel Liebisch, T., Knuffman, B. & Raithel, G. Level shifts of rubidium Rydberg states due to binary interactions. *Phys. Rev. A* **75**, 032712 (2007).
- Kaufman, A. M., Lester, B. J. & Regal, C. A. Cooling a single atom in an optical tweezer to its quantum ground state. *Phys. Rev. X* **2**, 041014 (2012).
- Thompson, J. D., Tiecke, T. G., Zibrov, A. S., Vuletić, V. & Lukin, M. D. Coherence and Raman sideband cooling of a single atom in an optical tweezer. *Phys. Rev. Lett.* **110**, 133001 (2013).
- Gurian, J. H. *et al.* Observation of a resonant four-body interaction in cold cesium Rydberg atoms. *Phys. Rev. Lett.* **108**, 023005 (2012).

Acknowledgements

We thank C. S. Adams for enlightening discussions, F. Nogrette for technical assistance and M. Besbes for finite-element calculations of the electric field configuration. This work was supported financially by the EU (ERC Stg Grant ARENA, FET-Open Xtrack project HAIRS, EU Marie-Curie program ITN COHERENCE FP7-PEOPLE-2010-ITN-265031 (H.L.)), by the DGA (L.B.), and by Région Île-de-France (LUMAT and Triangle de la Physique, LAGON project).

Author contributions

All authors contributed extensively to the work presented in this paper.

Additional information

Reprints and permissions information is available online at www.nature.com/reprints. Correspondence and requests for materials should be addressed to A.B.

Competing financial interests

The authors declare no competing financial interests.



Measurement of the angular dependence of the dipole-dipole interaction between two individual Rydberg atoms at a Förster resonance

Sylvain Ravets, Henning Labuhn, Daniel Barredo, Thierry Lahaye, and Antoine Browaeys
*Laboratoire Charles Fabry, UMR 8501, Institut d'Optique, CNRS, Univ Paris Sud 11, 2 avenue Augustin Fresnel,
 91127 Palaiseau cedex, France*

(Received 1 April 2015; published 25 August 2015)

We measure the angular dependence of the resonant dipole-dipole interaction between two individual Rydberg atoms with controlled relative positions. By applying a combination of static electric and magnetic fields on the atoms, we demonstrate the possibility to isolate a single interaction channel at a Förster resonance, that shows a well-defined angular dependence. We first identify spectroscopically the Förster resonance of choice and we then perform a direct measurement of the interaction strength between the two atoms as a function of the angle between the internuclear axis and the quantization axis. Our results show good agreement with the angular dependence $\propto(1 - 3 \cos^2 \theta)$ expected for this resonance. Understanding in detail the angular dependence of resonant interactions is important in view of using Förster resonances for quantum state engineering with Rydberg atoms.

DOI: 10.1103/PhysRevA.92.020701

PACS number(s): 34.20.Cf, 32.80.Ee

Among the systems currently considered for quantum engineering with applications to quantum simulation [1] and quantum information [2], ensembles of individual Rydberg atoms are promising [3–5], since they provide large interactions [6] and are scalable [7]. For that purpose, one needs to control pairwise interactions in the system. Significant achievements using small numbers of atoms have been obtained based on the phenomenon of Rydberg blockade [8–15]. The energy transfer between atoms [16,17] observed in the presence of resonant interactions also leads to interesting many-body dynamics governed by spin-exchange Hamiltonians [18,19]. In those examples, one has to pay attention to the angular dependence of the interaction [20–23].

The anisotropy of the dipole-dipole interaction plays a crucial role in solid-state nuclear magnetic resonance [24], and in systems such as cold polar molecules [25,26] or dipolar quantum gases [27]. Although experimental evidence of the anisotropy of the resonant dipole-dipole interaction between Rydberg atoms has been observed in confined geometries [28], to date, a direct measurement of this angular dependence has not been obtained due to the complexity introduced by multiple interaction channels and inhomogeneities in disordered ensembles [20,29]. Here we use a combination of electric and magnetic field to isolate a single interaction channel, by tuning two atoms separated by a controlled distance R to a Förster resonance. We measure the evolution of the system [30] to extract the interaction strength as a function of the angle θ between the interatomic axis and the quantization axis z . Our results further extend the possibilities offered by Rydberg atoms for quantum state engineering.

The electric dipole-dipole interaction between two atoms ($k = 1, 2$) is described by the operator

$$\hat{V}_{dd} = \frac{1}{4\pi\epsilon_0 R^3} [\mathcal{A}_1(\theta)(\hat{d}_{1+}\hat{d}_{2-} + \hat{d}_{1-}\hat{d}_{2+} + 2\hat{d}_{1z}\hat{d}_{2z}) + \mathcal{A}_2(\theta)(\hat{d}_{1+}\hat{d}_{2z} - \hat{d}_{1-}\hat{d}_{2z} + \hat{d}_{1z}\hat{d}_{2+} - \hat{d}_{1z}\hat{d}_{2-}) - \mathcal{A}_3(\theta)(\hat{d}_{1+}\hat{d}_{2+} + \hat{d}_{1-}\hat{d}_{2-})], \quad (1)$$

where $\hat{d}_{k,\pm} = \mp(\hat{d}_{k,x} \pm i\hat{d}_{k,y})/\sqrt{2}$ are the components of the dipole operator in the spherical basis. The

operator \hat{V}_{dd} in Eq. (1) contains terms with angular prefactors $\mathcal{A}_1(\theta) = (1 - 3 \cos^2 \theta)/2$, $\mathcal{A}_2(\theta) = 3 \sin \theta \cos \theta/\sqrt{2}$, and $\mathcal{A}_3(\theta) = 3 \sin^2 \theta/2$, that couple pair states where the total magnetic quantum number $M = m_1 + m_2$ changes by $\Delta M = 0$, $\Delta M = \pm 1$, and $\Delta M = \pm 2$, respectively. In the absence of external fields two atoms prepared in the same state generally interact in the van der Waals regime, where several states contribute to second order to the interaction [7]. Resonant dipole-dipole interactions occur when two pair states coupled by \hat{V}_{dd} are degenerate, giving rise to stronger interaction energies $E_{dd} \propto 1/R^3$ [6,7].

Resonant interactions between Rydberg atoms can be observed by applying an electric field to reach a Förster resonance [31–38]. Here we study the resonance

$$59D_{3/2} + 59D_{3/2} \longleftrightarrow 61P_{1/2} + 57F_{5/2} \quad (2)$$

for two rubidium atoms prepared in $|d\rangle = |59D_{3/2}, m_j = 3/2\rangle$ [30]. When $\theta = 0$, the angular prefactors \mathcal{A}_2 and \mathcal{A}_3 vanish, and we only need to consider dipolar couplings with $\Delta M = 0$. In this case, Eq. (2) describes the transition of one atom to the magnetic substate $|p\rangle = |61P_{1/2}, m_j = 1/2\rangle$ while the other atom evolves to the magnetic substate $|f_1\rangle = |57F_{5/2}, m_j = 5/2\rangle$. We define the symmetric state $|pf_1\rangle_s = (|pf_1\rangle + |f_1p\rangle)/\sqrt{2}$. In a zero electric field the energy splitting between $|dd\rangle$ and $|pf_1\rangle_s$ is only $h \times 8.5$ MHz, and vanishes for a small electric field ($F_{res} \simeq 33$ mV/cm) due to the differential Stark effect between the two states [39]. At resonance, the eigenstates of the system are the combinations $|\pm_1\rangle = (|dd\rangle \pm |pf_1\rangle_s)/\sqrt{2}$, that have energies $E_{\pm} = \pm\sqrt{2}C_3/R^3$. The coefficient C_3 , defined such that the matrix element of \hat{V}_{dd} between $|dd\rangle$ and $|pf_1\rangle$ for $\theta = 0$ is equal to C_3/R^3 , was measured previously in [30] to be $C_3/h = 2.39 \pm 0.03$ GHz μm^3 .

Here, we focus on the angular dependence of this interaction. When $\theta \neq 0$, \hat{V}_{dd} couples $|dd\rangle$ to different magnetic substates $|pf_i\rangle_s$, as detailed later (see Fig. 4). Since the states $|pf_i\rangle_s$ have different polarizabilities, it is possible, by a proper choice of parameters, to isolate one interaction channel [37,38] showing a well-defined angular dependence. This is what we

demonstrate here for the resonance between $|pf_i\rangle_s$ and $|dd\rangle$, with full control over the geometry of the system, which allows us to measure an interaction strength varying as $\mathcal{A}_1(\theta)$.

Our experiment starts by loading two ^{87}Rb atoms from a magneto-optical trap into two microscopic dipole traps, created by focusing a laser beam of wavelength 852 nm using a high-numerical aperture lens [40]. We control R and θ using a spatial light modulator to create arbitrary trap patterns [41]. Using a set of electrodes, we control the electric field F_z at the position of the atoms. We apply a 3.3 G magnetic field along z , and we optically pump the atoms in $|g\rangle = |5S_{1/2}, F=2, m_F=2\rangle$. For the Rydberg excitation from $|g\rangle$ to $|d\rangle = |59D_{3/2}, m_j=3/2\rangle$, we perform a two-photon transition using a π -polarized laser beam of wavelength 795 nm and a σ^+ -polarized laser beam of wavelength 474 nm. During that time, the microtraps are switched off. At the end of the sequence, we turn on the trapping light again and shine resonant light of wavelength 780 nm on the atoms. We read out the state of the system by detecting the fluorescence of ground-state atoms (atoms that are in a Rydberg state at the end of the excitation sequence are not recaptured in the microtraps). We repeat the sequence $\simeq 100$ times to reconstruct the two-atom state populations P_{gg} , P_{gr} , P_{rg} , and P_{rr} , where r stands for any Rydberg state and g stands for the ground state.

In a first experiment, we identify the various resonances by measuring Rydberg excitation spectra as a function of the electric field for two atoms with $R = 9.1 \mu\text{m}$ and $\theta = 32^\circ$. For electric field that vary between $F_z = 4 \text{ mV/cm}$ and $F_z = 44 \text{ mV/cm}$, we shine on the atoms an excitation laser pulse of Rabi frequency $\Omega/2\pi \simeq 0.76 \text{ MHz}$ and duration $\tau = 1 \mu\text{s}$. We record the probability P_{rr} to excite both atoms to a Rydberg state as we scan the frequency detuning δ of the excitation laser with respect to the Rydberg line measured in a zero electric field Figure 1(a) shows the result of this measurement. For electric field smaller than a few mV/cm, we observe a single excitation line showing the transfer of population from $|gg\rangle$ to $|dd\rangle$ via the pair states $|gd\rangle$ and $|dg\rangle$. At resonance between $|dd\rangle$ and $|pf_i\rangle_s$, the state $|gg\rangle$ is partially coupled to the eigenstates $|\pm_i\rangle = (|dd\rangle \pm |pf_i\rangle_s)$, and we observe the presence of two excitation lines. Because $|pf_i\rangle_s$ have different polarizabilities, resonances between $|dd\rangle$ and $|pf_i\rangle_s$ occur at distinct F_z , and we observe different avoided crossings between $|dd\rangle$ and $|pf_i\rangle_s$. The measured spectrum is in good agreement with the calculated spectrum shown in Fig. 1(b), obtained by simulating the experimental sequence for the system, as detailed later in this Rapid Communication (see Fig. 4). For $\theta = 0$, the same measurement (not shown here) gives a single avoided crossing between $|dd\rangle$ and $|pf_i\rangle_s$ [30]. The observation of multiple resonances when $\theta \neq 0$ is a first indication of the anisotropy of the interaction.

We now focus on the resonance at $F_z \simeq 33 \text{ mV/cm}$ (red dashed line in Fig. 1) and study its angular dependence. For a given angle θ , we obtain the interaction strength between the two atoms by measuring the time evolution of the system in the presence of resonant interactions [30]. In this experiment, $R = 9.1 \mu\text{m}$, $\Omega/2\pi \simeq 5 \text{ MHz}$, and θ varies between -90° and 90° . We first place the system out of resonance ($F_z = 64 \text{ mV/cm}$), where the atoms show weak van der Waals interactions $\leq 1 \text{ MHz}$. We apply an optical π pulse to prepare the two-atom system in the state $|dd\rangle$. We then

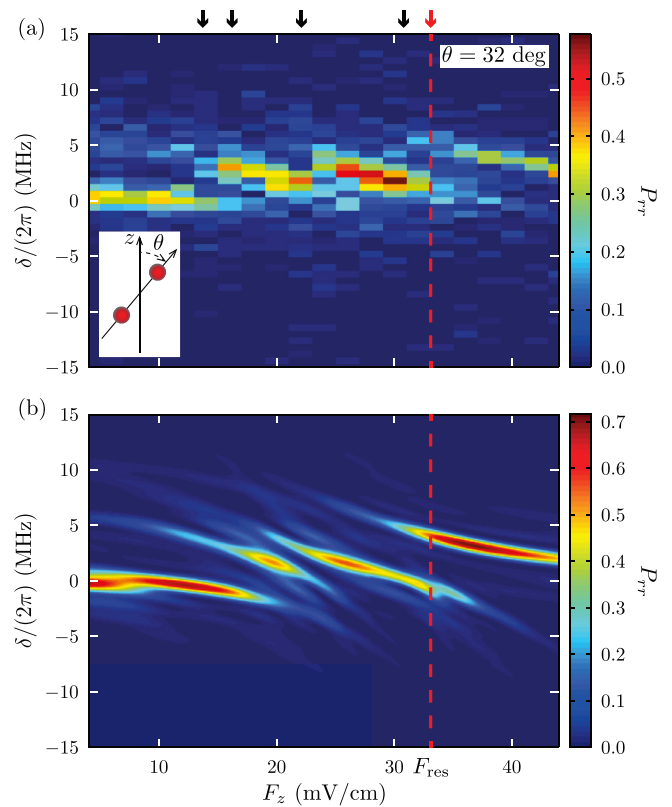


FIG. 1. (Color online) Rydberg excitation spectrum for two atoms with $R = 9.1 \mu\text{m}$ and $\theta = 32^\circ$. The double excitation probability P_{rr} is represented as a function of the detuning δ and the electric field F_z . The red vertical dashed line shows the measured position of the Förster resonance detailed in this Rapid Communication. The bold arrows show the calculated positions of the different resonances. (a) Experimental spectrum. (b) Theoretical spectrum obtained by solving the Schrödinger equation for the system (see text).

switch on abruptly strong resonant interactions by pulsing the electric field to 33 mV/cm with rise and fall times $\leq 10 \text{ ns}$, thus inducing back and forth oscillations between $|dd\rangle$ and $|pf_i\rangle_s$. After an interaction time t , the probability for both atoms to be in the state $|d\rangle$ reads

$$P_{dd}(t) = \cos^2\left(\frac{\sqrt{2}C_3\mathcal{A}_1(\theta)}{\hbar R^3}t\right), \quad (3)$$

where we neglect the influence of other interaction channels. At the end of the sequence, we freeze the dynamics by switching the electric field back to $F_z = 64 \text{ mV/cm}$. To read out the state of the system, we shine a second optical π pulse on the atoms, that couples $|dd\rangle$ back to $|gg\rangle$ while leaving $|pf_i\rangle_s$ unchanged. We measure the probability P_{gg} to detect both atoms in the ground state. Assuming perfect excitation and detection, P_{gg} coincides with P_{dd} .

Figure 2 shows the coherent oscillations observed for different angles θ . The anisotropy of the interaction is evident on the data. For $\theta = 0$ we observe contrasted oscillations with frequency $\nu \simeq 8.6 \pm 0.4 \text{ MHz}$, compatible with the value of C_3 measured using the same experimental sequence and varying R [30]. As we increase θ , we initially observe a decrease of ν . For $\theta \simeq 57^\circ$, the observed dynamics are

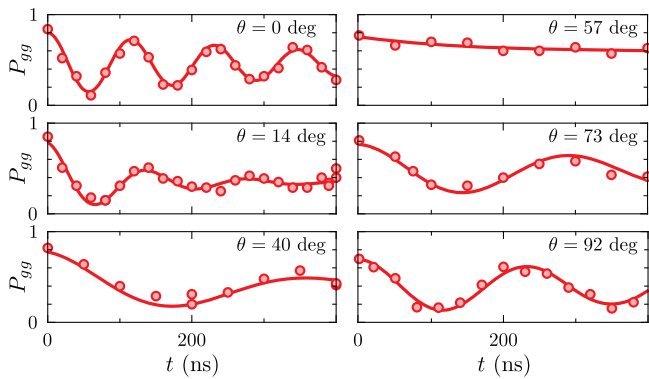


FIG. 2. (Color online) Coherent oscillations at resonance for angles varying between $\theta = 0$ and $\theta = 92^\circ$, where $R = 9.1 \mu\text{m}$. The typical error on P_{gg} is ± 0.05 . Lines are fit to the data by damped sines (see text).

essentially described by an exponential damping. This is compatible with the expected behavior close to the “magic angle” ($\theta_m \simeq 54.7^\circ$) where the strength of resonant interactions vanishes [$\mathcal{A}_1(\theta_m) = 0$], and where one thus expects P_{dd} to stay constant. Further increasing θ leads again to the observation of contrasted oscillations with increasing frequencies. The observed damping originates mainly from dephasing, due to the finite temperature of the atoms and fluctuation in the voltages applied to the electrodes leading, respectively, to shot-to-shot fluctuation of R and of the detuning between $|dd\rangle$ and $|pf_1\rangle_s$. The observation of mainly one frequency in the oscillations confirm that the interaction channel of choice is well isolated.

We obtain the interaction strength as a function of θ by fitting the measured coherent oscillations with damped sines of frequency ν . Figure 3(a) shows a plot of ν as a function of θ . Our measurement procedure does not give access to the sign of the interaction, and we thus infer it from the expected functional form. The error bars represent statistical errors from the fit. For $\theta \simeq 57^\circ$, close to the magic angle, we do not observe any significant oscillation within the limits of experimental accuracy. In this case, we assign the value 0 MHz to the frequency, with an error bar representing the upper frequency one could possibly infer from the measurement and equal to $1/(2t_{\text{max}})$, where $t_{\text{max}} = 700$ ns is our largest interaction time. The data show good agreement with the expected angular dependence $\propto \mathcal{A}_1(\theta)$ plotted as a solid line in Fig. 3(a), where we used the coefficient C_3 measured in [30]. The polar representation of the fitted frequencies as a function of θ exhibits the characteristic shape of the function $(1 - 3 \cos^2 \theta)$, as can be observed in Fig. 3(b).

In the remainder of this Rapid Communication, we analyze theoretically our results. We first consider the situation where no magnetic field is applied on the atoms. Coming back to Eq. (1), terms with the angular prefactor $\mathcal{A}_1(\theta)$ couple $|dd\rangle$ and $|pf_1\rangle_s$ ($\Delta M = 0$). Terms with the angular prefactor $\mathcal{A}_2(\theta)$ couple $|dd\rangle$ and $|pf_2\rangle_s$, with $|f_2\rangle = |57F_{5/2}, m_j = 3/2\rangle$ ($\Delta M = -1$). Finally, terms with the angular prefactor $\mathcal{A}_3(\theta)$ couple $|dd\rangle$ and $|pf_3\rangle_s$, with $|f_3\rangle = |57F_{5/2}, m_j = 1/2\rangle$ ($\Delta M = -2$). In the absence of magnetic field we thus expect three resonances between $|dd\rangle$ and the states $|pf_1\rangle$, $|pf_2\rangle$, and $|pf_3\rangle$.

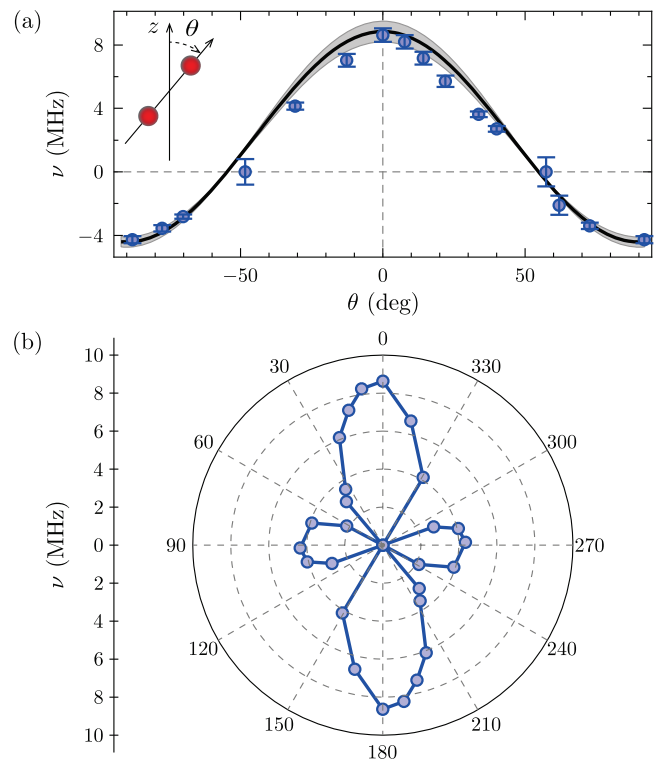


FIG. 3. (Color online) Angular dependence of the interaction. (a) Graph of ν as a function of θ . The solid line plots $-C_3 \mathcal{A}_1(\theta)/(hR^3)$. Error bars show statistical errors in the determination of ν . The shaded area corresponds to a systematic 5% error on the calibration of R . (b) Representation in polar coordinates. By symmetry, the points at angles at $\theta + 180^\circ$ are taken identical to the points at θ .

We now take into account the effect of the 3.3 G magnetic field applied on the atoms during our experiments, leading to energy shifts and to mixing of the different states [37,38]. Figure 4 shows the calculated Stark map for the relevant pair states, where the dipole-dipole interaction has not been included. It was obtained by calculating the (one-atom) level shifts of the states $|p\rangle$, $|d\rangle$, and $|f_i\rangle$ from the diagonalization of the total Hamiltonian, including the Stark and Zeeman effects [42]. The electric dipole matrix elements were obtained numerically using quantum defect theory [20,43,44]. We observe that the magnetic field shifts the pair states energies due to the Zeeman effect, and mixes $|pf_i\rangle_s$ to $|pf_{i+3}\rangle_s$ ($i = 1, 2, 3$), where $|f_4\rangle = |57F_{7/2}, m_j = 5/2\rangle$, $|f_5\rangle = |57F_{7/2}, m_j = 3/2\rangle$, and $|f_6\rangle = |57F_{7/2}, m_j = 1/2\rangle$ (see solid lines paired by colors in Fig. 4). Because all pair states have different polarizabilities, the system exhibits a discrete set of Förster resonances (see bold arrows), at the crossings between the solid colored lines and the black dashed line. The color bar represents the degree of admixture of the different states and shows that the presence of a magnetic field increases the number of expected resonances.

Based on this Stark map, we finally simulated numerically the experimental spectrum of the two-atom system of Fig. 1(a). For that purpose, we first truncated the two-atom basis, retaining only the two-atom states differing in energy by

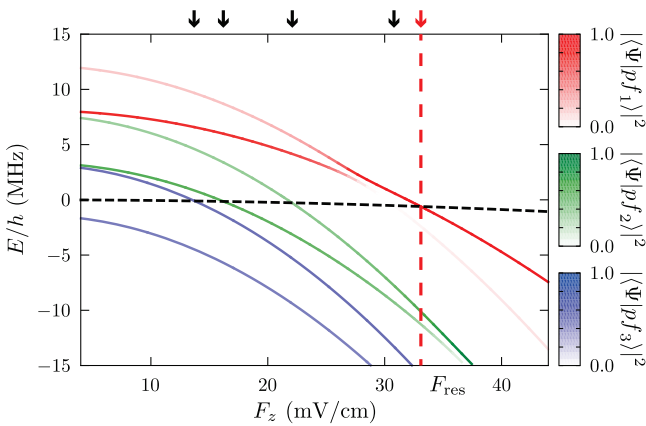


FIG. 4. (Color online) Stark map of the relevant pair states in the presence of a 3.3 G magnetic field. The colored lines plot the eigenenergies of the two-atom system as a function of the electric field. The color scale represents the overlap between the calculated eigenstates $|\Psi\rangle$ and the states $|pf_1\rangle_s$, $|pf_2\rangle_s$, and $|pf_3\rangle_s$. The black dashed line shows the energy of $|dd\rangle$. The solid arrows show the positions of the different resonances. The red vertical dashed line indicates the position of the resonance detailed in this Rapid Communication.

no more than 40 MHz from $|dd\rangle$, and then calculated the restriction of \hat{V}_{dd} to this truncated basis. The result of the calculation, shown in Fig. 1(b), is in good agreement with the experiment regarding the positions and the strengths of the different resonances. For our experimental parameters, we note that we resolve three avoided crossings. We focused in

this Rapid Communication on the crossing between the states $|dd\rangle$ and $|pf_1\rangle_s$ occurring at $F_z \simeq 33$ mV/cm. In this case, the states $|pf_2\rangle_s$ and $|pf_3\rangle_s$ are off-resonant by more than 10 MHz, which ensures that this resonance is well isolated from other interaction channels, as observed on the interaction dynamics. On the contrary, in the absence of magnetic field the energy splitting between the different states (≤ 10 MHz) would not be sufficient to isolate the different channels. Using a finite magnetic field was thus necessary to isolate a single resonance. By reproducing the same procedure with different interaction channels, one could in principle engineer other angular dependencies $\propto \mathcal{A}_2(\theta)$ or $\propto \mathcal{A}_3(\theta)$.

The control over the anisotropy of the dipole-dipole interaction demonstrated in this work will be useful for the implementation of quantum information protocols [45] or for the quantum simulation of many-body spin systems in large two-dimensional arrays of dipole traps [41]. It is also a motivation to revisit, in the presence of anisotropic interactions, effects discussed previously such as the prediction of the breakdown of the Rydberg blockade in the presence of nearly resonant interactions [46], the existence of few-body Förster resonances [47], or the diffusion of spin excitations in complex ensembles of spins with long-range interactions [48,49].

We thank T. Pfau and P. Cheinet for insightful discussions. We acknowledge financial support by the EU [ERC Stg Grant ARENA, Project HAIRS, H2020 FET Proactive project RySQ (Grant No. 640378), Marie-Curie Program ITN COHERENCE FP7-PEOPLE-2010-ITN-265031 (H.L.)], and by the PALM Labex (project QUANTICA).

- [1] I. M. Georgescu, S. Ashhab, and F. Nori, Quantum simulation, *Rev. Mod. Phys.* **86**, 153 (2014).
- [2] J. A. Jones and D. Jaksch, *Quantum Information, Computation and Communication* (Cambridge University Press, Cambridge, 2012).
- [3] D. Jaksch, J. I. Cirac, P. Zoller, S. L. Rolston, R. Côté, and M. D. Lukin, Fast Quantum Gates for Neutral Atoms, *Phys. Rev. Lett.* **85**, 2208 (2000).
- [4] M. D. Lukin, M. Fleischhauer, R. Cote, L. M. Duan, D. Jaksch, J. I. Cirac, and P. Zoller, Dipole Blockade and Quantum Information Processing in Mesoscopic Atomic Ensembles, *Phys. Rev. Lett.* **87**, 037901 (2001).
- [5] H. Weimer, M. Müller, I. Lesanovsky, P. Zoller, and H. P. Büchler, A Rydberg quantum simulator, *Nat. Phys.* **6**, 382 (2010).
- [6] T. F. Gallagher, *Rydberg Atoms* (Cambridge University Press, Cambridge, 1994).
- [7] M. Saffman, T. G. Walker, and K. Mølmer, Quantum information with Rydberg atoms, *Rev. Mod. Phys.* **82**, 2313 (2010).
- [8] E. Urban, T. A. Johnson, T. Henage, L. Isenhower, D. D. Yavuz, T. G. Walker, and M. Saffman, Observation of Rydberg blockade between two atoms, *Nat. Phys.* **5**, 110 (2009).
- [9] A. Gaëtan, Y. Miroshnychenko, T. Wilk, A. Chotia, M. Viteau, D. Comparat, P. Pillet, A. Browaeys, and P. Grangier, Observation of collective excitation of two individual atoms in the Rydberg blockade regime, *Nat. Phys.* **5**, 115 (2009).
- [10] T. Wilk, A. Gaëtan, C. Evellin, J. Wolters, Y. Miroshnychenko, P. Grangier, and A. Browaeys, Entanglement of Two Individual Neutral Atoms Using Rydberg Blockade, *Phys. Rev. Lett.* **104**, 010502 (2010).
- [11] L. Isenhower, E. Urban, X. L. Zhang, A. T. Gill, T. Henage, T. A. Johnson, T. G. Walker, and M. Saffman, Demonstration of a Neutral Atom Controlled-NOT Quantum Gate, *Phys. Rev. Lett.* **104**, 010503 (2010).
- [12] D. Comparat and P. Pillet, Dipole blockade in a cold Rydberg atomic sample, *J. Opt. Soc. Am. B* **27**, A208 (2010).
- [13] D. Barredo, S. Ravets, H. Labuhn, L. Béguin, A. Vernier, F. Nogrette, T. Lahaye, and A. Browaeys, Demonstration of a Strong Rydberg Blockade in Three-Atom Systems with Anisotropic Interactions, *Phys. Rev. Lett.* **112**, 183002 (2014).
- [14] A. M. Hankin, Y.-Y. Jau, L. P. Parazzoli, C. W. Chou, D. J. Armstrong, A. J. Landahl, and G. W. Biedermann, Two-atom Rydberg blockade using direct $6s$ to np excitation, *Phys. Rev. A* **89**, 033416 (2014).
- [15] Y.-Y. Jau, A. M. Hankin, T. Keating, I. H. Deutsch, and G. W. Biedermann, Entangling atomic spins with a strong Rydberg-dressed interaction, [arXiv:1501.03862](https://arxiv.org/abs/1501.03862).
- [16] W. R. Anderson, J. R. Veale, and T. F. Gallagher, Resonant Dipole-Dipole Energy Transfer in a Nearly Frozen Rydberg Gas, *Phys. Rev. Lett.* **80**, 249 (1998).

- [17] I. Mourachko, D. Comparat, F. de Tomasi, A. Fioretti, P. Nosbaum, V. M. Akulin, and P. Pillet, Many-Body Effects in a Frozen Rydberg Gas, *Phys. Rev. Lett.* **80**, 253 (1998).
- [18] G. Günter, H. Schempp, M. Robert-de-Saint-Vincent, V. Gavryusev, S. Helmrich, C. S. Hofmann, S. Whitlock, and M. Weidemüller, Observing the dynamics of dipole-mediated energy transport by interaction-enhanced imaging, *Science* **342**, 954 (2013).
- [19] D. Barredo, H. Labuhn, S. Ravets, T. Lahaye, A. Browaeys, and C. S. Adams, Coherent Excitation Transfer in a Spin Chain of Three Rydberg Atoms, *Phys. Rev. Lett.* **114**, 113002 (2015).
- [20] A. Reinhard, T. C. Liebisch, B. Knuffman, and G. Raitzel, Level shifts of rubidium Rydberg states due to binary interactions, *Phys. Rev. A* **75**, 032712 (2007).
- [21] T. G. Walker and M. Saffman, Consequences of Zeeman degeneracy for the van der Waals blockade between Rydberg atoms, *Phys. Rev. A* **77**, 032723 (2008).
- [22] L. G. Marcassa and J. P. Shaffer, Interactions in Ultracold Rydberg Gases, in *Advances in Atomic, Molecular, and Optical Physics*, edited by E. Arimondo, P. R. Berman, and C. C. Lin, Vol. 63 (Academic, New York, 2014), pp. 47–133.
- [23] B. Vermersch, A. W. Glaetzle, and P. Zoller, Magic distances in the blockade mechanism of Rydberg p and d states, *Phys. Rev. A* **91**, 023411 (2015).
- [24] C. Slichter, *Principles of Magnetic Resonance*, Springer Series in Solid-State Sciences (Springer, Berlin, Heidelberg, 1990).
- [25] K.-K. Ni, S. Ospelkaus, D. J. Nesbitt, J. Ye, and D. S. Jin, A dipolar gas of ultracold molecules, *Phys. Chem. Chem. Phys.* **11**, 9626 (2009).
- [26] K. R. A. Hazzard, B. Gadway, M. Foss-Feig, B. Yan, S. A. Moses, J. P. Covey, N. Y. Yao, M. D. Lukin, J. Ye, D. S. Jin, and A. M. Rey, Many-Body Dynamics of Dipolar Molecules in an Optical Lattice, *Phys. Rev. Lett.* **113**, 195302 (2014).
- [27] T. Lahaye, C. Menotti, L. Santos, M. Lewenstein, and T. Pfau, The physics of dipolar bosonic quantum gases, *Rep. Prog. Phys.* **72**, 126401 (2009).
- [28] T. J. Carroll, K. Claringbould, A. Goodsell, M. J. Lim, and M. W. Noel, Angular Dependence of the Dipole-Dipole Interaction in a Nearly One-Dimensional Sample of Rydberg Atoms, *Phys. Rev. Lett.* **93**, 153001 (2004).
- [29] J. S. Cabral, J. M. Kondo, L. F. Gonçalves, V. A. Nascimento, L. G. Marcassa, D. Booth, J. Tallant, A. Schwettmann, K. R. Overstreet, J. Sedlacek, and J. P. Shaffer, Effects of electric field on ultracold Rydberg atom interactions, *J. Phys. B* **44**, 184007 (2011).
- [30] S. Ravets, H. Labuhn, D. Barredo, L. Béguin, T. Lahaye, and A. Browaeys, Coherent dipole-dipole coupling between two single Rydberg atoms at an electrically-tuned Förster resonance, *Nat. Phys.* **10**, 914 (2014).
- [31] T. G. Walker and M. Saffman, Zeros of Rydberg–Rydberg Förster interactions, *J. Phys. B: At. Mol., Opt. Phys.* **38**, S309 (2005).
- [32] W. R. Anderson, M. P. Robinson, J. D. D. Martin, and T. F. Gallagher, Dephasing of resonant energy transfer in a cold Rydberg gas, *Phys. Rev. A* **65**, 063404 (2002).
- [33] M. Mudrich, N. Zahzam, T. Vogt, D. Comparat, and P. Pillet, Back and Forth Transfer and Coherent Coupling in a Cold Rydberg Dipole Gas, *Phys. Rev. Lett.* **95**, 233002 (2005).
- [34] T. Vogt, M. Viteau, A. Chotia, J. Zhao, D. Comparat, and P. Pillet, Electric-Field Induced Dipole Blockade with Rydberg Atoms, *Phys. Rev. Lett.* **99**, 073002 (2007).
- [35] C. S. E. van Ditzhuijzen, A. F. Koenderink, J. V. Hernández, F. Robicheaux, L. D. Noordam, and H. B. van Linden van den Heuvell, Spatially Resolved Observation of Dipole-Dipole Interaction between Rydberg Atoms, *Phys. Rev. Lett.* **100**, 243201 (2008).
- [36] I. I. Ryabtsev, D. B. Tretyakov, I. I. Beterov, and V. M. Entin, Observation of the Stark-Tuned Förster Resonance between Two Rydberg Atoms, *Phys. Rev. Lett.* **104**, 073003 (2010).
- [37] J. Nipper, J. B. Balewski, A. T. Krupp, B. Butscher, R. Löw, and T. Pfau, Highly Resolved Measurements of Stark-Tuned Förster Resonances between Rydberg Atoms, *Phys. Rev. Lett.* **108**, 113001 (2012).
- [38] J. Nipper, J. B. Balewski, A. T. Krupp, S. Hofferberth, R. Löw, and T. Pfau, Atomic Pair-State Interferometer: Controlling and Measuring an Interaction-Induced Phase Shift in Rydberg-Atom Pairs, *Phys. Rev. X* **2**, 031011 (2012).
- [39] The electric field required to reach the resonance is weak enough to be in a regime of induced dipoles, by opposition to rigid dipoles.
- [40] L. Béguin, A. Vernier, R. Chicireanu, T. Lahaye, and A. Browaeys, Direct Measurement of the van der Waals Interaction between Two Rydberg Atoms, *Phys. Rev. Lett.* **110**, 263201 (2013).
- [41] F. Nogrette, H. Labuhn, S. Ravets, D. Barredo, L. Béguin, A. Vernier, T. Lahaye, and A. Browaeys, Single-Atom Trapping in Holographic 2D Arrays of Microtraps with Arbitrary Geometries, *Phys. Rev. X* **4**, 021034 (2014).
- [42] For the Stark map calculation of the states $|f_i\rangle$, we found it necessary to include a large number of states in the basis to achieve convergence. Note that, due to the proximity of the hydrogenic manifold, the $B = 3.3$ G magnetic field cannot be taken into account perturbatively in the calculation. Here, we thus used a basis containing 756 states, with $3 \leq L \leq 56$, $-3 \leq m_L \leq 3$, and $-1/2 \leq m_S \leq 1/2$.
- [43] W. Li, I. Mourachko, M. W. Noel, and T. F. Gallagher, Millimeter-wave spectroscopy of cold Rb Rydberg atoms in a magneto-optical trap: Quantum defects of the ns , np , and nd series, *Phys. Rev. A* **67**, 052502 (2003).
- [44] J. Han, Y. Jamil, D. V. L. Norum, P. J. Tanner, and T. F. Gallagher, Rb nf quantum defects from millimeter-wave spectroscopy of cold ^{85}Rb Rydberg atoms, *Phys. Rev. A* **74**, 054502 (2006).
- [45] M. Müller, I. Lesanovsky, H. Weimer, H. P. Büchler, and P. Zoller, Mesoscopic Rydberg Gate Based on Electromagnetically Induced Transparency, *Phys. Rev. Lett.* **102**, 170502 (2009).
- [46] T. Pohl and P. R. Berman, Breaking the Dipole Blockade: Nearly Resonant Dipole Interactions in Few-Atom Systems, *Phys. Rev. Lett.* **102**, 013004 (2009).
- [47] J. H. Gurian, P. Cheinet, P. Huillery, A. Fioretti, J. Zhao, P. L. Gould, D. Comparat, and P. Pillet, Observation of a Resonant Four-Body Interaction in Cold Cesium Rydberg Atoms, *Phys. Rev. Lett.* **108**, 023005 (2012).
- [48] R. Côté, A. Russell, E. E. Eyler, and P. L. Gould, Quantum random walk with Rydberg atoms in an optical lattice, *New J. Phys.* **8**, 156 (2006).
- [49] S. Wüster, C. Ates, A. Eisfeld, and J. M. Rost, Newton’s Cradle and Entanglement Transport in a Flexible Rydberg Chain, *Phys. Rev. Lett.* **105**, 053004 (2010).

A highly-tunable quantum simulator of spin systems using two-dimensional arrays of single Rydberg atoms

Henning Labuhn,¹ Daniel Barredo,¹ Sylvain Ravets,¹ Sylvain de Léséleuc,¹ Tommaso Macrì,² Thierry Lahaye,¹ and Antoine Browaeys¹

¹Laboratoire Charles Fabry, Institut d'Optique, CNRS, Univ Paris Sud 11, 2 avenue Augustin Fresnel, 91127 Palaiseau cedex, France

²Departamento de Física Teórica e Experimental, Universidade Federal do Rio Grande do Norte, and International Institute of Physics, Natal-RN, Brazil.

(Dated: October 5, 2015)

Quantum simulation of spin Hamiltonians is currently a very active field of research, using different implementations such as trapped ions, superconducting qubits, or ultracold atoms in optical lattices. All of these approaches have their own assets and limitations. Here, we report on a novel platform for quantum simulation of spin systems, using individual atoms trapped in highly-tunable two-dimensional arrays of optical microtraps, that interact via strong, anisotropic interactions when excited to Rydberg D -states. We illustrate the versatility of our system by studying the dynamics of an Ising-like spin-1/2 system in a transverse field with up to thirty spins, for a variety of geometries in one and two dimensions, and for a wide range of interaction strengths. Our data agree well with numerical simulations of the spin-1/2 model except at long times, where we observe deviations that we attribute to the multilevel structure of Rydberg D -states.

Spin models are the prime example of simplified many-body Hamiltonians used to model complex, real-world strongly correlated materials [1, 2]. However, despite their simplified character, their dynamics often cannot be simulated exactly on classical computers as soon as the number of particles exceeds a few tens. For this reason, the quantum simulation [3] of spin Hamiltonians using the tools of atomic and molecular physics has become very active over the last years. A first, “top-down” approach consists in using ultracold atoms [4] or molecules [5] in optical lattices. Thousands of spins can then be studied, in one, two, or three dimensions, but couplings are weak, access to local observables is challenging, and geometries are relatively constrained. A second, “bottom-up” approach uses ions [6]; there, interactions are tunable and local measurements are easy, but the number of spins that can be simulated remains moderate, and extension beyond one dimension, although doable in principle [7], is technically challenging.

Rydberg atoms have recently attracted a lot of interest for quantum information processing [8] and quantum simulation [9]. For the simulation of spin Hamiltonians, arrays of single atoms trapped in optical tweezers and then excited to Rydberg states hold the promise to bridge the gap between trapped ions and quantum gases in lattices; moreover, the possibility to engineer anisotropic interactions using Rydberg states with an angular momentum $L > 0$ opens exciting prospects for creating intriguing states of matter [10]. Here, we demonstrate a scalable quantum simulator of the dynamics of spin Hamiltonians that combines, for up to $N \sim 30$ spins, (i) strong, highly-tunable, and anisotropic couplings, (ii) the possibility to vary at will the geometry of the array, in one and two dimensions, with e.g. 1D spin chains with periodic boundary conditions (PBC) and (iii) access to local observables. In addition, while for short times our observations validate a model of spin 1/2 particles with anisotropic interactions, residual deviations at long times show that the complex multilevel structure of Rydberg atoms [11–13] needs

to be taken into account for future experiments.

By shining on the array lasers that are resonant with the transition between the ground state $|g\rangle$ and a chosen Rydberg

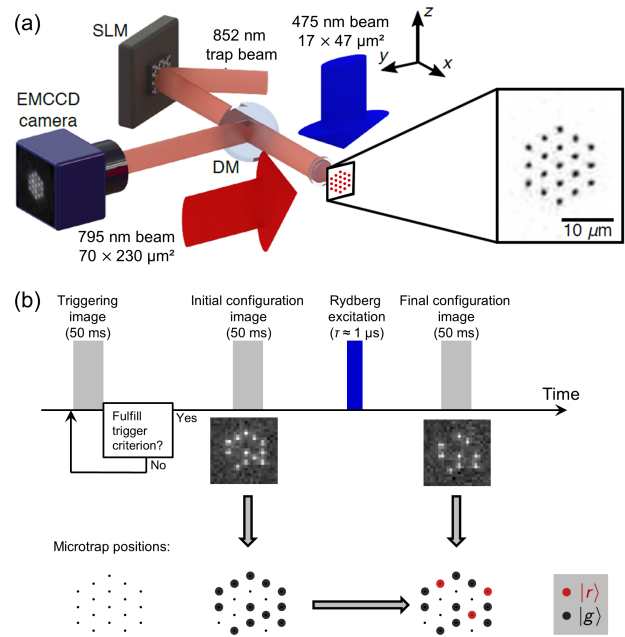


FIG. 1: Experimental platform. (a): An array of microtraps is created by imprinting an appropriate phase on a dipole-trap beam. Site-resolved fluorescence of the atoms, at 780 nm, is imaged on a camera using a dichroic mirror (DM). Rydberg excitation beams at 795 and 475 nm are shone onto the atoms. (b): Sketch of an experimental sequence. During loading, the camera images are analyzed continuously to extract the number of loaded traps. As soon as a triggering criterion is met, the loading is stopped and an image of the initial configuration is acquired. After Rydberg excitation, a final image is acquired, revealing the atoms excited to Rydberg states (red disks).

state $|r\rangle$, we implement the Ising-like Hamiltonian

$$H = \sum_i \frac{\hbar\Omega}{2} \sigma_x^i + \sum_{i<j} V_{ij} n^i n^j, \quad (1)$$

which acts on the pseudo-spin states $|\downarrow\rangle_i$ and $|\uparrow\rangle_i$ corresponding to states $|g\rangle$ and $|r\rangle$ of atom i , respectively. Here, Ω is the Rabi frequency of the laser coupling, the σ_α^i ($\alpha = x, y, z$) are the Pauli matrices acting on atom i , and $n^i = (1 + \sigma_z^i)/2$ is the number of Rydberg excitations (0 or 1) on site i . The coupling term V_{ij} arises from the van der Waals interaction between atoms i and j when they are both in $|r\rangle$, and scales as $C_6(\theta)|\mathbf{r}_i - \mathbf{r}_j|^{-6}$ with the separation between the atoms. Moreover, by using $|nD_{3/2}, m_j = 3/2\rangle$ states for $|r\rangle$, the interaction strength is anisotropic [14], varying by a factor ~ 3 when the angle θ between the interatomic axis and the quantization axis \hat{z} changes from 0 to $\pi/2$ [11, 15].

Our setup (Fig. 1a) has been described in [16, 17]. We trap cold ($T \simeq 30 \mu\text{K}$) single ^{87}Rb atoms in optical traps with a $1 \mu\text{m}$ waist. We create arbitrary, two-dimensional arrays containing $1 \leq N_t \leq 50$ traps, separated by distances $a > 3 \mu\text{m}$, using a spatial light modulator (SLM) to imprint an appropriate phase on the trapping beam prior to focusing. The atomic fluorescence at 780 nm is imaged onto a camera. We observe, in the single-atom regime [18], that the level of fluorescence for each trap alternates randomly between two levels, corresponding to the presence of 0 or 1 atom. The analysis of these N_t fluorescence traces allows us to record, with a time resolution of 50 ms, the current number N of single atoms in the array.

As illustrated in Figure 1b, as soon as N exceeds a pre-defined threshold, we trigger the following experimental sequence. First, the loading of the array is stopped, and a fluorescence image is acquired to record the *initial configuration* of the atoms, i.e. which traps are filled. After initializing all the atoms in $|g\rangle = |5S_{1/2}, F = 2, m_F = 2\rangle$ by optical pumping, a two-photon Rydberg excitation pulse of duration τ (up to a few microseconds) is shone onto the array; the Rabi frequency ($\Omega \simeq 2\pi \times 1 \text{ MHz}$) is uniform to within 10% over our largest arrays. At the end of the sequence, we acquire a new image, of the *final configuration*. Atoms excited to $|r\rangle$ have quickly escaped the trapping region, and thus we observe only the atoms that were in $|g\rangle$ after excitation. The atoms gone in between the initial and final images are thus assigned to Rydberg states (red dots in Figure 1b). This detection method has a high efficiency: it only gives a small number of “false positives”, as an atom also has a probability $\varepsilon \simeq (3 \pm 1)\%$ to be lost, independently of its internal state [14].

We first test our system in the conceptually simple situation of fully Rydberg-blockaded ensembles containing up to $N = 15$ atoms. Figure 2a shows, for various arrays, the probability that all N atoms are in $|g\rangle$ at the end of the sequence. We observe high-contrast coherent oscillations, with a frequency enhanced by a factor \sqrt{N} with respect to the single-atom case (Fig. 2b). This characteristic collective oscillation is the hallmark of Rydberg blockade [19–21], where multiple excitations are inhibited within a blockaded volume. Here, due to the anisotropy of the interactions, the blockade volume is well approximated by a slightly prolate ellipsoid with

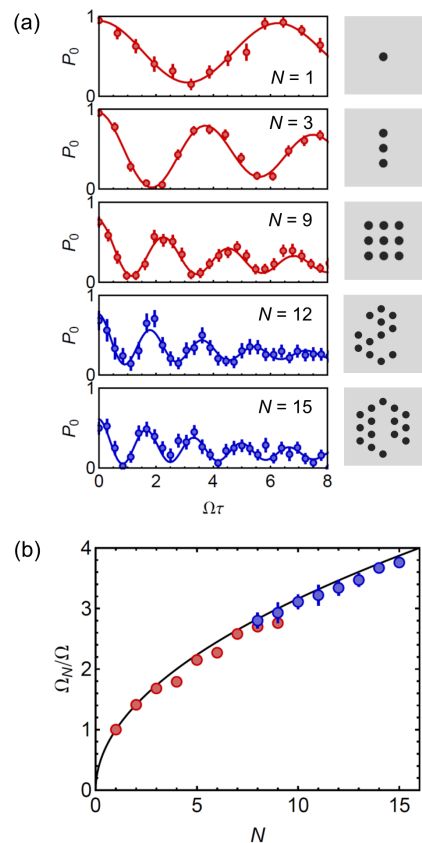


FIG. 2: Collective oscillations in the full Rydberg blockade regime. (a): Probability P_0 for all N atoms to be in $|g\rangle$ after an excitation pulse of area $\Omega\tau$. Red points: fully loaded arrays, $n = 82$; blue points: partially loaded triangular arrays of $N_t = 19$ traps, $n = 100$ (error bars show the quantum projection noise for ~ 100 repetitions of the experiment). Solid lines are fits by damped sines of frequency Ω_N [14]. (b): Collective oscillation frequency Ω_N/Ω versus N (error bars —sometimes smaller than the symbol size— are statistical). The solid line is the expected \sqrt{N} enhancement.

a major semi-axis R_b defined by $\hbar\Omega = |C_6(0)|/R_b^6$. This observation is a first step towards the creation of long-lived $|W\rangle$ states in the ground state [8].

The fully blockaded regime remains easy to describe theoretically as blockade naturally truncates the size of the Hilbert space. In contrast, a more challenging regime corresponds to the Rydberg blockade being effective only between nearest neighbors, such that for long enough excitation times, the number of excitations becomes $\sim N/2$. It is therefore desirable to be able to vary the ratio $\alpha = R_b/a$ of the blockade radius to the distance a between sites: for very small or large values of α , the dynamics is simple and the system can easily be compared to numerics, while, for intermediate values of α , the dynamics is challenging to calculate and experimental quantum simulation becomes a method of choice. Our setup is particularly adapted to this goal, as we can vary easily both a (reconfiguring the SLM) and R_b (changing the principal quantum number n , we dramatically tune C_6 , which scales

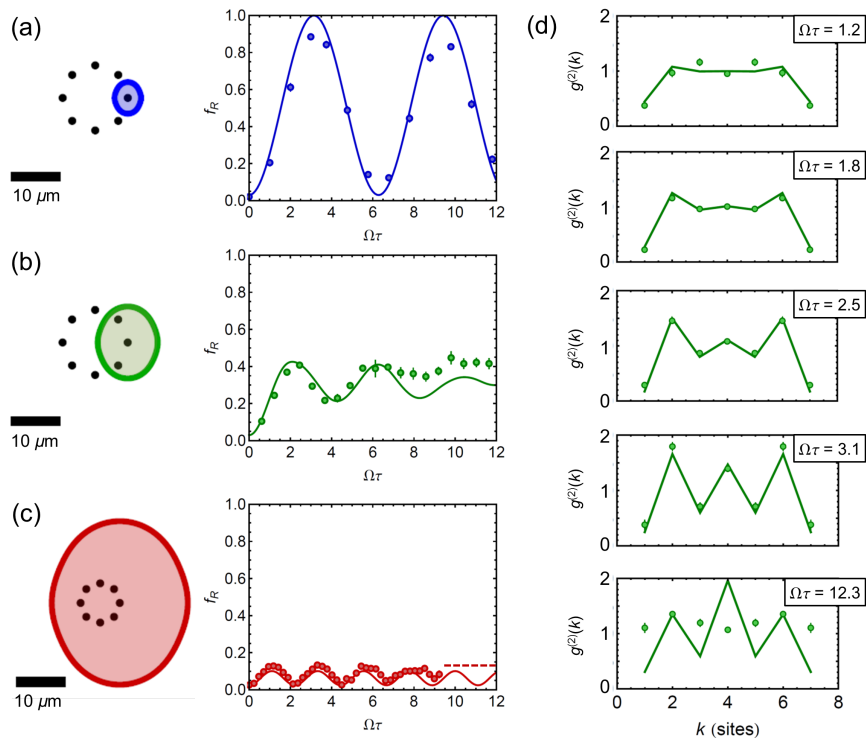


FIG. 3: Tuning interactions in an 8-spin chain with PBC. (a): Independent atoms ($R_b < a$). The Rydberg fraction f_R oscillates between $\simeq 0$ and $\simeq 1$, with the single-atom Rabi frequency Ω . (b): Strongly correlated regime ($R_b \simeq 1.5a$). The Rydberg fraction shows an oscillatory behavior involving several frequencies. (c): Fully blocked regime: f_R oscillates at $\sqrt{N}\Omega$, and reaches a maximum of $1/N$ (dashed line). (d): The Rydberg-Rydberg pair correlation function, for the parameters of (b), is shown for increasing values of $\Omega\tau$. In all plots, the solid lines are obtained by numerically solving the time-dependent Schrödinger equation, and then including detection errors ($\varepsilon = 3\%$). Error bars (often smaller than symbol size) denote s.e.m. The shaded ellipsoids illustrate the blockade volume.

approximately as n^{11} .

This versatility is illustrated in Fig. 3, where we use a fully loaded ring-shaped array of $N = 8$ traps, thus realizing a small spin chain with PBC. By varying both a and n , we tune the system all the way from independent atoms ($\alpha \ll 1$), where each atom undergoes a Rabi oscillation at frequency Ω , resulting in a *Rydberg fraction* f_R (defined as the average number of Rydberg excitations divided by N) periodically reaching $\simeq 1$ (Fig. 3a), to a fully blocked array ($\alpha \gg 1$, Fig. 3c) characterized by collective oscillations at frequency $\sqrt{N}\Omega$ and a maximum $f_R = 1/N$. In between (Fig. 3b, where $\alpha \simeq 1.5$), the evolution of $f_R(\tau)$ shows oscillations resulting from the beating of incommensurate frequencies. Our system allows us to detect the state of each atom, and thus to measure correlation functions. Figure 3d shows the dynamics of the Rydberg-Rydberg pair correlation function

$$g^{(2)}(k) = \frac{1}{N_t} \sum_i \frac{\langle n_i n_{i+k} \rangle}{\langle n_i \rangle \langle n_{i+k} \rangle}. \quad (2)$$

The averaging over all traps does not wash out correlations despite the fact that the system is not fully invariant by translation [14]. We observe a strong suppression of $g^{(2)}(k)$ for $k = 1$ and $k = 7$, i.e. a clear signature of nearest-neighbor blockade. For some times (see e.g. $\Omega\tau = 3.1$), an

antiferromagnetic-like staggered correlation function (while the average density is uniform [14]).

The solid lines in all panels of Figure 3 are obtained by solving the Schrödinger equation governed by (1) using the independently measured experimental parameters, and then including the effects of the finite detection errors ε [14]. One observes an overall agreement with the data, although some small discrepancies can clearly be noticed, especially at long times. We attribute them to the Zeeman structure of Rydberg D -states, which is not taken into account in our modeling by a spin-1/2: for $\theta \neq 0$, the van der Waals interaction couples $|r\rangle$ to other Zeeman states, leading to a slow increase in the number of excitations [14]. The overall agreement between the data and the numerics, however, suggests that our system is able to provide us with a correct picture of the dynamics in larger systems.

We now demonstrate this ability for two larger systems. We first consider a one-dimensional spin chain with PBC comprising $N_t = 30$ traps and partially loaded with $N = 20 \pm 1$ atoms (Figure 4a). Its ‘racetrack’ shape was chosen to optimize homogeneity of the Rabi frequency over the array. We chose parameters such that $\alpha \simeq 4.3(1)$. The Rydberg fraction $f_R(\tau)$ shows initial oscillations before reaching a steady state (Fig. 4b). The pair correlation function (shown in Fig. 4c for $\Omega\tau \simeq 2.0$) is strongly suppressed for $k < \alpha$, as expected from

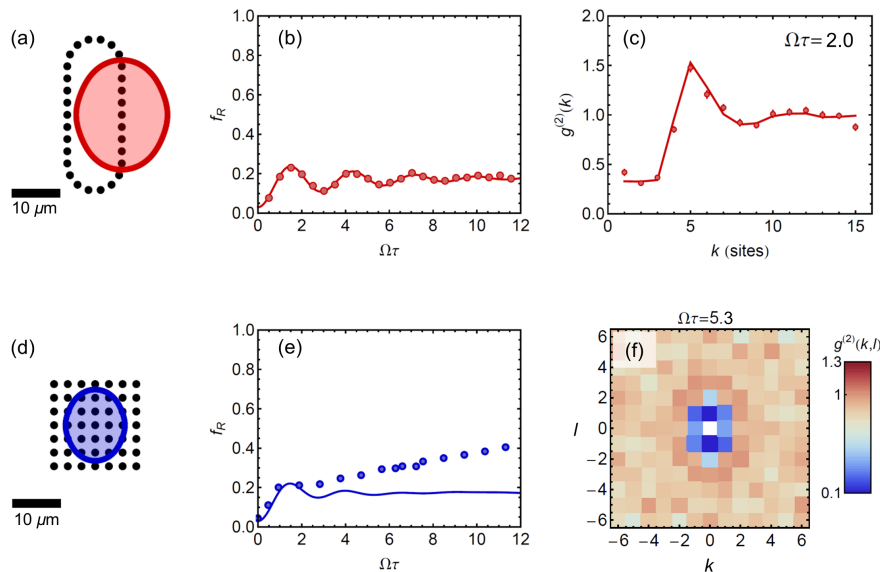


FIG. 4: Ising dynamics in large spin ensembles. (a): Racetrack-shaped array with $N_t = 30$ traps, loaded with $N = 20 \pm 2$ atoms. The blockade radius R_b is about $4.3a$ (shaded ellipsoid). (b): Time evolution of the Rydberg fraction f_R . (c): Rydberg pair correlation function $g^{(2)}(k)$ for $\Omega\tau \simeq 2.0$, showing a strong depletion for $k < R_b$, and contrasted oscillations around the asymptotic value 1. Error bars (most of the time smaller than symbol size) denote the s.e.m. Solid lines are the simulation results without any adjustable parameters (see [14] for details). (d): Square array of 7×7 traps loaded with $N = 28 \pm 2$ atoms. The blockade radius is about $2.6a$. (e): Evolution of f_R . (f): Rydberg-Rydberg correlation function $g^{(2)}(k, l)$ for $\Omega\tau = 5.3$.

blockade physics, before oscillating towards the asymptotic value $g^{(2)}(k \gg \alpha) = 1$ [22, 23]. A similar liquid-like correlation function has been observed in two dimensions in [24]. The solid lines in Fig. 4b,c give the result of a full numerical simulation, without any adjustable parameters. Here the agreement with the spin-1/2 model is excellent, as many atom pairs are aligned along the quantization axis, thus making the effects of the anisotropy small. We included the finite value of ε , which has a strong effect for $k < \alpha$ as it increases $g^{(2)}(k)$ from 0 to $2\varepsilon/f_R$ [14].

As a final setting, we use a $N_t = 7 \times 7$ two-dimensional square array, loaded with $N = 28 \pm 2$ atoms (Fig. 4d). The blockade is effective between nearest and next-nearest neighbors ($\alpha = 2.6$). The dynamics of f_R now appears monotonous, without the initial oscillations seen above for smaller systems (Fig. 4e). This suggests that already with $N \sim 30$ atoms, the behavior of the system is close to the many-body one observed in large ensembles (see e.g. [25]) with an initial fast rise of the Rydberg fraction, before it saturates. The simulation captures well the initial rise of f_R , but does not reproduce the slow increase observed at long times, which we attribute again to multilevel effects (that are indeed expected to be strong in this array where the internuclear axis of many pairs lie at a large angle θ). Figure 4f shows the two-dimensional Rydberg-Rydberg correlation function

$$g^{(2)}(k, l) = \frac{1}{N_t} \sum_{i,j} \frac{\langle n_{i,j} n_{i+k,j+l} \rangle}{\langle n_{i,j} \rangle \langle n_{i+k,j+l} \rangle} \quad (3)$$

where $n_{i,j}$ refers to the site with coordinates (ia, ja) . Although the system has open boundaries and thus does not

show translational invariance, the averaging over the traps in Eq. (3) does not wash out correlations as R_b is small compared to the system size. We observe a clear depletion of the correlation function close to the origin due to blockade. The anisotropy of the interaction is visible, as the depletion region is roughly elliptical, with a ratio of principal axes of about 1.2 compatible with the expected ‘flattening’ $3^{1/6}$ of the surfaces of constant interaction. The full time evolution of the correlation function is shown in the Supplementary Material [14].

The tunability of geometry and interactions demonstrated here opens many avenues for the quantum simulation of spin systems with tens of particles. Our platform is ideal for studying the transition from few- to many-body physics [26], thermalization in strongly interacting closed quantum systems [27], or the dynamical emergence of entanglement following a quantum quench [28]. Using resonant dipole-dipole interactions between different Rydberg states [29], one can also implement XY Hamiltonians with long-range couplings [30]. Finally, exploiting the Zeeman structure of Rydberg states holds the promise of implementing more complex Hamiltonians, to explore for instance the physics of higher spins [31], or realize topological insulators [32].

We thank H. Busche for contributions in the early stages of the experiment, I. Lesanovsky, H.P. Büchler, and T. Pohl for useful discussions, and Y. Sortais for a careful reading of the manuscript. This work benefited from financial support by the EU [FET-Open Xtrack Project HAIRS, H2020 FET-PROACT Project RySQ, and EU Marie-Curie Program ITN COHERENCE FP7-PEOPLE-2010-ITN-265031 (H. L.)], by the ‘PALM’ Labex (project QUANTICA) and by the Region

-
- [1] S. Sachdev, *Quantum phase transitions* (Cambridge University Press, Cambridge, 2011).
- [2] A. Auerbach, *Interacting Electrons and Quantum Magnetism* (Springer-Verlag, New York, 1994).
- [3] I.M. Georgescu, S. Ashhab, F. Nori, *Quantum simulation*. *Rev. Mod. Phys.* **86**, 153 (2014).
- [4] I. Bloch, J. Dalibard, S. Nascimbène, *Quantum simulations with ultracold quantum gases*. *Nature Phys.* **8**, 267 (2012).
- [5] B. Yan, S. A. Moses, B. Gadway, J. P. Covey, K. R. A. Hazzard, A. M. Rey, D. S. Jin, J. Ye, *Observation of dipolar spin-exchange interactions with lattice-confined polar molecules*. *Nature* **501**, 521 (2013).
- [6] R. Blatt, C. F. Roos, *Quantum simulations with trapped ions*. *Nature Phys.* **8**, 277 (2012).
- [7] S. Korenblit, D. Kafri, W.C. Campbell, R. Islam, E.E. Edwards, Z.-X. Gong, G.-D. Lin, L.-M. Duan, J. Kim, K. Kim., C. Monroe, *Quantum simulation of spin models on an arbitrary lattice with trapped ions*. *New J. Phys.* **14**, 095024 (2012).
- [8] M. Saffman, T. G. Walker, K. Mølmer, *Quantum information with Rydberg atoms*. *Rev. Mod. Phys.* **82**, 2313 (2010).
- [9] H. Weimer, M. Müller, I. Lesanovsky, P. Zoller, H. P. Büchler, *A Rydberg quantum simulator*. *Nat. Phys.* **6**, 382 (2010).
- [10] A.W. Glaetzle, M. Dalmonte, R. Nath, I. Rousochatzakis, R. Moessner, P. Zoller, *Quantum Spin-Ice and Dimer Models with Rydberg Atoms*. *Phys. Rev. X* **4**, 041037 (2014).
- [11] B. Vermersch, A.W. Glaetzle, P. Zoller, *Magic distances in the blockade mechanism of Rydberg P and D states*. *Phys. Rev. A* **91**, 023411 (2015).
- [12] C. Tresp, P. Bienias, S. Weber, H. Gorniaczyk, I. Mirgorodskiy, H.P. Büchler, S. Hofferberth, *Dipolar dephasing of Rydberg D-state polaritons*. *Phys. Rev. Lett.* **115**, 083602 (2015).
- [13] A. Derevianko, P. Komar, T. Topcu, R.M. Kroeze, M.D. Lukin, *Effects of molecular resonances on Rydberg blockade*. [arXiv:1508.02480](https://arxiv.org/abs/1508.02480).
- [14] See Supplementary Material for details.
- [15] D. Barredo, S. Ravets, H. Labuhn, L. Béguin, A. Vernier, F. Nogrette, T. Lahaye, and A. Browaeys, *Demonstration of a Strong Rydberg Blockade in Three-Atom Systems with Anisotropic Interactions*. *Phys. Rev. Lett.* **112**, 183002 (2014).
- [16] L. Béguin, A. Vernier, R. Chicireanu, T. Lahaye, A. Browaeys, *Direct Measurement of the van der Waals Interaction between Two Rydberg Atoms*. *Phys. Rev. Lett.* **110**, 263201 (2013).
- [17] F. Nogrette, H. Labuhn, S. Ravets, D. Barredo, L. Béguin, A. Vernier, T. Lahaye, A. Browaeys, *Single-Atom Trapping in Holographic 2D Arrays of Microtraps with Arbitrary Geometries*. *Phys. Rev. X* **4**, 021034 (2014).
- [18] N. Schlosser, G. Reymond, I. Protsenko, P. Grangier, *Subpoissonian loading of single atoms in a microscopic dipole trap*. *Nature* **411**, 1024 (2001).
- [19] Y. O. Dudin, L. Li, F. Bariani, A. Kuzmich, *Observation of coherent many-body Rabi oscillations*. *Nat. Phys.* **8**, 790 (2012).
- [20] M. Ebert, A. Gill, M. Gibbons, X. Zhang, M. Saffman, T.G. Walker, *Atomic Fock state preparation using Rydberg blockade*. *Phys. Rev. Lett.* **112**, 043602 (2014).
- [21] J. Zeiher, P. Schauß, S. Hild, T. Macrì, I. Bloch, C. Gross, *Microscopic Characterization of Scalable Coherent Rydberg Superatoms*. *Phys. Rev. X* **5**, 031015 (2015).
- [22] C. Ates, I. Lesanovsky, *Entropic enhancement of spatial correlations in a laser-driven Rydberg gas*. *Phys. Rev. A* **86** 013408 (2012).
- [23] D. Petrosyan, M. Hönig, M. Fleischhauer, *Spatial correlations of Rydberg excitations in optically driven atomic ensembles*. *Phys. Rev. A* **87**, 053414 (2013).
- [24] P. Schauss, M. Cheneau, M. Endres, T. Fukuhara, S. Hild, A. Omran, T. Pohl, C. Gross, S. Kuhr, I. Bloch, *Observation of Spatially Ordered Structures in a Two-Dimensional Rydberg Gas*. *Nature* **491**, 87 (2012).
- [25] R. Löw, H. Weimer, U. Krohn, R. Heidemann, V. Bendkowsky, B. Butscher, H.P. Büchler, T. Pfau, *Universal scaling in a strongly interacting Rydberg gas*. *Phys. Rev. A* **80**, 033422 (2009).
- [26] A. Gaj, A. T. Krupp, J. B. Balewski, R. Löw, S. Hofferberth, T. Pfau, *From molecular spectra to a density shift in dense Rydberg gases*. *Nature Comm.* **5**, 4546 (2014).
- [27] C. Ates, J. P. Garrahan, I. Lesanovsky, *Thermalization of a Strongly Interacting Closed Spin System: From Coherent Many-Body Dynamics to a Fokker-Planck Equation*. *Phys. Rev. Lett.* **108**, 110603 (2012).
- [28] K.R.A. Hazzard, M. van den Worm, M. Foss-Feig, S.R. Manmana, E.G. Dalla Torre, T. Pfau, M. Kastner, A.M. Rey, *Quantum correlations and entanglement in far-from-equilibrium spin systems*. *Phys. Rev. A* **90**, 063622 (2014).
- [29] D. Barredo, H. Labuhn, S. Ravets, T. Lahaye, A. Browaeys, C. S. Adams, *Coherent Excitation Transfer in a Spin Chain of Three Rydberg Atoms*. *Phys. Rev. Lett.* **114**, 113002 (2015).
- [30] P. Hauke, F.M. Cucchietti, A. Müller-Hermes, M.-C. Bañuls, J. I. Cirac, M. Lewenstein, *Complete devil's staircase and crystal-superfluid transitions in a dipolar XXZ spin chain: a trapped ion quantum simulation*. *New J. Phys.* **12**, 113037 (2010).
- [31] C. Senko, P. Richerme, J. Smith, A. Lee, I. Cohen, A. Retzker, C. Monroe, *Realization of a Quantum Integer-Spin Chain with Controllable Interactions*. *Phys. Rev. X* **5**, 021026 (2015).
- [32] D. Peter, N. Y. Yao, N. Lang, S. D. Huber, M. D. Lukin, H.-P. Büchler, *Topological bands with a Chern number $C = 2$ by dipolar exchange interactions*. *Phys. Rev. A* **91**, 053617 (2015).

Supplementary material

In this supplementary material, we first give extra details about the experimental setup and procedures, then provide supplemental experimental data for the settings of Figs. 2-4 of main text, and finally describe our theoretical modeling of the experiments.

S.1. EXPERIMENTAL DETAILS

This section is devoted to the description of experimental details not included in the main text. We first give extra details on the loading of arrays, then summarize the parameters (array geometry and interactions between chosen Rydberg states) used for the various experiments described in the main text, and finally we describe quantitatively the effect of the finite detection errors on the measured quantities.

S.1.1. Loading of trap arrays

In the single-atom loading regime of optical microtraps, the probability to have a given trap filled with a single atom is $p \simeq 1/2$. Therefore, when we monitor the number of loaded traps in view of triggering the experiment, N fluctuates in time around a mean value $N_t/2$, with fluctuations $\sim \sqrt{N_t}$.

When the number of traps is small, we can impose, as the triggering criterion, to wait until all traps are filled. The average triggering time T_N then increases exponentially with N , as can be seen in Fig. S.1a. We used this ‘full-loading mode’ for the data of Fig. 1 ($1 \leq N \leq 9$) and Fig. 3 ($N = 8$) of main text. This exponential scaling sets a practical limit of $N \sim 9$ for fully loaded arrays. Already for $N = 9$, the experimental duty cycle exceeds one minute.

Due to this limitation, for larger N_t we use partially-loaded arrays. We set the triggering threshold in the tail of the binomial distribution of N , i.e. close to $N_t/2 + \sqrt{N_t}$. This allows us to keep a fast repetition rate for the experiment, on the order of 1 s^{-1} , enabling fast data collection. Figure S.1b shows the distribution of loaded traps for the ‘racetrack’ array with $N_t = 30$ (respectively, for the $N_t = 7 \times 7$ square array), where we set the triggering condition to $N = 20$ (resp. $N = 30$). Using this triggering procedure, we thus end up with a narrow distribution of atom numbers $N = 20 \pm 1.5$ (resp. $N = 28 \pm 1.6$), corresponding to a filling fraction of 67% (resp. 57%), significantly above the average $N_t/2$. These strongly subpoissonian distributions of atom numbers are such that the variation in N from experiment to experiment has a negligible effect on the physics studied in Fig. 4 of main text; however, as for each experiment the initial configuration image is saved, one can if needed post-select experiments where an exact number of atoms was involved (this is how the data in Fig. 2 of main text for $N \geq 10$ were obtained).

Recently, several experiments [1, 2] demonstrated quasi-deterministic loading of single atoms in optical tweezers, reaching $p \sim 90\%$ using modified light-assisted collisions that lead to the loss of only one of the colliding atoms instead of both. A preliminary implementation of these ideas on our setup gave $p \sim 80\%$ for a single trap. In future work, by using such loading in combination with the real-time triggering based on the measured number of loaded traps, it seems realistic to reach, even in large arrays, filling fractions in excess of 0.9, i.e. approaching those obtained in quantum gas microscope experiments using Mott insulators.

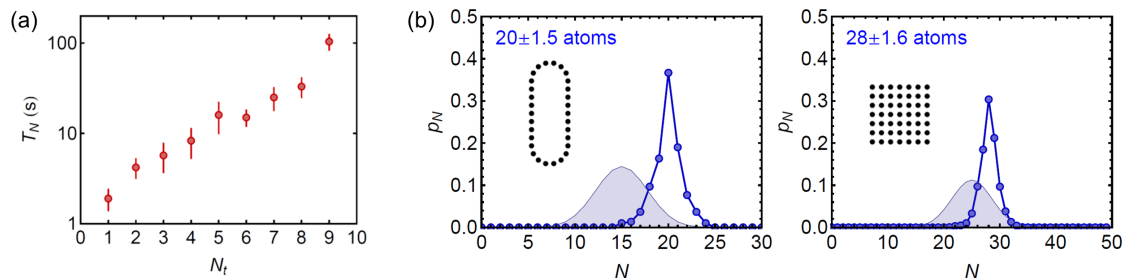


FIG. S.1: Full and partial loading of arrays. (a): Average triggering time T_N when the triggering criterion is set to $N = N_t$: achieving full loading requires an exponentially long time, limiting in practice the method to $N_t \leq 9$. The triggering times can vary substantially depending on the density of the magneto-optical trap used to load the array, and the data points shown here correspond to typical conditions used for the data of main text. (b): Distribution of the number of loaded traps in the partially loaded regime for the 30-trap ‘racetrack’ and the 49-trap square array (blue dots). The shaded distributions correspond to what would be observed with random triggering.

Figure	Trap array parameters			Rydberg state parameters				α
	Spacing a (μm)	N_t	N	n	Calculated C_6/h (GHz μm^6)	$\Omega/(2\pi)$ (MHz)	R_b (μm)	
2a (full)	3.0	1–9	N_t	82	-8.9×10^3	1.5	14	4.5
2a (partial)	3.2	19	10–15	100	-8.0×10^4	1.1	20	6.4
3a	6.3	8	8	54	-6.7	1.6	4.0	0.63
3b	6.3	8	8	61	-7.6×10^2	1.3	9.1	1.4
3c	3.8	8	8	100	-8.0×10^4	0.95	21	5.5
4abc	3.1	30	20 ± 1.5	79	-6.0×10^3	1.0	13.5	4.3
4def	3.5	49	28 ± 1.6	61	-7.6×10^2	1.4	9.1	2.6

TABLE S.1: Experimental parameters used for the data presented in the main text. Wide tuning of $\alpha = R_b/a$, over one order of magnitude, is achieved by a combination of changes in a and n (while Ω is kept almost constant).

S.1.2. Experimental parameters

Table S.1 summarizes the various values of the parameters of the arrays of traps and of the Rydberg states used for the data presented in the main text, and the resulting values of the dimensionless parameter α . It illustrates the wide tunability offered by the system.

S.1.3. Finite detection errors

Our way to detect that a given atom has been excited to a Rydberg state relies on the fact that we do not detect fluorescence from the corresponding trap in the final configuration image. There is however a small probability ε to lose an atom during the sequence, even if it was in the ground state, thus incorrectly inferring its excitation to a Rydberg state (see Ref. [15] of main text). These ‘false positive’ detection events affect the measured populations of the N -atom system. One can show that, if P_q is the *observed* probability to have q Rydberg excitations, and \tilde{P}_p the *actual* probability to have p Rydberg excitations,

$$P_q = \sum_{p=0}^q \binom{N-p}{q-p} \varepsilon^{q-p} (1-\varepsilon)^{N-q} \tilde{P}_p. \quad (\text{S1})$$

In principle, one can invert the above linear system relating the observed and actual probabilities, as described in [3], to correct the experimental data for the detection errors. Here we have chosen on the contrary to show the uncorrected populations, and to include detection errors on the theoretical curves instead.

In order to determine the experimental value of ε , we use the initial datapoints ($\tau = 0$) of the data of Fig.2 of main text. Since no Rydberg pulse is sent, we have $\tilde{P}_0 = 1$, and from (S1) the observed probability $P_0(\tau = 0)$ reads $(1-\varepsilon)^N$. Figure S.2a shows the variation of $P_0(0)$ as a function of N , together with a fit which allows us to extract $\varepsilon = (3 \pm 1)\%$, the value we use for the theoretical curves in the main text (see below).

Figure S.2b shows the effect of this finite value of ε on the probabilities P_0 , P_1 and P_2 in the full blockade regime, for atom numbers $N = 3, 9, 15$, clearly illustrating that the ‘false positive’ detection events (i) yield non-zero (and increasing with N) double excitation probabilities (that oscillate in phase with P_1) (ii) multiply the amplitude of P_0 by a factor $(1-\varepsilon)^N$ and (iii) reduce the contrast of the P_1 oscillations. Globally, the experimental data (see Fig. S.3) shows these features, superimposed with other imperfections such as damping, not related to the finite value of ε .

Finally, let us mention the effect of the detection errors on the correlation functions. In the fully blockaded region $k < \alpha$, one ideally expects a vanishing $g^{(2)}$ for $\varepsilon = 0$. However, to lowest order in ε , this value is increased substantially (see e.g. Fig. 4c of main text) to $2\varepsilon/f_R$ where f_R is the Rydberg fraction. Indeed, $g^{(2)}(k = 1)$ is given by an average of quantities of the form $\langle n_i n_{i+1} \rangle / (\langle n_i \rangle \langle n_{i+1} \rangle)$. For $\varepsilon = 0$, the numerator vanishes due to blockade; the only possibility to have a non-zero value comes from detection errors. To lowest order in ε , the probability to get a nonzero value for $n_i n_{i+1}$ is that either atom i is in $|r\rangle$ (probability f_R) and atom $i + 1$ is lost (probability ε), or vice-versa. This results in a value $2\varepsilon f_R$ for the numerator, while for the denominator we can use the zeroth-order values $\langle n_i \rangle = \langle n_{i+1} \rangle = f_R$, thus giving $g^2(1) \simeq 2\varepsilon/f_R$, which experimentally can be as large as 0.5.

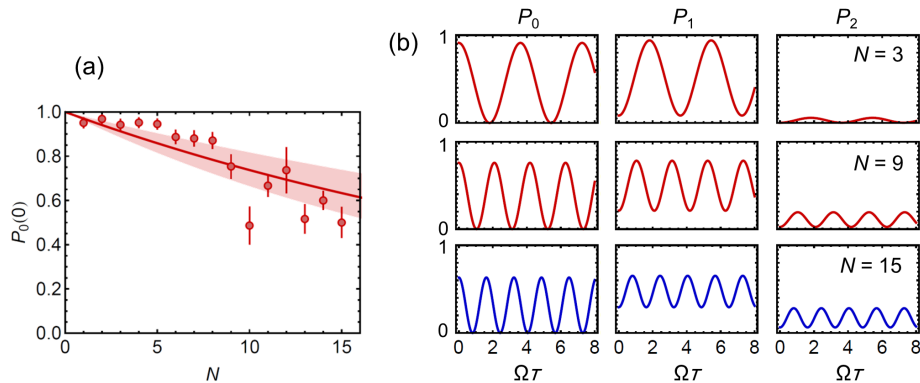


FIG. S.2: Effect of detection errors. (a): Experimental determination of ε . From the data of the full blockade experiments (Fig. 2 of main text), we plot the probability P_0 to recapture all N atoms for $\tau = 0$. The solid line is a fit to the expected dependence $(1 - \varepsilon)^N$, giving $\varepsilon = 3\%$ (the shaded area corresponds to $2\% < \varepsilon < 4\%$). (b): Calculated probabilities to observe 0, 1 or 2 excitations assuming a perfect blockade and $\varepsilon = 3\%$, for atom numbers $N = 3, 9, 15$.

S.2. ADDITIONAL EXPERIMENTAL DATA

This section is devoted to presenting additional experimental data for the settings of the main text.

S.2.1. Full Rydberg blockade

Figure S.3 shows additional data in the full blockade regime (Fig. 2 of main text). In Figure S.3a, the arrays of 1 to 9 traps are fully loaded, while in Figure S.3b, the 19-trap triangular array is partially loaded with 10 to 15 atoms. In both panels, the left column shows the time evolution of the probability P_0 to recapture all atoms at the end of the sequence, the middle column shows P_1 , and the right column shows P_2 . The points in Fig. 2a of main text corresponding to $N = 8$ and $N = 9$ in partially loaded arrays were taken in a similar configuration as for $N = 10$ to 15, but the array contained only $N_t = 17$ traps. The curves (not shown here) do not show any noticeable difference with other sets of data.

- We recognize the effects of the finite detection errors $\varepsilon \neq 0$ on the amplitude and contrast of the collective oscillations discussed in section S.1.3. above;
- In addition, the oscillations exhibit some damping, which seems to increase with N . To quantify this, we fit the data by the function

$$P(\tau) = ae^{-\gamma\tau} (\cos^2(\Omega_N\tau/2) + b) + c, \quad (\text{S2})$$

where a, b, c, γ and Ω_N are adjustable parameters (solid lines). This functional form was chosen to account in a simple way for the asymmetry in the damping. Figure S.3c shows the damping rates γ , extracted from the probabilities P_0 as a function of N . We observe an initial increase in the damping rates, which then saturates above $N = 5$. An increase with N of the damping rate was observed in other similar blockade experiments (see e.g. Refs. [19,20,21] of the main text).

- In addition, we observe that P_2 slowly increases over time for some specific values of N (see in particular $N = 4, 6, 9, 13$), corresponding to particular geometries.

We do not have a full understanding of these last two observations, but they may originate from the breaking of the blockade due to the Zeeman structure of the Rydberg states $nD_{3/2}$ (see discussion in section S.3.4.).

S.2.2. 8-atom ring

Figure S.4 shows that, within statistical fluctuations, the density of excitations on the 8-atom ring is homogeneous (this remains true at all times), and that the antiferromagnetic-like or crystal-like features obtained for some times, e.g. for $\Omega\tau = 3.1$, can only be observed in the correlation functions. This illustrates the interest of our setup in which spin chains with PBC can be realized easily. On the contrary, in a 1D chain with open boundary conditions, ‘pinning’ of the excitations would occur due to edge effects.

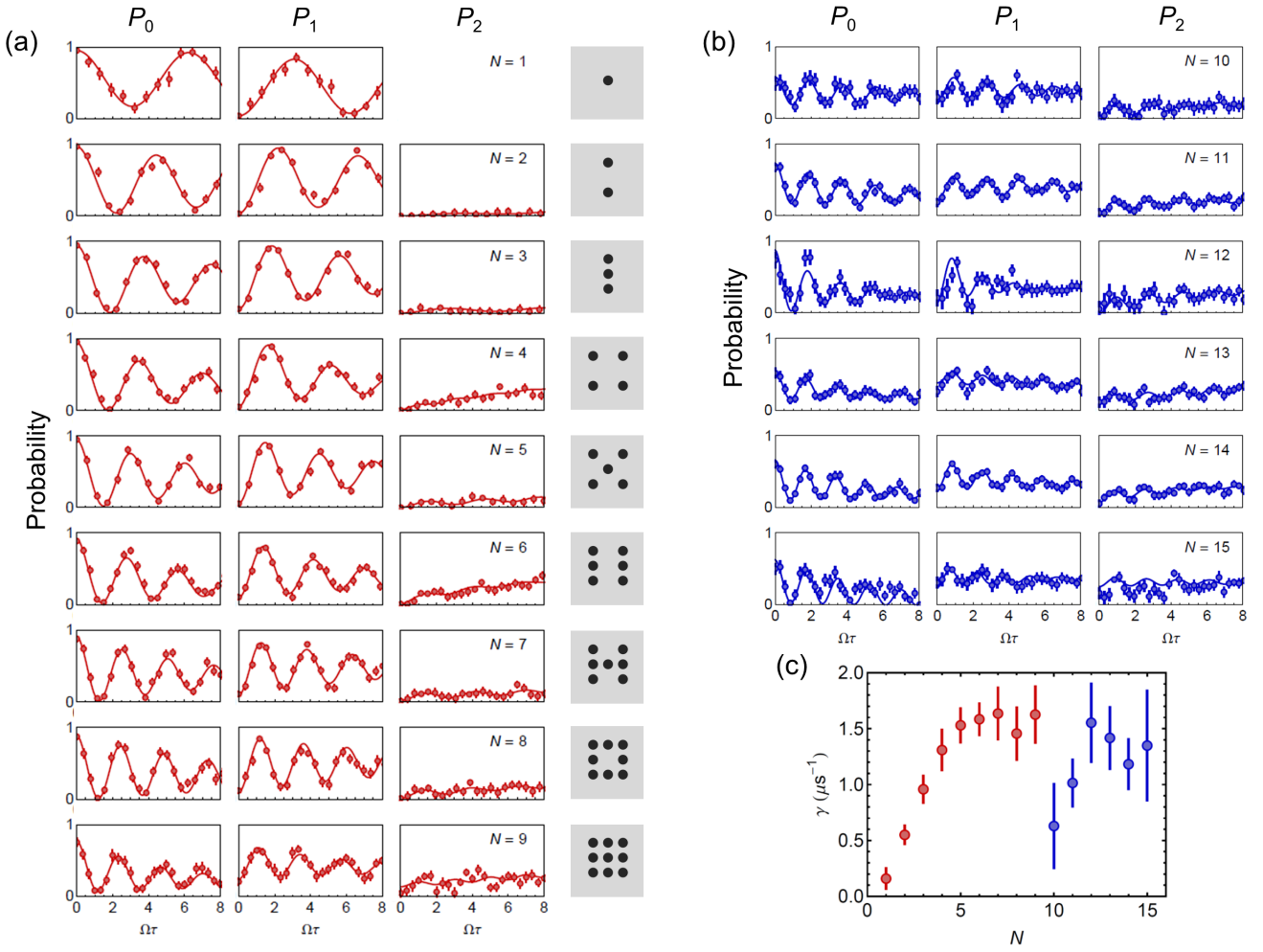


FIG. S.3: **Full dataset for the Rydberg blockade data.** (a): Fully loaded arrays of 1 to 9 traps ($n = 82$). (b): partially loaded array of $N_t = 19$ traps, containing from $N = 10$ to $N = 15$ atoms ($n = 100$). The column on the left shows the probability P_0 to recapture all atoms, the center column the probability P_1 to lose just one atom out of N , and the column on the right the probability P_2 to lose two atoms out of N . The solid lines are fits by (S2). (c): Damping rate γ extracted from the P_0 data as a function of the number of atoms in the array.

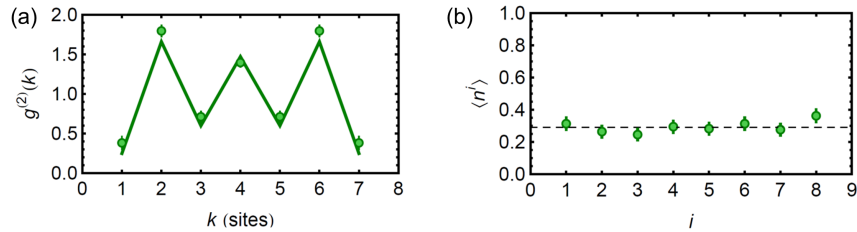


FIG. S.4: Homogeneous excitation in the 8-atom ring. (a): For $\Omega\tau = 3.1$, we observe strongly contrasted oscillations in the pair correlation function $g^2(k)$. (b): The average density of Rydberg excitations, however, is approximately the same on every site. The horizontal dashed line indicates the mean over all sites.

S.2.3. Racetrack-shaped array

Figure S.5a shows the full evolution of the time correlation function for the data of Fig. 4abc of the main text ($R_b = 4.3a$). Figure S.5b corresponds to the same settings except for the fact that one now has $R_b = 2.4a$.

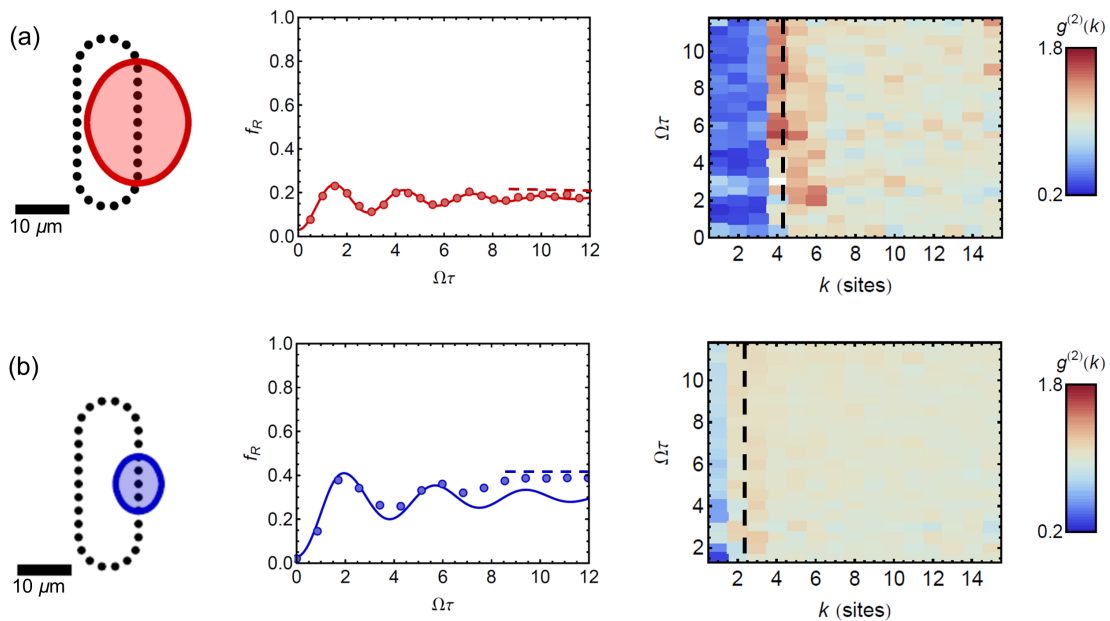


FIG. S.5: Full time evolution of the correlation functions for the 30-trap, racetrack-shaped chain. (a): Same as for Figure 3abc of main text. The right panel is the time evolution of the pair correlation function, clearly showing that, for times longer than a few Ω^{-1} , the pair correlation function does not evolve significantly anymore. The vertical dashed line indicates the value of the blockade radius. (b): The principal quantum number is now $n = 57$, and the Rabi frequency $\Omega = 2\pi \times 1.7$ MHz, such that $R_b = 2.4a$. The central panel shows the time evolution of the Rydberg fraction, and the right panel the time evolution of the pair correlation function. For both (a) and (b), f_R approaches, at long times, the close-packing limit a/R_b of hard rods of length R_b (dashed horizontal lines) [4].

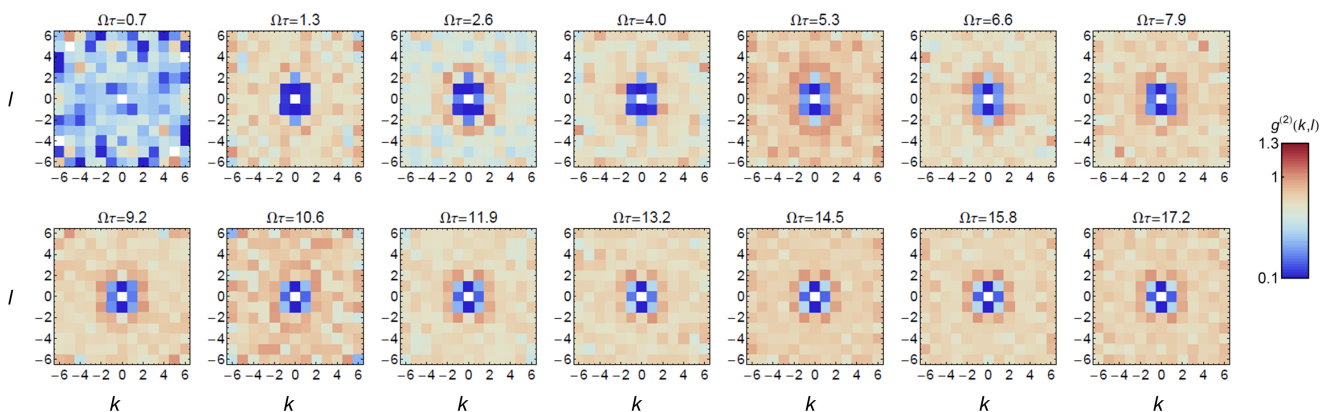


FIG. S.6: Full time evolution of the correlation function for the 7×7 square array. One observes the blocked region around $(k, l) = (0, 0)$, with a slight flattening reflecting the anisotropy of the interaction. After a few Ω^{-1} , the correlation function does not evolve any more.

S.2.4. Square array of 7×7 traps

Figure S.6 shows the full time evolution of the two-dimensional Rydberg-Rydberg correlation function $g^{(2)}(k, l)$ for the 7×7 square lattice of Fig. 4def of main text.

S.3. THEORETICAL MODELING

In this section, we first describe the effective, anisotropic van der Waals potential used for modeling the dynamics of the system in the simplest way. We then give details about our numerical simulations, and then use them to assess to which extent the assumption of approximate translational invariance discussed in the main text is supported by these simulations. Finally, we

speculate on possible causes for the deviations observed between our data and the simulation at long times, ascribing them to small van der Waals couplings to other Zeeman substates that result in an effective loss mechanism.

S.3.1. Anisotropy of the interaction

For a pair of atoms in a $nD_{3/2}$ Rydberg state with the internuclear axis not aligned with the quantization axis, the rigorous description of the van der Waals interaction requires to include all various Zeeman sublevels; the interaction then takes the form of a 16×16 matrix. To keep the description of a system of N atoms tractable, one can, in the blockade regime, define an effective, anisotropic van der Waals potential (Ref. [11] of main text) reducing the previous matrix to a single scalar. For $nD_{3/2}$ states, the anisotropy reported in Refs. [11,15] of main text is well reproduced by the simple expression

$$V_{\text{eff}}(r, \theta) = \frac{C_6(0)}{r^6} \left(\frac{1}{3} + \frac{2}{3} \cos^4 \theta \right) \quad (\text{S3})$$

with θ the angle between the quantization axis and the internuclear axis, giving a reduction by a factor of three in interaction strength when θ goes from 0 to $\pi/2$.

Due to the anisotropy in (S3), the shape of the blockade volume centered on a Rydberg atom is also anisotropic. However, due to the r^6 -scaling of the interaction, the surface $r(\theta)$ defined by $V_{\text{eff}}(r, \theta) = \hbar\Omega$ is quite well approximated by a prolate spheroid with an aspect ratio of $3^{1/6} \simeq 1.2$. In the figures of the main text, the shaded regions depicting the blockade volume have the polar equation $r(\theta) = R_b \left(\frac{1}{3} + \frac{2}{3} \cos^4 \theta \right)^{1/6}$.

S.3.2. Numerical simulation of the dynamics

Our theoretical description of the system is based on the mapping of its dynamics into a pseudo-spin 1/2 model with anisotropic long range interactions. We therefore neglect the rich Zeeman structure of the $nD_{3/2}$ states. The numerical calculations rest on the solution of the Schrödinger equation for the Hamiltonian of Eq. (1) of the main text in a reduced Hilbert space \mathcal{H} . We first write the wave function $|\psi\rangle$ of the system with N atoms in terms of states with fixed number of Rydberg excitations and ground state atoms, which correspond to the eigenstates of the Hamiltonian with vanishing Rabi frequency Ω (Ref. [22] of the main text and [5]). Then the truncation procedure is based on two complementary steps: first we define the maximum number of Rydberg excitations N_r^{max} that we include in our basis, second we eliminate those states which display excitations closer than a fixed distance R_0 . Both N_r^{max} and R_0 are adjusted to ensure the convergence of the dynamics. For small samples (Fig. 3 of the main text) we performed simulations including all 256 basis states, whereas for the racetrack configurations we typically set R_0 smaller than the lattice constant but include up to $N_r^{\text{math}} = 10$ excitations at most, reducing the dimension of \mathcal{H} from $2^{20} \simeq 10^6$ to $\sum_{q=0}^{N_r^{\text{max}}} \binom{20}{q} \simeq 6 \times 10^5$. For the 7×7 square array with 30 atoms, we set $R_0 = 1.3a$ (much smaller than the blockade radius $R_b = 2.6a$), thus reducing the dimension of \mathcal{H} to $\simeq 3 \times 10^6$ (the full Hilbert space is of dimension $2^{30} \simeq 10^9$, and using only the truncation criterion on the number of excitations would reduce it to about 5×10^7 , still intractably large). The Schrödinger equation within the truncated Hilbert space is then solved with standard split-step method for the two non-commuting parts of the Hamiltonian of Eq. (1) of the main text. All these calculations were repeated for several realizations of the loading of the arrays (50 realizations for the squared 7×7 configurations and 200 realizations for the case with fewer traps), taking into account the anisotropic interparticle interaction of Eq. (3). The comparison with experimental data of the average fraction of excitations $f_R = \sum_{q=0}^N qP_q/N$ is done by including the “false positive” detection events as described by Eq. (1).

The calculation of the $g^{(2)}(k)$ correlation function in Fig.3d and Fig.4c of the main text follows the definition of Eq. (4). However, contrarily to the calculation of the average fraction of the excitations it is not possible to derive an analytical formula for $g^{(2)}(k)$ to properly take into account the detection efficiency of Rydberg excitations (unless $k < \alpha$ as described in section S.1.3.). Therefore we implement a standard Monte Carlo algorithm to perform the average of the correlation function over randomly generated configurations which are weighted in $g^{(2)}(k)$ with the initial (quantum) probability extracted from the real time dynamics of the Schrödinger equation. For example the state $|r_i r_j\rangle$ which contains $N_r = 2$ Rydberg excitations and amplitude $c_{ij}(t)$ can wrongly be detected as the state $|r_i r_j r_q\rangle$ with probability $p = \varepsilon(1-\varepsilon)^{N-2}$. If the latter state is generated from our sampling algorithm then its weight in the correlation function corresponds to $|c_{ij}(t)|^2$. Finally we average over several hundreds randomly generated configurations to obtain well converged results for the correlation function.

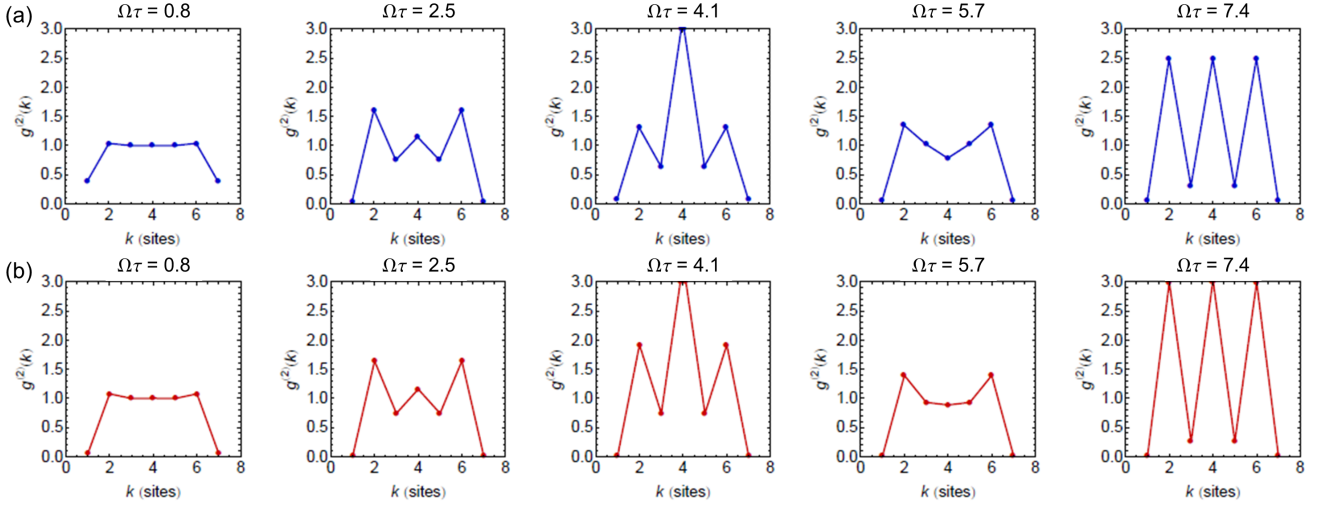


FIG. S.7: Assessing the validity of the approximation of translational invariance in the 8-atom ring. Calculated pair correlation function $g^{(2)}(k)$ as a function of the excitation time, for the 8-atom ring. (a): simulation using the experimentally relevant anisotropic interaction, which breaks translational invariance. (b): simulation with the same parameters as in (a), except that the angular dependence is neglected (we replace (S3) by its value for $\theta = 0$), thus reestablishing translational invariance. One observes that the contrast in (a) is reduced, as expected, but only in a marginal way.

S.3.3. Assumption of translational invariance

For the one-dimensional configurations of the main text (8-atom ring of Fig.3b and racetrack-shaped array of 30 traps of Fig.4a of main text) we plot the spatially averaged pair correlation function

$$g^{(2)}(k) = \frac{1}{N_t} \sum_i \frac{\langle n_i n_{i+k} \rangle}{\langle n_i \rangle \langle n_{i+k} \rangle}, \quad (\text{S4})$$

where the subscripts label sites. For a system invariant by translation, all terms in the sum are identical, and the averaging over i simply improves the signal to noise ratio. However, our systems are not translationally invariant, in particular because of the anisotropy of the interaction, and a natural question to address is whether the averaging reduces the contrast of the correlation functions. To answer this question, we have calculated the dynamics of the pair correlation function for the 8-atom ring, taking or not into account the anisotropy of the interaction (Figure S.7). One observes that the contrast reduction due to averaging is very small, thereby validating our choice to perform it for the data shown in the main text.

S.3.4. Effective loss mechanism arising from anisotropic interactions of D states

The agreement between our measurements and the results of the simulations is not perfect for the largest excitation times, in particular for some settings (e.g. for some configurations in the full blockade regime, for the 8-atom ring in the partial blockade regime, and for the 7×7 square array), where we observe a gradual increase in the number of measured Rydberg excitations.

These effects could be qualitatively reproduced if the detection errors ε would increase in time. However, the main reason for these losses is due to the fact that the microtraps are switched off during the excitation (to avoid inhomogeneous light-shifts), and as they are off for a fixed amount of time ($3 \mu\text{s}$), independent of τ , we do not, at first sight, expect ε to increase in time. One could imagine however that the presence of the Rydberg excitation lasers may induce extra loss (due to off-resonant scattering for instance), and in this case one would end up having an ε increasing with τ . We have experimentally ruled out this possibility by measuring the recapture probability when shining the Rydberg excitation lasers, detuned from the Rydberg line by $\sim 100 \text{ MHz}$, for the full $3 \mu\text{s}$, without measuring any detrimental effect.

A second possible reason would be the motion of the atoms. Due to their finite temperature, the atoms move during free flight with a velocity $v \sim 50 \text{ nm}/\mu\text{s}$. Now, strictly speaking, the terms corresponding to the laser coupling in Eqn. (1) of main text are not $\Omega \sigma_x^i$, but $\Omega e^{i\mathbf{k} \cdot \mathbf{r}_i(t)} \sigma_+^i + \text{h.c.}$, where \mathbf{k} is the sum of the wavevectors of the excitation lasers at 795 and 475 nm, and $\mathbf{r}_i(t)$ the position of atom i . Thus, because of the motion, the phase factors of the couplings become time-dependent, which e.g. yields a dephasing of the spin wave corresponding to $|W\rangle$ states. However, a numerical simulation of this effect shows that the induced dephasing rates are negligible for our parameters.

We thus believe that the cause for the observed extra losses lies in the interplay between the large number of interacting Zeeman sublevels when two atoms are excited to $nD_{3/2}$ states: for $\theta \neq 0$ all 16 pair state Zeeman sublevels are coupled together by the van der Waals interaction. For a large number of atoms, this may lead to an effective loss rate from the targeted $|r\rangle$ states into a quasi-continuum comprising all other (weakly interacting) Zeeman states, and hence to a gradual increase of population of the Rydberg manifold. Qualitatively, this interpretation is corroborated by the fact that the observed increase in the number of observed excitations seems to depend quite strongly on the array geometry: for instance, the data of the racetrack-shaped array, for which a majority of interacting atom pairs are almost aligned along the quantization axis z , are well reproduced by the simulations, unlike in the case of the 8-atom ring or the 7×7 square array, for which many interacting pairs have their internuclear axes strongly inclined with respect to z .

Achieving a quantitative understanding of these observed imperfections, using approaches similar to the ones of Refs. [10,11,12] of the main text, is a challenging task. However, it will be an important step in view of future applications of Rydberg blockade for quantum simulation, and will thus be the subject of future work.

-
- [1] B.J. Lester, N. Luick, A.M. Kaufman, C.M. Reynolds, C.A. Regal, *Rapid production of uniformly-filled arrays of neutral atoms*. *Phys. Rev. Lett.* **115**, 073003 (2015).
- [2] Y.H. Fung, M.F. Andersen, *Efficient collisional blockade loading of single atom into a tight microtrap*. *New J. Phys.* **17**, 073011 (2015).
- [3] C. Shen and L.-M. Duan, *Correcting detection errors in quantum state engineering through data processing*. *New J. Phys.* **14**, 053053 (2012).
- [4] M. Viteau, M. G. Bason, J. Radogostowicz, N. Malossi, D. Ciampini, O. Morsch, E. Arimondo, *Rydberg Excitations in Bose-Einstein Condensates in Quasi-One-Dimensional Potentials and Optical Lattices*. *Phys. Rev. Lett.* **107**, 060402 (2011).
- [5] P. Schauß, J. Zeiher, T. Fukuhara, S. Hild, M. Cheneau, T. Macrì, T. Pohl, I. Bloch, C. Gross, *Crystallization in Ising quantum magnets*. *Science* **347**, 1455 (2015).

Bibliography

Anderson, P. W., “*Absence of Diffusion in Certain Random Lattices*,” *Physical Review* **109**, 1492–1505 (1958).

Anderson, W. R., Veale, J. R., and Gallagher, T. F., “*Resonant Dipole-Dipole Energy Transfer in a Nearly Frozen Rydberg Gas*,” *Physical Review Letters* **80**, 249–252 (1998).

Ates, C., Garrahan, J. P., and Lesanovsky, I., “*Thermalization of a Strongly Interacting Closed Spin System: From Coherent Many-Body Dynamics to a Fokker-Planck Equation*,” *Physical Review Letters* **108**, 110603 (2012).

Auerbach, A., *Interacting electrons and quantum magnetism* (Springer Science & Business Media, 2012).

Balewski, J. B., Krupp, A. T., Gaj, A., Peter, D., Büchler, H. P., Löw, R., Hofferberth, S., and Pfau, T., “*Coupling a single electron to a Bose-Einstein condensate*,” *Nature* **502**, 664–667 (2013).

Balmer, J. J., “*Notiz über die Spectrallinien des Wasserstoffs*,” *Annalen der Physik* **261**, 80–87 (1885).

Barredo, D., Labuhn, H., Ravets, S., Lahaye, T., Browaeys, A., and Adams, C. S., “*Coherent Excitation Transfer in a Spin Chain of Three Rydberg Atoms*,” *Physical Review Letters* **114**, 113002 (2015).

Barredo, D., Ravets, S., Labuhn, H., Béguin, L., Vernier, A., Nogrette, F., Lahaye, T., and Browaeys, A., “*Demonstration of a Strong Rydberg Blockade in Three-Atom Systems with Anisotropic Interactions*,” *Physical Review Letters* **112**, 183002 (2014).

Bässler, H., “*Charge Transport in Disordered Organic Photoconductors a Monte Carlo Simulation Study*,” *physica status solidi (b)* **175**, 15–56 (1993).

Baur, S., Tiarks, D., Rempe, G., and Dürr, S., “*Single-Photon Switch Based on Rydberg Blockade*,” *Physical Review Letters* **112**, 073901 (2014).

- Becker, C., Stellmer, S., Soltan-Panahi, P., Dörscher, S., Baumert, M., Richter, E.-M., Kronjäger, J., Bongs, K., and Sengstock, K., “*Oscillations and interactions of dark and darkbright solitons in Bose-Einstein condensates,*” *Nature Physics* **4**, 496–501 (2008).
- Béguin, L., Measurement of the van der Waals interaction between two Rydberg atoms, *Ph.D. thesis*, Université Paris IX (2013).
- Béguin, L., Vernier, A., Chicireanu, R., Lahaye, T., and Browaeys, A., “*Direct Measurement of the van der Waals Interaction between Two Rydberg Atoms,*” *Physical Review Letters* **110**, 263201 (2013).
- Bergamini, S., Darquié, B., Jones, M., Jacubowicz, L., Browaeys, A., and Grangier, P., “*Holographic generation of microtrap arrays for single atoms by use of a programmable phase modulator,*” *Journal of the Optical Society of America B* **21**, 1889 (2004).
- Beugnon, J., Tuchendler, C., Marion, H., Gaëtan, A., Miroshnychenko, Y., Sortais, Y. R. P., Lance, A. M., Jones, M. P. A., Messin, G., Browaeys, A., and Grangier, P., “*Two-dimensional transport and transfer of a single atomic qubit in optical tweezers,*” *Nature Physics* **3**, 696–699 (2007).
- van Bijnen, R. M. W., Quantum Engineering with Ultracold Atoms, *Ph.D. thesis*, Technische Universiteit Eindhoven (2013).
- van Bijnen, R. M. W., Ravensbergen, C., Bakker, D. J., Dijk, G. J., Kokkelmans, S. J. J. M. F., and Vredenburg, E. J. D., “*Patterned Rydberg excitation and ionization with a spatial light modulator,*” *New Journal of Physics* **17**, 023045 (2015).
- Blatt, R. and Roos, C. F., “*Quantum simulations with trapped ions,*” *Nature Physics* **8**, 277–284 (2012).
- Bohnet, J. G., Sawyer, B. C., Britton, J. W., Wall, M. L., Rey, A. M., Foss-feig, M., and Bollinger, J. J., “*Quantum spin dynamics and entanglement generation with hundreds of trapped ions,*” (2015), [arXiv:1512.03756](https://arxiv.org/abs/1512.03756) .
- Bohr, N., “*I. On the constitution of atoms and molecules,*” *Philosophical Magazine Series 6* **26**, 1–25 (1913).
- Born, M., Wolf, E., Bhatia, A. B., Clemmow, P. C., Gabor, D., Stokes, A. R., Taylor, A. M., Wayman, P. A., and Wilcock, W. L., *Principles of Optics* (Cambridge University Press, Cambridge, 1999).

- Boyer, V., Godun, R. M., Smirne, G., Cassettari, D., Chandrashekar, C. M., Deb, A. B., Laczik, Z. J., and Foot, C. J., “*Dynamic manipulation of Bose-Einstein condensates with a spatial light modulator,*” *Physical Review A* **73**, 031402 (2006).
- Bozinovic, N., Yue, Y., Ren, Y., Tur, M., Kristensen, P., Huang, H., Willner, A. E., and Ramachandran, S., “*Terabit-Scale Orbital Angular Momentum Mode Division Multiplexing in Fibers,*” *Science* **340**, 1545–1548 (2013).
- Branden, D. B., Juhasz, T., Mahlokozera, T., Vesa, C., Wilson, R. O., Zheng, M., Kortyna, A., and Tate, D. A., “*Radiative lifetime measurements of rubidium Rydberg states,*” *Journal of Physics B: Atomic, Molecular and Optical Physics* **43**, 015002 (2010).
- Britton, J. W., Sawyer, B. C., Keith, A. C., Wang, C.-C. J., Freericks, J. K., Uys, H., Biercuk, M. J., and Bollinger, J. J., “*Engineered two-dimensional Ising interactions in a trapped-ion quantum simulator with hundreds of spins.*” *Nature* **484**, 489–92 (2012).
- Brunner, N., Cavalcanti, D., Pironio, S., Scarani, V., and Wehner, S., “*Bell nonlocality,*” *Reviews of Modern Physics* **86**, 419–478 (2014).
- Carroll, T. J., Claringbould, K., Goodsell, A., Lim, M. J., and Noel, M. W., “*Angular Dependence of the Dipole-Dipole Interaction in a Nearly One-Dimensional Sample of Rydberg Atoms,*” *Physical Review Letters* **93**, 153001 (2004).
- Castro Neto, A. H., Guinea, F., Peres, N. M. R., Novoselov, K. S., and Geim, A. K., “*The electronic properties of graphene,*” *Reviews of Modern Physics* **81**, 109–162 (2009).
- Cheneau, M., Barmettler, P., Poletti, D., Endres, M., Schauß, P., Fukuhara, T., Gross, C., Bloch, I., Kollath, C., and Kuhr, S., “*Light-cone-like spreading of correlations in a quantum many-body system.*” *Nature* **481**, 484–7 (2012).
- Cohen-Tannoudji, C., Dupont-Roc, J., and Grynberg, G., *Atom-Photon Interactions: Basic Processes and Applications* (Wiley-VCH, New York, 1998).
- Collini, E., Wong, C. Y., Wilk, K. E., Curmi, P. M. G., Brumer, P., and Scholes, G. D., “*Coherently wired light-harvesting in photosynthetic marine algae at ambient temperature,*” *Nature* **463**, 644–647 (2010).

- Comparat, D. and Pillet, P., “*Dipole blockade in a cold Rydberg atomic sample,*” *JOSA B* **27**, 208–232 (2010).
- Cooley, J. W. and Tukey, J. W., “*An algorithm for the machine calculation of complex Fourier series,*” *Mathematics of Computation* **19**, 297–297 (1965).
- Curtis, J. E. and Grier, D. G., “*Structure of Optical Vortices,*” *Physical Review Letters* **90**, 133901 (2003).
- Darquié, B., Manipulation d’atomes dans des pièges dipolaires microscopiques et émission contrôlée de photons par un atome unique, *Ph.D. thesis*, Université Paris Sud - Paris XI (2005).
- Derevianko, A., Kómár, P., Topcu, T., Kroeze, R. M., and Lukin, M. D., “*Effects of molecular resonances on Rydberg blockade,*” *Physical Review A* **92**, 063419 (2015).
- van Ditzhuijzen, C. S. E., Koenderink, A. F., Hernández, J. V., Robicheaux, F., Noordam, L. D., and van den Heuvel, H. B. v. L., “*Spatially Resolved Observation of Dipole-Dipole Interaction between Rydberg Atoms,*” *Physical Review Letters* **100**, 243201 (2008).
- Dudin, Y. O., Bariani, F., and Kuzmich, A., “*Emergence of Spatial Spin-Wave Correlations in a Cold Atomic Gas,*” *Physical Review Letters* **109**, 133602 (2012).
- Dudin, Y. O., Li, L., Bariani, F., and Kuzmich, A., “*Observation of coherent many-body Rabi oscillations,*” *Nature Physics* **8**, 790–794 (2012).
- Ebert, M., Gill, A., Gibbons, M., Zhang, X., Saffman, M., and Walker, T. G., “*Atomic Fock State Preparation Using Rydberg Blockade,*” *Physical Review Letters* **112**, 043602 (2014).
- Ebert, M., Kwon, M., Walker, T. G., and Saffman, M., “*Coherence and Rydberg Blockade of Atomic Ensemble Qubits,*” *Physical Review Letters* **115**, 093601 (2015).
- Faoro, R., Pelle, B., Zuliani, A., Cheinet, P., Arimondo, E., and Pillet, P., “*Borromean three-body FRET in frozen Rydberg gases,*” *Nature Communications* **6**, 8173 (2015).
- Feldker, T., Bachor, P., Stappel, M., Kolbe, D., Gerritsma, R., Walz, J., and Schmidt-Kaler, F., “*Rydberg Excitation of a Single Trapped Ion,*” *Physical Review Letters* **115**, 173001 (2015).

- Feynman, R. P., “*Simulating physics with computers,*” *International Journal of Theoretical Physics* **21**, 467–488 (1982).
- Friedrich, H., *Theoretical Atomic Physics*, Vol. 1 (Springer, Berlin Heidelberg, 1991).
- Fuhrmanek, A., Bourgain, R., Sortais, Y. R. P., and Browaeys, A., “*Light-assisted collisions between a few cold atoms in a microscopic dipole trap,*” *Physical Review A* **85**, 062708 (2012).
- Fung, Y. H. and Andersen, M. F., “*Efficient collisional blockade loading of a single atom into a tight microtrap,*” *New Journal of Physics* **17**, 073011 (2015).
- Gabor, D., “*A New Microscopic Principle,*” *Nature* **161** (1948).
- Gaëtan, A., Miroshnychenko, Y., Wilk, T., Chotia, A., Viteau, M., Comparat, D., Pillet, P., Browaeys, A., and Grangier, P., “*Observation of collective excitation of two individual atoms in the Rydberg blockade regime,*” *Nature Physics* **5**, 115–118 (2009).
- Gallagher, T. F., *Rydberg atoms*, 3rd ed. (Cambridge University Press, 2005).
- Gaunt, A. L. and Hadzibabic, Z., “*Robust Digital Holography For Ultracold Atom Trapping,*” *Scientific Reports* **2**, 1–5 (2012).
- Georgescu, I. M., Ashhab, S., and Nori, F., “*Quantum simulation,*” *Reviews of Modern Physics* **86**, 153–185 (2014).
- Gerchberg, R. W. and Saxton, W. O., “*A practical algorithm for the determination of the phase from image and diffraction plane pictures,*” *Optik* **35** (1972).
- Gibson, G., Courtial, J., Padgett, M. J., Vasnetsov, M., Pas’ko, V., Barnett, S. M., and Franke-Arnold, S., “*Free-space information transfer using light beams carrying orbital angular momentum,*” *Optics Express* **12**, 5448 (2004).
- Glaetzle, A. W., Dalmonte, M., Nath, R., Roussochatzakis, I., Moessner, R., and Zoller, P., “*Quantum Spin-Ice and Dimer Models with Rydberg Atoms,*” *Physical Review X* **4**, 041037 (2014).
- Goodman, J. W., *Introduction to Fourier Optics*, 2nd ed. (Roberts & Company Publishers, 1996).

- Gorniaczyk, H., Tresp, C., Schmidt, J., Fedder, H., and Hofferberth, S., “*Single-Photon Transistor Mediated by Interstate Rydberg Interactions*,” *Physical Review Letters* **113**, 053601 (2014).
- Greenberger, D. M., Horne, M. A., and Zeilinger, A., “*Going Beyond Bell’s Theorem*,” in *Bell’s Theorem, Quantum Theory, and Conceptions of the Universe* (ed. M. Kafatos, 1989).
- Grier, D. G., “*A revolution in optical manipulation*,” *Nature* **424**, 810–816 (2003).
- Grimm, R., Weidemüller, M., and Ovchinnikov, Y. B., “*Optical Dipole Traps for Neutral Atoms*,” in *Advances In Atomic, Molecular, and Optical Physics*, Vol. 42 (2000) pp. 95–170.
- Gunter, G., Schempp, H., Robert-de Saint-Vincent, M., Gavryusev, V., Helmrich, S., Hofmann, C. S., Whitlock, S., and Weidemuller, M., “*Observing the Dynamics of Dipole-Mediated Energy Transport by Interaction-Enhanced Imaging*,” *Science* **342**, 954–956 (2013).
- Haas, F., Volz, J., Gehr, R., Reichel, J., and Esteve, J., “*Entangled States of More Than 40 Atoms in an Optical Fiber Cavity*,” *Science* **344**, 180–183 (2014).
- Han, J., Jamil, Y., Norum, D. V. L., Tanner, P. J., and Gallagher, T. F., “*Rb nf quantum defects from millimeter-wave spectroscopy of cold 85Rb Rydberg atoms*,” *Physical Review A* **74**, 054502 (2006).
- Hankin, A. M., Jau, Y.-Y., Parazzoli, L. P., Chou, C. W., Armstrong, D. J., Landahl, A. J., and Biedermann, G. W., “*Two-atom Rydberg blockade using direct $6S$ to nP excitation*,” *Physical Review A* **89**, 033416 (2014).
- Hardy, J. W., *Adaptive Optics for Astronomical Telescopes* (Oxford University Press, 1998).
- Haroche, S., “*Controlling Photons in a Box and Exploring the Quantum to Classical Boundary (Nobel Lecture)*,” *Angewandte Chemie International Edition* **52**, 10158–10178 (2013).
- Hauke, P., Cucchietti, F. M., Tagliacozzo, L., Deutsch, I., and Lewenstein, M., “*Can one trust quantum simulators?*” *Reports on Progress in Physics* **75**, 082401 (2012).
- Hauke, P. and Heyl, M., “*Many-body localization and quantum ergodicity in disordered long-range Ising models*,” *Physical Review B* **92**, 134204 (2015).

- Hazzard, K. R. A., van den Worm, M., Foss-Feig, M., Manmana, S. R., Dalla Torre, E. G., Pfau, T., Kastner, M., and Rey, A. M., “*Quantum correlations and entanglement in far-from-equilibrium spin systems,*” *Physical Review A* **90**, 063622 (2014).
- Heidemann, R., Raitzsch, U., Bendkowsky, V., Butscher, B., Löw, R., and Pfau, T., “*Rydberg Excitation of Bose-Einstein Condensates,*” *Physical Review Letters* **100**, 033601 (2008).
- Heidemann, R., Raitzsch, U., Bendkowsky, V., Butscher, B., Löw, R., Santos, L., and Pfau, T., “*Evidence for Coherent Collective Rydberg Excitation in the Strong Blockade Regime,*” *Physical Review Letters* **99**, 163601 (2007).
- Heidrich-Meisner, F., Honecker, A., and Brenig, W., “*Transport in quasi one-dimensional spin-1/2 systems,*” *The European Physical Journal Special Topics* **151**, 135–145 (2007).
- Isenhower, L., Urban, E., Zhang, X. L., Gill, A. T., Henage, T., Johnson, T. A., Walker, T. G., and Saffman, M., “*Demonstration of a Neutral Atom Controlled-NOT Quantum Gate,*” *Physical Review Letters* **104**, 010503 (2010).
- Jaksch, D., Cirac, J. I., Zoller, P., Rolston, S. L., Côté, R., and Lukin, M. D., “*Fast Quantum Gates for Neutral Atoms,*” *Physical Review Letters* **85**, 2208–2211 (2000).
- Jau, Y.-Y., Hankin, A. M., Keating, T., Deutsch, I. H., and Biedermann, G. W., “*Entangling atomic spins with a Rydberg-dressed spin-flip blockade,*” *Nature Physics* **12**, 71–74 (2015).
- Johnson, T. A., Urban, E., Henage, T., Isenhower, L., Yavuz, D. D., Walker, T. G., and Saffman, M., “*Rabi Oscillations between Ground and Rydberg States with Dipole-Dipole Atomic Interactions,*” *Physical Review Letters* **100**, 113003 (2008).
- Jungen, C., “*Quantum Defect Theory for Molecules,*” in *Reports on Progress in Physics*, Vol. 46 (1988) pp. 79–103.
- Jurcevic, P., Lanyon, B. P., Hauke, P., Hempel, C., Zoller, P., Blatt, R., and Roos, C. F., “*Quasiparticle engineering and entanglement propagation in a quantum many-body system,*” *Nature* **511**, 202–205 (2014).
- Kaufman, A. M., Lester, B. J., and Regal, C. A., “*Cooling a Single Atom in an Optical Tweezer to Its Quantum Ground State,*” *Physical Review X* **2**, 041014 (2012).

- Kazimierczuk, T., Fröhlich, D., Scheel, S., Stolz, H., and Bayer, M., “*Giant Rydberg excitons in the copper oxide Cu₂O*,” *Nature* **514**, 343–347 (2014).
- Kruse, J., Gierl, C., Schlosser, M., and Birkel, G., “*Reconfigurable site-selective manipulation of atomic quantum systems in two-dimensional arrays of dipole traps*,” *Physical Review A* **81**, 060308 (2010).
- Kübler, H., Shaffer, J. P., Baluktsian, T., Löw, R., and Pfau, T., “*Coherent excitation of Rydberg atoms in micrometre-sized atomic vapour cells*,” *Nature Photonics* **4**, 112–116 (2010).
- Labuhn, H., Barredo, D., Ravets, S., de Léséleuc, S., Macrì, T., Lahaye, T., and Browaeys, A., “*A highly-tunable quantum simulator of spin systems using two-dimensional arrays of single Rydberg atoms*,” *Nature* (accepted for publication) (2016), [arXiv:1509.04543](https://arxiv.org/abs/1509.04543) .
- Labuhn, H., Ravets, S., Barredo, D., Béguin, L., Nogrette, F., Lahaye, T., and Browaeys, A., “*Single-atom addressing in microtraps for quantum-state engineering using Rydberg atoms*,” *Physical Review A* **90**, 023415 (2014).
- Lee, J. H., Montano, E., Deutsch, I. H., and Jessen, P. S., “*Robust site-resolvable quantum gates in an optical lattice via inhomogeneous control*,” *Nature Communications* **4** (2013).
- Lengwenus, A., Kruse, J., Schlosser, M., Tichelmann, S., and Birkel, G., “*Coherent Transport of Atomic Quantum States in a Scalable Shift Register*,” *Physical Review Letters* **105**, 170502 (2010).
- Lesanovsky, I., “*Many-body spin interactions and the ground state of a dense Rydberg lattice gas*.” *Physical review letters* **106**, 025301 (2011).
- Lester, B. J., Luick, N., Kaufman, A. M., Reynolds, C. M., and Regal, C. A., “*Rapid Production of Uniformly Filled Arrays of Neutral Atoms*,” *Physical Review Letters* **115**, 073003 (2015).
- Li, W., Mourachko, I., Noel, M. W., and Gallagher, T. F., “*Millimeter-wave spectroscopy of cold Rb Rydberg atoms in a magneto-optical trap: Quantum defects of the ns , np , and nd series*,” *Physical Review A* **67**, 052502 (2003).
- Lochead, G., Boddy, D., Sadler, D. P., Adams, C. S., and Jones, M. P. A., “*Number-resolved imaging of excited-state atoms using a scanning autoionization microscope*,” *Physical Review A* **87**, 053409 (2013).

- López-Quesada, C., Andilla, J., and Martín-Badosa, E., “Correction of aberration in holographic optical tweezers using a Shack-Hartmann sensor,” *Applied Optics* **48**, 1084 (2009).
- Loudon, R., *The Quantum Theory of Light (Oxford Science Publications)*, 3rd ed. (Oxford University Press, USA, 2000).
- Lów, R., Weimer, H., Krohn, U., Heidemann, R., Bendkowsky, V., Butscher, B., Büchler, H. P., and Pfau, T., “Universal scaling in a strongly interacting Rydberg gas,” *Physical Review A* **80**, 033422 (2009).
- Lukin, M. D., Fleischhauer, M., Cote, R., Duan, L. M., Jaksch, D., Cirac, J. I., and Zoller, P., “Dipole Blockade and Quantum Information Processing in Mesoscopic Atomic Ensembles,” *Physical Review Letters* **87**, 037901 (2001).
- Lundblad, N., Obrecht, J. M., Spielman, I. B., and Porto, J. V., “Field-sensitive addressing and control of field-insensitive neutral-atom qubits,” *Nature Physics* **5**, 575–580 (2009).
- Maller, K. M., Lichtman, M. T., Xia, T., Sun, Y., Piotrowicz, M. J., Carr, A. W., Isenhower, L., and Saffman, M., “Rydberg-blockade controlled-not gate and entanglement in a two-dimensional array of neutral-atom qubits,” *Physical Review A* **92**, 022336 (2015).
- Mantney, T., Weber, T. M., Niederprüm, T., Langer, P., Guarrera, V., Barontini, G., and Ott, H., “Scanning electron microscopy of Rydberg-excited BoseEinstein condensates,” *New Journal of Physics* **16**, 083034 (2014).
- MathWorks,, “Matlab Fast Fourier Transform (FFT): <http://mathworks.com/help/matlab/math/fast-fourier-transform-fft.html>,” (2015).
- Matsumoto, N., Inoue, T., Ando, T., Takiguchi, Y., Ohtake, Y., and Toyoda, H., “High-quality generation of a multispot pattern using a spatial light modulator with adaptive feedback,” *Optics Letters* **37**, 3135 (2012).
- Mattioli, M., Glätzle, A. W., and Lechner, W., “From classical to quantum non-equilibrium dynamics of Rydberg excitations in optical lattices,” *New Journal of Physics* **17**, 113039 (2015).

- Maxwell, D., Szwer, D. J., Paredes-Barato, D., Busche, H., Pritchard, J. D., Gauguet, A., Weatherill, K. J., Jones, M. P. A., and Adams, C. S., “*Storage and Control of Optical Photons Using Rydberg Polaritons*,” *Physical Review Letters* **110**, 103001 (2013).
- Miroshnychenko, Y., Gaëtan, A., Evellin, C., Grangier, P., Comparat, D., Pillet, P., Wilk, T., and Browaeys, A., “*Coherent excitation of a single atom to a Rydberg state*,” *Physical Review A* **82**, 013405 (2010).
- Monroe, C., Campbell, W. C., Edwards, E. E., Islam, R., Kafri, D., Lee, A., Richerme, P., Senko, C., and Smith, J., “*Quantum Simulation of Spin Models with Trapped Ions*,” *Proceedings of the International School of Physics ‘Enrico Fermi’* **189** (2015).
- Monroe, C. and Kim, J., “*Scaling the ion trap quantum processor*.” *Science* **339**, 1164–9 (2013).
- Moses, S. A., Covey, J. P., Miecnikowski, M. T., Yan, B., Gadway, B., Ye, J., and Jin, D. S., “*Creation of a low-entropy quantum gas of polar molecules in an optical lattice*,” *Science* **350**, 1507.02377 (2015).
- Mourachko, I., Comparat, D., de Tomasi, F., Fioretti, A., Nosbaum, P., Akulin, V. M., and Pillet, P., “*Many-Body Effects in a Frozen Rydberg Gas*,” *Physical Review Letters* **80**, 253–256 (1998).
- Mudrich, M., Zahzam, N., Vogt, T., Comparat, D., and Pillet, P., “*Back and Forth Transfer and Coherent Coupling in a Cold Rydberg Dipole Gas*,” *Physical Review Letters* **95**, 233002 (2005).
- Müller, M., Lesanovsky, I., Weimer, H., Büchler, H. P., and Zoller, P., “*Mesoscopic Rydberg Gate Based on Electromagnetically Induced Transparency*,” *Physical Review Letters* **102**, 170502 (2009).
- Nägerl, H. C., Leibfried, D., Rohde, H., Thalhammer, G., Eschner, J., Schmidt-Kaler, F., and Blatt, R., “*Laser addressing of individual ions in a linear ion trap*,” *Physical Review A* **60**, 145–148 (1999).
- Najafov, H., Lee, B., Zhou, Q., Feldman, L. C., and Podzorov, V., “*Observation of long-range exciton diffusion in highly ordered organic semiconductors*,” *Nature Materials* **9**, 938–943 (2010).

- Nielsen, M. A. and Chuang, I. L., *Quantum Computation and Quantum Information: 10th Anniversary Edition*, 10th ed. (Cambridge University Press, New York, NY, USA, 2011).
- Nogrette, F., Labuhn, H., Ravets, S., Barredo, D., Béguin, L., Vernier, A., Lahaye, T., and Browaeys, A., “*Single-Atom Trapping in Holographic 2D Arrays of Microtraps with Arbitrary Geometries*,” *Physical Review X* **4**, 021034 (2014).
- Olmos, B., Lesanovsky, I., and Garrahan, J. P., “*Facilitated Spin Models of Dissipative Quantum Glasses*,” *Physical Review Letters* **109**, 020403 (2012).
- Olmos, B., Müller, M., and Lesanovsky, I., “*Thermalization of a strongly interacting 1D Rydberg lattice gas*,” *New Journal of Physics* **12**, 013024 (2010).
- Ortner, M., Micheli, A., Pupillo, G., and Zoller, P., “*Quantum simulations of extended Hubbard models with dipolar crystals*,” *New Journal of Physics* **11**, 055045 (2009).
- Osten, W., “*Holography in New Shoes: A Digital-Analogue Interface*,” in **2006 IEEE LEOS Annual Meeting Conference Proceedings** (IEEE, 2006) pp. 72–73.
- Peter, D., Yao, N. Y., Lang, N., Huber, S. D., Lukin, M. D., and Büchler, H. P., “*Topological bands with a Chern number $C=2$ by dipolar exchange interactions*,” *Physical Review A* **91**, 053617 (2015).
- Petrosyan, D., Mølmer, K., and Fleischhauer, M., “*On the adiabatic preparation of spatially-ordered Rydberg excitations of atoms in a one-dimensional optical lattice by laser frequency sweeps*,” *Journal of Physics B: Atomic, Molecular and Optical Physics* **49**, 084003 (2016).
- Platt, B. C. and Shack, R., “*History and principles of Shack-Hartmann wavefront sensing*,” *Journal of Refractive Surgery* **17**, 573–577 (2001).
- Pohl, T., Demler, E., and Lukin, M. D., “*Dynamical Crystallization in the Dipole Blockade of Ultracold Atoms*,” *Physical Review Letters* **104**, 043002 (2010).
- Ravets, S., *Development of tools for quantum engineering using individual atoms: optical nanofibers and controlled Rydberg interactions*, **Ph.D. thesis**, Université Paris XI (2014).
- Ravets, S., Labuhn, H., Barredo, D., Béguin, L., Lahaye, T., and Browaeys, A., “*Coherent dipole-dipole coupling between two single Rydberg atoms at an electrically-tuned Förster resonance*,” *Nature Physics* **10**, 914–917 (2014).

- Ravets, S., Labuhn, H., Barredo, D., Lahaye, T., and Browaeys, A., “*Measurement of the angular dependence of the dipole-dipole interaction between two individual Rydberg atoms at a Förster resonance,*” *Physical Review A* **92**, 020701 (2015).
- Reinhard, A., Liebisch, T. C., Knuffman, B., and Raithel, G., “*Level shifts of rubidium Rydberg states due to binary interactions,*” *Physical Review A* **75**, 032712 (2007).
- Reinhard, A., Younge, K. C., and Raithel, G., “*Effect of Förster resonances on the excitation statistics of many-body Rydberg systems,*” *Physical Review A* **78**, 060702 (2008).
- Reymond, G., Schlosser, N., Protsenko, I., and Grangier, P., “*Single-atom manipulations in a microscopic dipole trap,*” *Philosophical Transactions of the Royal Society A: Mathematical, Physical and Engineering Sciences* **361**, 1527–1536 (2003).
- Reymond, G.-O., Etudes expérimentales d’atomes dans un piège dipolaire microscopique, *Ph.D. thesis*, Université Paris Sud - Paris XI (2002).
- Richerme, P., Gong, Z.-X., Lee, A., Senko, C., Smith, J., Foss-Feig, M., Michalakis, S., Gorshkov, A. V., and Monroe, C., “*Non-local propagation of correlations in quantum systems with long-range interactions.*” *Nature* **511**, 198–201 (2014).
- Robicheaux, F. and Hernández, J. V., “*Many-body wave function in a dipole blockade configuration,*” *Physical Review A* **72**, 063403 (2005).
- Rydberg, J., *Recherches sur la constitution des spectres d’émission des éléments chimiques*. (Norstedt, 1890).
- Saffman, M. and Walker, T. G., “*Analysis of a quantum logic device based on dipole-dipole interactions of optically trapped Rydberg atoms,*” *Physical Review A* **72**, 022347 (2005).
- Saffman, M., Walker, T. G., and Mølmer, K., “*Quantum information with Rydberg atoms,*” *Reviews of Modern Physics* **82**, 2313–2363 (2010).
- Santos, L., Baranov, M., Cirac, J., Everts, H.-U., Fehrmann, H., and Lewenstein, M., “*Atomic Quantum Gases in Kagomé Lattices,*” *Physical Review Letters* **93**, 030601 (2004).
- Schauß, P., High-resolution imaging of ordering in Rydberg many-body systems, *Ph.D. thesis* (2014).

- Schauß, P., Cheneau, M., Endres, M., Fukuhara, T., Hild, S., Omran, A., Pohl, T., Gross, C., Kuhr, S., and Bloch, I., “*Observation of spatially ordered structures in a two-dimensional Rydberg gas,*” *Nature* **491**, 87–91 (2012).
- Schauss, P., Zeiher, J., Fukuhara, T., Hild, S., Cheneau, M., Macri, T., Pohl, T., Bloch, I., and Gross, C., “*Crystallization in Ising quantum magnets,*” *Science* **347**, 1455–1458 (2015).
- Schempp, H., Günter, G., Robert-de Saint-Vincent, M., Hofmann, C. S., Breyel, D., Komnik, A., Schönleber, D. W., Gärttner, M., Evers, J., Whitlock, S., and Weidemüller, M., “*Full Counting Statistics of Laser Excited Rydberg Aggregates in a One-Dimensional Geometry,*” *Physical Review Letters* **112**, 013002 (2014).
- Schlosser, M., Tichelmann, S., Kruse, J., and Birkel, G., “*Scalable architecture for quantum information processing with atoms in optical micro-structures,*” *Quantum Information Processing* **10**, 907–924 (2011).
- Schlosser, N., Reymond, G., and Grangier, P., “*Collisional Blockade in Microscopic Optical Dipole Traps,*” *Physical Review Letters* **89**, 023005 (2002).
- Schlosser, N., Reymond, G., Protsenko, I., and Grangier, P., “*Sub-poissonian loading of single atoms in a microscopic dipole trap.*” *Nature* **411**, 1024–1027 (2001).
- Schneider, C., Porras, D., and Schaetz, T., “*Experimental quantum simulations of many-body physics with trapped ions.*” *Reports on progress in physics. Physical Society (Great Britain)* **75**, 024401 (2012).
- Scholak, T., de Melo, F., Wellens, T., Mintert, F., and Buchleitner, A., “*Efficient and coherent excitation transfer across disordered molecular networks,*” *Physical Review E* **83**, 021912 (2011).
- Schrader, D., Dotsenko, I., Khudaverdyan, M., Miroshnychenko, Y., Rauschenbeutel, A., and Meschede, D., “*Neutral Atom Quantum Register,*” *Physical Review Letters* **93**, 150501 (2004).
- Schrödinger, E., “*Are there Quantum Jumps?*” *The British Journal for the Philosophy of Science* **III**, 233–242 (1952).
- Schwarzkopf, A., Sapiro, R. E., and Raithel, G., “*Imaging Spatial Correlations of Rydberg Excitations in Cold Atom Clouds,*” *Physical Review Letters* **107**, 103001 (2011).

- Shih, C.-Y. and Chapman, M. S., “*Nondestructive light-shift measurements of single atoms in optical dipole traps,*” *Physical Review A* **87**, 063408 (2013).
- Simon, J., Bakr, W. S., Ma, R., Tai, M. E., Preiss, P. M., and Greiner, M., “*Quantum simulation of antiferromagnetic spin chains in an optical lattice.*” *Nature* **472**, 307–12 (2011).
- Singer, K., Reetz-Lamour, M., Amthor, T., Marcassa, L. G., and Weidemüller, M., “*Suppression of Excitation and Spectral Broadening Induced by Interactions in a Cold Gas of Rydberg Atoms,*” *Physical Review Letters* **93**, 163001 (2004).
- Somaroo, S., Tseng, C. H., Havel, T. F., Laflamme, R., and Cory, D. G., “*Quantum Simulations on a Quantum Computer,*” *Physical Review Letters* **82**, 5381–5384 (1999).
- Sortais, Y. R. P., Marion, H., Tuchendler, C., Lance, A. M., Lamare, M., Fournet, P., Armellin, C., Mercier, R., Messin, G., Browaeys, A., and Grangier, P., “*Diffraction-limited optics for single-atom manipulation,*” *Physical Review A* **75**, 013406 (2007).
- Struck, J., Ölschläger, C., Le Targat, R., Soltan-Panahi, P., Eckardt, A., Lewenstein, M., Windpassinger, P., and Sengstock, K., “*Quantum simulation of frustrated classical magnetism in triangular optical lattices.*” *Science* **333**, 996–9 (2011).
- Texas Advanced Computing Center,, “*8 Things You Should Know About GPGPU Technology,*” Tech. Rep. (<https://www.tacc.utexas.edu/documents/13601/88790/8Things.pdf>, 2010).
- Tey, M. K., Chen, Z., Aljunid, S. A., Chng, B., Huber, F., Maslennikov, G., and Kurtsiefer, C., “*Strong interaction between light and a single trapped atom without the need for a cavity,*” *Nature Physics* **4**, 924–927 (2008).
- Tong, D., Farooqi, S. M., Stanojevic, J., Krishnan, S., Zhang, Y. P., Côté, R., Eyler, E. E., and Gould, P. L., “*Local Blockade of Rydberg Excitation in an Ultracold Gas,*” *Physical Review Letters* **93**, 063001 (2004).
- Tresp, C., Bienias, P., Weber, S., Gorniaczyk, H., Mirgorodskiy, I., Büchler, H. P., and Hofferberth, S., “*Dipolar Dephasing of Rydberg D-State Polaritons,*” *Physical Review Letters* **115**, 083602 (2015).
- Tuchendler, C., Lance, A. M., Browaeys, A., Sortais, Y. R. P., and Grangier, P., “*Energy distribution and cooling of a single atom in an optical tweezer,*” *Physical Review A* **78**, 033425 (2008).

- Urban, E., Johnson, T. A., Henage, T., Isenhower, L., Yavuz, D. D., Walker, T. G., and Saffman, M., “*Observation of Rydberg blockade between two atoms,*” *Nature Physics* **5**, 110–114 (2009).
- Urvoy, A., Ripka, F., Lesanovsky, I., Booth, D., Shaffer, J. P., Pfau, T., and Löw, R., “*Strongly Correlated Growth of Rydberg Aggregates in a Vapor Cell,*” *Physical Review Letters* **114**, 203002 (2015).
- Vermersch, B., Glaetzle, a. W., and Zoller, P., “*Magic distances in the blockademechanism of Rydberg p and d states,*” *Physical Review A* **91**, 023411 (2015).
- Viteau, M., Bason, M. G., Radogostowicz, J., Malossi, N., Ciampini, D., Morsch, O., and Arimondo, E., “*Rydberg Excitations in Bose-Einstein Condensates in Quasi-One-Dimensional Potentials and Optical Lattices,*” *Physical Review Letters* **107**, 060402 (2011).
- Vogt, T., Viteau, M., Chotia, A., Zhao, J., Comparat, D., and Pillet, P., “*Electric-Field Induced Dipole Blockade with Rydberg Atoms,*” *Physical Review Letters* **99**, 073002 (2007).
- Volkov, S. and Wong, T., “*A note on random walks in a hypercube,*” *Pi Mu Epsilon journal* **9**, 551–557 (2008).
- Walker, T. G. and Saffman, M., “*Zeros of RydbergRydberg Förster interactions,*” *Journal of Physics B: Atomic, Molecular and Optical Physics* **38**, S309–S319 (2005).
- Weimer, H. and Büchler, H. P., “*Two-Stage Melting in Systems of Strongly Interacting Rydberg Atoms,*” *Physical Review Letters* **105**, 230403 (2010).
- Weimer, H., Löw, R., Pfau, T., and Büchler, H. P., “*Quantum Critical Behavior in Strongly Interacting Rydberg Gases,*” *Physical Review Letters* **101**, 250601 (2008).
- Weiner, A. M., “*Femtosecond pulse shaping using spatial light modulators,*” *Review of Scientific Instruments* **71**, 1929 (2000).
- Weise, T., *Global Optimization Algorithms, Theory and Application*, 2nd ed. (<http://it-weise.de>, 2009).
- Weitenberg, C., Endres, M., Sherson, J. F., Cheneau, M., Schauß, P., Fukuhara, T., Bloch, I., and Kuhr, S., “*Single-spin addressing in an atomic Mott insulator,*” *Nature* **471**, 319–324 (2011).

- Wilk, T., Gaëtan, A., Evellin, C., Wolters, J., Miroshnychenko, Y., Grangier, P., and Browaeys, A., “*Entanglement of Two Individual Neutral Atoms Using Rydberg Blockade,*” *Physical Review Letters* **104**, 010502 (2010).
- Windpassinger, P. and Sengstock, K., “*Engineering novel optical lattices,*” *Reports on Progress in Physics* **76**, 086401 (2013).
- Wineland, D. J., “*Nobel Lecture: Superposition, entanglement, and raising Schrödinger’s cat,*” *Reviews of Modern Physics* **85**, 1103–1114 (2013).
- Yan, S., Huse, D. A., and White, S. R., “*Spin-Liquid Ground State of the $S = 1/2$ Kagome Heisenberg Antiferromagnet,*” *Science* **332**, 1173–1176 (2011).
- Yao, N. Y., Zaletel, M. P., Stamper-Kurn, D. M., and Vishwanath, A., “*A Quantum Dipolar Spin Liquid,*” (2015), [arXiv:1510.06403](https://arxiv.org/abs/1510.06403) .
- Zeihner, J., Schauß, P., Hild, S., Macrì, T., Bloch, I., and Gross, C., “*Microscopic Characterization of Scalable Coherent Rydberg Superatoms,*” *Physical Review X* **5**, 031015 (2015).
- Zernike, v. F., “*Beugungstheorie des schneidenverfahrens und seiner verbesserten form, der phasenkontrastmethode,*” *Physica* **1**, 689–704 (1934).

Acknowledgements

At the end of this thesis I would like to take the opportunity to thank the people that allowed me to have a truly enjoyable and productive time in these three years of my PhD.

Above all I would like to thank my thesis supervisor Antoine Browaeys for giving me the great opportunity to work on such an ingeniously conceived experiment as CHADOQ. I think few PhD students are lucky enough to have a thesis director with such an immense knowledge of physics, who is supportive in every aspect, curious on the progress of the work on a day-to-day basis, as you have been.

Likewise I want to thank my co-supervisor Thierry Lahaye. Your compassion for the experiment and physics in general was contagious. You always took the time, no matter what you were doing at the given moment, to explain me anything about physics, electronics, how to give good presentations, how to write good scientific articles, or the particularities of the french language.

I thank the members of the jury, Pierre Pillet, Matthias Weidemüller, Gerhard Birkl, and Matt Jones, for reading my manuscript and for taking the (mostly) long journeys to the Institut d'Optique for my thesis defence. In particular I would like to thank Matthias for sparking my interest in the physics of cold atoms during his lectures and my thesis in my Master program in Heidelberg, and for giving me the opportunity to participate in the Rydberg workshop in Pisa where I had the chance to meet Antoine and Thierry for the first time.

A big thanks also goes to Lucas Béguin and Aline Vernier, for having started this amazing experiment, and thus laid the more than solid foundation for my PhD. Thank you Florence for all the help with the SLM and other stuff concerning the experiment, and bringing your patience and your contagious, never-ending positive mood to the group.

The most important people of my PhD-life were surely Sylvain Ravets and Daniel Barredo. I don't know how many countless hours we spent in the lab, realigning the MOT, taking data, coupling fibres, taking data, relocking lasers, taking data, coding, and taking data. Still, no matter what problems were awaiting us in the lab, every morning in the RER I was looking forward to tweaking the experiment with you guys to get to still a little bit more out of it. I could not have imagined a better team to work with. You guys have truly been the best. That's what it is.

I was lucky enough to be part of and being financed through the COHERENCE ITN, having allowed me to attend various conferences and workshops. Most notably I thank Hannes Busche, for the great times at and around the COHERENCE events. It also was a great time having you in Paris, working together on the experiment and enjoying the city.

Also the people not directly involved deserve a big thanks. Stephan Jennewein for not letting me forget my German here in France. Ronan Bourgain for being a great office and rue Daguerre neighbour. Yvan Sortais for all the advice concerning any type of optics. Imam for discoveries of bike tours, the swiss cuisine, and for being a great friend. Jean for the talks about music and the badminton sessions. Martin for your good mood, your motivation for physics, and for doing the longest marathon in the world together. Mauro for raising the bar in the many football matches. Erwan for your company during the cumulated weeks of RER rides. Rajiv for your tranquility in every situation. Sylvain for knowing the experiment in good hands. The rest of the Quantum Optics and the Atom Optics group. The mechanical and optical workshop of the Institut, for their support for the experiment, and for printing my posters last minute before leaving for a conference. The Football, Badminton, Tennis, biking and running groups, for the most welcome distraction from the dark lab.

Mon groupe de professeurs particuliers de Français, notamment Iman, Florence, et Ingrid, pour m'apprendre cette belle langue si facilement.

Catriona, for having been a great, midnight-dinner-providing housemate and friend.

My friends, at the IOGS, in Paris, and all over the world.

My parents, for always supporting me in everything I ever did.

My sisters, for always being there for me, making me feel at home in Paris from the very beginning, and being the best housemates and neighbours.

And Ingrid, for being there.

Titre : La dynamique et corrélations d'excitations Rydberg dans des matrices 2D des atomes unique

Mots clés : création des états quantiques, piégeage d'atomes uniques, atomes Rydberg, SLM

Résumé : Dans cette thèse, nous mesurons la dynamique cohérente et les corrélations spatiales des excitations Rydberg dans des matrices 2D d'atomes uniques. Nous utilisons un modulateur spatial de lumière pour façonner la phase spatiale d'un faisceau laser de piégeage optique avant de le focaliser avec une lentille asphérique de grande ouverture numérique. En imprimant une phase appropriée sur le faisceau laser, nous pouvons créer des matrices 2D de pièges optiques, de forme arbitraire et facilement reconfigurables, avec jusqu'à 100 pièges séparées de quelques micromètres. Les pièges sont chargés à partir d'un nuage d'atomes froids de 87Rb , et due aux collisions assistées par la lumière, au plus un seul atome peut être présent dans chaque piège en même temps. Une caméra CCD sensible permet en temps réel l'imagerie de la fluorescence atomique émanant des pièges, ce qui nous permet de détecter individuellement la présence d'un atome dans chaque piège avec une précision presque parfaite. Pour créer des interactions importantes entre les atomes uniques, nous les excitons vers des états de Rydberg, qui sont des états électroniques avec un nombre quantique principal élevé. Un faisceau supplémentaire d'adressage permet la manipulation individuelle d'un atome sélectionné dans la matrice. La connaissance précise, de la fois de la matrice des atomes préparé et des positions des excitations Rydberg, nous a permis de mesurer l'augmentation collective de la couplage optique dans le régime de blocage Rydberg, où une seule excitation est partagée de façon symétrique entre tous les atomes de la matrice. Dans le régime où l'interaction ne s'étend que sur quelques sites, nous avons mesuré la dynamique et les corrélations spatiales des excitations Rydberg, dans des matrices d'atomes à une et deux dimensions. La comparaison à une simulation numérique d'un modèle d'Ising quantique d'un système de spin-1/2 montre un accord exceptionnel pour les matrices où l'effet de l'anisotropie de l'interaction Rydberg-Rydberg est faible. Les résultats obtenus démontrent que les atomes Rydberg uniques sont une plate-forme bien adaptée pour la simulation quantique des systèmes de spin.

Title : Rydberg excitation dynamics and correlations in arbitrary 2D arrays of single atoms

Keywords : quantum state engineering, single atom trapping, Rydberg atoms, spatial light modulator

Abstract : In this thesis, we measure the coherent dynamics and the pair correlations of Rydberg excitations in two-dimensional arrays of single atoms. We use a spatial light modulator to shape the spatial phase of a single optical dipole trap beam before focusing it with a high numerical-aperture aspheric lens. By imprinting an appropriate phase pattern on the trap beam, we can create arbitrarily shaped and easily reconfigurable 2D arrays of high-quality single-atom traps, with trap-spacings of a few micrometers for up to 100 traps. The traps are loaded from a cloud of cold 87Rb atoms, and due to fast light-assisted collisions of atoms inside the traps, at most one atom can be present in each trap at the same time. A sensitive CCD camera allows the real-time, site-resolved imaging of the atomic fluorescence from the traps, enabling us to detect the presence of an atom in each individual trap with almost perfect accuracy. In order to induce strong, tunable interactions between the atoms in the array, we coherently laser-excite them to Rydberg states, which are electronic states with a high principal quantum number. An additional addressing beam allows the individual manipulation of an atom at a selected site in the array. The precise knowledge of both the prepared atom array and the positions of the Rydberg excitations allowed us to measure the collective enhancement of the optical coupling strength in the regime of full Rydberg blockade, where one single excitation is shared symmetrically among all atoms in the array. In the regime where the strong interaction only extends over a few sites, we measured the dynamics and the spatial pair-correlations of Rydberg excitations, in one- and two-dimensional atom arrays. The comparison to a numerical simulation of a quantum Ising model of a spin-1/2 system shows an exceptional agreement for trap geometries where the effect of the anisotropy of the Rydberg-Rydberg interaction is small. The obtained results demonstrate that single Rydberg atoms are a suitable platform for the quantum simulation of spin systems.

